OPTOGENETIC FEEDBACK CONTROL OF NEURAL ACTIVITY

A Thesis
Presented to
The Academic Faculty

by

Jonathan P. Newman

In Partial Fulfillment
of the Requirements for the Degree
Doctor of Philosophy in the
School of Engineering

Georgia Institute of Technology
December 2013

OPTOGENETIC FEEDBACK CONTROL OF NEURAL ACTIVITY

Approved by:

Professor Steve M. Potter, Advisor
Department of Biomedical Engineering
Georgia Institute of Technology

Professor Garrett B. Stanley
Department of Biomedical Engineering
Georgia Institute of Technology

Professor Robert J. Butera
Department of Biomedical Engineering & Department of Electrical Engineering
Georgia Institute of Technology

Professor Daniel A. Wagenaar
Department of Biological Sciences
University of Cincinnati

Professor Astrid A. Prinz
Department of Biology
Emory University

Date Approved: October 24, 2013

To my family

ACKNOWLEDGEMENTS

I would like to express the deepest appreciation to my mentor, Dr. Steve Potter, who has been a constant supporter of my ideas and allowed me the freedom to explore far too many projects during my thesis work. The practical knowledge and maturity-concerning-failure that I have gained as a result of Steve's do-it-yourself approach to science has made me confident in my own abilities and eager to take the next steps in my scientific career.

I also gratefully acknowledge the efforts of the members of my thesis committee, Dr. Robert Butera, Dr. Garrett Stanley, Dr. Astrid Prinz, and Dr. Daniel Wagenaar, whose advice has greatly improved the quality of this work.

I am greatly indebted to my wonderful colleagues and collaborators at Georgia Tech: Sharanya, Daniel, Yogi, J.T., Garrett, and Rob, Emory University: Bob, Ming, and Pete, and the Max Planck Institute for Brain Research: Tatjana. Each of you has, on at least one (and probably several) occasions contributed to me a kernel of knowledge that was completely orthogonal to my understanding of the universe at that time. When it happened I probably did not even acknowledge it, in order to maintain some air of professionalism, even though I wanted to jump up and down.

Especially important has been my collaboration with Ming-fai. Ming has been a great friend and scientific collaborator over the past five years. Through many discussions and a number of collaborative projects, she has contributed enormously to the quality and breadth of the work presented here. I am deeply thankful for opportunity to work with Ming, and I look forward to continuing our mutual scientific journey.

I want to thank the innumerable, faceless contributors to my work that exist on

Internet forums for open-source hardware and software development. The the drive of the open-content community towards the 'unconditional understanding, and subsequent modification, of all things' is a consistent and practical source of inspiration.

I want to acknowledge a few of my friends here in Atlanta who have privileged me with with good conversation (about science mostly, and, sometimes, other stuff). In no particular order, Chris, Stef, Damon, Dave, Riley, Eric, Jeenah, Mei, Michelle, Neal, Jack, Yogi, Jeff, and Stephen: thank you, sincerely. You are all wonderful.

Finally, Mom (Carol) and Dad (Leon) and Brother (Eric): Thank you for believing in me and pushing me, even though, during the 6th-14th grades, I got Cs in my classes. I love you all very, very much.

This work was supported by U.S.A National Science Foundation Cognitive Optimization and Prediction grant 1238097, U.S.A National Institutes of Health grant 1R01NS079757-01, U.S.A. National Science Foundation Graduate Research Fellowship 08-593, and U.S.A National Science Foundation Integrative Graduate Education and Research Traineeship DGE-0333411.

TABLE OF CONTENTS

LIST OF TABLES

LIST OF FIGURES

SUMMARY

Optogenetics is a set of technologies that enable optically triggered gain or loss of function in genetically specified populations of cells. Optogenetic methods have revolutionized experimental neuroscience by allowing precise excitation or inhibition of firing in specified neuronal populations embedded within complex, heterogeneous tissue. Although optogenetic tools have greatly improved our ability manipulate neural activity, they do not offer control of neural firing in the face of ongoing changes in network activity, plasticity, or sensory input. In this thesis, I develop a feedback control technology that automatically adjusts optical stimulation in real-time to precisely control network activity levels. I describe hardware and software tools, modes of optogenetic stimulation, and control algorithms required to achieve robust neural control over timescales ranging from seconds to days. I then demonstrate the scientific utility of these technologies in several experimental contexts. First, I investigate the role of connectivity in shaping the network encoding process using continuously-varying optical stimulation. I show that synaptic connectivity linearizes the neuronal response, verifying previous theoretical predictions. Next, I use long-term optogenetic feedback control to show that reductions in excitatory neurotransmission directly trigger homeostatic increases in synaptic strength. This result opposes a large body of literature on the subject and has significant implications for memory formation and maintenance. The technology presented in this thesis greatly enhances the precision with which optical stimulation can control neural activity, and allows causally related variables within neural circuits to be studied independently.

CHAPTER I

INTRODUCTION

Innumerable distinct mechanisms give rise the brain's multiplex functionality. These mechanisms act over time scales ranging from single action potentials to long-term memories, and spatial scales ranging from individual dendritic spines to connections between brain regions. The chemical, morphological, electrical, and genetic processes required for neural function coexist and interact, resulting in tangled webs of cause and effect. This complexity makes the brain a very difficult system to approach scientifically because the experimental perturbation of one variable inevitably affects many others. Therefore, despite tremendous progress in genetics, microbiology, microelectronics, data acquisition, and computer processing, neuroscientists still possesses only a rudimentary understanding of how the brain develops and operates. Further, the existing knowledge set is diverse, and has yet to be stitched into a cohesive set of principles that adequately describe the most interesting aspects of brain function - information processing, learning, and memory.

Rather than dealing with neural complexity on nature's terms, our lab has chosen to investigate simplified systems that capture some of the brain's essential features. We study cultured cortical networks which are grown on beds of microelectrodes. The utility of this approach is evidenced by previous successes in other fields of science, most notably in physics. By performing careful measurements on a cleverly devised, simplified system, fundamental principles can be derived that are accurate in a much broader context. Analogously, we believe that many important aspects of neural function exist in cultured networks and that the study of these reduced preparations may inform the development of fundamental principles that apply to the intact brain.

1.1 *A minimal* in-vitro *model to study neural connectivity, signal-transduction, and stability*

When supplied with an appropriate mixture of nutrients and a protein bed to grow upon, dissociated neurons and glial cells will form a densely connected, highly-active signaling network. Primary neuronal cultures offer unmatched experimental access for imaging, neural stimulation, genetic manipulation, and pharmacology (Fig. 1). For instance, cultured cortical networks can be maintained on top of microelectrode arrays (MEAs), which are embedded in the culturing surface. This allows the continuous, non-invasive, electrical readout of spatio-temporal activity patterns produced by the network as it develops (Jimbo *et al.*, 1999; Potter and DeMarse, 2001; Wagenaar *et al.*, 2006c; Minerbi *et al.*, 2009; Gal *et al.*, 2010; Hales *et al.*, 2012) (Fig. 1(c)). Because of their experimental accessibility, cultured cortical networks have often served as a testing ground for new genetic and electrophysiology tools (Hamill *et al.*, 1981; Fiscella *et al.*, 2012; Robinson *et al.*, 2012; Bakkum *et al.*, 2013) and as a generalized model for neuronal plasticity (Bi and Poo, 1998; Turrigiano *et al.*, 1998; Bakkum *et al.*, 2008b). Our lab has previously developed hardware and software tools to better exploit the experimental advantages afforded by cultured cortical networks (Wagenaar and Potter, 2002, 2004; Rolston *et al.*, 2009a), and we have used these tools to make insights into learning and plasticity at the network level (Madhavan *et al.*, 2007; Bakkum *et al.*, 2008a,b; Chao *et al.*, 2008), spontaneous network dynamics (Wagenaar *et al.*, 2006b,c; Rolston *et al.*, 2007), and to control aberrant network dynamics using electrical stimulation (Wagenaar *et al.*, 2005). Other labs have also leveraged cultured cortical networks and MEA technology to study long-term modulations in neural excitability over extended timescales (Gal *et al.*, 2010), homeostatic plasticity (Minerbi *et al.*, 2009), and rhythmic motor activity (Darbon *et al.*, 2002). Additionally, researchers have produced new MEAs with improved spatial resolution (Bakkum *et al.*, 2013; Müller *et al.*, 2013; Fiscella *et al.*, 2012) and signal-to-noise ratios approaching

those of intracellular recordings (Robinson *et al.*, 2012) .

Because MEAs offer many simultaneous measurements of spiking activity, they are especially well suited for rapid, accurate estimation of the population firing rate. The population firing rate within a functional region is the most robust correlate of sensory and motor information in the brain. It can be used to decode the direction of arm movements (Georgopoulos *et al.*, 1988), the perception of visual motion (Steinmetz *et al.*, 1987), and an animal's physical location within an environment (Brown *et al.*, 1998). Obtaining robust control of the firing rate of precisely defined neural populations will allow more straightforward investigations of causal links between neural activity and sensation or behavior. Further, improved control over activity in neural tissue involved in sensory or motor processing will enable improved sensory and motor prosthetic devices. Finally, technologies that allow precise, external control over population firing levels will confer the ability to experimentally decouple firing activity from potentially related system variables. For instance, spiking and neurotransmission, which are highly interdependent processes, could be decoupled if direct experimental control of firing was achieved. This would allow the independent roles of neural firing to be parsed out from a complex web of other related processes.

The feasibility of firing rate control hinges on the functionality of three components that are common to every control system:

1. **The plant:** The system to be controlled.

2. **The sensor:** A device used to measure some aspect of the the plant's state(s).

3. **The actuator:** A device used to affect the plant's state(s).

Given their accessibility and built-in electrophysiological readout, cultured cortical networks (the plant) grown on microelectrode arrays (the sensor) offer an ideal starting point for the development of technologies aimed at precisely controlling neural activity. It has been shown previously that multisite electrical micro-stimulation can

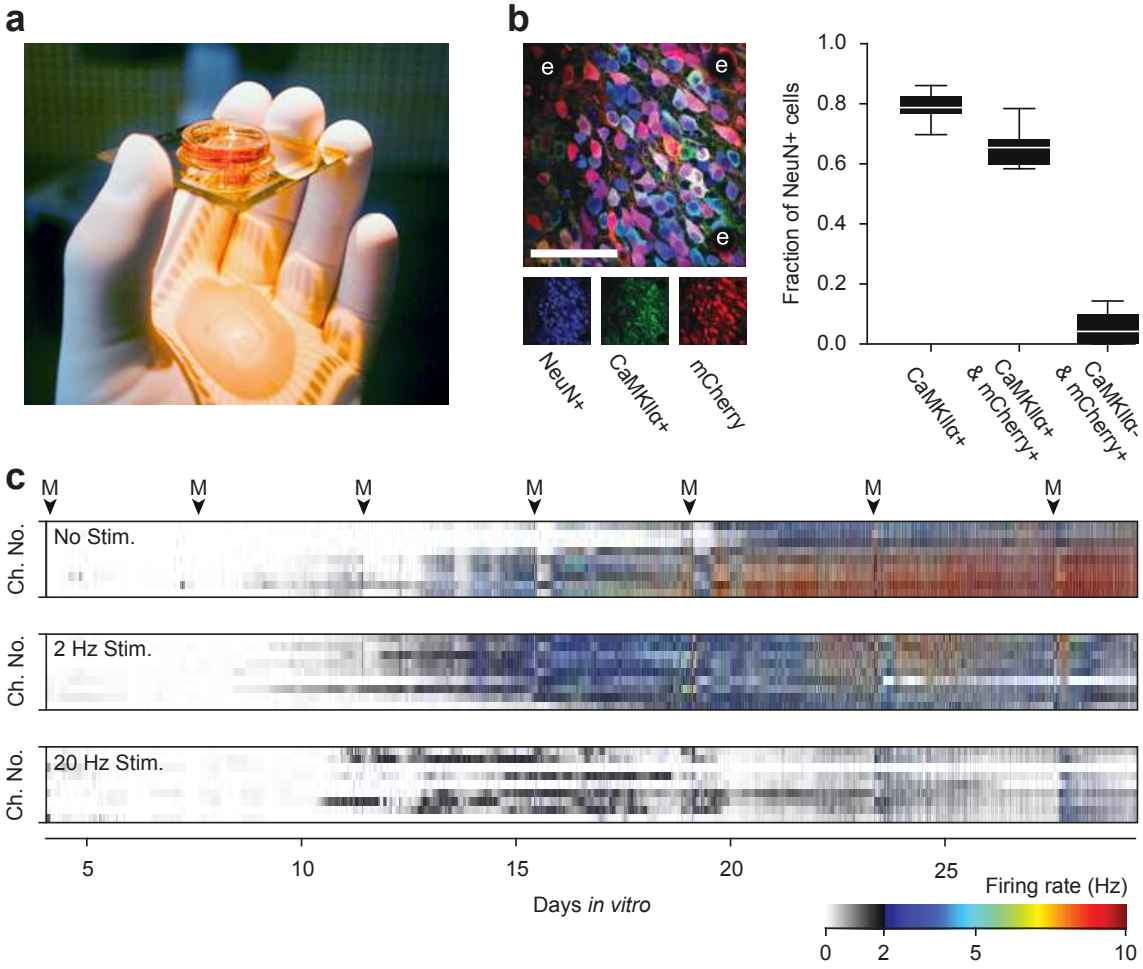

Figure 1: MEAs offer superb experimental access. **(a)** An MEA is held by a researcher. Sixty electrical leads, which emanate from mirco-electrodes embedded at the culturing well's center, cast shadows onto the researcher's hand (photo courtesy of Dr. Steve M. Potter). **(b)** Cultured networks on MEAs allow excellent molecular, genetic, and optical access. *Left,* An overlaid confocal photomicrograph shows cell bodies with immunoreactivity against neuronal nuclear protein (NeuN; blue) and Ca^2+/calmodulin-dependent protein kinase IIα (CaMKIIα; green) which is preferentially expressed in excitatory neurons. Red fluorescence indicates the expression of the fluorescent protein mCherry, which in this case is driven by a CaMKIIα promoter. The mCherry construct was transduced using a bath-delivered adeno-associated viral vector. 'e' denotes electrode locations. Scalebar, 100 μm. *Right,* A box plot quantifies the expression efficiency and specificity of mCherry in NeuN-expressing cells (putative neurons). Data from 3 cultures over 12 regions of interest. **(c)** MEAs allow excellent electrophysiology access. One month of simultaneous, continuous multi-site electrical recordings was performed on 6 sister cultures using an MEA with 6 integrated culturing/recording chambers. The colormaps show detected firing activity on each electrode in three of these cultures over their first 29 days *in vitro*. Two of these cultures were chronically stimulated with spatially random 2 or 20 Hz aggregate-rate electrical pulses for the duration of their development. Bin size, 1 minute. 'M' denotes the occurrence of a medium exchange.

serve as a powerful actuator of cultured network firing activity (Wagenaar *et al.*, 2005; Newman *et al.*, 2013; Wallach *et al.*, 2011), and can be used for successful control of population firing. However, recent genetic approaches offer powerful alternatives for neural actuation.

1.2 Optogenetics - controlling neurons with photons

In spite of our lab's progress using spatiotemporal electrical stimulation for controlling neural activity (Wagenaar *et al.*, 2005; Wagenaar, 2006; Newman *et al.*, 2013), the control of genetically-defined neural populations relies on a fundamental change in stimulation technology. 'Optogenetics' encompasses a set of techniques that permit the expression of microbial opsins in genetically-specified cell populations, including mammalian neuron subtypes (Boyden *et al.*, 2005; Zhang *et al.*, 2006; Mattis *et al.*, 2011; Yizhar *et al.*, 2011a) (Fig. 2). These proteins allow electophysiological manipulation of neurons using light. The advent of optogenetics has filled a long standing technology gap in cellular-resolution electrophysiology. The use of electrical stimulation techniques to perturb neural activity, starting with experiments performed circa 1771 by Luigi Aloisio Galvani, long precedes the introduction of technologies for reading bioelectric signals. However, there have only been incremental improvements in electrical stimulation techniques during the past ∼200 years. Meanwhile, methods for electrical or optical readout of neural activity have far surpassed electrical stimulation technologies in terms of resolution and bandwidth.

Optogenetic techniques have provided a transformative step away from electrical micro-stimulation (Wagenaar *et al.*, 2004), or optical uncaging of neuro-active substances (Nerbonne *et al.*, 1984), for controlling the activity of neural circuits. This is due to several key characteristics of optogenetic tools. First, the expression of optogenetic proteins can be targeted to genetically-defined populations of cells using promoter sequences. This enables communication with specific neuronal sub-populations

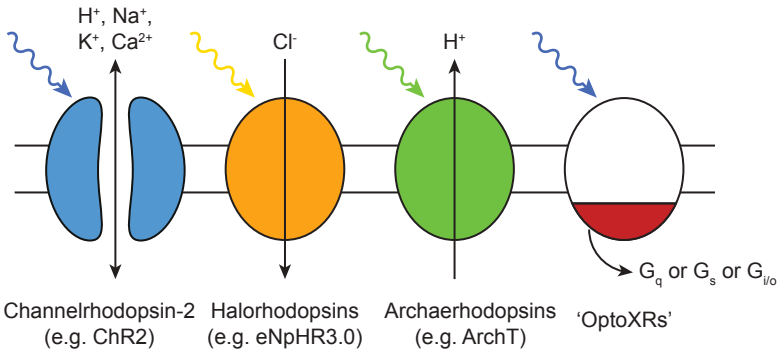

Figure 2: Optogenetic tools for perturbing neural activity. Left to right: Non-specific light-gated cation channels, such as channelrhodopsin-2 (ChR2), can be used to depolarize the resting membrane. Light-powered chloride pumps, such as enhanced halorhopsin3.0 (eNpHR3.0), pump chloride into the cell, causing a drop in membrane potential, which quiets neural activity. Light-powered proton pumps, such as archaerhodopsin-T (ArchT), pump protons out of the cell, causing a drop in membrane potential that can completely silence spiking activity. Engineered G-protein-coupled opsins, 'optoXRs', can be used to optically manipulate various receptor-initiated intracellular biochemical signaling cascades, which can affect cellular excitability and developmental processes. Hundreds of opsin variants, each conferring some specialization in function, are currently in active laboratory use.

whilst using optical signals that are spatially homogeneous. Therefore, the specificity of neuronal stimulation is no longer contingent on precisely controlling the spatial characteristics of chemical gradients or electrical fields, both of which are difficult to govern within the complex, non-homogeneous structure of neural tissue.

Second, interference between electrical recording and optical stimulation is negligible when a few precautions are respected. Therefore, sensitive electrical recordings can be conducted simultaneous to optical stimulation without incurring artifacts on recording lines. This is not the case for electrical stimulation, since the voltages and currents required to produce a neural response are many orders of magnitude larger than those used to detect neural activity (Wagenaar and Potter, 2002). In the same vein, the excitation spectra of different opsin types occupy relatively narrow regions of the UV through IR electromagnetic spectrum. This implies that different opsin types, supporting unique functions, can be activated independently within the same experimental preparation (Chow *et al.*, 2010).

Third, the optogenetic tool-set is expanding. The first optogenetic tools required the coexpression of three *Drosophila*-derived genes, including an opsin, arrestin-2

as a regulatory element, and the α G-protein subunit. The opsin then needed to be functionalized via a covalent bond with exogenous retinal. When activated it produced slow, imprecise current waveforms, but was able to grossly modulate spiking activity (Zemelman *et al.*, 2002). Secondary tools derived from Shaker K^+ channels improved the temporal characteristics of firing control, but conferred abnormal resting conductances and still required exogenous co-factors (Banghart *et al.*, 2004). The first truly practical optogenetic tool was channelrhodopsin-2 (Boyden *et al.*, 2005) (ChR2; Fig 2) which facilitated millisecond-timescale photocurrents to precisely drive spiking using a single-component ion channel, required no co-factors, and had no apparent effect on normal physiology (although, see Miyashita *et al.* 2013, which shows that long-term, *in-vivo* expression of ChR2 can induce irregular axon morphology and targeting).

Following the introduction of ChR2 to neuroscience, the natural diversity of the micobial family of opsin genes (Chow *et al.*, 2010; Zhang *et al.*, 2011), and their amenability to genetic manipulation, has provided a diverse set of optogenetic actuators for achieving specific effects on neural activity. New light-sensitive proteins, obtained through genetic screens of different microbial species (Chow *et al.*, 2010) or site-directed mutagenesis of existing constructs (Gunaydin *et al.*, 2010), are continuously being identified (Zhang *et al.*, 2011; Mattis *et al.*, 2011; Yizhar *et al.*, 2011a; Zhao *et al.*, 2008; Berndt *et al.*, 2011). These proteins offer increasingly specialized functionality in order to optimize some feature of their dynamics or specificity. Particularly useful examples of this trend include inward chloride (Gradinaru *et al.*, 2008) and outward proton (Chow *et al.*, 2010) pumps that can be used to suppress neuronal activity (Fig. 2). Such activity reductions cannot be robustly achieved using electrical techniques, and are slow and imprecise using pharmacological methods. Additionally, there are ultra-fast channels, whose kinetics keep pace with the rapid dynamics of fast-spiking interneurons (Gradinaru *et al.*, 2010; Lin *et al.*, 2009). Bi-stable channels,

which support photocurrents long after the optical stimulator is turned off, have also been produced (Yizhar *et al.*, 2011b). Further, opsins can be used to activate intracellular biosignaling cascades (Airan *et al.*, 2009), and provide direct modulation of synaptic activity (Lin *et al.*, 2013; Volgraf *et al.*, 2006). Finally, recent developments in optical sensing technologies, for example to monitor millisecond time-scale glutamatatergic neurotransmission (Marvin *et al.*, 2013), and intracellular calcium sensors designed to occupy excitation spectra that do not overlap with that of ChR2 (Akerboom *et al.*, 2013), promise future avenues for all-optical investigations of neural circuit function.

Because of its advantages over electrical and chemical stimulation techniques, optogenetics opens the door to many new methodologies that offer vastly improved control over activity in complex neural circuitry. As a result, optogenetic techniques have been widely adopted in studies that require control of neural activity. However, in an engineering context, the concept of control involves a critical element, feedback, which is currently missing from most labs that use optogenetic stimulation methods.

1.3 Optogenetic feedback - an opportunity for neural control

Together, optogenetic stimulation and artifact-free electrical recordings can be used as an actuator and sensor within a feedback loop to control neural activity. Feedback is used in many fields of science and engineering to stabilize system variables, linearize input/output relationships, and provide real-time compensation for external perturbations. In neuroscience, feedback has been used most widely in the context of the voltage clamp, which relies on a proportional gain circuit to linearize the relationship between a command potential and the transmembrane potential (Cole, 1949; Marmont, 1949; Hamill *et al.*, 1981). More recently, a diverse set of specialized techniques that employ feedback have emerged for studying adaptation in neuronal

micro-circuits (Ahrens *et al.*, 2012), using electrical stimulation to control spike latency (Wallach *et al.*, 2011) and firing levels (Wagenaar *et al.*, 2005; Newman *et al.*, 2013), improving brain-computer interfaces (Velliste *et al.*, 2008), inducing motor plasticity (Jackson *et al.*, 2006a), and improving motor rehabilitation (Moritz *et al.*, 2008). Additionally, real-time optogenetic stimulation has been used to engage motor patterns in freely moving *Caenorhabditis elegans* (Stirman *et al.*, 2011; Leifer *et al.*, 2011) and introduce artificial sensory information into somatosensory cortex during active whisking in mice (O'Connor *et al.*, 2013). Further, real-time feedback has recently proven useful for on-demand optogenetic seizure suppression. Closed-loop activation of halorhodopsin expressed in excitatory principal cells (Paz *et al.*, 2012), or channelrhodopsin expressed in inhibitory interneurons (Krook-Magnuson *et al.*, 2013; Armstrong *et al.*, 2013), was capable of suppressing epileptic activity upon the detection of a seizure event *in vivo*.

Previous closed-loop optogenetic methods provide examples of how optogenetic stimulation can be improved by feedback within specific experimental contexts. However, the closed-loop strategies used by these studies do not continuously update stimuli based on ongoing neural activation and do not use neural firing as a readout to drive feedback. Given the importance of firing levels in the basic function of all neural circuits, we reasoned that using closed-loop optogenetic feedback to control firing activity presented a great opportunity. My thesis work focuses on the creation and demonstration of tools and techniques that allow successful closed-loop optical control of network activity *in vitro* and *in vivo*. I have successfully generalized these tools for use in a variety of experimental contexts, and used them to advance our understanding of neural coding at the network level and homeostatic plasticity.

1.4 Thesis Organization

The rest of the dissertation is organized as follows:

Chapter 2, *Hardware and Software for real-time network electrophysiology*, discusses the motivation, design philosophy, and performance characteristics of the open-source NeuroRighter electrophysiology platform. NeuroRighter was created by John Rolston in 2009 (Rolston *et al.*, 2009b). My contributions to the project include an overhaul of NeuroRighter's real-time subsystem, the addition of processing components for filtering and spike sorting, and the creation of a programming interface for 'plugin' modules that specify custom closed-loop algorithms and experiments.

The majority of studies that employ optogenetic stimulation to modulate neural activity use pulses of light. In Chapter 3, *Delivery of continuously-varying stimuli using channelrhodopsin-2*, I collaborate with Tatjana Tchumatchenko to investigate the capabilities of several ChR2 variants for conveying time-varying input signals. We show that, in comparison with pulsed stimuli, continuously-varying photocurrents better mimic natural synaptic input and increase the bandwidth over which stimuli can be used to drive neural activity.

In Chapter 4, *Effects of connectivity on signal transduction in recurrent cortical networks*, I investigate the ability of continuously-varying optical stimulation to elicit precise spiking patterns at the network level. I demonstrate how continuously-varying optical stimuli can be used in conjunction with pharmacological manipulation of synaptic activity to study the effects of recurrent connectivity on signal transduction in dissociated cortical networks. I show that, in agreement with theoretical predictions, recurrent connectivity linearizes the network's population spiking response. Also, I show that excitatory connectivity increases cell-to-cell firing correlations, which leads to a reduction of information present in the spiking response due to an increase in coding redundancy. In addition to these scientific results, Chapters 3 and 4 indicate that continuously-varying optical stimulation can serve as a powerful actuator of neural activity during closed-loop control.

Chapter 5, *Optogenetic feedback control of neuronal firing*, details the motivation,

design specification, and performance of a real-time optogenetic feedback technology to control neural activation. The system is capable of controlling neural activity over time-scales ranging from seconds to days. I demonstrate how optical feedback control can be used to decouple spiking and neurotransmission in order to study their independent roles in the induction of homeostatic changes in network excitability. Finally, in collaboration with Daniel Millard and Garrett Stanley, I demonstrate that optogenetic feedback can be used to control firing activity in somatosensory thalamus of anesthetized rats. We find that this firing is statistically similar to that of awake animals, and that feedback control can compensate for impinging vibrissal sensory input in real-time.

In Chapter 6, *Direct induction of synaptic scaling by reduced AMPA receptor activation*, working in collaboration with Ming-fai Fong and Dr. Pete Wenner of Emory University, I show that techniques presented in Chapter 5 can be used to disentangle the causal roles of spiking and neurotransmission during the induction of upward scaling of synaptic strength. Our team finds, in opposition to a large body of literature, that decreases in glutamaterigic neurotransmission, and not network firing, triggers the induction of upward scaling. Our results specify a new role for synaptic scaling in the context of memory formation and maintenance.

In Chapter 7, I conclude the thesis by discussing the implications for the technologies and results produced during my thesis work, and explore future directions for their usage and improvement.

Following the main text, I include three appendices that cover software and hardware design and usage. Appendix A, *NeuroRighter usage and examples*, provides detailed usage information and example code for the NeuroRighter electrophysiology system. Often, labs using inexpensive lasers for optogenetic stimulation are constrained to pulse-based stimuli because of low-performance control circuitry and the highly nonlinear characteristics of laser light sources. In Appendix B, *Cyclops: an*

ultra-precise, fast LED driver, I describe a low-cost, high-power LED driver that uses optical feedback to deliver extremely repeatable optical stimulus waveforms over a wide bandwidth. In Appendix C, *A servo-controlled Peltier heater/cooler for regulating culture temperature*, I describe a Peltier-based thermal regulator used to precisely maintain culture temperature during long-term recordings.

All hardware and software produced during the course this thesis work is covered by open access licenses (either the GPL3.0 or the Creative Commons BY-SA). Therefore all hardware designs and software code repositories are publicly available for download. Links to these web resources are provided in the thesis text and appendices where appropriate.

Portions of this thesis have been published previously. Chapters based upon published work are presented here with permission from the relevant publisher and include a citation at the start of the chapter. These chapters are unchanged from their original form with the exception of minor typographic and stylistic modifications.

CHAPTER II

HARDWARE AND SOFTWARE FOR REAL-TIME NETWORK ELECTROPHYSIOLOGY*

Single neuron feedback control techniques, such as voltage clamp and dynamic clamp, have enabled numerous advances in our understanding of ion channels, electrochemical signaling, and neural dynamics. Although commercially available multichannel recording and stimulation systems are commonly used for studying neural processing at the network level, they provide little native support for real-time feedback. We developed the open-source NeuroRighter multichannel electrophysiology hardware and software platform for closed-loop multichannel control with a focus on accessibility and low cost. NeuroRighter allows 64 channels of stimulation and recording for around US $10,000, along with the ability to integrate with other software and hardware. Here, we present substantial enhancements to the NeuroRighter platform, including a redesigned desktop application, a new stimulation subsystem allowing arbitrary stimulation patterns, low-latency data servers for accessing data streams, and a new application programming interface (API) for creating closed-loop protocols that can be inserted into NeuroRighter as plugin programs. This greatly simplifies the design of sophisticated real-time experiments without sacrificing the power and speed of a compiled programming language. Here we present a detailed description of NeuroRighter as a stand alone application, its plugin API, and an extensive set of case studies that highlight the system's abilities for conducting closed-loop, multichannel interfacing experiments.

* Newman, J.P., Zeller-Townson, R, Fong, M.-f., Desai, S.A., Gross, R.E., Potter, S.M. Closed-loop, multichannel experimentation using the open-source NeuroRighter electrophysiology platform. *Front. Neural Circuits* **6:98**, 2013.

2.1 Introduction

Multielectrode neural interfacing systems, such as planar electrode arrays, silicon probes, and microwire arrays are commonly used to record spatially-distributed neural activity *in vitro* and *in vivo*. Advances in nanoscale fabrication techniques have continued to push channel counts and electrode resolution (Fiscella *et al.*, 2012; Du *et al.*, 2011; Robinson *et al.*, 2012), allowing for increasingly detailed measurements of network activity states. Because multi-electrode neural interfaces provide many parallel measurements, they can be used to rapidly estimate ensemble features of network activity (e.g. the population firing rate or network level synchronization). This makes them well suited for real-time applications.

However, most commercial software interfaces for controlling multichannel hardware lack flexible support for real-time, bi-directional communication with neural tissue. Additionally, commercial software is often hard to integrate into complex multicomponent experimental configurations. As a result, multichannel hardware has not been incorporated into closed-loop interfacing schemes to the degree of single cell recording systems, such as voltage and dynamic clamp (Marmont, 1949; Cole, 1949; Hamill *et al.*, 1981; Prinz *et al.*, 2004; Kispersky *et al.*, 2011; Arsiero *et al.*, 2007). There are some exceptions to this trend (Jackson *et al.*, 2006b; Zanos *et al.*, 2011; Azin and Guggenmos, 2011). These systems are typically limited to low channel counts and/or low recording resolution in order to achieve embedded real-time performance at the recording site using a microcontroller or DSP. This approach has clear advantages for experiments on freely moving animals, but is limited in terms of input and output bandwidth, processing power to enable complex experimental protocols, and ease of programming. Neuroscience research would benefit from a multichannel acquisition platform that (1) enables bi-directional interaction with neuronal networks, (2) is practical for everyday use, (3) is straightforwardly extensible for complex closed-loop protocols, (4) works with a variety multi-electrode interfaces, (5) provides large

channel counts and high recording resolution, and (6) is low cost. This type of system would be particularly applicable to three areas of neuroscience research:

- **Feedback Control of Network Variables**: Neuronal networks are complex systems with many recurrently interacting components. This often results in ambiguity in cause and effect relationships between network variables (Turrigiano, 2011b; Rich and Wenner, 2007). Feedback control can be used to parse variables of neural activation that are causally linked (Cole, 1949). Feedback control of network-level variables (e.g., population firing rate, neuronal synchronization, or neurotransmission levels) can potentially clarify their causal relationships (Wagenaar *et al.*, 2005; Wallach *et al.*, 2011).

- **Artificial Embodiment**: Dissociated neural cultures, slice preparations, and anaesthetized or paralyzed animals allow stable electrophysiological access but cannot engage in natural behaviors with their environment. By artificially embodying reduced neuronal preparations using a virtual environment or a robot, experimental access is maintained while neural tissue is engaged in complex behaviors (Potter, 2001; Reger *et al.*, 2000; DeMarse *et al.*, 2001; Ahrens *et al.*, 2012).

- **Clinical Applications**: Responsive (Morrell, 2011) or predictive (Mormann *et al.*, 2007) application of neural therapies have the potential to improve the efficacy and safety of treatments that are currently used in open-loop. Examples include brain stimulation and local drug perfusion techniques that are used to treat movement disorders, clinical depression, chronic pain, and epilepsy. Additionally, electrical stimuli delivered to one region of motor cortex in response to spiking activity in another motor area has been shown to facilitate a functional reorganization of motor output, indicating a potential role for activity-dependent stimulation in rehabilitation therapy (Jackson *et al.*, 2006a).

Here, we present substantial improvements to NeuroRighter, an open-source, multichannel neural interfacing platform which we designed specifically to enable bidirectional, real-time communication with neuronal networks (Rolston *et al.*, 2009a, 2010). In the first half of the paper, we provide a description of NeuroRighter's capabilities, including an application programming interface (API) that facilitates the creation of custom real-time experiment protocols. In the second half of the paper, we demonstrate these features with a variety of case studies. Each case-study highlights a different aspect of NeuroRighter's abilities in the areas of network level feedback control, artificial embodiment, and closed loop control of aberrant activity states in freely moving animals.

2.2 Experimental methods

2.2.1 Tissue culture

Our culturing methods are described and demonstrated elsewhere (Hales *et al.*, 2010) and here we provide a brief overview. MEAs (59 electrode + common ground, 200 uM electrode spacing, 30 um electrode diameter, titanium-nitride conductor, with silicon nitride insulation) were obtained from Multichannel Systems (Reutlingen, Germany). MEAs were sterilized using 70% ethanol and exposure to UV light, and coated with polyethyleneimine and laminin to promote surface hydrophilicity and cell adhesion, respectively. All dissections were carried out in accordance with the National Research Council's Guide for the care and use of laboratory animals using a protocol approved by the Georgia Tech IACUC. Whole neocortex was isolated from E18 rats under sterile conditions and stored in Hibernate-E medium (Invitrogen, Carlsbad, California, USA) for up to two hours before plating. The cortical tissue was digested in a solution containing 20 $U \cdot ml^{-1}$ papain (Sigma-aldrich, St. Louis, Missouri, USA) in a culturing medium described in (Hales *et al.*, 2010; Potter and DeMarse, 2001) without antibiotics or antimycotics. Cells were dissociated mechanically using 3-10

trituration passes through a 1 mL conical pipette tip. The cell suspension was diluted to 2500 cells/μL in culturing medium. Cells were centrifuged and strained to remove small and large debris. Fifty thousand cells in a 20 uL drop were plated onto a 2 mm diameter area on precoated MEAs, which results in $\sim$16000 cells/mm^2 on the culturing surface (Wagenaar *et al.*, 2006c). The culturing well of each MEA was sealed with either a fluorinated ethylene-propylene (FEP) (Potter and DeMarse, 2001) or molded polydimethylsiloxane (Blau *et al.*, 2009) membrane to prevent infection and changes in osmolarity due to evaporation (fig.3). After a 30 minute adhesion period, culturing wells were flooded with 1 mL culturing medium, adapted from (Jimbo *et al.*, 1999), but without antibiotics. 0.75 mL of fresh culturing medium was exchanged every 3 days.

2.2.2 In-vitro MEA electrophysiology

All experiments and culture storage were carried out in an incubator regulated to 35°C, 5% CO_2, 65% relative humidity, which is safe for MEA recording and stimulation electronics. Electrode voltages were amplified 1200X and bandpass filtered between 10 Hz and 10 kHz using a 60 channel analog amplifier (MEA1060-Up; Fig. 3(c)). Because the amplifier dissipated heat during operation, culture temperature was precisely controlled to 35°C using a servo-control Peltier device (Appendix C). All MEA recording and stimulation were performed using the NeuroRighter multichannel electrophysiology platform[1]. Within NeuroRighter, amplified electrode voltages were digitally filtered using a 3rd order Butterworth design with a passband of 300 to 5000 Hz. Spike events were detected as events exceeding 5 times V_{RMS} noise on a given channel. Spike waveforms were collected as 2 millisecond snippets about the peak voltage inflection following a threshold crossing and validated by the slope of the waveform. A 1 millisecond detector pause following the peak of each waveform

[1] `https://sites.google.com/site/neurorighter/`

during which no spiking events can be detected was enforced (Fig. 55). Spike waveforms were sorted according to the methods described in section A.3.2 and outliers were rejected using a p-value of 0.005.

Multichannel stimulation was delivered using the NeuroRighter stimulus generation boards along with 4 stimulation multiplexing boards to route electrical pulses to any of the 59 recording electrodes (Wagenaar and Potter, 2004). Stimulation multiplexer boards are shown in figure 3(c).

For experiments involving perfusion of d(-)-2-amino-5-phosphonopentanoic acid (AP5), 50 μM dilution of AP5 in culturing medium was used. NeuroRighter triggered perfusion of the AP5 solution to the culture through a custom, gas-permeable perfusion cap via a kdScientific (Holliston, MA, USA) model 780262 syringe pump running at 1 mL/minute for 5 minutes (Fig. 3). AP5 was washed from the culture in the same way, using 10 mL of normal culturing medium at 1 mL/minute. The perfusion cap and attached FEP membrane were autoclaved prior to use.

2.2.3 Animal surgery, recordings, and multielectrode stimulation

All animal procedures were conducted in accordance with the National Institutes of Health Guide for the Care and Use of Laboratory Animals and approved by the Emory University Institutional Animal Care and Use Committee. A 300-gram male Sprague-Dawley rat was anaesthetized with 1.5-3% inhaled isoflurane. A craniectomy was made over the right dorsal hippocampus. Seven 69 nL injections of tetanus toxin (concentration 50 ng/μL) were made into the right dorsal hippocampus at coordinates -3.3 AP, - 3.2 ML and -3.1 DV over 4 minutes. A microelectrode array (MEA) with 16 electrodes (each electrode with 33 μm diameter; Tucker-Davis Technologies) was implanted with 8 electrodes targeted at the CA1 and 8 electrodes targeted at the CA3 cell layers (Fig. 11(b)). The microelectrode array had a row separation of 1 mm and the electrodes within each row were separated by 175 μm. 5 smaller craniectomies

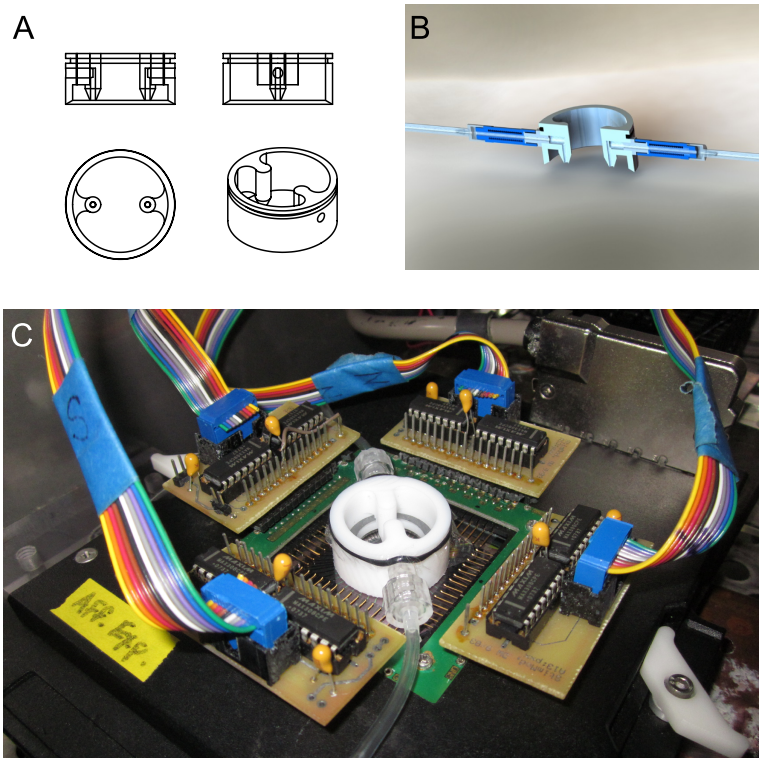

Figure 3: Gas permeable perfusion system for bath application of drugs during multi-channel recording and stimulation, *in-vitro*. **(a)** Drawing of perfusion cap design. The cap is machined from Teflon and fits tightly over the planar MEA's culturing well. The groove at the top of the cap holds a sheet of gas-permeable, water- and contaminant-impermeable FEP in place over the culturing well using an o-ring. FEP allows gas exchange between the incubator's regulated atmosphere and the culturing well, while preventing contamination and evaporation, which can lead to harmful changes in osmolarity and pH (Potter and DeMarse, 2001). Two perfusion ports allow input and output of culturing medium via a syringe pump. **(b)** Three dimensional rendering of the cap showing needle-less septa interfacing with the cap using Luer taper connectors. This allows the removal of input and output tubing without exposing the culturing well to outside air. **(c)** Photograph of a functioning perfusion lid, integrated with an MEA1060-Up amplifier (black) and stimulus multiplexing boards (brown with multicolored ribbon cables) (Wagenaar and Potter, 2004). This lid was designed and fabricated by Ted French while working as an undergraduate research assistant.

were made for skull screws. The reference for microelectrode electrode array recording was tied to the skull screw over the cerebellum and the ground was tied to the remaining skull screws. Single unit recording performed during the implantation process guided the final positioning of the microelectrode array. Dental acrylic was used to seal the craniectomy and secure the MEA. The rat was allowed to rest for 6 days before electrical recording and stimulation experiments began.

2.3 The NeuroRighter multichannel electrophysiology platform

NeuroRighter is an open-source, low-cost multichannel electrophysiology system designed for bi-directional neural interfacing (Rolston *et al.*, 2009a, 2010). A complete system, including all necessary electronics and a host computer, can be assembled for less than $10,000 USD. The NeuroRighter software is free. Extensive documentation on the construction and usage of a NeuroRighter system is available online at: `https://sites.google.com/site/neurorighter/`. NeuroRighter's source code, the API reference, and demonstration closed-loop protocol code, are available from the NeuroRighter code repository: `http://code.google.com/p/neurorighter/`. Questions on NeuroRighter assembly and usage can be submitted to the NeuroRighter-Users forum: `http://groups.google.com/group/neurorighter-users`. Tutorials on API usage are provided in Appendix A.

2.3.1 Hardware

Here we provide a summary of NeuroRighter's hardware building blocks. Hardware components can be used with neural interfaces designed for applications both *in vivo* and *in vitro*. Printed circuit board (PCB) performance specifications are provided in (Rolston *et al.*, 2009a) and layouts are available online. A complete NeuroRighter system meets or exceeds the performance of commercial alternatives in terms of noise levels, stimulation channel count, stimulation recovery times, and flexibility (Rolston

et al., 2009a). NeuroRighter's PCBs are designed to be modular: electrode interfacing and stimulation PCBs have identical footprints and use vertical headers to route power between boards. This allows interfacing PCBs to be stacked on top of one another for increased channel counts and the use of a single DC power supply (or set of batteries) for all hardware.

ADC/DAC boards. NeuroRighter uses National Instruments (NI; National Instruments Corp, Austin, TX) data acquisition hardware driven with NI's hardware control library, DAQmx. NI PCI-6259, PCIe-6259, PCIe-6353, and PCIe-6363 16-bit, 1 Msample/sec data acquisition cards are currently supported. Each card supports 32 analog inputs (AI), 4 analog outputs (AO), and 48 I/O-configurable digital channels. NI SCB-68 screw-terminal connector boxes are used to interface each data acquisition card with external hardware. Up to 3 cards can be used in a single NeuroRighter system to meet channel count requirements.

Multichannel amplifier interfacing boards. NeuroRighter provides two types of PCB to interface the NI data acquisition cards with multi-electrode amplifier systems. For *in-vivo* applications, a 16 channel filter module provides 1.6X signal buffering, anti-aliasing filtering (-3 dB point at 8.8 KHz), DC offset subtraction (-3 dB point at 1 Hz), and regulated power to the headstage. Up to four of these modules can be stacked together in order to meet channel count requirements. For *in-vitro* applications, a 68 channel conversion board provides power and signal routing for planar electrode array amplifier systems, e.g. Multichannel Systems' 60 channel amplifiers (Multichannel Systems, Reutlingen, Germany), which have a manufacturer settable passband. Both boards interface with the SCB-68 connector boxes using 34-channel ribbon cables, wired as signal/ground pairs to reduce capacitive crosstalk between adjacent lines during stimulation.

Electrical micro-stimulation hardware. NeuroRighter includes all-channel (up to 64 electrodes) stimulation capabilities for both *in-vivo* and *in-vitro* systems.

This system is based upon the circuits presented in (Wagenaar and Potter, 2004; Wagenaar *et al.*, 2004) and includes two separate PCBs: (1) a voltage- or current-controlled signal generation PCB, and (2) a signal multiplexing and isolation PCB to select different electrodes for stimulation and isolate recording electrodes from stimulation cables between stimulus pulses.

(1) *Signal generation board.* The signal generation PCB is identical for all applications. This board provides both voltage controlled or constant current stimulation modes. It stacks into the amplifier interfacing board(s) and therefore does not require an additional power source. Aside from stimulus generation, this PCB can be used to perform electrode impedance measurements, which are useful for diagnosing the health of micro-electrodes and their insulated leads, and for electroplating (Desai *et al.*, 2010). Only one signal generation PCB is required for up to 64 electrodes.

(2) *Signal multiplexing boards.* Stimulus multiplexing and isolation occurs at PCBs that piggyback directly on electrode pre-amplifiers. These PCBs are located close to the initial stages of electrode amplification so that the recording amplifier can be isolated from long electrical leads, which reduces capacitive pickup. Because recording amplifiers (e.g. headstages *in vivo* or multichannel amplifiers *in vitro*) come in many shapes and sizes, the design of the multiplexer PCBs is application dependent. For *in-vivo* applications, we have designed multiplexer systems that use an 18-pin Omnetics Nano connector, which interfaces with headstages from Triangle Biosystems (Durham, NC), Tucker-Davis Technologies (Alachua, FL), and Neurolinc Corporation (New York, NY), among others (Rolston *et al.*, 2009a). This board employs a single 1-of-16 multiplexer. For *in vitro* applications, four separate multiplexing modules, each of which houses two 1-of-8 multiplexers, plug directly into exposed 0.1" pitch sockets of a 60 channel Multichannel Systems amplifier (Wagenaar and Potter, 2004). The creation of custom multiplexer boards or adapters for other systems is straightforward due to the simplicity of these PCBs (they generally consist of a single multiplexer

integrated circuit).

Generic I/O. NeuroRighter provides 4 analog output channels and 32 bits of programmable digital I/O for controlling or recording digital signals from laboratory equipment. An auxiliary set of up to 32 analog input channels and 32 bits of digital I/O can also be used. Channel counts of generic I/O in a NeuroRighter system depend on the number of data acquisition cards in the user's system, and the amount of analog input channels reserved for the electrodes.

NeuroRighter's hardware serves as an adaptable interface between multi-electrode sensors and data acquisition cards for recording and microstimulation. There are many other options for routing signals to and from the acquisition cards. Therefore, except for the acquisition cards themselves, the hardware we present here is not required to make use of NeuroRighter's software.

2.3.2 Software

The NeuroRighter software application was written in C♯ (pronounced "C-Sharp"). C♯ is a modern, general purpose, object-oriented programming language. The software is free and its source code is maintained on a publicly accessible repository[2]. For standard installations, NeuroRighter is distributed as an installation package for 32- or 64-bit Windows operating systems (Microsoft Corp., Redmond, WA). NeuroRighter installations contain two software components:

1. A stand-alone multichannel recording and stimulation application. This includes a graphical user interface (GUI) for data visualization, hardware configuration, data filtering, spike detection and sorting, all-channel stimulation, stimulus artifact rejection, and data recording (section 2.3.2.1).

2. An application programming interface (API) that allows NeuroRighter to be

[2] `http://code.google.com/p/neurorighter/`

used as a real-time hardware interface and data server for user-coded protocols (section 2.3.2.2).

2.3.2.1 The NeuroRighter application

As a stand-alone application, NeuroRighter can be used for high-quality multichannel recordings (16-bit resolution, 31 kSamples/sec/channel) and all-channel stimulation protocols. NeuroRighter's graphical interface is organized into tabbed pages, each of which encapsulates a particular group of functions or visualization tools (Figure 4). In the following section, we discuss the main functional aspects of the stand-alone NeuroRighter application.

Main interface. The main NeuroRighter interface (Figure 4(c)) is an access point for all of the application's functionality. It faciltates user manipulation of hardware settings, online filter settings, data visualization windows, stimulation tools, and other features, which are discussed below. Additionally, some recording settings can be manipulated within the main interface itself:

Online acquisition settings. Many filter settings can be adjusted during data collection. This allows the user to fine tune acquisition settings while gaining visual feedback of the effect on incoming data streams. Bandpass, spike detection, and spike sorting parameters can be adjusted during a recording.

Data visualization. Data visualization tools in NeuroRighter use the Microsoft XNA game development framework. This ensures that online visualization does not consume CPU cycles by offloading plotting routines to a supported graphics card. Visualization tools are provided for single unit activity, local field potentials (LFP), multiunit activity (MUA), electroencephalograph (EEG) traces, and auxiliary analog input streams. Additionally, overlay plots are used to display sorted spike waveforms for each channel (Figure 4(c)).

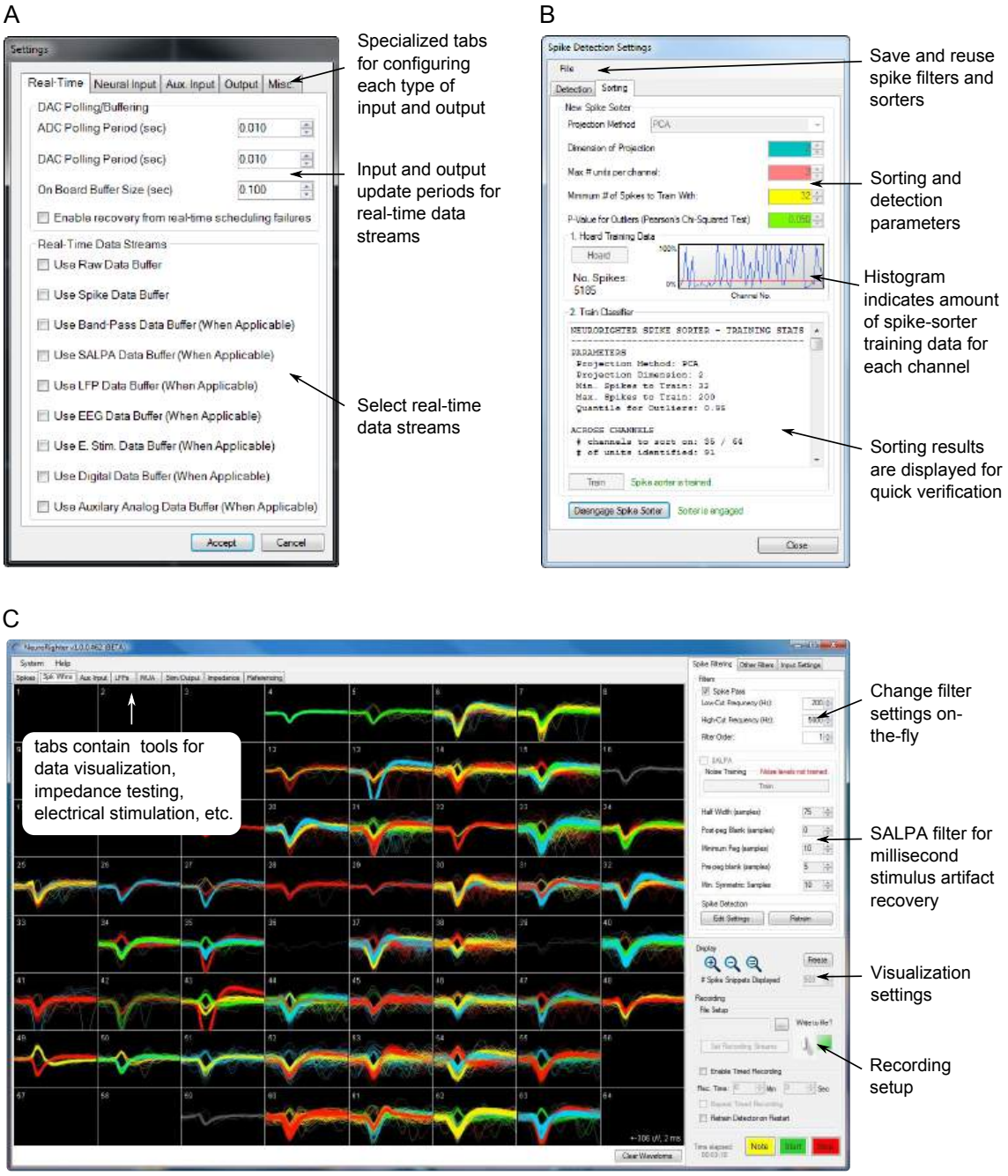

Figure 4: Portions of NeuroRighter's graphical user interface. **(a)** The hardware settings interface. **(b)** The spike detection filter and spike sorting interface. **(c)** The main application window. Sorted spike waveforms recorded from a 59-channel, planar electrode array are shown on the spike visualization tab of the main GUI. The position of each waveform corresponds to the position of the recording electrode on which it was detected.

File saving. Data streams selected by the user are written to disk with a unique file extension that designates their type. These binary files can be read with MATLAB functions included with NeuroRighter installations.

Hardware configuration. Correctly specifying mixed digital and analog signal routing, clock synchronization, and trigger synchronization on a multi-board data acquisition system can be complicated. NeuroRighter simplifies this process using a graphical hardware settings interface (Figure 4(a)). Here, the user specifies the types of signals carried by the NI acquisition cards in his or her system, amplifier gain settings, auxiliary input and output channels, options for electrode impedance measurement, signal referencing, and real-time data streaming options. Upon closing the settings dialogue, NeuroRighter performs the required signal routing and clock synchronization. All NI cards are synchronized to a single clock oscillator using an NI real-time system integration bus (RTSI, Figure 6).

Time series filtering. Incoming data from the A/D converters are passed through a cascade of digital filters to produce different neural data streams. First, channel voltages are passed through several linear filters to extract frequency bands for single-unit activity ($\simeq$ 200-5000 Hz) and LFP ($\simeq$ 1-500 Hz). MUA, which reflects the firing rate of neurons within the vicinity of the recording electrode, is extracted by rectifying and then low pass filtering the single-unit activity data stream (Supèr and Roelfsema, 2005).

In addition to traditional filtering methods, NeuroRighter provides several specialized filtering options. Common-mode noise sources such as AC mains pickup or movement artifacts in freely moving animals can corrupt neural recordings. NeuroRighter allows the mean or median of all recording electrodes (with appropriate scaling) to be subtracted from individual electrode voltage streams to combat common mode interference (Rolston *et al.*, 2009b). This is an effective method for reducing non-periodic common-mode interference, such as movement artifacts, where template subtraction

Table 1: Overview of NeuroRighter's input and output streams. Each stream is accessed using a dedicated server that includes functions for reading from, or writing to, its data buffer.

Input	Source	Server (DataSrv.*)	Buffer Type	Max. Channel Count
	Raw Electrodes	RawElectrodeSrv	Circular double[ ][ ]	64
	SALPA Filter	SalpaSrv	Circular double[ ][ ]	64
	Spike-Band Filter	SpikeBandSrv	Circular double[ ][ ]	64
	Spike Filter	SpikeSrv	List<SpikeEvent>	64 or No. units
	LFP Filter	LFPSrv	Circular double[ ][ ]	64
	EEG Filter	EEGSrv	Circular double[ ][ ]	64
	MUA Filter	MUASrv	Circular double[ ][ ]	64
	Electrical Stimuli	ElecStimuliSrv	List<SpikeEvent>	64
	Auxiliary Analog	AuxAnalogSrv	Circular double[ ][ ]	32
	Auxiliary Digital	AuxDigitalSrv	List<DigitalEvent>	32 bits
Output	**Source**	**Server (StimSrv.*)**	**Buffer Type**	**Max. Channel Count**
	Electrical Stimuli	StimOut	List<StimulusEvent>	64
	Analog Output	AnalogOut	List<AnalogEvent>	4
	Digital Output	DigitalOut	List<DigitalEvent>	32 bits

methods are inappropriate. Finally, NeuroRighter includes an implementation of the SALPA filter (Wagenaar and Potter, 2002), which subtracts locally fit cubic splines from electrode traces following the application of a stimulus pulse. This removes the capacitive artifacts from non-saturated recording channels and allows online action potential detection within 2 milliseconds after a stimulus pulse.

Sampling rates for different data streams can be set independently. Filter settings (pass-band and filter order) can be modified during data acquisition (Figure 4(c)). Raw data, as well as the result of each filtering stage, yield separate data streams (table 1).

Spike filtering. Spike filtering in NeuroRighter is a three-step process: (1) detection, (2) validation, and (3) sorting. NeuroRighter detects spikes using a threshold criterion that compares individual voltage samples to the estimated RMS voltage on the corresponding electrode. Upon threshold crossing, a peak-aligned voltage 'snippet' is extracted from the raw voltage stream. Each snippet is validated using a series of ad-hoc criteria based upon waveform slope, width, and peak-to-peak amplitude. Finally, spikes can be sorted online using an automated Gaussian mixture modeling algorithm. Details of the spike detection and sorting algorithms used by NeuroRighter

are provided in Chapter A, Section A.3.

The spike detection/sorting configuration is controlled through a child GUI (Figure 4(b)). All relevant spike detection, validation, and sorting parameters are under user control and are manipulated using the spike detection GUI. Because spike-detection settings are changed using a secondary GUI, the effects of parameter changes can be simultaneously monitored on the visualization tabs in the main interface while data collection occurs. A complete list of these parameters is shown in table 9. Spike filters, including trained spike sorters, can be saved and reused.

Stimulation. NeuroRighter provides several options for delivering complex stimulus patterns to neural tissue either manually through the NeuroRighter application or using scripted protocols. Simple, periodic stimulation protocols, consisting of single or double phase, square, current- or voltage-controlled pulses on any electrode, can be performed directly from the main GUI. Stimuli can be triggered 'on demand' in response to a mouse click or by using hardware timed, periodic sequence of triggers.

Scripted protocols can be used to deliver complex, potentially non-periodic stimulus patterns and to access general purpose analog and digital output lines. Neurorighter uses a double-buffered output engine, called `StimSrv` (table 2), to produce arbitrary, hardware-timed stimulation, analog-output, or digtial output signals (table 1, bottom). `StimSrv` can be accessed on-the-fly using NeuroRighter's API (section 2.3.2.2) or with user-written scripts. The schemeatic in Fig. 5(A) demonstrates how `StimSrv` delivers uninterrupted output. First, a block of the NI cards' memory is reserved and divided into two sections, each of which comprises a single output buffer. At a given instant, one buffer is reserved for sample generation and one is available for writing. When the all samples in the read buffer are exhausted, the buffers switch roles, allowing seamless delivery of constantly varying output signals. This allows the delivery of complex, aperiodic stimulation patterns and the orchestration of experimental apparatuses using analog and digital output lines. All output

is clock-sychronized to input data streams, allowing a-priori specification of stimulus delivery times, relative to the start of the experiment, with single-sample precision. Stimulation scripts can be created with a set of MATLAB functions that are included with NeuroRighter installations (see Chapter A, Section A.1).

Figure. 5(B) demonstrates the use of a scripted stimulation protocol to deliver spatio-temporal patterns of electrical stimuli. One-second trials of spatially uniform, and temporally Poissonian random stimulus pulses were delivered to a dissociated cortical network. Each trial consisted of either a new, random stimulus realization or a single repeated realization. Each type of stimulus sequence was interleaved with no delay between adjacent trials. Figure. 5(B.ii) shows stimulus raster plots for 100 trials of each stimulus type, with a grey-scale indicating the stimulus trial. For repeated stimuli, individual trials cannot be seen since the recording and stimulation subsystems are clock-synchronized and every repeated stimulus sequence occupies the same set of samples relative to the start of a trial. Figure. 5(B.i) shows spiking patterns in response to random and repeated stimuli for 4 units, across trials. The delivery of repeated stimuli to the network results in extremely reproducible spiking patterns, and non-repeated, random stimuli probe the variability of population spiking response. This type of stimulus protocol is commonly used to estimate the mutual information between a stimulation process and the population spiking response (Strong *et al.*, 1998; Yu *et al.*, 2010).

2.3.2.2 NeuroRighter's application programming interface

NeuroRighter installations include an API that facilitates the creation of real-time protocols. The API comprises a set of tools for interacting with NeuroRighter's input and output streams. Protocols written using the API are externally compiled libraries that can 'plug in' to the NeuroRighter application in order to impart real-time and closed-loop functionality. The software packages included with the API are

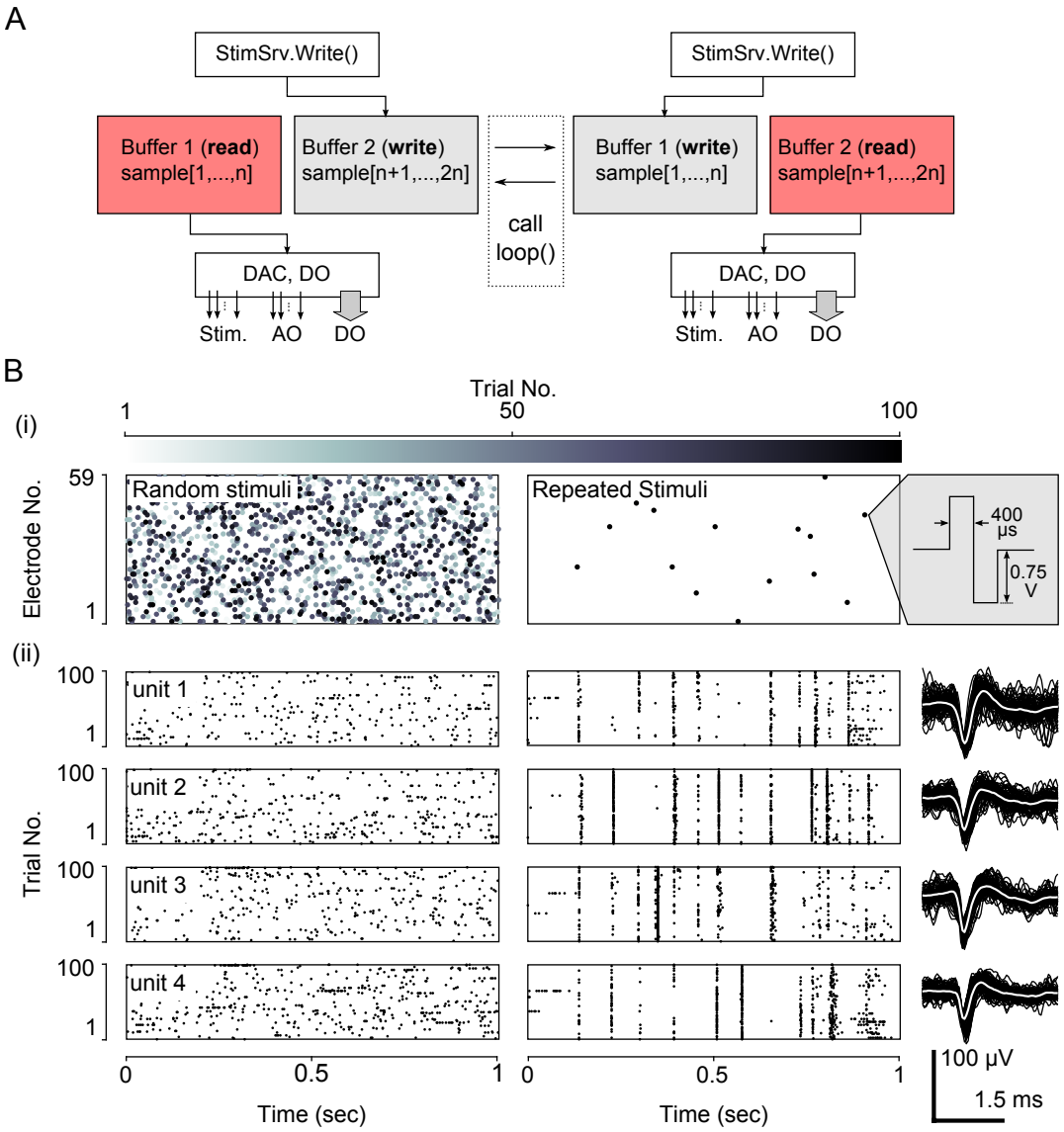

Figure 5: NeuroRighter's `StimSrv` subsystem. **(a)** To deliver complex, non-periodic stimuli, NeuroRighter uses a double-buffering system. This allows samples to be generated and written to the NI cards' analog and digital outputs simultaneously. At a given instant, one buffer is reserved for reading (pink) and one from writing (grey). When the all samples in the read buffer are generated, the buffers swich roles, allowing seamless delivery of constantly varying stimulus patterns and generic analog and digital signals. When using `StimSrv` for closed-loop protocols, the `loop()` function is called at the instant of a buffer switch. **(b)** Example open-loop stimulus protocol using `StimSrv`. 100, 1 second Poisson sequences of electrical stimuli and a single repeated sequence, were delivered to a dissociated cortical network (bi-phasic, voltage controlled, $\pm$0.75 volts, 800 μs period). Top plots show stimulus rasters with grey scale indicating the trial. For repeated stimuli, stimulus points are overlaid since stimulus delivery is clock-synchronized with the acquisition subsystem. Rastergrams of 4 units are shown below each stimulus raster across trials. Example waveforms for each of the 4 units are shown to the right.

Table 2: Packages included with NeuroRighter's Plugin API.

Package	Component	Description
Server	DataSrv	Contains input servers objects (Table 1, top)
	StimSrv	Contains output servers objects (Table 1, bottom)
DataTypes	MultiChannelBuffer	Circular buffer for time series data
	SpikeEvent	Spike event type (time, channel, waveform, unit)
	DigitalEvent	Digital event type (time, 32-bit port state)
	StimulusEvent	Stimulus event type (time, channel, waveform)
	AuxEvent	Auxiliary voltage event (time, channel, voltage)
NeuroRighterTask	NRTask	Abstract class for real-time NeuroRighter interfacing
Log	Logger	Debugging real-time protocols

shown in table 2. Each package contains a different set of tools for interacting with NeuroRighter's data streams. Here we discuss the contents and usage of each of these tools. Additionally, a detailed API reference is available online[3].

NeuroRighterTask. User-defined protocols employ the NeuroRighter application as a real-time data server. These protocols are inherited from a base component called `NRTask`, which belongs to the NeuroRighterTask package. Closed-loop protocols created with the plugin API are derived from `NRTask` (see supplmentary section A.2 for details). Three functions included in `NRTask` can then be accessed to impart real-time functionality.

1. `NRTask.Setup()`: This function is called when the base `NRTask` component is instantiated. It allows one-time setup operations to take place, such as the declaration of variables, allocation of internal buffers, file streaming setup, GUI initialization, etc.

2. `NRTask.Loop()`: This function is executed periodically by a hardware-timed clock. Execution periods of 1 to 150 milliseconds are allowed and can be set from the Hardware Settings GUI in the main application (Figure 4(a)). To achieve closed-loop functionality, code within the `Loop` function should access other components of the API, most importantly components from the Server

[3] `https://potterlab.gatech.edu/main/neurorighter-api-ref/`

and DataTypes packages (table 2). These packages provide access to incoming neural data streams and output buffers and can be used to form a bidirectional interface with neural tissue. Output can be sent from within the `Loop` function using the StimSrv package (table 2) or through natively supported communication interfaces such as TCP/IP ports, serial ports, or USB communication.

3. `NRTask.Cleanup()`: This function is called a single time when the protocol is stopped from the NeuroRighter GUI. It allows the deconstruction of GUIs, the closure of file streams that may have been created during the execution of the plugin, and other cleanup routines.

Listing 1(a) provides pseudocode for a real-time plugin that responds to a spike produced by a particular detected unit. All real-time protocols written using the API will follow the structure of this code skeleton, regardless of their complexity. First, the user references the required packages from the API. Next, the plugin is designated to be a child of `NRTask`, which provides the protocol with automatic access to NeuroRighter's data servers. Finally, the `Setup()`, `Loop()` and `Cleanup()` functions are overridden to impart real-time functionality. After it is compiled (either using Visual Studio or Mono[4]), the plugin can be executed through NeuroRighter's GUI. Plugin protocols executed through NeuroRighter operate on a high-priority thread to decrease closed-loop response latency. The diagram shown in Fig. 6 shows the interaction between a plugin created using the API, the NeuroRighter executable, and hardware. Functional examples of plugin protocols are provided in Appendix A, Section A.4.1.

Server. Components derived from `NRTask` have automatic access to NeuroRighter's input and output servers, which belong to the Server package. There are two banks of data servers: (1) `DataSrv`, which can be used to read NeuroRighter's input

[4] `http://www.mono-project.com/Main_Page`

A

```
/// StimSrv-based plugin
using NeuroRighter.NeuroRighterTask;
using NeuroRighter.DataTypes;
using NeuroRighter.DatSrv;
using NeuroRighter.StimSrv;
namespace Example
{
  public class MyTask : NRTask
  {
 // Called once at plugin start
    protected override void Setup(){
    }
    // Called by output buffer
    protected override void Loop(){
      data = NRDataSrv.SpikeSrv.Read();
      if (myUnit member of data)
      {
        NRStimSrv.Write();
      }
    }
    // Called upon plugin termination
    protected override void Cleanup(){
    }
  }
}
```

B

```
/// NewData-based plugin
using NeuroRighter.NeuroRighterTask;
using NeuroRighter.DataTypes;
using NeuroRighter.DatSrv;

namespace Example
{
  public class MyTask : NRTask
  {
    // Called once at plugin start
    protected override void Setup(){
      SpikeSrv.NewData +=
              NewData_Handler();
    }
    // Called on NewData event
    private void NewData_Handler(){
      if(myUnit member of data)
      {
        NI Card sends output;
      }
    }
    // Called upon plugin termination
    protected override void Cleanup(){
    }
  }
}
```

Listing 1: Code structure for two types of real-time plugin implemented with the API. **(a)** Pseudocode for a StimSrv-based real-time plugin. **(b)** Pseudocode for real-time plugin triggered by NewData events.

streams (table 1, top) and (2) `StimSrv`, which can be used to write to output streams (table 1, bottom). `DataSrv` and `StimSrv` objects encapsulate isolated data servers, each of which handles a particular data stream. Each server includes methods for reading the hardware clock, reading and writing to its own data buffer, and accessing stream meta data. Because input and output servers are simultaneously accessible from within a user-defined `NRTask`, sending output signals (e.g., stimuli) contingent on recorded input is straightforward. The user can select which data streams are sent to `DataSrv` or available for writing on `StimSrv` using the Hardware Settings GUI (Fig. 4(a)).

A final important feature of each data server within `DataSrv` is a `NewData` event. A `NewData` event is fired for a given stream each time it receives new data for the A/D card or a digital filter. Functions within a plugin can subscribe to these events so that feedback processing only occurs when new data is acquired. This reduces computational overhead and the latency of the closed loop response. Plugins that use `NewData` events to generate feedback are not required to include a `NRTask.Loop()` function or to use `StimSrv` to send output signals. Instead, standard calls to the National Instruement driver library (DAQmx) can be used to access the NI cards' directly. Alternatively, output can be generated using natively supported external communication protocols (USB, TCP/IP, UDP, serial, etc.). Listing 1(b) provides pseudocode for a real-time protocol analogous to listing 1(a), but using the `NewData` event to trigger a response. This type of plugin provides a lower response latencies but is less capable of producing complex, precisely timed output signals. A functional example of a `NewData`-based plugin is provided in Chapter A, Section A.4.2.

DataTypes. NeuroRighter's input and output servers operate on high-level data types that encapsulate different forms of multichannel input and output data. These include multichannel buffers for continuous data streams (such as raw electrode voltages or LFP recordings) and discrete event types (such a detected spikes or stimulation

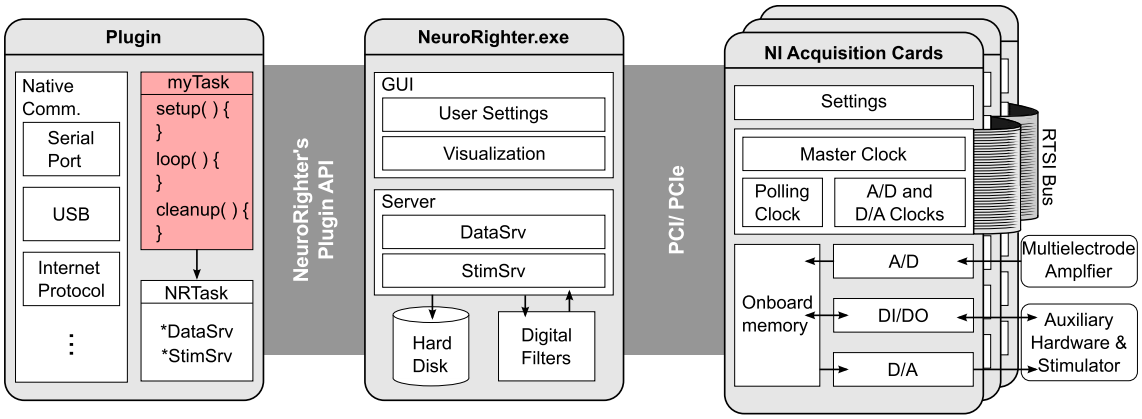

Figure 6: Conceptual schematic of NeuroRighter's hardware and software elements. NeuroRighter serves as a high-level interface between hardware and custom user-written protocols (pink box). NeuroRighter simplifies hardware level programming by using datatypes and methods that are specialized for multichannel neural recording and stimulation. This facilitates the creation of low-latency, closed-loop protocols. Neural signals and secondary data streams are fed into the the NI cards' analog and digital inputs where they are digitized and stored temporarily in on-board memory. NeuroRighter periodically transfers data from the acquisition cards' FIFO memory to RAM using direct memory access. Data is then pushed to NeuroRighter's `DataSrv` server object. `DataSrv` serves data to NeuroRighter's visualization tools, filtering algorithms, and externally compiled plugins. The plugin API provides functions for safe interaction with `DataSrv` so that custom operations can be performed on incoming data streams. User-written plugins can interact with any of the computer's native communication ports, or write data back to `StimSrv` in order to control external hardware as a function of recorded neural signals.

events). Extensive documentation on each of these data types is provided in the API reference.

Log. The Log package provides accesses to a data logging tool that operates within the NeuroRighter executable, but can be invoked from a user protocol. This tool can be used to write information to a log file using a separate, low-priority thread. This is useful in the development of real-time protocols because core NeuroRighter operations (such as the timing of hardware reads, writes, and other triggers) are logged to this file as well, providing context for messages written from the plugin.

2.4 Case studies

NeuroRighter's abilities for orchestrating closed-loop experiments are best demonstrated through example. Here we present five case studies in which protocols created with the API were used to measure NeuroRighter's closed-loop reaction time, clamp network firing levels in dissociated cultured cortical networks, react to seizures in

freely moving animals with multi-electrode electrical stimulation, and control robots serving as artificial embodiments. The plugin code used in these case studies is available for download on NeuroRighter's code repository. [5]. Additionally, we provide all code used in the reaction-time case study in Appendix A.

2.4.1 Low latency control of real-time hardware

Rapid response times are critical for maintaining a tight feedback loop in which features of incoming data streams (e.g. spikes, EEG, temperature, or animal motion) are used to trigger or adjust the delivery of stimuli. To benchmark the response speed of protocols written using the API, we wrote a protocol that generated output signals in response to recorded action potentials. We picked two sorted units from a dissociated neural culture to serve as triggers for hardware activation. When either one of these units fired, it triggered the output of a digital word encoding the identity of the detect unit. These signals serve as a generic stand-in for a stimulation pattern or any other hardware control signal that might be used in a feedback control scheme. Output signals were then recorded using NeuroRighter's digital input port. The delay between action potential detection and signal generation could then be measured using the same sample clock. A diagram of the experimental protocol is shown in figure 7(a). We wrote protocols to test three hardware options for generating the required digital output:

1. **StimSrv**: Buffered manipulation of the NI cards using NeuroRighter's native stimulation server (Fig. 5 and listing 1(a)).

2. **NewData**: Unbuffered manipulation of the NI cards whenever new data enters NeuroRighter's spike server (listing 1(b)).

[5] `http://code.google.com/p/neurorighter/source/browse/NR-ClosedLoop-Examples/`

3. **Arduino**: An Arduino ATmega2560-based microcontroller board[6] communicating via serial port (RS-232).

The response latency, calculated from the time of an action potential peak to the corresponding change in the digital port was calculated for each hardware option (Figure 7). Mean response latencies were 46.9 ± 3.1 milliseconds for `StimSrv`, 7.1 ± 1.5 milliseconds for `NewData`, and 9.2 ± 1.3 milliseconds for the Arduino board. Latencies where measured while NeuroRighter performed bandpass filtering, spike detection, spike sorting, data streaming, and data saving for 64 electrode inputs, each sampled at 25 kHz. Experiments were conducted on a desktop computer using an Intel Core i7 processor (Santa Clara, California, U.S.A.) and running 64-bit Windows Vista.

The differences in reaction latency for different hardware options are a result of both the method used to communicate with the hardware and the how the input sent from NeuroRighter is interpreted and transformed into a physical output signal. The differences in response times for NewData and Arduino are largely attributable to the different communication protocols and command interpretation by the client device. For instance the Arduino used a RS232 serial interface where as NewData communicates with the NI cards via PCIe. StimSrv's long latency in comparison to other options is a result of its double buffering system, which requires a relatively long time period between updates to the NI D/A's output buffer. While StimSrv is slow in comparison to the NewData and microcontroller options, it provides an interface that is easier to use and allows the uninterrupted delivery of arbitrary complex singal outputs. On the other hand, the Arduino and NewData methods can only respond by generating finite-sample or periodic control signals. We have found that StimSrv is fast enough for most of our closed-loop requirements. For this reason, we used

[6] `http://www.arduino.cc/`

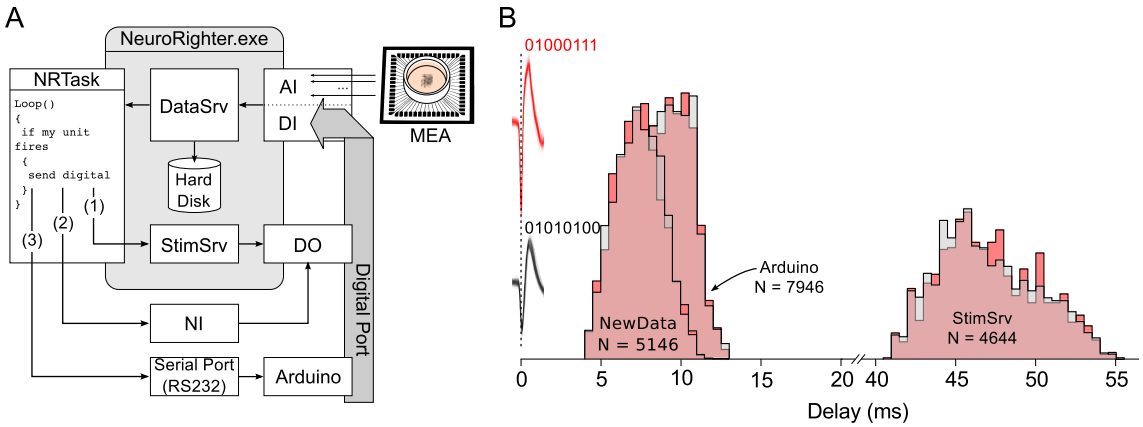

Figure 7: Estimated loop times for bi-directional communication using different hardware configurations. **(a)** Schematic of experiment used to test reaction delays for different real-time hardware options. Spikes detected and sorted from 59-channel planar electrode array were passed to the real-time plugin. The plugin determined if a spike originated from one of two units of interest. In the case that a spike was produced by one of the two units, the plugin triggered the generation of an 8-bit digital word from StimSrv, Daniel Wagenaars real-time all channel stimulator (Wagenaar and Potter, 2004), or an Arduino board, which was recorded though NeuroRighter's digital input port. **(b)** Normalized histogram of time delays from spikes produced by the two units of interest (action potential waveforms are shown in pink and grey and occur at 0 milliseconds) to the recorded digital signals produced by the plugin to encode the units (01000111 or 01010100). Delay histograms are shown for each unit (pink and grey) and the three different hardware options. N is the number of spikes recorded for each hardware option.

StimSrv to generate physical outputs for the remainder of the case studies. However, as demonstrated above, the API's modularity allows the use of faster hardware options with little change in coding complexity.

2.4.2 Multichannel electrical population firing clamp

The population firing rate is a building block of the neural code. The ability to precisely control population firing in the face of experimental perturbations can be used to understand its role in network function (Chapters 5 and 6). To demonstrate NeuroRighter's ability to control network firing rate, we implemented the feedback controller presented in (Wagenaar *et al.*, 2005) to control the firing activity in dissociated cortical cultures grown on 59-channel micro-electrode arrays. This algorithm adjusts the stimulation amplitude of voltage controlled, biphasic pulses on 10 electrodes to desynchronize population firing and force the network firing rate to track

target values. The control law is given by

$$v_k[t + \Delta T] = v_k[t] - \alpha v_k[t] \left(\frac{\langle f_u[t] \rangle}{f^*} - 1 \right), \tag{1}$$

where v_k is the stimulation voltage on electrode k, $\langle f_u[t] \rangle$ is the average firing rate across sorted units detected with the 59 electrode array extending over a 2 second window into the past, f^* is the target firing rate, ΔT is the update period of the feedback loop (as defined within NeuroRighter's Hardware Settings GUI), and α defines the time constant of the feedback controller as

$$\tau_{FB} = \Delta T / \alpha. \tag{2}$$

We used $\Delta T = 10$ milliseconds and $\alpha = 0.002$ so that $\tau_{FB} = 5$ seconds. Electrodes were stimulated at a 10 Hz aggregate frequency (1 Hz per electrode for 10 electrodes) in a random, repeating sequence. Additionally, individual electrode voltages were multiplied by a tuning factor that was inversely proportional to the number of spikes that occurred within 30 milliseconds following a stimulus pulse on that electrode, as described in (Wagenaar *et al.*, 2005). This factor equalizes each electrode's ability to evoke a spiking response, and is critical for achieving the desynchronizing effect of the controller on population activity.

We used the controller to clamp network firing at target rates for 5 minute epochs. These results are shown in Figure 8. The controller was able to follow target rates within the range of $f^* = 1.5$ to 4.5 Hz/Unit.

The monotonically increasing relationship between the mean stimulation voltage, $\overline{\langle v_k[t] \rangle}$, and target firing rate f^* (Figure 8(d)) might indicate that knowledge of the stimulation voltage versus firing rate relationship is sufficient to design an open loop controller capable of holding network firing rates. To test this, we clamped firing at $f^* = 3.0$ Hz/Unit over 10 minute epochs for 15 trials. Five minutes into each 10 minute protocol, we stopped updating stimulation voltages on the ten stimulating electrodes, but continued multi-electrode stimulation in open-loop mode (Figure 9).

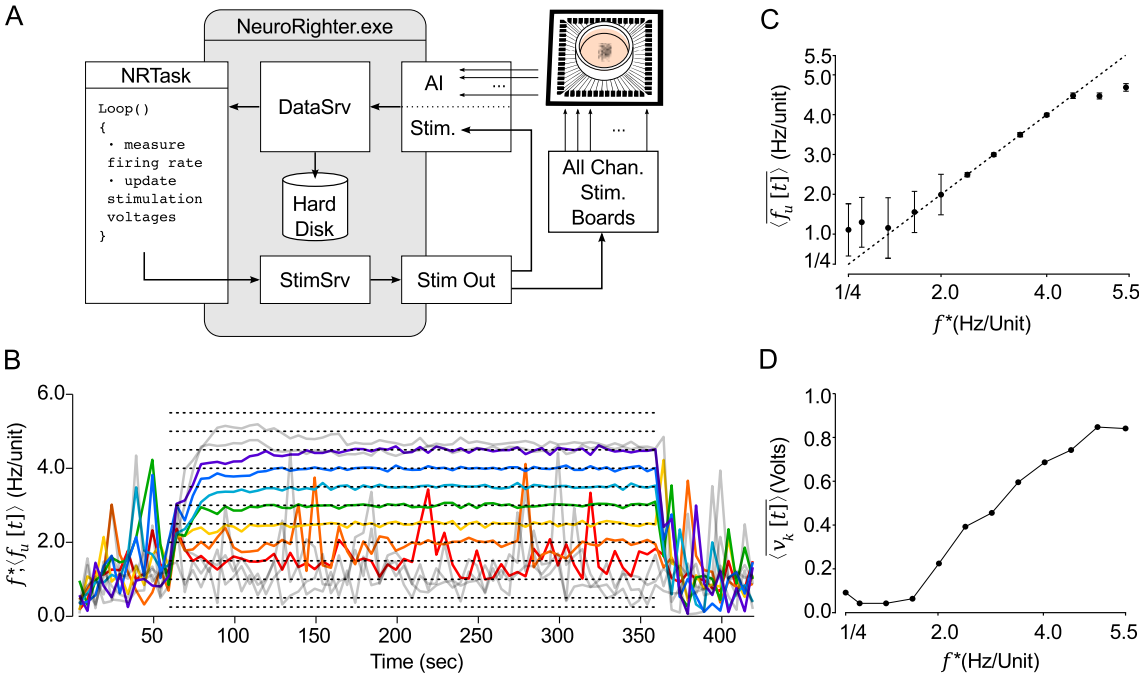

Figure 8: NeuroRighter can be used to clamp population firing rates *in vitro* using closed-loop electrical stimulation.(a) Schematic of the multielectrode population firing clamp. (b) Step tracking performance is shown for a range of target firing rates, f^* (dotted lines). The average neuronal firing rate across detected units, $\langle f_u[t] \rangle$ (colored lines), is shown for each step in f^*. Tacking failures are colored grey.(c) Time averaged neuronal firing rate for the last 2.5 minutes of each 5 minute protocol are compared to the reference signal, f^*. The dotted line is identity. (d) The mean control voltage across the stimulating electrodes over the final 2.5 minutes of each step protocol is plotted as a function of the target firing rate, f^*.

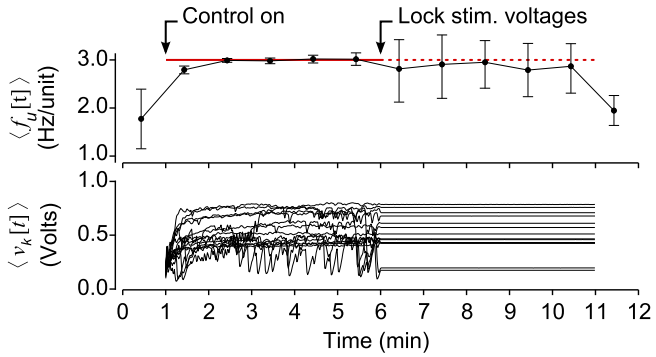

Figure 9: Closed-loop stimulation is required to robustly clamp population firing. (Top) The average neuronal firing rate over 1 minute periods across 15 trials. Halfway through a multichannel population clamp protocol, real-time voltage updates stop and microstimulation is applied in open loop. Error bars are ±standard deviation. (Bottom) The mean electrode stimulation voltage across 10 stimulating electrodes, for each of the 15 trials.

Although the desired mean firing rate was achieved fairly consistently, the open-loop control scheme could not react to the rapid changes in excitability that are typical of cultured cortical networks (Wagenaar *et al.*, 2006c). This variability is reflected in the large range of control signals required to track the target rate over the first 5 minutes of each trial . As a result, the RMS error of $\langle f_u[t] \rangle$ about f^* increased by a factor of 5.1 for open-loop compared to closed-loop epochs. The variance of firing during open-loop stimulation is comparable to that of spontaneous (non-evoked) firing behavior that was recorded before the controller was switched on (Figure 9, top).

2.4.3 Long term electrical population firing clamp with synaptic decoupling

2.4.3.1 Experiment 1

In-vitro neural preparations allow continuous experimental access to neural tissue over very long time scales (Potter and DeMarse, 2001), and therefor serve as important models for understanding slowly occurring developmental processes (Turrigiano *et al.*, 1998; Minerbi *et al.*, 2009; Gal *et al.*, 2010). To demonstrate that NeuroRighter is capable of stable closed-loop neural interfacing over long time scales, we used the multi-electrode feedback controller used in section 2.4.2 for 6-hour epochs. This protocol started with a 1 hour recording of spontaneous activity. Then, the controller

was engaged to clamp population firing to $f^* = 3.0$ Hz/Unit for 6 hours. Following the clamping protocol, spontaneous network activity was recorded for an additional hour.

Figure 10(a) shows the resulting multichannel stimulation signal (Figure 10(a.i)), neuronal firing rate in relation to f^* (Figure 10(a.ii)), individual unit firing rates (Figure 10(a.iii)), and zoomed rastergrams before, during and after multi-electrode stimulation was applied (Figure 10(a.iv)). The controller achieved the $f^* = 3.0$ Hz/Unit tracking over the duration of the 6-hour protocol. Additionally, network activity was desynchronized through most of the control epoch, but occasionally the controller allowed bursts of synchronized network activity (Wagenaar *et al.*, 2006c).

2.4.3.2 Experiment 2

Spiking and neurotransmission have a strong reciprocal influence on one another, making their individual effects on network development difficult to quantify (Turrigiano, 2011b). For instance, N-methyl-D-aspartate (NMDA)-ergic neurotransmission plays a large role in sustained network recruitment (Nakanishi and Kukita, 1998). For this reason, long term changes in the state of *in-vitro* networks following the application synaptic blockers (e.g., changes in firing rate, spiking patterns, or synaptic-strength) is difficult to attribute directly to effects on neurotransmission because of secondary, confounding effects on network activity levels. However, the closed-loop population clamp provides a solution to this problem. A firing rate controller has the potential to compensate for changes in network excitability induced by the application of a drug, removing its confounding effect on network activity.

To test this, we used the multichannel population clamp during the bath application of d(-)-2-amino-5- phosphonopentanoic acid (AP5), a competitive antagonist of NMDA receptors. This protocol proceeded identically to Experiment 1 except that at 1-hour following the start of closed-loop stimulation, NeuroRighter triggered the

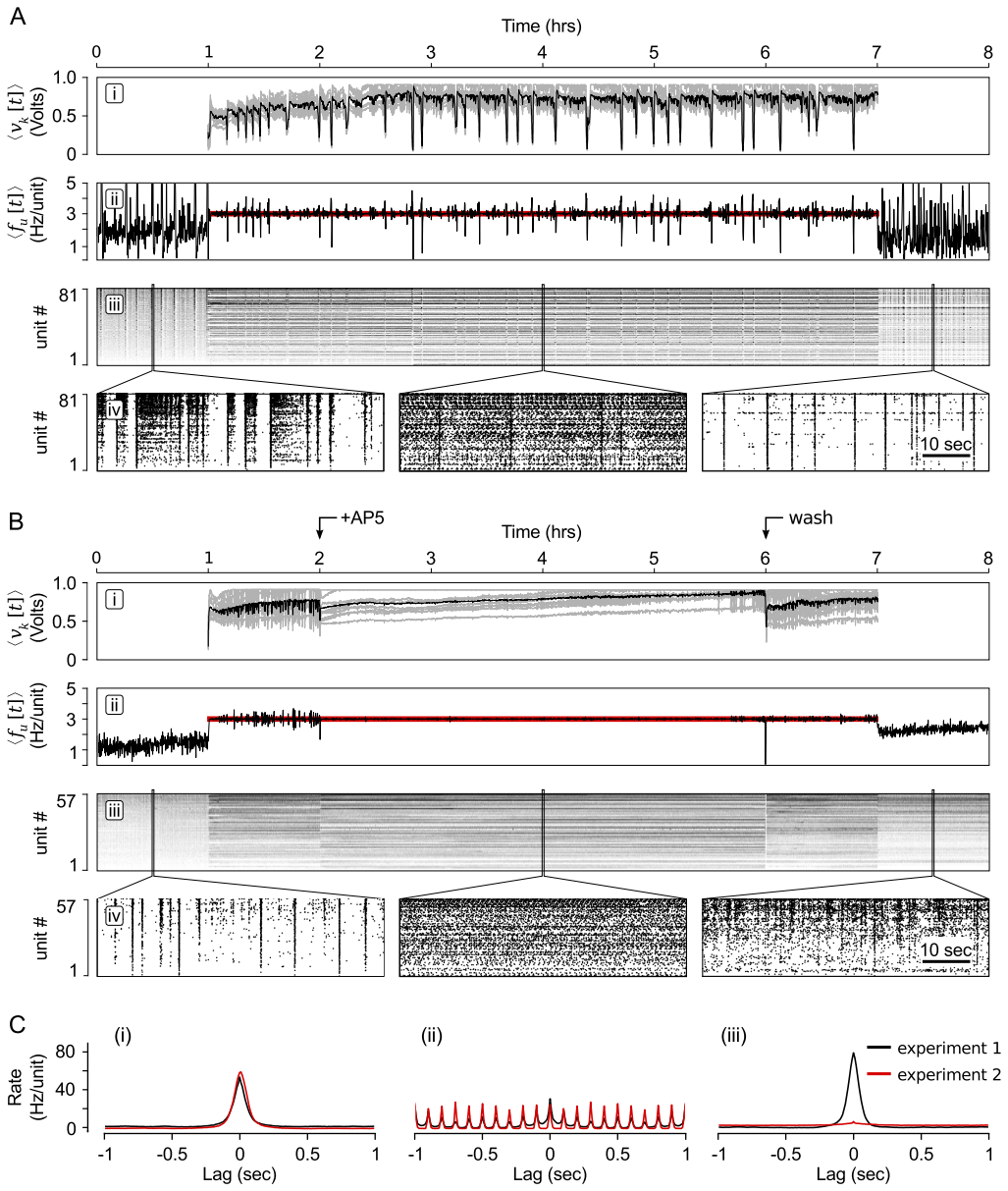

Figure 10: Long term electrical population firing clamp. **(a)** (i) The mean stimulation voltage (black) and individual electrode stimulation voltages (grey) over the course of the 6-hour clamping protocol. (ii) The neuronal firing rate (black) compared to the target rate (red line). (iii) Individual unit firing rates, sorted in order of increasing rate during the 1 hour period prior to the start of closed-loop control. (iv) Zoomed rastergrams showing short time scale network spiking before, during, and after the controller was engaged. **(b)** Same as (A) except that AP5 was added 1 hour after the start of the closed-loop controller and removed 4 hours later. This is indicated by the arrows at the top of the figure. **(c)** Average pair-wise correlation functions between units for experiments with and without AP5 application (red and black lines, respectively). Cross-correlations were created from spiking data during spontaneous activity before the closed-loop controller was engaged, (ii) half-way through the closed loop-control period, and (iii) during spontaneous network activity following closed-loop control. The data used to create the correlation functions is centered about locations used to create the rastergrams shown in (A.iv) and (B.iv). To create the correlation functions, unit firing rates were calculated using 10 millisecond time bins.

perfusion of 50 μm AP5 into the culturing medium using a syringe pump and a custom, gas-permeable perfusion lid (Potter and DeMarse, 2001) (Figure 3). Four hours after AP5 was applied, NeuroRighter triggered the pump a second time to perform a series of washes with normal culturing medium that removed AP5 from the bath.

Time-series results of this protocol are shown in figure 10(b). The contents of these plots are analogous to figure 10(a) but have arrows to indicate when AP5 was added to, and removed from, the culturing chamber. The controller was able to successfully compensate for changes in network excitability caused by the addition of AP5. Changes in network dynamics were reflected in the control signal, which became smoother in the presence of the AP5 (Figure 10(b.i)).

2.4.3.3 Comparing Experiments 1 and 2

Figure 10(c) shows the average, pairwise firing rate correlation functions (Tchumatchenko *et al.*, 2010) for 30 randomly selected units from experiment 1 (black lines) and experiment 2 (red lines). Figure 10 (c.i) and (c.iii) show the correlation functions of spontaneous network activity before and after the the controller was engaged, respectively. Figure 10 (c.ii) shows correlation functions for epochs during the clamping phase (which included the AP5 treatment for experiment 2). The periodicity of this correlation function follows the 10 Hz aggregate stimulation frequency during the clamping period.

Intriguingly, although the pairwise spiking correlations for experiments 1 and 2 were very similar for epochs of spontaneous activity before and during multichannel stimulation (Figure 10 (c.i) and (c.ii)), they were remarkably different once the stimulator was turned off (Figure 10(c.iii)). When AP5 was not present during the clamping phase (experiment 1), the firing correlation between units appeared to be enhanced following multichannel stimulation. In contrast, pairwise correlations were

almost non-existant following the a population clamp in which AP5 was present (experiment 2). Because the firing statistics (firing rate and correlation structure) during the 6-hour clamping period were nearly identical for the both experiments 1 and 2, this effect on the correlation structure of network activity can not be due to effects on firing activity, but required blocking NMDAergic transmission. Without the closed-loop controller in place, AP5 would have affected network activity levels, obfuscating the mechanism of AP5's effect.

This case study demonstrates the ability of the closed-loop controller to quickly adapt to drug-induced changes in network excitability, to decouple network variables that are normally causally intertwined, and to operate robustly over many hours. Additionally, this case study demonstrates NeuroRighter's ability control peripheral equipment aside from electrical stimulators.

2.4.4 Real-time seizure intervention in freely moving rats

Aside from *in-vitro* recording hardware, NeuroRighter can interface with many different types of neural probes, including those designed to record from and stimulate freely moving animals. To demonstrate this, we performed electrical microstimulation in response to paroxysmal activity of hippocampal recordings taken from a rat with induced temporal lobe epilepsy. Many studies have shown potentially therapeutic effects of electrical stimulation on epileptic brain tissue, which could serve as an alternative to pharmacological or surgical treatment methods. For instance, electrical stimulation triggered by characteristic field potential abnormalities can potentially abrogate seizures and lead to a decreased frequency of behavioral symptoms (Nelson *et al.*, 2011; Mormann *et al.*, 2007; Morrell, 2011).

We used the plugin API to create a closed-loop protocol that could detect temporal lobe seizures in freely moving rats and react with multi-electrode stimulation (Figure 11(a)). This control scheme is similar to that of the NeuroPace responsive

neurostimulation (RNS) system (Sun *et al.*, 2008) (NeuroPace Inc. Moutain View, CA, USA), with the exception that we used multi-micro-electrode stimulation instead of driving a single macroelectrode.

Rats were rendered epileptic using focal injections of tetanus toxin into the right dorsal hippocampus (Hawkins and Mellanby, 1987). LFPs were recorded from CA1 and CA3 regions of the hippocampus using a chronically implanted 16 channel microwire array (Tucker Davis Technologies, Alachua, FL) (Figure 11(b)). The microwire array consisted of two rows of electrodes, with 8 electrodes per row. Multi-electrode stimulation was triggered in response to detected seizures while the rat moved around its cage. To accomplish this, a 'line length' measure on each LFP channel, which has been shown to be effective for threshold-based seizure detection, was calculated online (Esteller *et al.*, 2001). A line length increment for a single LFP channel is defined as as absolute difference between successive samples of the LFP,

$$l_k[t] = |x_k[t] - x_k[t - T_s]| \tag{3}$$

where $x_k[t]$ is the LFP value on the kth channel at time t, and T_s is the LFP sampling period of 500 μsec. $l_k[t]$ was passed through a first order averaging filter,

$$L_k^{\tau_{filt}}[t + T_s] = l_k[t] + \exp\left(\frac{-T_s}{\tau_{filt}}\right) \cdot (L_k^{\tau_{filt}}[t] - l_k[t]) \tag{4}$$

where τ_{filt} is the filter time constant. For each recording channel, we calculated $L_k^{\tau_{filt}}[t + T_s]$ using two values of τ_{filt}, 1 and 60 seconds, which resulted in short and long time averages that could be compared to detect rapidly occurring trends in $l_k[t]$. Specifically, seizures were defined as events for which the criterion

$$L_k^{1sec}[t] > 2 \cdot L_k^{60sec}[t] \tag{5}$$

was met on at least 4 of the 16 recordings channels. Upon seizure detection, 10 randomly chosen electrodes were stimulated sequentially at 45 Hz (aggregate frequency) for 10 seconds using biphasic, 1 volt, 400 μs per phase, square waves. Figure 11(c,d)

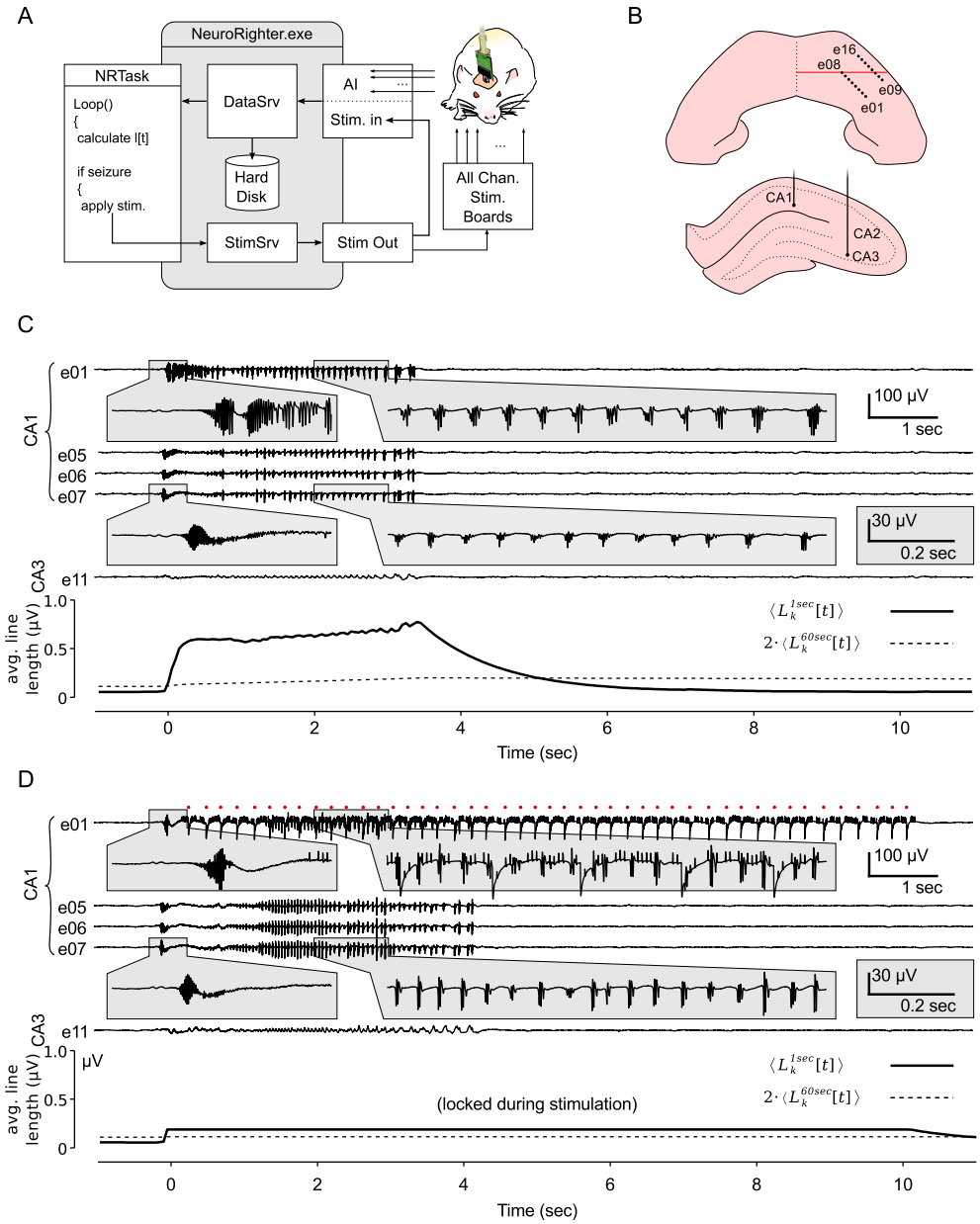

Figure 11: Closed-loop seizure intervention in a freely moving rat. **(a)** Schematic of the closed-loop seizure intervention protocol. A 16-channel microwire array, with two rows of 8 electrodes, was used to record LFP signals in the CA1 and CA3 regions of the hippocampus of a epileptic rat. Paroxysmal activity in CA1 triggered the application of multichannel electrical stimulation through the recording electrodes via a stimulation multiplexing board (green). **(b)** Implantation sites of the microwire array. Top view shows the electrode penetration sites (black dots) in the right-dorsal hippocampus. The red line indicates position of the coronal view shown below. **(c)** A 12 second epoch of hippocampal LFPs during a seizure event. Electrodes 1-8 were located in CA1 and 9-16 in CA3. The line length measures, averaged across channels, are shown below the LFP traces. Seizure detection occurs at 0 seconds. **(d)** Same as (c) except with closed-loop stimulation engaged. Electrical stimulation was applied on electrode 1 along with nine other electrodes (not shown). Red dots indicate stimulation times for e01 and stimulation artifacts appear on the LFP trace. e05-e07 and e11 were not used for stimulus application.

shows seizure events without and with closed-loop stimulation engaged. During stimulus application, $L_k^{\alpha}[t]$ values were frozen to prevent stimulation artifacts from affecting the line length averages.

There was no easily discernible effect of microsimulation on seizure duration or intensity during this pilot experiment. However, this proof of concept demonstrates the API's utility in experiments conducted on freely moving animals to modulate aberrant neural activity states. These features are useful for testing stimulation algorithms that do not just react to a seizure occurrence, but *predict* oncoming seizures ahead of time in order to apply a preventative action, which has proven a difficult goal to achieve (Mormann *et al.*, 2007).

2.4.5 Silent Barrage and robotic embodiment

The complexity of neural systems often necessitates intricate experimental protocols for proper investigation. To meet this requirement, the plugin API can be used to integrate NeuroRighter with complicated configurations of external hardware and software. Working in collaboration with the SymbioticA group at the University of Western Australia, we used NeuroRighter for intercontinental neural control of a robotic system. This project was part of an art-science collaboration called Silent Barrage[7] (Zeller-Townson *et al.*, 2011), in which a dissociated cortical culture in our lab in Atlanta was embodied with a remote array of robotic drawing machines situated in an interactive art gallery. This system is an extension of the MEART project (Bakkum *et al.*, 2007).

Figure 12(a) shows an illustration of the Silent Barrage system. Using the plugin API, a protocol was written to communicate between NeuroRighter and a custom web server running on the same computer. The web server in turn communicated with a client computer controlling a robotic body consisting of 32 independent robots. Each

[7] `http://silentbarrage.com/`

robot had a rotating actuator capable of climbing up and down a vertical column (Figure 12(c)). Columns were arranged in a grid that reflected the electrode layout of the MEA (Figure 12(a,b)). The height of each rotating actuator at a given moment was determined by the instantaneous firing rate detected on two adjacent electrodes from the 59 channel MEA. As the actuators traveled up and down, they periodically marked their positions on the vertical poles using an ink pen. Over time, this resulted in a visual record of spatiotemportal activity of the culture inscribed on each column (Figure 12(c)).

Silent Barrage was exhibited in the United States (New York), Spain (Madrid), Brazil (Sao Paolo), Ireland (Dublin), and China (Bejing). Visitors to the exhibitions were encouraged to mingle amongst the the robotic embodiment and they were observed using overhead cameras (Figure 12(a,b)). The resulting video feed was processed on site to extract features of audience movement (Horn and Schunck, 1981) and these data were streamed back to NeuroRighter's web server in Atlanta. Audience movement measures were then used to adjust stimulation patterns delivered through NeuroRighter's all-channel stimulator. The relationship between incoming video data and electrical stimulation varied from exhibit to exhibit, from simple single-electrode rate coding schemes to more complex multi-electrode schemes where artificial neural networks were used to deliver certain stimulus pattern based upon learned features of incoming video data. Electrical stimulation modulated the activity state of the culture's firing patterns, thus closing the loop around the dissociated culture, robotic body, and audience members separated by thousands of kilometers. While on exhibit in the National Art Museum of China, Silent Barrage was perhaps the Earth's largest behaving 'organism'.

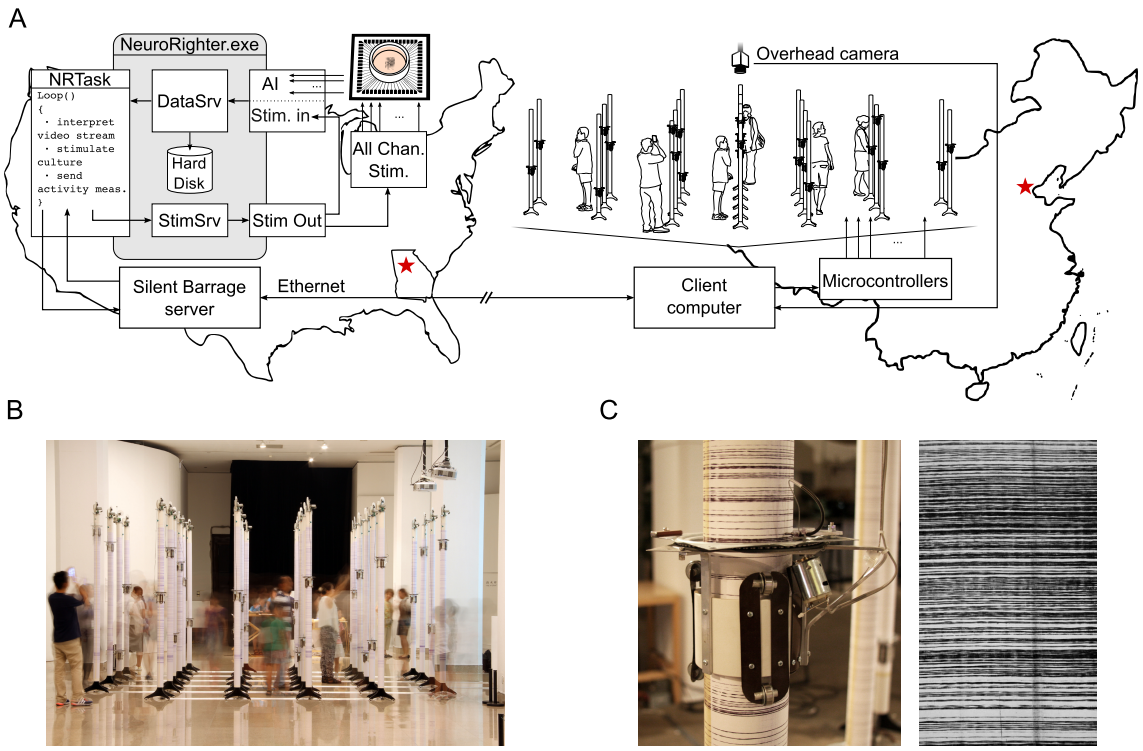

Figure 12: The Silent Barrage robotic embodiment. **(a)** Illustration of the Silent Barrage 'organism' during its exhibition at the National Art Museum of China (NAMOC), in Bejing. Spatial patterns of action potentials recorded from a dissociated cortical culture are used to drive the robotic body. A video stream of visitors to the exhibition are interpreted by NeuroRighter's plugin protocol and used to control multichannel electrical stimulation though the MEA, closing the loop around audience members, robotic system, and neural tissue over thousands of kilometers. **(b)** Audience members viewing the exhibition at NAMOC. Simultaneously, NeuroRighter translated the overhead video feed to stimulation patterns delivered to the culture and then translated resulting neuronal activity patterns to robotic actuation at the exhibit. **(c)** Photograph of an individual robot and the traces it produced during the NAMOC exhibition.

2.5 Discussion

Closed-loop electrophysiology systems are powerful tools for neuroscience research because they can be used to parse recurrent systems into independently manipulable components. Voltage clamp techniques use feedback control to separate membrane potential from the recurrent influence of voltage-dependent ionic conductances (Marmont, 1949). Seminal experiments using voltage clamp have fostered our understanding of ion channels, neuronal excitability, and synaptic transmission. More recently, dynamic clamp has been used to deliver artificial transmembrane or synaptic conductances into living neurons (Prinz *et al.*, 2004; Kispersky *et al.*, 2011). Using these approaches, feedback control transforms dynamic features of *individual neurons* into controlled experimental variables. Similarly, closed-loop multichannel systems like NeuroRighter can transform features of *neural networks* into controlled experimental variables (Arsiero *et al.*, 2007). NeuroRighter is a powerful tool for controlling network variables, improving upon currently available systems in terms of cost, usability, accessibility, extensibility, and hardware standardization (Ahrens *et al.*, 2012; Stirman *et al.*, 2011; Wallach *et al.*, 2011; Wagenaar *et al.*, 2006a). We have demonstrated NeuroRighter's power in conducting basic and translational neuroscience research through a variety of case studies.

Altered gene expression, synaptic input, or environmental conditions can induce changes in spiking activity, which in turn trigger activity-dependent processes. Because of this, it becomes difficult to distinguish the role these factors play in shaping network dynamics and neural plasticity independent of firing rate. Closed-loop multichannel feedback systems provide an opportunity to render the population firing rate a controlled experimental variable and enable study of cellular and network processes as a function of a defined activity state. We used Neurorighter to clamp the firing rate of a living neural network to user-defined setpoints over both short and long timescales (Sections 2.4.2, 2.4.3). Further, we were able to control population

firing rate during prolonged application of the NMDA receptor antagonist, AP5 (Sections 2.4.3). Our controller compensated for the loss of NMDA-mediated excitation and maintained network spiking at the target firing rate. Therefore, the effects of AP5 could be deduced through comparison with a control culture that underwent an identical clamping protocol but with intact synaptic transmission. In most studies that use long-term drug application, the individual roles of spiking and excitatory neurotransmission on plasticity are ambiguous (Turrigiano, 2011b; Rich and Wenner, 2007). By using a real-time multichannel feedback system, we have begun to unravel the independent effects of spiking and NMDAergic transmission on network behavior. This approach could also be used to more directly study the effects of altered genetic or environmental factors on network activity.

In addition to better controlled experimental variables, real-time feedback can be used to improve the relevance of experiments using reduced neural preparations in studies of behavior. Implicit to animal behavior is the interplay between motor output and sensory perception (e.g., head movement affects the visual input stream and vice-versa). While reduced neural preparations or immobilized animals provide excellent experimental accessibility, their major weakness is that they do not preserve a functional sensory-motor loop. We have demonstrated that Neurorighter is well-equipped for performing closed-loop experiments that restore the sensory-motor loop by interfacing living neural networks with artificial bodies (Section 2.4.5). The advantages of this approach over traditional open-loop techniques are twofold. First, neural systems can engage in 'motor' behaviors without sacrificing delicate optical (Ahrens *et al.*, 2012) or electrophysiological (Harvey *et al.*, 2009) access due to actual motion. Secondly, the experimenter has complete control over the mapping between a recorded neural signal and its resulting 'motor' effect (Ahrens *et al.*, 2012; DeMarse *et al.*, 2001). For example, Ahrens and colleagues recently examined optomotor adaptation in paralysed larval zebrafish by embedding them in a virtual environment (Ahrens

et al., 2012). Visual stimuli in the virtual environment provided a perception of motion, and induced fictive motor-nerve activity. Recorded motor-nerve activity was used to drive motion of the virtual environment. Changes in sensory-motor feedback gain could be achieved by adjusting the efficacy by which fictive motor patterns propelled the fish through its virtual world. All the while, full brain activity was recorded through single-cell resolution imaging, which would be nearly impossible to achieve in a freely moving animal. This study highlights how closed-loop interfaces between artificial bodies or environments and a living neural system allow excellent experimental access during behaviors requiring an intact sensory-motor loop.

Aside from basic research, closed-loop multichannel electrophysiology has possible medical applications. Predictive application of drugs or electrical stimulation has the potential to increase the efficacy and safety of treatments for various neurological disorders (Rosin *et al.*, 2011; Mormann *et al.*, 2007) and improve neural rehabilitation procedures (Jackson *et al.*, 2006a). For example, a reliable seizure prediction algorithm would open the possibility for targeted interventions that abort seizures before they occur. Mormann and colleagues provide an extensive comparison of different methods for seizure prediction (Mormann *et al.*, 2007). Unfortunately, the clinical applicability of these algorithms remains quite pessimistic and future studies will require a high-throughput validation system to test robustness of seizure prediction algorithms under a variety of circumstances. We have demonstrated that NeuroRighter can be used for this purpose (Section 2.4.4). The stimulation algorithm we used is very similar to a method called responsive neurostimulation (RNS, NeuroPace Inc. Mountain View, CA, USA) that recently showed very promising results in a large, double-blind pivotal clinical study (Morrell, 2011). This form of closed-loop seizure modulation is not truly predictive as it was triggered on the occurrence of 'unequivocal seizure onset' (Litt and Echauz, 2002). However, the API provides a means for easy reconfiguration in order to test alternative, predictive methods to abort seizures

before they begin, using multichannel electrical stimulation or the local application of an anti-convulsive drug. Additionally, a plugin could be reconfigured for closed-loop modulation of other pathological neuronal activities or to facilitate motor rehabilitation (Jackson *et al.*, 2006a).

Tools that enable closed-loop interaction with neural tissue at the network level have great potential to advance experimental neuroscience. Historically, open-source projects have been extremely good at adapting equipment and code designed for a singular purpose to other uses. For this reason, we envision a large role for open-source software and open-access hardware communities in the development of technologies for closed-loop eletrophysiology systems. Rapid improvements in microprocessor performance, embedded computer systems, on-chip multichannel signal processing, and A/D conversion technology must be matched by projects that can expose their powerful features for researchers with little or no background in embedded systems or computer science. NeuroRighter is one of several open-source hardware/software projects that are enabling more labs to carry out sophisticated electrophysiology with less money and more experimental flexibility[8].

[8] `www.danielwagenaar.net/res/software/meabench`; `http://code.google.com/p/arte-ephys/`; `http://open-ephys.com/`; `http://www.backyardbrains.com/Home.aspx`

CHAPTER III

DELIVERY OF CONTINUOUSLY-VARYING STIMULI USING CHANNELRHODOPSIN-2*

To study sensory processing, stimuli are delivered to the sensory organs of animals and evoked neural activity is recorded downstream. However, noise and uncontrolled modulatory input can interfere with repeatable delivery of sensory stimuli to higher brain regions. Here we show how channelrhodopsin-2 (ChR2) can be used to deliver continuous, subthreshold, time-varying currents to neurons at any point along the sensory-motor pathway. To do this, we first deduce the frequency response function of ChR2 using a Markov model of channel kinetics. We then confirm ChR2's frequency response characteristics using continuously-varying optical stimulation of neurons that express one of three ChR2 variants. We find that wild-type ChR2 and the E123T/H134R mutant ('CheTA') can pass continuously-varying subthreshold stimuli with frequencies up to ∼70 Hz. Additionally, we find that wild-type ChR2 exhibits a strong resonance at ∼6-10 Hz. Together, these results indicate that ChR2-derived optogenetic tools are useful for delivering highly repeatable artificial stimuli that mimic *in-vivo* synaptic bombardment.

*Tchumatchenko, T.†, Newman, J.P.†, Fong, M.-f., Potter, S.M. Delivery of continuously-varying stimuli using ChR2. *Front. Neural Circuits*, **7:194**, 2013. † *Equal contributions; co-first authors.*
 Contributions: J.P.N, T.T., and S.M.P. designed all experiments. J.P.N. and M.F. carried out all experiments. J.P.N. designed and built all custom equipment and performed all data analysis. T.T. derived the frequency response function of ChR2. J.P.N and T.T. wrote the paper. All authors edited the paper.

3.1 Introduction

The network response to continuously-varying stimuli is at the core of cognitive and sensory processing. To understand how neuronal networks encode and process continuously-varying input, a sensory organ is presented with a precisely-defined stimulus and evoked spiking activity is recorded from a corresponding brain region. The power of this technique for deducing network encoding properties has been demonstrated in numerous preparations, including the retina, (Warland *et al.*, 1997; Chichilnisky, 2001), antennal and mechanosensory systems of insects (Geffen *et al.*, 2009; Warland *et al.*, 1992), and somatosenory, auditory, and visual systems of mammals (Arabzadeh *et al.*, 2003; Kayser *et al.*, 2010; Lesica *et al.*, 2007). However, as stimuli delivered to sensory organs propagate to higher brain areas, intrinsic noise and modulatory input from secondary brain regions can interfere with controlled input signals. For studies concerning the function of neural circuits that are several synapses removed from sensory input, the direct introduction of continuously-varying currents to a neural population may provide a more straightforward way to deduce circuit response dynamics.

Optogenetic methods allow precise control of spike times using brief light pulses to excite light-gated ion channels and pumps, such as channelrhodopsin-2 (ChR2) (Boyden *et al.*, 2005; Mattis *et al.*, 2011; Gunaydin *et al.*, 2010). Pulsed optical stimulation using ChR2 dictates a spiking response that is tightly locked to each stimulus by briefly overriding neuronal dynamics. This stands in contrast to the highly variable, subthreshold currents recorded from cortical neurons during natural sensory processing *in vivo* (Destexhe *et al.*, 2003). We hypothesized that using relatively low intensity, continuously modulated optical stimuli to excite ChR2 might allow conductance fluctuations that mimic *in-vivo*-like synaptic bombardment and leave the decision of when and how often to spike to individual cells (Mainen and Sejnowski, 1995; Tchumatchenko *et al.*, 2011). Surprisingly, while the response properties of

microbial opsins to optical pulses have been studied extensively (Mattis *et al.*, 2011), little is known about their ability to relay fluctuating light signals.

In order for ChR2 to be useful for delivering continuously-varying currents, it must allow (1) sufficient bandwidth to mimic synaptic communication and (2) repeatable current waveforms to be delivered across trials. Here, we address these requirements theoretically and experimentally. We find that wild-type ChR2 (ChR2) (Boyden *et al.*, 2005) supports significant photocurrents up to 69 Hz, the H134R mutant ($\mathrm{ChR2_R}$) (Nagel *et al.*, 2005) up to 37 Hz, and E123T/H134R mutant ($\mathrm{ChR2_A}$; also known as 'ChETA') (Gunaydin *et al.*, 2010) up to 73 Hz, and show that evoked current waveforms are extremely repeatable across trials. Using the model, we find that the bandwidth over which $\mathrm{ChR2_R}$ and ChR2 can convey time-varying stimuli is reduced with increasing membrane potential but that $\mathrm{ChR2_A}$'s passband is unaffected. Finally, we show that wild type ChR2 supports a strong resonance with a natural frequency around 10 Hz. This resonance is present, but significantly attenuated, in the H134R and E123T/H134R mutants.

3.2 Results

3.2.1 ChR2's frequency response

In this study, we sought a general description of ChR2's dynamics that captured the ability of both ChR2 and its engineered variants to convey continuously-varying stimuli. To do this, we determined the frequency response function of a population of channels expressed by a single cell, $F_{\mathrm{ChR2}}(\omega)$, using a three-state Markov model of ChR2's channel kinetics (Fig. 13(a)) Nagel *et al.* (2003). The rate equations governing the model's state transitions are

$$\dot{O}(t) = \epsilon\phi(t)C(t) - \Gamma_d O(t) \tag{6}$$

$$\dot{D}(t) = \Gamma_d O(t) - \Gamma_r D(t) \tag{7}$$

$$C(t) = 1 - O(t) - D(t), \tag{8}$$

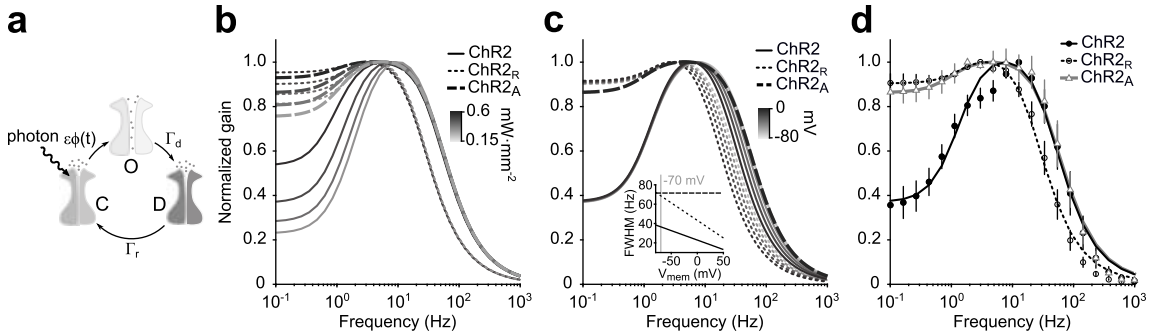

Figure 13: ChR2's amplitude response function. **(a)** Illustration of the three-state Markov channel model described by Eqs. 6-8. The transition rates between open, O, desensitized, D, and closed, C, states are $\epsilon\phi(t)$, Γ_r, and Γ_d, respectively. **(b)** Amplitude response functions $F_{ChR2}(2\pi f)$ for the model are shown for three ChR2 variants using different mean illumination intensities (0.15 through 0.6 mW·mm^{-2}) and parameters in Table 3. **(c)** Voltage dependence of ChR2's amplitude response function. ChR2 and ChR2$_{\mathrm{R}}$ both have a voltage-dependent desensitization rate, $\Gamma_d(v)$, which results in decreased bandwidth as the membrane potential increases. ChR2$_{\mathrm{A}}$ does not have a voltage dependent desensitization rate and therefore has a stable bandwidth across membrane potentials. **(d)** Predicted amplitude response of each ChR2 variant compared to the estimated amplitude response derived from evoked currents recorded from neurons during continuously-varying photostimulation with a mean illumination intensity of 0.35 mW·mm^{-2}. Error bars are ± 1 STD.

where the state variables O, D, and C are the probabilities of a channel being open, desensitized, or closed, respectively. Γ_d and Γ_r are the rates of channel desensitization and recovery. ϵ is the quantum efficiency of ChR2 and $\phi(t)$ is the instantaneous photon flux (light intensity) impinging on a single channel. $\phi(t)$ can be modulated by changing the light intensity of a stimulating light source as a function of time.

The conductance of ChR2 across the cell membrane is proportional to the number of channels that occupy the open state. Therefore, $F_{\mathrm{ChR2}}(\omega)$ can be thought of as a frequency- and phase-dependent transition rate from the channels' closed to open state in response to a continuously-varying stimulus. Since individual channels switch between states discretely, $F_{\mathrm{ChR2}}(\omega)$ describes the transformation of arbitrary optical waveforms to intracellular current under the assumption that a large number of channels are present in the cell's membrane. $F_{\mathrm{ChR2}}(\omega)$ is given by

$$F_{\mathrm{ChR2}}(\omega) = \frac{C_0(j\omega + \Gamma_r)}{-\omega^2 + j\omega(\Gamma_r + \epsilon\phi_0 + \Gamma_d) + \epsilon\phi_0\Gamma_r + \epsilon\phi_0\Gamma_d + \Gamma_r\Gamma_d}.. \tag{9}$$

A detailed derivation of $F_{\mathrm{ChR2}}(\omega)$ can be found in the Methods section.

The amplitude response function, $|F_{\mathrm{ChR2}}(\omega)|$ (Eqs. 9 and 24), is the component

Table 3: Markov model parameters for each ChR2 variant. Values were obtained from fitting the amplitude of the frequency response function (Eq. 9) to the empirically derived response function.

Variant	$\epsilon\phi_0$ (s^{-1})	Γ_d (s^{-1})	Γ_r (s^{-1})
ChR2	6.51	236.35	3.60
$ChR2_R$	1.16	126.74	8.38
$ChR2_A$	0.96	254.63	5.57

of $F_{ChR2}(\omega)$ that indicates the frequency-dependent gain of the channel population in response to fluctuating light signals. The predicted amplitude response functions for ChR2, $|F_{ChR2}(\omega)|$, $ChR2_R$, $|F_{ChR2_R}(\omega)|$, and $ChR2_A$,$|F_{ChR2_A}(\omega)|$, are shown in Fig. 13(b) for different mean illumination intensities. Model parameters were obtained for each ChR2 variant by fitting the predicted amplitude response function in Eq. 24 to the experimental estimate (Table 3; Methods Section 'Delivering time varying currents using ChR2').

$|F_{ChR2}(\omega)|$ has a high frequency cutoff (width at half maximum) of 69 Hz. It should be noted that this cutoff value is defined relative to ChR2's peak conductance, and not in terms of absolute photocurrents. For this reason, it is still possible to use ChR2 to deliver physiologically significant photocurrents at stimulation frequencies exceeding 69 Hz. The shape of $|F_{ChR2}(\omega)|$ indicates that ChR2 exhibits a significant resonance with a natural frequency around 6-10 Hz. This feature explains the large peak to steady-state (DC) ratio of ChR2-mediated photocurrents in response to pulsed stimuli Gunaydin *et al.* (2010); Mattis *et al.* (2011).

In agreement with previous characterizations, $ChR2_R$ is significantly slower than ChR2 and $|F_{ChR2_R}(\omega)|$ has a cutoff frequency at 37 Hz Mattis *et al.* (2011). While $ChR2_R$ supports a resonance in the 3-4 Hz range, its effect is significantly reduced compared to ChR2. The bandwidth of $ChR2_A$ was similar to that of ChR2 with a high frequency cutoff of 73 Hz. $|F_{ChR2_A}(\omega)|$ displayed a moderate resonance that peaked at 3-5 Hz depending on the mean light intensity of the stimulation waveform.

3.2.2 Voltage dependence of channel kinetics

For some ChR2 variants, channel kinetics are dependent on the membrane potential. The off time of ChR2- and $ChR2_R$-evoked currents grow with increasing membrane potentials Mattis *et al.* (2011). Additionally, the time-to-peak conductance for ChR2 increases approximately linearly with membrane potential Mattis *et al.* (2011); Berndt *et al.* (2011). $ChR2_A$ does not have voltage dependent kinetics Mattis *et al.* (2011); Berndt *et al.* (2011). Therefore, for the ChR2 and $ChR2_R$ variants, the transition rates Γ_r and Γ_d in the Markov model, Eqs.6-8, both could be voltage dependent. To understand how voltage-dependent kinetics affect the bandwidth of each ChR2 variant, we derived the transient response of our model to a delta pulse of magnitude ϕ_0 and to a downward step to zero from initial intensity ϕ_0. The response to a delta light pulse, ('on-dynamics') is given by

$$O^{\text{on}}(t) = \epsilon\phi_0 \exp(-\Gamma_d t)\theta(t) \tag{10}$$

where $\theta(t)$ is the Heaviside theta function. The response to a downward step ('off-dynamics') is given by

$$O^{\text{off}}(t) = \exp(-\Gamma_d t)\theta(t)\frac{\Gamma_r \epsilon\phi_0}{\Gamma_d\Gamma_r + \Gamma_d\epsilon\phi_0 + \Gamma_r\epsilon\phi_0}. \tag{11}$$

The long time dynamics of both O^{on} and O^{off} are dominated by Γ_d when using biophysically relevant parameters. Therefore, to capture the effect of voltage on channel kinetics, we assumed a linear relationship between the voltage and Γ_d according to $\Gamma_d(v) = \Gamma_d(1 - 0.0056(v + 70\text{ mV}))$ Mattis *et al.* (2011). We then recalculated the amplitude response function at membrane potentials ranging from -80 to 0 mV (Fig. 13(c)). Increases in membrane potential affected the high-frequency cutoff for the ChR2 and $ChR2_R$ and had a large effect on channel bandwidth. As the membrane voltage increased from -80 to 0 mV, the bandwidth of the amplitude response function decreased by 37% for both variants (Fig. 13(c), inset). In contrast, $ChR2_A$'s constant

bandwidth across voltages makes it well suited for introducing continuously-varying conductances into cells that are not voltage-clamped.

3.2.3 Robustness of the frequency response function

The linear time-invariant frequency response function has the greatest predictive power for stimuli with low peak-to-peak amplitudes. To test the robustness of the frequency response function when using larger amplitude inputs, we compared it with the complete response arising from time-varying light amplitude. Sinusoidal inputs with mean intensity of $\phi_0 = 0.35$ mW·mm^{-2} and different amplitudes $\delta\phi$ were used to drive the linear time-invariant frequency response (Eq. 9) according to

$$O(t) = O_0 + \epsilon\delta\phi F_{ChR2}(\omega)\exp(j\omega t) \tag{12}$$

The complete response dynamics of the Markov model were obtained by inserting the offset and amplitude parameters, ϕ_0 and $\delta\phi$, into the sinusoidal drive (Eq. 13) and numerically integrating the corresponding differential equations (Eqs. 6-8) to obtain $O(t)$.

The response predicted by $F_{ChR2}(\omega)$ and complete solutions will match when $|i\omega + \epsilon\phi_0| \gg \epsilon\delta\phi$. This condition guarantees that terms proportional to $\exp(j\omega t)$ dominate over higher order terms in the derivation of the $F_{ChR2}(\omega)$ response function (Eqs. 18, 19). This condition is fulfilled when $\delta\phi \ll \phi_0$ or for frequencies $\omega \gg \epsilon\phi_0$. We compared simulated and time-invariant solutions to Eqs. 6- 8 and found that the frequency response function provided a good approximation of the complete dynamics, even for relatively large stimulus amplitudes and low stimulus frequencies, where deviations between the linear time-invariant response and complete model dynamics are largest (5 Hz input; Fig. 14).The deviation between $F_{ChR2}(\omega)$ and complete dynamics was negligible for higher stimulus frequencies (20 Hz input; Fig. 15).

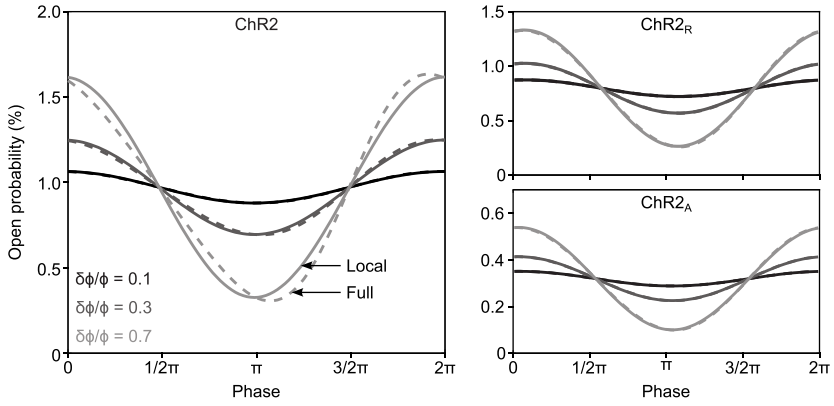

Figure 14: Time-invariant versus complete ChR2 responses to 5 Hz stimuli. The time-invariant $F_{ChR2}(\omega)$ approximation (solid lines) and the complete dynamics (dashed lines) of $O(t)$ are shown in response to 5 Hz sinusoidal stimuli for ChR2 (left), $\mathrm{ChR2_R}$ (right, top) and $\mathrm{ChR2_A}$ (right, bottom). Gray shades represent different sinusoidal amplitudes normalized to the mean stimulus intensity, $\delta\phi/\phi_0 = 0.1, 0.3$, and 0.7.

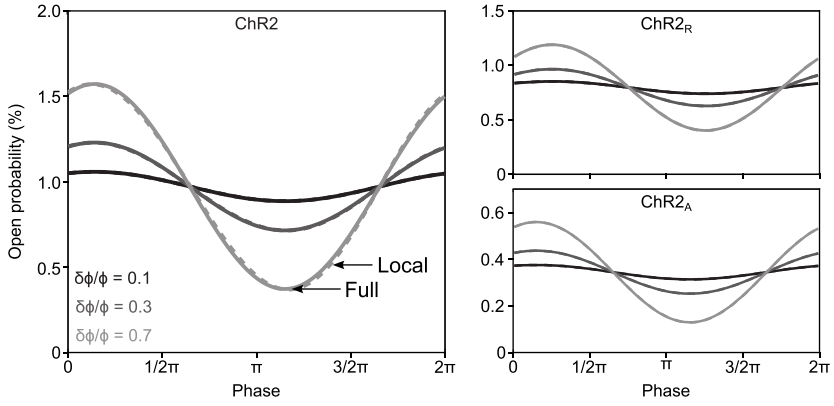

Figure 15: Time-invariant versus complete model dynamics for different ChR2 variants for 20 Hz stimuli. The time-invariant approximation (solid lines) and the complete linear response (dashed lines) of $O(t)$ are shown in response to 20 Hz sinusoidal stimuli for ChR2 (left), $\mathrm{ChR2_R}$ (right, top) and $\mathrm{ChR2_A}$ (right, bottom). Gray shades represent different sinusoidal amplitudes normalized to the mean stimulus intensity, $\delta\phi/\phi_0 = 0.1, 0.3$, and 0.7.

3.2.4 Delivering continuously-varying currents using ChR2

To verify $F_{\mathrm{ChR2}}(\omega)$ experimentally, cultured cortical cells expressing either ChR2, $\mathrm{ChR2_R}$, or $\mathrm{ChR2_A}$ were stimulated with spatially uniform blue light (465 nm at peak intensity) using a light emitting diode (LED), while somatic photocurrents were recorded using whole-cell patch clamp (Methods). To ensure that optical stimuli tracked intended stimulus waveforms, we developed a custom LED driver that used optical feedback to compensate for the static non-linearities and temperature dependence associated with the LED light source (Fig. 16(a-c); Methods; Appendix B).

To gain an initial confirmation of each variant's ability to relay continuously-varying photocurrents, we stimulated cells with swept frequency cosine ('chirp') stimuli (Fig. 16(d); Methods). Chirp inputs allow time and frequency characteristics of each variant to be read directly from the photocurrent time-series. Each variant displayed a characteristic decay in evoked current amplitude with increasing frequency, consistent with the model prediction. Additionally, the slightly increased midband amplitude of ChR2-evoked photocurrents provided indications of a bandpass effect.

Because the full dynamics of ChR2 are time-variant, the estimated frequency response (Eq. 27; Methods) will vary depending on the stimulus choice. Our goal was to use ChR2 to deliver stimuli that mimic *in vivo*-like synaptic bombardment. Therefore, we used optical stimuli consisting of 10-second realizations of a filtered Gaussian noise signal (time constant: $\tau_s = 50$ ms, mean$\pm$standard deviation: $\mu_s = 0.4 \pm \sigma_s = 0.08$ mW$\cdot$mm^{-2}; Methods). We chose stimuli with these parameters because they evoked membrane voltage waveforms with similar amplitude and frequency characteristics to those obtained from *in vivo* recordings of sensory cortical neurons in the high-conductance state (Fig. 17) (Destexhe *et al.*, 2003).

We measured the empirical frequency response function to the Gaussian noise stimulus, $\hat{F}_{\mathrm{ChR2}}(\omega)$, of cells expressing ChR2 ($n = 9$ cells), $\mathrm{ChR2_R}$ ($n = 4$ cells), or

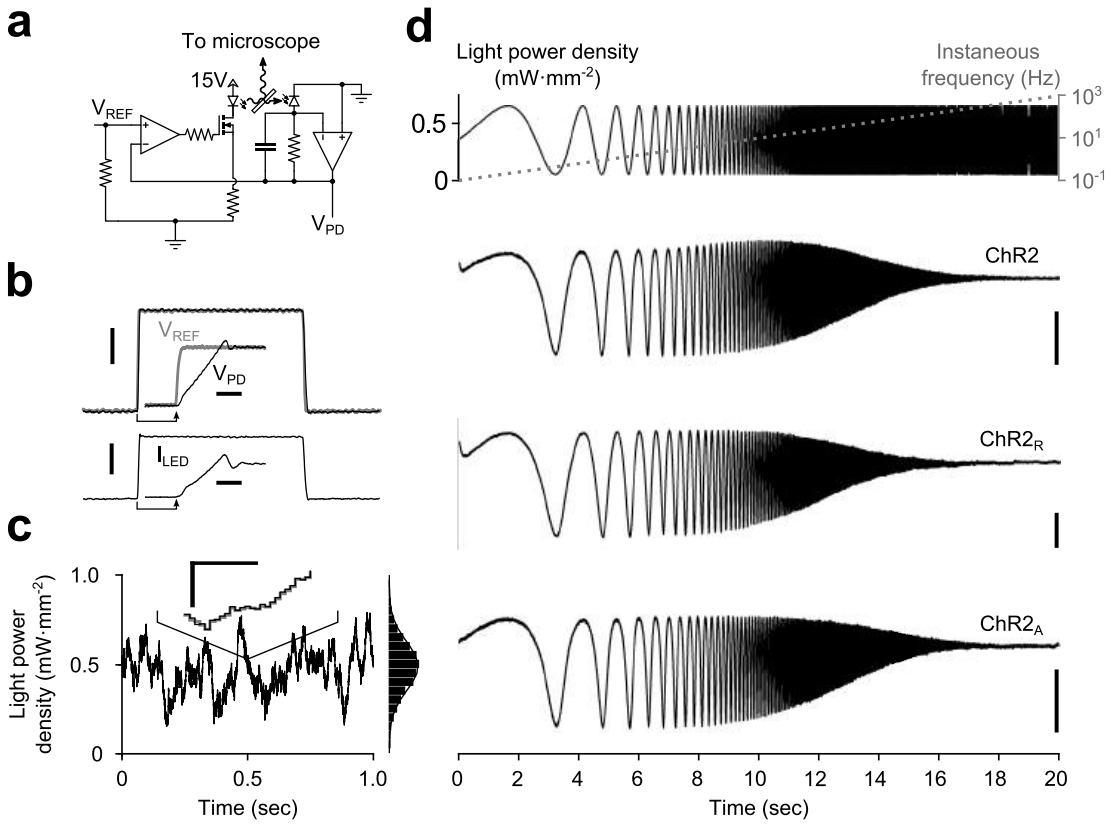

Figure 16: Delivery of continuously-varying stimuli to neurons using ChR2. Delivery of continuously-varying stimuli to neurons using ChR2. **(a)** Simplified schematic of the LED driver in optical feedback mode. The circuit uses an amplified photodiode to compensate for the non-linearities and temperature dependence of the LED, allowing arbitrary waveforms to be delivered to cells. **(b)** A one millisecond LED pulse, $\mathrm{V_{PD}}$ (black), versus the reference voltage, $\mathrm{V_{REF}}$ (gray). The current sourced to the LED is shown in the lower plot. Scale bars, 1 mW·mm^{-2} (top) and 250 mA (bottom). Insets show the zoomed step onset with corresponding 5 μs scale bars. **(c)** A computer generated Gaussian stimulus (gray) signal and the recorded light waveform (black).. The lines overlap almost perfectly, making the reference voltage (gray) difficult to see. An inset shows a zoomed portion of the sequence. Scale bars, 0.05 mW·mm^{-2} and 500 μs. An amplitude histogram of the sequence, with a best-fit Gaussian distribution, is shown to the right. **(d)** Responses to frequency chirp stimuli for each ChR2 variant tested. The top plot shows the stimulus waveform (black) along with the instantaneous frequency profile (gray) and bottom plots show evoked current waveforms. Scale bars, 100 pA.

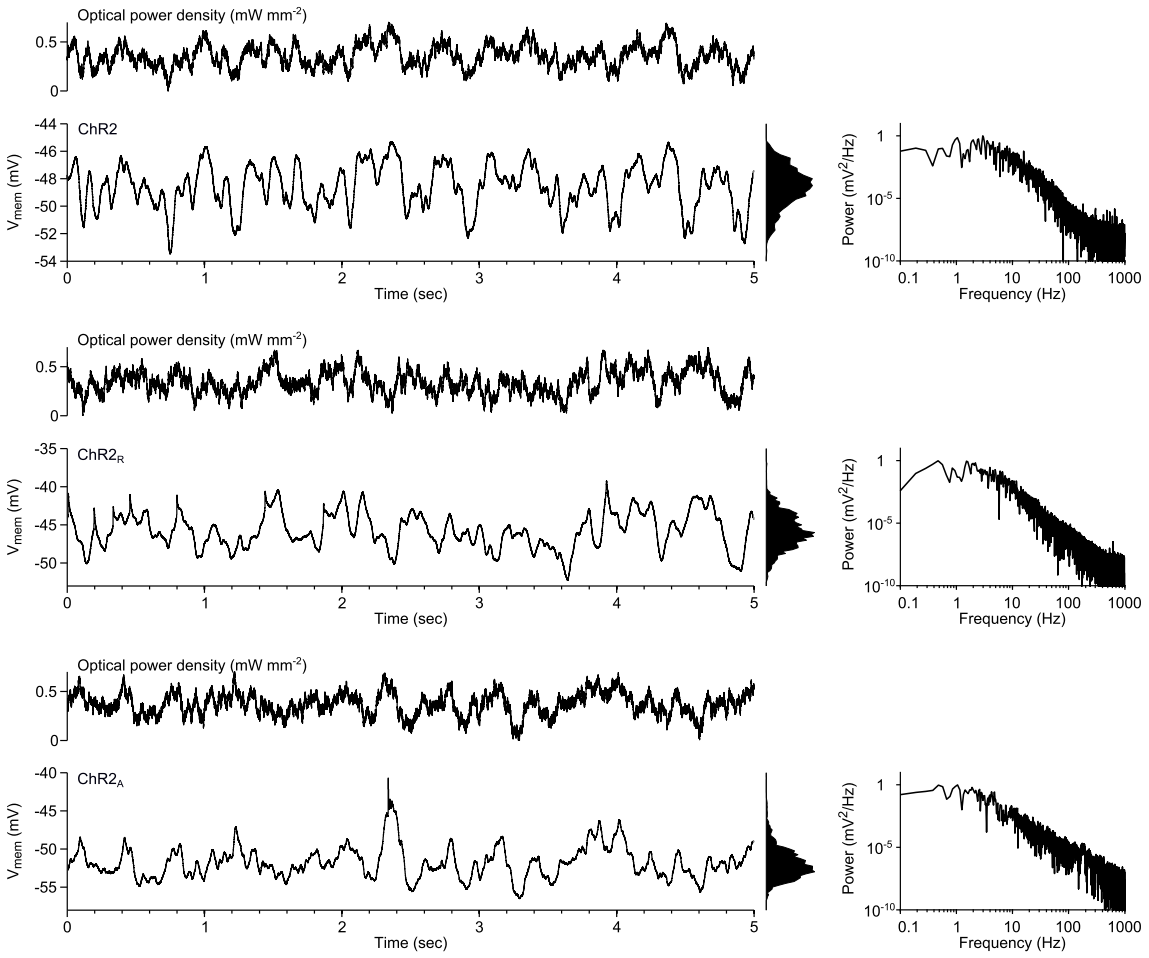

Figure 17: Example membrane voltages during Gaussian photostimulation. (Left) Evoked voltage fluctuations obtained from current-clamp recordings performed during time-varying photostimulation are shown for each ChR2 variant used in this study. Each trace is the average of 10 stimulus-response pairs to a repeated Ornstein-Uhlenbeck stimulus waveform. A voltage histogram is shown to the right of each trace. (Right) Power spectral density estimates for the voltage response. Compare this figure to box 1 in (Destexhe *et al.*, 2003).

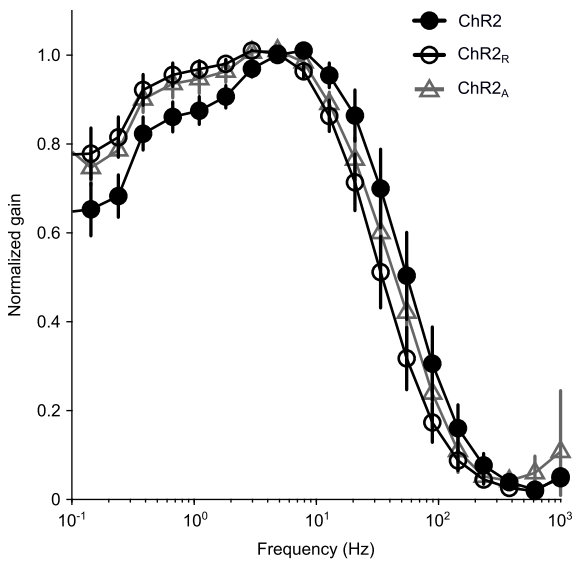

Figure 18: Empirical amplitude response functions of wtChR2 and engineered variants derived from chirp stimuli.

$\mathrm{ChR2_A}$ ($n = 6$ cells) (Methods; Eq. 26-29). We then compared the empirical amplitude responses for each variant, $|\hat{F}_{\mathrm{ChR2}}(\omega)|$, with their theoretical counterparts. We observed good agreement between the empirically derived and predicted amplitude response functions, although some differences exist (Fig. 13(d)). For instance, both $|\hat{F}_{\mathrm{ChR2_R}}(\omega)|$ and $|\hat{F}_{\mathrm{ChR2}}(\omega)|$ have small downward deviations from the predicted response at $\sim$5 Hz, which is more pronounced for ChR2. Additionally, the predicted frequency response tends to slightly overestimate the measured gain at frequencies above 100 Hz. Because stimuli were spatially homogeneous and applied over the extent of the dentritic arbor, the lower-than-predicted response to high frequency stimuli may result from passive dendritic filtering of evoked currents.

To examine how the choice of stimulus waveform might change the channels' response properties, we recalculated the amplitude response function using photocurrents recorded in response to chirp stimuli (Fig. 18). Since chirp stimuli are sinusoidal, they result in a U-shaped amplitude distribution that emphasizes extreme stimulus amplitudes (0.05 and 0.65 $\mathrm{mW{\cdot}mm^{-2}}$; Fig. 19). Because of large sinusoidal amplitude relative to the steady state light level ($\delta\phi/\phi_0 \approx 1$) and the overabundance of extreme

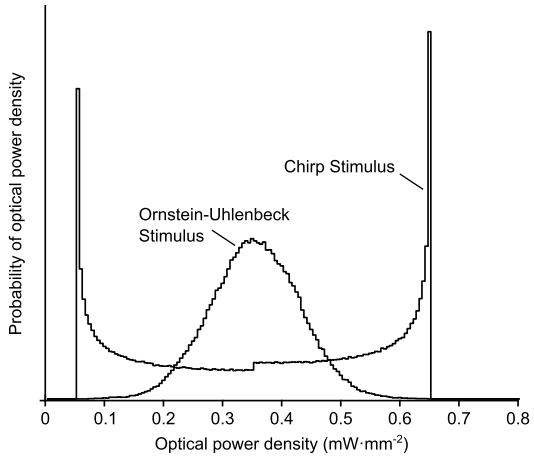

Figure 19: Light power distributions for chirp and Ornstein-Uhlenbeck stimuli.

values, chirp stimuli were less capable of meeting the condition $|(i\omega + \epsilon\phi_0)| \gg \epsilon\delta\phi$, which ensures agreement between the response predicted by $F_{ChR2}(\omega)$ and complete model solutions. Consequently, the amplitude response function estimated from chirp inputs deviates from the analytical amplitude response (Eq. 24). As predicted using the model, these deviations primarily affect low frequencies $f \leq 5$Hz and are most prominent in wild-type ChR2 (see Section 3.2.3; Fig. 14).

Despite these imperfections, both our theoretical and our empirical results indicate that all three channel types are capable of transmitting fluctuating current stimuli to populations of cells in a physiologically relevant frequency range (up to ∼100 Hz). Furthermore, because the model provides a tractable description of channel dynamics, it serves as a useful tool for predicting the bandwidth and resonance of new channels based on measurable physiological parameters.

3.2.5 Reliability of continuously-varying ChR2-evoked currents

In order for continuously-varying photostimulation to be useful in experimental settings, evoked current waveforms must be highly repeatable. Therefore, we measured the reliability of photocurrent waveforms across trials. As expected, evoked photocurrents looked like smoothed versions of the stimulus signal due to the low-pass effect of ChR2's amplitude response function (Fig. 20). Evoked current waveforms

were remarkably stable across trials. There there was no systematic change in the amplitude of evoked currents during repeated applications of a stimulus waveform (Fig. 20(a,c)).

We next examined the distribution of evoked current amplitudes across cells (Fig. 20(f)). The average standard deviation of photocurrents evoked by ChR2 was 26.7 pA. $ChR2_R$ and $ChR2_A$ delivered only slightly larger current fluctuations than ChR2, with a mean standard deviations of 32.0 pA and 31.4 pA, respectively. The similarity in evoked current amplitudes between ChR2 and the engineered variants is likely due to ChR2's resonance, which makes the channel most sensitive to fluctuating stimuli with power in the 10 Hz range, as opposed to steady state inputs.

Finally, to determine the reliability of evoked currents across cells, we calculated the normalized cross-correlation function, c_{s,I_i}, between the light power density, $s(t)$ and photocurrents $I_i(t)$ for each cell, i, and across cells, c_{I_i,I_j}. For ChR2, the median peak value of c_{I_i,I_j} was 0.96, indicating strong correlations between evoked currents in different cells (Fig. 20(d)). The median peak value of c_{s,I_i} was 0.92, indicating strong correlations between evoked currents and the stimulus waveform (Fig. 20(e)). Additionally, the similarity in shape between c_{I_i,I_j} and the autocorrelation of the stimulation process, $c_{s,s}$, indicates that temporal features of the stimulus were accurately converted into photocurrents, as predicted by the passband of the frequency response function (Fig 13(e)).

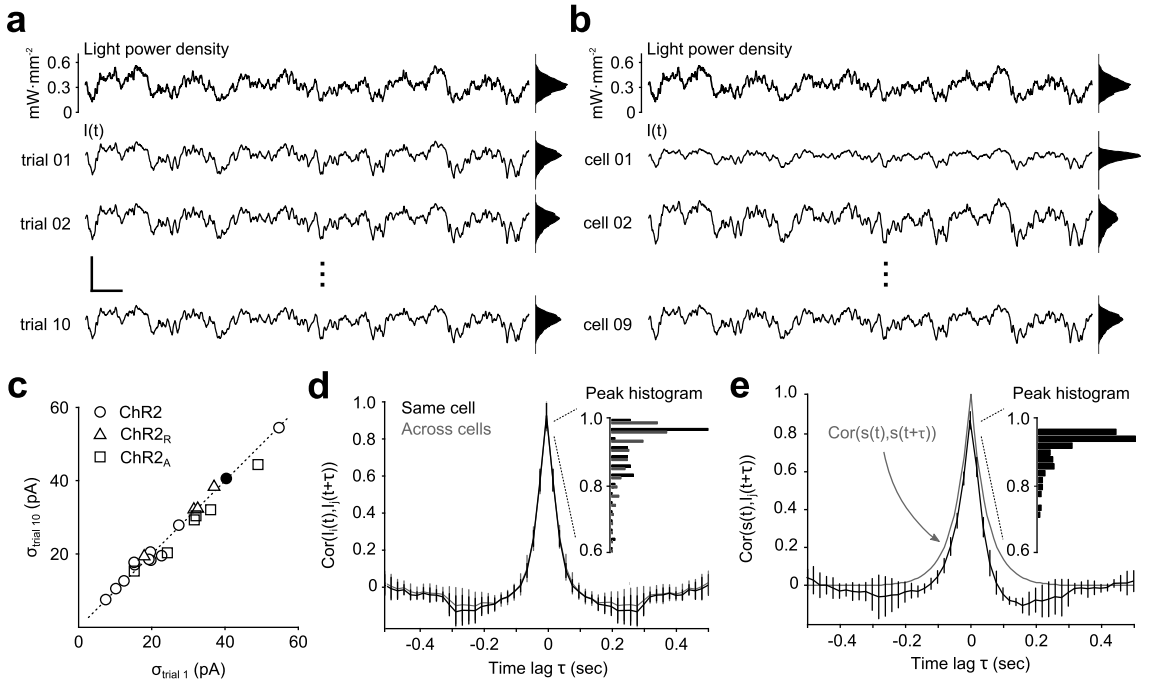

Figure 20: Reliability of continuously-varying neuronal photostimulation. **(a)** Intracellular currents from a single cell during Gaussian stimuli. The top trace is a portion of a 10 second Gaussian stimulus sequence. The bottom three traces show the intracellular currents recorded during different presentations of the same stimulus waveform. Scale bars, 200 pA and 200 ms. Scale bars apply to all time series traces in the figure. **(b)** The same stimulus waveform used in (a), and the corresponding evoked responses from different cells. **(c)** The standard deviation of the photocurrent induced on the first trial of stimulation versus on the last trial. The dotted line is identity. Points near the identity line indicate that there was little or no decrease in stimulus efficacy across trials. The filled dot corresponds to the cell in (a). **(d)** Normalized cross-correlation functions of photocurrents between neurons (gray) or autocorrelation function of photocurrents within the same neuron (black). The inset shows a histogram of peak correlation coefficients. **(e)** Normalized cross-correlation function between the stimulation process $s(t)$ and recorded photocurrents. The gray line is the autocorrelation function of the stimulation process. The inset shows a histogram of peak correlation coefficients. Unless otherwise noted, data in this figure were obtained from cells expressing ChR2.

3.3 Discussion

Optogenetic methods offer genetic specificity, elimination of electrical recording artifacts, and increasingly specialized functionality (Mattis *et al.*, 2011; Berndt *et al.*, 2011). Because of these advantages, optogenetic methods are often used for direct manipulation of neuronal subpopulations in order to understand their function (Cardin *et al.*, 2009; Sohal *et al.*, 2009). Typically, pulsed optical stimuli are used to elicit neural responses. However, for studies that seek to understand information transmission in neural circuits, continuously modulated photocurrents that mimic synaptic bombardment offer several advantages over pulsed stimuli. Continuously modulated photocurrents provide highly controlled subthreshold inputs, while leaving the the decision of when and how often to spike to individual neurons. Therefore, the spikes recorded from the network response to such continuously modulated photocurrents carry the signatures of innate spike generation mechanisms as well as those of interneuronal connectivity and thereby offer the possibility of revealing underlying network encoding strategies.

Previous studies of ChR2's response function have provided mixed results for understanding the channel's ability to relay time-varying input. A preliminary abstract on the ChIEF (Lin *et al.*, 2009) variant's response dynamics in HEK cells described a low-pass rather than a band-pass response (Neef *et al.*, 2011). On the other hand, characterizations of numerous ChR2 variants have focused on step or pulse stimuli (Mattis *et al.*, 2011; Gunaydin *et al.*, 2010). To the best of our knowledge, this study is the first to both theoretically and experimentally derive the ChR2 channel's linear and complete response function in three ChR2 variants.

In this study, we demonstrated the ability of ChR2 to evoke continuously modulated photocurrents in neurons in response to continuously modulated light signals. We used a three-state Markov model (Nagel *et al.*, 2003) to derive an analytical frequency response function for ChR2 variants (Eq. 9). We confirmed these model

predictions experimentally and have shown that the model is sufficient to capture dynamical properties of ChR2 in neurons within a physiologically relevant frequency range. Additionally, we found that the passband of ChR2, $ChR2_R$ and $ChR2_A$ are broad enough to support photocurrents that mimic the noisy synaptic input received by neurons in the high conductance state, *in vivo* (Destexhe *et al.*, 2003) (Fig. 17).

Aside from channel bandwidth, we found that temporal characteristics of continuously-varying photocurrents were highly repeatable across trials and cells. This contrasted with the amplitude distributions of the light-evoked currents across cells, which were highly variable (Fig. 20(c)). The variability of photocurrent amplitudes results from nonhomogeneous expression levels across cells. Potentially, this variability in channel expression could be used to simulate natural sources of noise in neural circuits such as variability in the number of incoming projections (Abbott and Dayan, 2001), variable spiking thresholds (Azouz and Gray, 2000), and sodium channel noise (Jacobson *et al.*, 2005).

Continuously-varying optical stimuli allow subthreshold conductance modulations that can be spatially and genetically targeted. The spatially uniform optical stimuli used in our study produced highly correlated photocurrents across cells (Fig. 20(d)). These temporally locked photocurrents mimic the highly correlated state of subthreshold thalamic drive to sensory cortical neurons that share a receptive field (Lampl *et al.*, 1999; Roy and Alloway, 2001; Okun and Lampl, 2008). However, the incorporation of spatial light modulation would open the door to more complex experimental questions. For instance, spatial modulation of continuously-varying stimuli would allow control over the degree of synchronization between subthreshold currents across cells (Reutsky-Gefen *et al.*, 2013). Additionally, spatial light modulation could be used to isolate continuously-varying input to particular regions of individual neurons (Grossman *et al.*, 2010). For instance, by targeting the soma and axon-hillock, any low-pass effect resulting from the integrative properties of the dendritic arbor

might be avoided. Conversely, targeting dendrites might provide more biophysically realistic input compared to stimuli covering the entire cell. However, even without spatial control of stimuli, we have shown that spatially homogeneous stimuli provide a wide bandwidth to deliver complex stimulus waveforms to populations of cells. Additionally, spatially homogeneous continuously-varying stimulation has the added benefit that it can be readily incorporated into existing experimental setups that use multi-mode optical fiber to deliver light *in vivo*.

Finally, we showed that ChR2's frequency response function supports a resonance. The degree of resonance is dependent on the values of free model parameters, which change for different ChR2 variants and stimulus signals. This finding is especially relevant for studies that use ChR2 to examine the frequency-dependence of neural circuitry (Cardin *et al.*, 2009), since it is important to separate the intrinsic dynamics of ChR2 from those that belong to the network under study. We found the most pronounced resonance for ChR2 with a natural frequency of ∼6-10 Hz. ChR2 was cloned from the green algae *Chlamydomonas reinhardtii*. Interestingly, the algae's phototaxic flagellar movement is tuned to the resonant frequency band of ChR2 (Josef *et al.*, 2006), indicating a potential behavioral significance of ChR2's bandpass effect for algae in their natural environment.

ChR2's amplitude response function indicates that the sum of channel recovery and desensitization transition rates determines its frequency cut-off. Therefore, opsins with faster transition rates will allow a broader passband for time-varying inputs. As new optogenetic tools are discovered and existing ones improved, their increased bandwidth may eventually offer an artificial, optical neural communication channel that actually exceeds the bandwidth of natural sensory organs. This would have tremendous implications for how neural computation and processing are studied and for the advancement of brain-machine interfaces. For the purposes of continuously-varying photostimulation with existing tools, we found that the $ChR2_A$

variant offered the widest dynamic range, did not display voltage-dependent channel kinetics, and exhibited only a mild resonance. This makes it a good choice for delivering continuously-varying stimuli to populations of cells embedded within functioning neural circuits.

ChR2 was derived from microbes that use it for optical sensation in natural environments. It is therefore not surprising that the channel is excellent at conveying continuously-varying input signals. Using channelrhodopsins as a means for delivering repeatable, continuously-varying stimuli to genetically defined populations of cells will be a powerful method for probing the dynamics of neural circuits and modulating their activity to provide artificial sensation.

3.4 Experimental methods

3.4.1 ChR2 expression system

Cell culture was performed as described in Chapter 2, Section 2.2.1. AAV2-CaMKllα-ChR2-mCherry at $4{\cdot}10^{12}$ c.f.u.$\cdot$ml^{-1} was produced by the Kaplitt lab (Cornell University) using plasmid DNA for CaMKIIα::ChR2-mCherry obtained from the K. Deisseroth (Standford University). AAV2-CaMKllα::hChR2(H134R)-mCherry at $4{\cdot}10^{12}$ c.f.u.$\cdot$ml^{-1} was produced by the University of North Carolina at Chapel Hill Vector Core. AAV9-CaMKllα::hChR2(E123A/H134R)-eYFP at $4{\cdot}10^{12}$ c.f.u.$\cdot$ml^{-1} was produced by the University of Pennsylvania Vector Core. At 1 to 5 days *in vitro* (DIV), viral aliquots were diluted to $1{\cdot}10^{12}$ c.f.u.$\cdot$ml^{-1} using culturing medium. 1 μL of diluted viral solution was added to 1 mL culturing medium for a final infection concentration of $1{\cdot}10^{9}$ c.f.u.$\cdot$ml^{-1}. Cultures were then incubated for 3 days before the culturing medium was exchanged. The fluorescent signal of the reporter protein was monitored for several days post infection to ensure channel expression. All experiments were carried out at 3 to 4 weeks *in vitro*.

3.4.2 Intracellular recordings

Whole-cell voltage-clamp recordings were conducted on pyramidal neurons expressing the mCherry ($ChR2_R$ and ChR2) or eYFP ($ChR2_A$) reporter protein. Recordings were performed in a continuous perfusion of artificial cerebrospinal fluid (aSCF) bubbled with 95% O_2 and 5% CO_2 to maintain a pH of 7.4. The aSCF solution contained (in mM) 126 NaCl, 3 KCl, 2 $CaCl_2$, 1 NaH_2PO_4, 25 $NaHCO_3$, 1.5 $MgSO_4$ and 25 D-glucose. The temperature of the extracellular medium was regulated to 35 °C using an inline heater (Warner Instruments, Hamden, CT). 1.5 mm outer diameter, 1.1 mm inner diameter borosilicate glass capilaries (Sutter Instruments, Novato, CA) were pulled into patch pipettes and filled with a solution containing (in mM) 100 K-gluconate, 30 KCl, 3 ATP, 2 $MgSO_4$, 0.5 ethylene glycol tetraacetic acid and 10 HEPES adjusted to pH 7.4 using 0.1 M KOH. Filled pipettes had resistances of 4-8 MΩ. Voltage clamp recordings were performed using HEKA EPC8 amplifier and PatchMaster control software in whole-cell mode. Cells were held at -70 mV and membrane current measurements were amplified and low-pass filtered at 3 kHz before being digitized at 20 kHz and streamed to disk. Access resistance and seal resistance were monitored between stimulation protocols. Current clamp recordings were performed in 'fast' mode using the same filter setting as voltage clamp. All experiments were performed in the presence of 40 μM 6-cyano-7-nitroquinoxaline-2,3-dione (CNQX), 50 μM (2R)-amino-5-phosphonovaleric acid (AP5), 20 μM bicuculline in order to block most synaptic transmission. Whole-cell recordings were analyzed offline in MATLAB (The MathWorks, Natick, MA).

3.4.3 Optical stimulation

A 10-watt (electrical power) light emitting diode (LED) was used for optical stimulation, with peak emission wavelength of 465 nm and ∼20 nm full width at half

maximum intensity (LZ4-00B200, LEDEngin, San Jose, CA). To deliver optical stimuli to cultured neurons, the LED was focused into the epi-illumination port of an E600FN upright microscope (Nikon Corporation, Tokyo, Japan) and passed through a 40X objective lens. The light power produced by LEDs is affected by their temperature. Additionally, the relationship between forward diode current and irradiance is a static non-linearity. To compensate for these factors and deliver distortion-free optical stimuli, we designed a precision current source with integrated optical-feedback to drive our LED (Fig. 16(a)). This circuit measures the instantaneous optical power produced by the LED using an amplified photodiode. It then adjusts the current sourced to the LED such that the optical power measurement matches a reference voltage supplied by a digital to analog converter (DAC; LIH 1600, HEKA Electronik, Lambrecht/Pfalz, Germany). The circuit can precisely modulate the LED brightness over a bandwidth of 50 kHz (Appendix B). A full design specification for the device is available in Appendix B.

3.4.4 Derivation of ChR2's frequency response

The differential equations governing the Markov model, (Eqs. 6-8), are nonhomogeneous with continuously-varying coefficients. For this reason, the frequency response function does not provide a full description of the model's dynamics. However, it serves as a useful simplification for describing ChR2's bandpass characteristics within local regions of optical intensity (Fig. 13(b)). The full time-variant dynamics are not analytically solvable and required numerical simulations of response trajectories (Figs. 14 and 15).

ChR2's frequency response function, $F_{\mathrm{ChR2}}(\omega)$, can be obtained by considering the channels' response to a small sinusoidal light signal with a constant light level ϕ_0,

$$\phi(t) = \phi_0 + \delta\phi \exp(j\omega t), \tag{13}$$

where $\omega = 2\pi f$ and f is the frequency of the sinusoid in Hz and $j = \sqrt{-1}$. The first

order response dynamics of the open and closed probabilities can then be described by a constant offset and periodic component,

$$O(t) = O_0 + \delta O \exp(j\omega t) \tag{14}$$

$$D(t) = D_0 + \delta D \exp(j\omega t). \tag{15}$$

Within a local region of optical intensities, $\phi_0 \pm \delta\phi$, changes in the open state, δO, or the desensitized state, δD, are proportional to changes in optical input, $\epsilon\delta\phi$. The proportionality factors for the open and desensitized states are the frequency response functions $F_{\mathrm{ChR2}}(\omega)$ and $G_{\mathrm{ChR2}}(\omega)$, respectively,

$$\delta O = \epsilon\delta\phi F_{\mathrm{ChR2}}(\omega) \tag{16}$$

$$\delta D = \epsilon\delta\phi G_{\mathrm{ChR2}}(\omega). \tag{17}$$

Differentiating equations 14 and 15 and inserting the result into Eqs. 6 and 7 leads to

$$\begin{aligned} j\omega\delta O \exp(j\omega t) = {} & [\epsilon\phi_0(1 - O_0 - D_0)] + \Big[\epsilon\delta\phi(1 - O_0 - D_0) \\ & + \epsilon\phi_0(\delta O - \delta D) - \Gamma_d \delta O\Big] \exp(j\omega t) + \mathcal{O}(2) \end{aligned} \tag{18}$$

$$j\omega\delta D \exp(j\omega t) = [\Gamma_d O_0 - \Gamma_r D_0] + [\Gamma_d \delta O - \Gamma_r \delta D] \exp(j\omega t). \tag{19}$$

By dropping all but the first-order terms of Eqs. 18 and 19 (meaning those terms proportional to $\exp(j\omega t)$), and removing the common factor $\exp(j\omega t)$, changes in the open and desensitized states due to changes in light power are given by

$$j\omega\delta O = \epsilon\delta\phi(1 - O_0 - D_0) + (\epsilon\phi_0 - \Gamma_d)\delta O - \epsilon\phi_0\delta D \tag{20}$$

$$j\omega\delta D = \Gamma_d \delta O - \Gamma_r \delta D, \tag{21}$$

where $(1 - O_0 - D_0) = C_0$ is the steady-state probability of the channel being closed. Performing the necessary algebra to solve for δO results in

$$\delta O = \epsilon\delta\phi \left[\frac{C_0(j\omega + \Gamma_r)}{-\omega^2 + j\omega(\Gamma_r + \epsilon\phi_0 + \Gamma d) + \epsilon\phi_0\Gamma_r + \epsilon\phi_0\Gamma_d + \Gamma_r\Gamma_d} \right]. \tag{22}$$

Finally, referencing Eq. 16, ChR2's frequency response function for a local region of light intensities is calculated by dividing the left hand side of Eq. 22 by $\epsilon\delta\phi$,

$$F_{\mathrm{ChR2}}(\omega) = \frac{\delta O}{\epsilon\delta\phi} = \frac{C_0(j\omega + \Gamma_r)}{-\omega^2 + j\omega(\Gamma_r + \epsilon\phi_0 + \Gamma_d) + \epsilon\phi_0\Gamma_r + \epsilon\phi_0\Gamma_d + \Gamma_r\Gamma_d} \tag{23}$$

and the amplitude response is then given by

$$|F_{\mathrm{ChR2}}| = \frac{C_0\sqrt{\omega^2 + \Gamma_r^2}}{\sqrt{(-\omega^2 + \epsilon\phi_0\Gamma_r + \epsilon\phi_0\Gamma_d + \Gamma_r\Gamma_d)^2 + (\omega(\Gamma_r + \epsilon\phi_0 + \Gamma_d))^2}}. \tag{24}$$

In the high frequency limit, Eq. 23 reduces to $\frac{C_0(j\omega)}{-\omega^2 + j\omega(\Gamma_r + \epsilon\phi_0 + \Gamma_d)} \propto \frac{C_0}{j\omega/(\Gamma_r + \epsilon\phi_0 + \Gamma_d) + 1}$.

3.4.5 Experimental verification of frequency response functions

To estimate the frequency response of ChR2, $\hat{F}_{\mathrm{ChR2}}(\omega)$, we delivered optical stimuli, $s(t)$, consisting of T=10 second realizations of a Gaussian (Ornstein-Uhlenbeck) noise process while recording evoked intracellular currents, $I_i(t)$, within a single cell, i. $s(t)$ was generated according to

$$s(t_{n+1}) = \mu_s + s(t_n)\exp(-dt/\tau_s) + \sigma_s\xi(t_n)\sqrt{1 - \exp(-2dt/\tau_s)}, \tag{25}$$

where $s(t_1) = 0$ mW·mm^{-2}, $\mu_s \simeq 0.35$ mW·mm^{-2}, and $\sigma_s \simeq 0.08$ mW·mm^{-2} are the initial condition, mean, and standard deviation of the process, respectively. $\tau_s = 50$ ms is the correlation time of $s(t)$, $dt = 40$ μs is the DAC update period, and $\xi(t_n)$ is a random variable drawn from the standard normal distribution. Each cell was exposed to a single, repeated realization of $s(t)$ for $k = 10$ trials. The first 500 ms of each trial was ignored to remove the non-stationary effects of the stimulator turning on. The recorded intracellular currents were averaged across trials,

$$\langle I_i \rangle = \frac{1}{10}\sum_{k=1}^{10} I_{i,k}(t) \tag{26}$$

to remove trial-to-trial noise. We then calculated the empirical frequency response function for each cell,

$$\hat{F}_{\mathrm{ChR2},i}(\omega) = \frac{S_{s\langle I_i \rangle}}{S_{ss}}, \tag{27}$$

where S_{ss} is the power spectrum of $s(t)$ and $S_{s\langle I_i\rangle}$ is the cross spectrum of $\langle I_i\rangle$ and $s(t)$. S_{ss} and $S_{s\langle I_i\rangle}$ are defined as the Fourier transforms of the corresponding correlation function,

$$c_{ss}(\tau) = \int_{-T}^{T} s(t)s(t+\tau)\,\mathrm{d}\tau \tag{28}$$

$$c_{s\langle I_i\rangle}(\tau) = \int_{-T}^{T} s(t)I(t+\tau)\,\mathrm{d}\tau. \tag{29}$$

Finally, we averaged $\hat{F}_{\mathrm{ChR2},i}(\omega)$ across cells to obtain the empirical frequency response for each construct, $\hat{F}_{\mathrm{ChR2}}(\omega)$. To improve our estimate of the power spectra, we followed the procedure introduced in Higgs and Spain (2009) and used a frequency dependent window, equivalent to a Gaussian bandpass filter with standard deviation of $\sigma = 2\pi/\omega$ in the frequency domain. Spectra were evaluated at discrete increments, $\omega_n = 2\pi 10^n$, $n = 0.1, 0.2, ..., 3$. Model parameters were obtained for each ChR2 variant by fitting the predicted frequency response function in Eq. 24 to the experimental estimate, Eq. 27.

In addition to Gaussian stimuli, we used cosine frequency sweeps ('chirps') consisting of $T = 20$ second sinusoidal sweeps of constant amplitude a_s and exponentially increasing frequency from $f_0 = 0.1$ to $f_T = 1000$ Hz. They were defined as

$$s(t) = a_s \cos(2\pi f(t)) + a_0 \tag{30}$$

where

$$f(t) = f_0(f_T/f_0)^{\frac{t}{T}} \tag{31}$$

and $a_s \simeq 0.3$ mW·mm^{-2} and $a_0 \simeq 0.35$ mW·mm^{-2}. The empirical frequency response was then estimated directly from the intracellular current recordings according to

$$\hat{F}^{\mathrm{chirp}}_{\mathrm{ChR2},i}(\omega) = \frac{\mathcal{F}\langle I_i\rangle}{\mathcal{F}\langle s\rangle}, \tag{32}$$

where $\mathcal{F}$ denotes the Fourier transform.

CHAPTER IV

EFFECTS OF CONNECTIVITY ON SIGNAL TRANSDUCTION IN RECURRENT CORTICAL NETWORKS

Network function emerges from the collective activity of populations of neurons coordinated by synaptic interactions. Here we directly investigate the role of synaptic connectivity on population encoding of time-varying stimuli in randomly connected networks of cortical neurons. Using continuously-varying optogenetic stimulation, we deliver stimuli that mimic the afferent sensory drive to a genetically defined input layer of excitatory neurons, while monitoring the network spiking response using a microelectrode array. We then investigate how defined changes in connectivity, due to selective blockade of excitatory and inhibitory synaptic receptors, affects the population spiking response. We find that pairwise neuronal response correlations are increased by excitatory connectivity, but that inhibitory connectivity actively decorrelates neuronal firing. Additionally, we find that excitatory connectivity decreases spike-timing precision and information rates of the individual unit and pairwise spiking response, but linearizes individual units' encoding dynamics.

4.1 Introduction

How are the encoding properties of neural circuits affected by connectivity? Network architecture is thought to play an important role in population coding in many different sensory systems. In the retina, lateral connectivity has long been hypothesized to decorrelate the strong, potentially redundant spatial correlations present in natural visual stimuli, allowing retinal ganglion cells to transmit information with high efficiency (Barlow, 1961). In the somatosensory and visual pathways, thalamic projections account for only a small fraction of synapses to sensory cortical circuits (da Costa and Martin, 2011), and are relatively weak (Bruno and Sakmann, 2006) (although,

these inputs are highly convergent so they exert a post-synaptic effect larger than their low numbers and strengths might suggest). The majority of synaptic connections to cells in these areas originate locally (Sáez and Friedlander, 2009), resulting in highly recurrent cortico-cortical circuitry that is thought to play a role in sensory transduction and processing (Martin, 2002; Sharon and Grinvald, 2002).

Are the effects of connectivity on encoding sensitive to architectural nuance, or are there emergent effects of connectivity on encoding that persist even in randomly connected networks? Computational studies indicate that randomly connected networks can exhibit low-pass or resonant dynamics in response to time-varying stimuli depending on the statistics of network connectivity (Ledoux and Brunel, 2011). Similarly, computational studies of balanced networks, where excitatory synaptic inputs are roughly canceled by inhibition, indicate that recurrent synaptic drive acts as a strong negative feedback, which can linearize the population response despite the highly nonlinear properties of constituent neurons (van Vreeswijk and Sompolinsky, 1996, 1998; Douglas *et al.*, 1995). Perhaps the most robust effect of connectivity is on the strength of stimulus-induced activity correlations. The clearest work concerning the roles of activity correlations on population encoding comes from experimental work performed in the retina. Based on the multi-cell response to continuous optical stimuli, it has been demonstrated that the evoked responses of retinal ganglion cells to naturalistic stimuli are highly correlated across cells (Warland *et al.*, 1997; Puchalla *et al.*, 2005) and that structure within the multi-neuron response is largely accounted for by pairwise firing correlations (Schneidman *et al.*, 2006). However it has also been shown that this hight correlated response provides is decorrelated, both temporally and spatially compared to the stimulus input (Pitkow and Meister, 2012) and that decoders that incorporate activity correlations produce improved stimulus reconstructions compared to those that do not (Pillow *et al.*, 2008). The progress made in understanding population encoding properties of the retina is a result of its

amenability to multi-electrode recordings and built-in sensory transduction machinery (Warland *et al.*, 1997; Field *et al.*, 2010; Puchalla *et al.*, 2005).

We have developed a new experimental technique that translates the advantages of the retinal preparation to cultured cortical networks, which support a comparatively recurrent and random connectivity structure (Nakanishi and Kukita, 1998) and are composed of a simpler set of neuronal subtypes. In Chapter 3, I showed how continuous time-varying optical stimulation could be used to deliver arbitrary time-varying stimuli to isolated cells. Here, we use this technique to provide continuously modulated, temporally-precise, and extremely repeatable subthreshold stimulus waveforms to a genetically specified 'input layer' composed of excitatory pyramidal cells while the full network spiking response is monitored with a microelectrode array (MEA). This experimental configuration closely resembles computer models of cortical networks that assume random connectivity and external driving input to a subset of cells (Brunel, 2000; Vogels *et al.*, 2005; Vogels and Abbott, 2009; van Vreeswijk and Sompolinsky, 1996, 1998; Douglas *et al.*, 1995; Izhikevich *et al.*, 2004; Izhikevich, 2006), but is composed of real neurons.

Using this system, we measure the response properties of networks that receive identical stimuli before and after we have manipulated connectivity using selective synaptic blockade. We demonstrate that time-varying optical stimuli evoke extremely repeatable population spiking responses. We find that, in line with previous theoretical predictions, recurrent connectivity linearizes the network's population spiking response. However, we also find that connectivity also reduces spike timing precision compared to disconnected network states, and that changes in spike timing precision are dictated by the non-linear portion of the neuronal response process. Further, we show that in the absence of synaptic connectivity, spike trains become less correlated but the relative timing precision across pairs of cells increases. Finally, we find that recurrent excitatory input reduces information rates and increases encoding

redundancy. Taken together, these results indicate that linearization of the network response and resultant changes in spike timing precision and pairwise activity correlations may not depend critically on the structural nuances of cortical connectivity, but can emerge in networks with random connectivity.

4.2 Experimental Methods

4.2.1 Viral transduction

Cell culture was performed as described in Chapter 2, Section 2.2.1. AAV2-CaMKllα-hChR2(H134R)-mCherry with a genomic titer of $3{\cdot}10^{12}$ c.f.u.$\cdot$ml^{-1} was produced by the University of North Carolina at Chapel Hill Vector Core. At 1 to 5 days *in vitro* (DIV), viral aliquots were diluted to $2{\cdot}10^{12}$ c.f.u.$\cdot$ml^{-1} using conditioned culturing medium from sister cultures. 4 μL of this diluted viral solution was added to 1 mL culturing medium for a final infection concentration of $8{\cdot}10^{9}$ c.f.u.$\cdot$ml^{-1}. Infected cultures were incubated for 3 days before the culturing medium was exchanged. The fluorescent signal of the mCherry reporter protein was monitored in 3 sister cultures over the days post infection to ensure robust expression (Fig. 31). All experiments were carried out on cultures at 3 to 4 weeks *in vitro*.

To ensure the genetic specificity of the calmodulin-dependent protein kinase IIα (CaMKllα) promotor, and therefore the pyramidal-specific information channel to the recurrent network, immuncytochemistry was performed against Neuronal Nuclear protein (NeuN) and CaMKIIα in cultures expressing ChR2(H134R)-mCherry. A DAPI stain was used to identify cell bodies. We fixed, stained, and imaged 2 sister cultures at 26 DIV (25 days post transfection) using a Zeiss LSM 510 microscope (Carl Zeiss AG, Oberkochen, Germany). We then counted instances of co-localization of DAPI, NeuN, CaMKllα and mCherry in 12 distinct regions of interest (7 in one

culture, 5 in the other) using the cell counter plugin[1] for ImageJ[2]. 79.0±1.5% of neuronal somata (identified by expression of NeuN) also expressed CaMKllKα. Of the CaMKllα-expressing somata, 65.9±2.0% expressed the mCherry reporter protein. 12.6±3.9% of somata that showed no sign of CaMKllα-expression also expressed mCherry (Fig. 1(b)).

4.2.2 Multielectrode recordings

Microelectrode array recordings were conducted using the open-source NeuroRighter multichannel electrophysiology platform (Chapter 2) (Rolston *et al.*, 2009a; Newman *et al.*, 2013). Neurorighter was used to control multichannel data acquisition, perform online processing, generate stimulus signals, and stream data to disk. Microelectrode voltages were amplified and bandpass filtered between 1 Hz and 5 kHz using a 60 channel analog amplifier (MEA 1060, Multichannel Systems, Reutlingen, Germany). Because the amplifier can exceed 37 °C during long experiments, it requires active cooling to maintain the culture's health. Therefore, during all experiments, the temperature of the culture was regulated to 35 °C using a servo-controlled solid state Peltier heater/cooler mounted below the recording amplifier (Fig. 33(a); Appendix C).

Amplified electrode voltages were digitized using two synchronized PCIe-6259 multichannel data acquisition cards (National Instruments, Austin, Texas) and then read by NeuroRighter for digital processing. Amplified electrode voltages were digitally filtered using a 3rd-order Butterworth filter with a passband of 300 to 5000 Hz. Action potentials were detected using a threshold of $6\times V_{\mathrm{RMS}}$ and sorted online using an automated classification algorithm (Newman *et al.*, 2013) (Appendix A, Section A.3). For each culture, the spike sorter was trained based on evoked responses to a small set of stimulus trials, which used the same stimulus parameters as were used during experiments, but in the absence of drugs. The sorter was not retrained thereafter

[1] `http://rsbweb.nih.gov/ij/plugins/cell-counter.html`

[2] `http://rsbweb.nih.gov/ij/`

so that the same units could be tracked across experimental conditions. Following sorting, spikes were saved to disk. Using a third PCIe-6259 card, NeuroRighter collected auxiliary analog signals from the amplified photodiode (Section 4.2.4) and digital signals encoding the start and end of stimulation epochs. The recording clocks of all acquisition cards were synchronized using a real-time system integration bus (National Instruments).

4.2.3 Pharmacology

We investigated three network connectivity states which were defined by the combination of synaptic blockers present in the bath. Synaptic blockers were applied in the same order for all cultures.

- **Drug-free network ('DF'):** 100 uL of culturing medium was extracted and reapplied to the culture.
- **Excitatory block ('EB'):** 6-cyano-7-nitroquinoxaline-2,3-dione (CNQX, 20 μM final concentration) and D(-)-2-amino-5-phosphonopentanoic acid (AP5, 50 μM final concentration) was added to the culture.
- **'Complete Block' ('CB') :** CNQX and AP5 remained in bath. Bicuculline was added to the bath to achieve a final concentration of 20 μM .

Each culturing well contained 1.5 mL of culturing medium. To administer excitatory synaptic blockers, 100 μL of culturing medium was extracted from the culture well and mixed with 3 μL of 10 mM CNQX and 3 μL of 25 mM AP5 in an 0.5 mL centrifuge tube. This mixture was then pipetted back into to the culturing medium. After the experiments with CNQX/AP5 combination had finished, 100 μL of culturing medium was extracted and mixed with 3 μL of 10 mM bicuculline. Every time a drug was added, fifteen minutes were provided prior to optical stimulus application, so the blockers could thoroughly diffuse through the culture well and mechanical and

temperature fluctuations could dissipate. Network connectivity states are referred to in the results using the acronyms presented above: DF, EB, and CB.

4.2.4 Optical stimulation

ChR2 requires relatively strong incident light intensity to generate physiologically useful photocurrents (compared to, for example, retinal studies relying on the activation of photoreceptors). Additionally, the light source must be modulated over a wide frequency range in order to characterize the full ChR2 frequency response (Chapter 3). High-power light emitting diodes (LEDs) can supply the required optical power and can be modulated over a wide bandwidth. Additionally, they provide a smooth, monotonic conversion of forward current to light intensity, which allows their intensity to be modified smoothly (unlike highly non-linear sources, such as lasers). For these reasons, a 10-watt light emitting diode was used for optical stimulation (LZ4-00B200, LEDEngin, San Jose, EB). This LED has a peak emission wavelength of 465 nm with ∼20 nm full width at half maximum.

NeuroRighter's 16-bit digital-to-analog converters (DACs) were used to generate control voltages to drive fluctuations in optical power. The relationship between an LED's forward current and the resulting irradiance is approximately logarithmic, which acts as a static nonlinear transformation on time-varying currents driving the LED. Additionally, LED irradiance is inversely related to the diode junction temperature, which increases as the LED operates. For these reasons, simply controlling the current through the LED is not sufficient to ensure that the emitted light power precisely follows the control signals generated by the DAC (Wagenaar, 2012). Therefore, we constructed an optical feedback circuit to drive our LED (Appendix B). Briefly, a PDA36 amplified photodiode (Thorlabs, Newton, NJ) was used to measure scattered light from the LED. These measurements of instantaneous light power were then passed to a custom, feedback-assisted N-MOSFET current driver. The circuit

compared the measure of instantaneous light power to the reference signal produced by the DAC to ensure that the LED's brightness followed the DAC stimulus signal.

Finally, to ensure that unstimulated groups of cells could not act as an uncontrolled noise source during repeated application of the same waveform, we needed to deliver spatially homogeneous optical stimuli. A custom light delivery system was used to homogenize and concentrate LED light onto the plane of the culture. The delivery system was housed inside of an incubator, allowing long-term experimental access (Fig. 33(a)). The LED stimulator consisted of 4 independently addressable LEDs butt-coupled to a 4-to-1 Schott randomized fiber bundle (Schott, Elmsford, NY). To ensure that the light at the culture was spatially uniform, the bundle terminated in a Köhler illumination train beneath the MEA's Peltier temperature regulator. The spatial power distribution at the MEA surface was imaged to ensure illumination uniformity using a BC106-VIS CCD-based beam profiler (Thorlabs) and is shown in Fig. 32(b).

4.2.5 Experimental protocols and sample sizes

Optical stimuli consisted of spatially uniform, filtered Gaussian (Ornstein-Uhlenbeck) noise defined by

$$s(t+dt) = \mu_s + s(t)\exp(-dt/\tau_s) + \sigma_s \xi(t)\sqrt{1-\exp(-2dt/\tau_s)}. \tag{33}$$

where $s(0) = 0$ mW·mm^{-2}, $\mu_s \simeq 0.35$ mW·mm^{-2}, $\sigma_s \simeq 0.08$ mW·mm^{-2}, $\tau_s = 50$ ms, $dt = 1$ ms is the DAC update period, and $\xi(t)$ is a random value drawn from the standard normal distribution. K trials of two stimulus subtypes were administered during each drug condition (Section 4.2.3). During *'repeated'* stimulus trials (s_k^{rep}), the same realization of s was applied for every stimulus trial so that $s_1^{\text{rep}} = s_2^{\text{rep}} = \cdots = s_K^{\text{rep}}$. An example of the network spiking response to repeated stimuli is shown in Fig. 23. During *'unique'* stimulus trials (s_k^{uni}), a new realization of s was applied during each trial so that $s_1^{\text{uni}} \neq s_2^{\text{uni}} \neq \cdots \neq s_K^{\text{uni}}$. Unique and repeated stimuli were

Table 4: Summary of experiments. 'Preserved units' refers to units that were identifiable in all drug conditions. Additional units, that appeared in some drug conditions but not others, were used to calculate general firing statistics (Figs. 24, 23) but were not used for further analysis.

Culture	Repeats	Uniques	# Trials (K)	Trial length (T; sec)	Intact (DF)	Inhib. intact (EB)	Decoup. (CB)	Preserved units
Tommy-20709	x	-	50	30	x	-	-	13
Venus-20708	x	-	50	30	x	x	-	7
Xeko-20709	x	x	50	30	x	x	x	10
Zeno-00358	x	x	100	30	x	x	x	2
Fatty-I5372	x	x	50	30	x	-	-	36
Fatty-I5369	x	x	60	10	x	x	x	7
Wingnut-22567	x	x	70	10	x	x	x	26
Hamhock-22467	x	x	70	10	x	x	x	15
Totals	8	6	500	-	8	6	5	116

interleaved, one after another, with no gaps between adjacent trials. Exactly the same stimulus protocol (the same repeated realization and the same set of unique realizations) were used during different drug conditions for a single culture. A new set of realizations was created for each of the 8 cultures tested. Table 4 provides a summary of experimental parameters and sample sizes for each of the cultures used in this study. Aside from drug conditions, experimental parameters included the length of the stimulus realization, number of trials, and whether or not unique stimuli were administered varied across experiments.

4.2.6 Data processing

Following data collection, recordings were imported into MATLAB version 2012b (Natick, MA) using scripts included with the NeuroRighter package. Offline analysis was carried out using my open-source SqueakySpk MATLAB package for multichannel single-unit data processing[3] and custom scripts. Sorted units that had ambiguous spike shapes (e.g. multi-modal spikes due to the misclassification of two obviously different waveforms as a single unit or a lack of any clear waveform) were removed from further analysis.

[3] `http://code.google.com/p/squeakyspk/`

4.2.7 Statistics

All statistical analysis was performed using MATLAB. Hypothesis tests involved multiple comparisons across three drug conditions: DF, EB, and CB (Methods Section 4.2.3; Table 4). Our procedure for performing multiple comparisons of sample distributions proceeded as follows. First, we used a Lilliefors test (α=0.05) to determine whether each data set followed a normal distribution. For cases in which the null hypothesis of normality was rejected for one or more sample distribution(s), we log-transformed each data set to stabilize the sample variance (except for the results in Table 5, since the information-theoretic calculations used in this study require the raw Fourier coefficients to be Gaussian). We the re-performed the Lilliefors test to see if the transformed data could be considered approximately Gaussian. If the non-transformed or transformed data could be considered Gaussian, we the performed one-way ANOVA. If the data were detectably non-Gaussian, we used a Kruskal-Wallis test. In either case, we then performed a post-hoc multiple comparisons test using the Bonferroni correction to control the familywise error rate to determine which pairs were significantly different. Significance thresholds were always set at $P >$0.05 (n.s), $P <$0.05 (ˆ), $P < 0.01$ (*), $P < 0.001$ (**), $P < 0.0001$ (***), $P < 10^{-5}$ (%), $P < 10^{-6}$ (&), and $P < 10^{-7}$ (#) for the entire family of comparisons. All data in bar-charts are shown as mean±s.e.m. Some analyses required data that had not been collected for certain cultures (Table 4). For instance, information spectra (Section 4.4.5) could only be computed from response to networks exposed to both unique and repeated stimuli, but some networks were only exposed to repeated stimuli. This resulted in different sample sizes depending on the measurements being compared.

4.3 Mathematical Methods

4.3.1 The peristimulus time histogram

Our procedure for producing the peristimulus time-histogram for unit j ($\mathrm{PSTH}_j(t)$) in response to K repeated stimulus trials of length T is as follows. First, the time of occurrence of each spike produced by unit j was taken relative to the start of the corresponding stimulus trial. Spike times, t_i, were then down-sampled at 1 kHz to form a raw response to stimulus s_k,

$$r_{j,k}(t) = \sum_{i=1}^{n^k_{spk}} \delta(t - t_i), \tag{34}$$

where n^k_{spk} are the number of spikes produced by unit j on the kth stimulus trial, t_i are spike times, and δ is the Dirac delta function. If we denote the set of repeated stimulus trials as K_{rep}, the raw response density is given by

$$r_j(t) = \frac{1}{K} \sum_{k \in K_{rep}} r_{j,k}(t). \tag{35}$$

The raw population response density, $r_{pop}(t)$, was defined analogously using spikes from all units simultaneously. Using the raw population response density, we obtained an optimal-bandwidth Gaussian smoothing kernel, $\varphi(\tau; w)$, where the bandwidth parameter w denotes one standard deviation (Shimazaki and Shinomoto, 2010). w was constrained between 1 and 10 ms for our analyses. This kernel-based smoothing method provides a firing rate estimate with a minimized mean integrated squared error compared to an unknown underlying rate. This method also better preserves rapid transitions between high and low firing levels than ad-hoc smoothing or binning methods. The PSTH for each unit was given by

$$\mathrm{PSTH}_j(t) = \int_0^T r_j(t - \tau)\varphi(\tau)d\tau. \tag{36}$$

and the population PSTH was given by

$$\mathrm{PSTH}_{pop}(t) = \int_0^T r_{pop}(t - \tau)\varphi(\tau)d\tau. \tag{37}$$

Note that the same smoothing kernel is used in both operations.

4.3.2 Linear-nonlinear modeling of the neuronal and population responses

We characterized the neuronal and population response to repeated stimuli using a linear-nonlinear (LN) model (Chichilnisky, 2001; Ostojic and Brunel, 2011; Geffen *et al.*, 2009). Using an LN model, the stimulus sequence, $s(t)$, which consisted of a series of photodiode measurements taken from the optical stimulator (Methods Section 4.2.4), is convolved with a linear filter, $h(\tau)$, resulting in a 'filtered stimulus' signal, $g(t)$. $g(t)$ is then passed through a static, rectifying nonlinearity, F, to produce an estimate of the PSTH,

$$\widehat{\mathrm{PSTH}}(t) = F\left[\int_0^T s(t-\tau)h(\tau)d\tau\right]. \tag{38}$$

The LN model is useful because it breaks the neuronal response into linear and nonlinear components, each of which has a intuitive link to physiological features of neurons. The linear component of the model corresponds to the subthreshold, RC-circuit characteristics of the cell membrane and the static nonlinearity represents the neuron's rectifying spiking threshold. The model can be fit to the PSTH of individual cells, $\mathrm{PSTH}_j(t)$, or to the population response, $\mathrm{PSTH}_{pop}(t)$. The procedure for fitting each type of response is identical. Therefore, in the following paragraphs, we refer to the generic single unit or population response as the 'PSTH'.

Fitting F and h involves minimizing the difference between the predicted and measured PSTH. To do this, we followed a procedure from (Chichilnisky, 2001) that we modified to account for the temporal correlations in our stimulus signal (Paninski, 2003). Let $\vec{s}_i$ be a row vector defined by the mean-subtracted stimulus waveform preceding the ith time bin for 250 ms. Let S be a matrix whose ith row is $\vec{s}_i$. When the stimulus distribution is elliptically symmetric, the whitened spike triggered average (STA) provides an unbiased estimate of a neuron's or population's linear receptive field (Sharpee *et al.*, 2004). Since our stimuli are Gaussian, they satisfy the symmetry

requirement, so we calculated the STA according to

$$\mathrm{STA} = \frac{T}{\langle n_{spk} \rangle_K} \left(S^{\mathrm{T}} S + \xi I \right)^{-1} S^{\mathrm{T}} \mathrm{PSTH} \tag{39}$$

where $\langle n_{spk} \rangle_K$ is the average number of spikes per trial, I is the identity matrix and $S^{\mathrm{T}}S$ is the stimulus covariance matrix, which is required to divide out correlations in the stimulus distribution (i.e. 'whiten' it). $\xi = 10$ is a regularization parameter for the inversion of the stimulus covariance matrix since this operation amplifies noise along stimulus dimensions with low variance (i.e. those which result in division by $\sim$0). To make the linear response comparable across cells and populations, we normalized by the variance of the STA to produce the linear filter,

$$h = \frac{\mathrm{STA}}{\mathrm{var}(\mathrm{STA})}. \tag{40}$$

h is then convolved with the stimulus time series to produce the filtered stimulus,

$$g(t) = \int_0^T s(t-\tau) h(\tau) d\tau. \tag{41}$$

Finally, nonlinear regression is performed to fit a rectifying nonlinearity of the form

$$F = \ln(1 + \exp(\alpha g(t) - \theta)) \tag{42}$$

to data on the scatter graph produced by plotting $g(t)$ against the measured PSTH. α defines the steepness or 'gain' of the rectifying function and θ defines the 'threshold' after which $g(t)$. The gain determines how much changes in the filtered stimulus value will affect changes in firing level. The threshold determines the critical value of the filtered stimulus that maps to non-zero firing rates (Fig. 26(b)).

4.3.3 Precision and correlation measures

We calculated the auto- and cross-correlation functions for and between PSTHs, respectively, using standard methods (Abbott and Dayan, 2001). Cross-correlation functions were only produced for pairs of units from the same culture. To measure

the temporal precision of the neuronal response to repeated stimuli, the center bin was removed (Abbott and Dayan, 2001) and the central peak ±8 ms was fit with a Gaussian function using nonlinear regression. The width of the fitted Gaussian function provides a measure of trial-to-trial jitter in the neuronal response under the assumption that this jitter is uncorrelated across trials and repeated spike events are well separated in time. Therefore, the response precision, τ_R, was defined as the standard deviation of the resulting Gaussian fit to the PSTH autocorrelation function for each unit.

We performed an identical procedure on unit-to-unit PSTH cross-correlation functions with the exception that the Gaussian fit was centered at the peak of the correlation function instead of $\tau = 0$, to produce the PSTH cross-precision, $\tau_R^{i,j}$. To understand the meaning of $\tau_R^{i,j}$, consider that the PSTH cross-correlation is defined as

$$C_{i,j}(\tau) = \mathrm{E}\left[\mathrm{PSTH}_i(t)\mathrm{PSTH}_j(t+\tau)\right], \tag{43}$$

where E is the expectation operator. Recalling Eq. 35 and discounting the effects of smoothing,

$$\mathrm{PSTH}_j(t) \simeq \frac{1}{K}\sum_{k\in K_{rep}}^{K} r_{j,k}(t). \tag{44}$$

Therefore Eq. 43 can be rewritten as

$$C_{i,j} \simeq \frac{1}{K^2}\sum_{k_i\in K_{rep}}^{K}\sum_{k_j\in K_{rep}}^{K} \mathrm{E}\left[r_{i,k_i}(t)r_{j,k_j}(t+\tau)\right]. \tag{45}$$

Therefore, during the calculation of the PSTH cross-correlation function, the response of a unit j is compared with the response of unit i that occurred on all other trials of the repeated stimulus. This is equivalent to the 'shuffled' spike correlation. If two units consistently fire within a short window of one another, and do so at the same time relative to the stimulus each trial, then the width of the cross-correlation function, $\tau_R^{i,j}$, will be narrow indicating precise co-activation across trials.

To measure the correlation strength between units' firing patterns, ρ_R, we normalized the cross-correlation functions such that their peaks were equivalent to Pearson's product-moment correlation coefficient,

$$\rho_R = \text{peak}\left[\frac{C_{i,j}}{\sigma_i \sigma_j}\right]. \tag{46}$$

4.3.4 Information in the Fourier domain

A number of model-based (Warland *et al.*, 1997; Pillow *et al.*, 2008) and direct (Strong *et al.*, 1998; Borst and Theunissen, 1999; Magri *et al.*, 2009) methods are available to estimate the information content of spike trains. Each method has advantages and disadvantages. Direct methods, which estimate entropy values by measuring the probabilities of all possible binary spike combinations (or 'words') using a pre-defined time bin, require very large data sets to be useful for large populations of neurons. The problem gets worse if the temporal arrangement of action potentials within individual spike trains are considered (Strong *et al.*, 1998). Model-based approaches circumvent the 'curse of dimensionality' by representing the spiking activity using a model with a small number of variables and parameters (Warland *et al.*, 1997; Pillow *et al.*, 2008; McFarland *et al.*, 2013; Truccolo *et al.*, 2005). However these methods can miss features of the encoding or decoding processes, and generally produce conservative bounds on information content.

A recently introduced method (Yu *et al.*, 2010; Crumiller *et al.*, 2011) offers a new avenue for estimating the information content of multiple, correlated, stationary spike trains. This method takes advantage of two mathematical observations to efficiently estimate entropy and information measures for large populations of cells. First, mutual information measures are not dependent on the coordinate system used to represent the process under study (Shannon, 1948; Warland *et al.*, 1997). This means that the neural response can be projected into any orthogonal basis in which information calculations are convenient, and those results will carry over to the time domain. To

be clear, entropy measures *are* dependent on the coordinate system, but differences between entropies (information measures) are not (Shannon and Weaver, 1949, Ch. 4). The second observation is that the Fourier coefficients of a stationary process are asymptotically Gaussian. This theorem states that if a data sequence of length T is produced by a stationary random process with temporal correlation $\tau_c \ll T$, its Fourier coefficients, $u^{(n)}$ are complex random variables drawn from independent multivariate Gaussian distributions (Grenander and Rosenblatt, 1957) (Brillinger, 1981, pg. 94). In this case, the entropy of a single Fourier coefficient, can be calculated analytically

$$H^{(n)} = \frac{1}{2}\log_2(2\pi e \mathrm{Var}\{u^{(n)}\}), \tag{47}$$

where the $\mathrm{Var}\{u^{(n)}\}$ is the variance of the nth Fourier coefficient, and is estimated from the data (Crumiller *et al.*, 2011; Yu *et al.*, 2010). Since the Fourier coefficients are independent random variables, $H^{(n)}$ forms an entropy spectrum, with each frequency component contributing independently to the complete entropy of the process. Entropy contributions of individual coefficients can simply be added to obtain the total entropy of the process.

The conditions required to arrive at these results translate into two assumptions concerning the nature of our data.

- **Assumption 1:** Stimulus-response pairs, each of which produces a sample spike train from which to obtain Fourier coefficients, are very long in comparison with the correlation time of the spiking process.

- **Assumption 2:** The Fourier coefficients computed across trials are Gaussian and independent across frequencies for all cells.

In the following paragraphs, we provide evidence for the validity of these assumptions and describe the details of the method.

To be concrete, our goal is to calculate the mutual information between a univariate stimulation process, s, and the population spiking response, r. A single stimulation trial, s_k, consisted of a $T = 30$ s realization of Ornstein-Uhlenbeck (OU) noise with a time constant of 50 ms. K trials of two stimulus subtypes were administered during each drug condition (Table 4; Section 4.2.3), resulting in a total of $2 \times K$ stimulus trials per drug condition, with K trials of repeated stimuli and K trials of unique stimuli (Section 4.2.5).

If the spiking response is noise-free, stationary, and has a finite temporal correlation then application of a repeated stimulus input will result in precisely the same network response for each trial. In reality, the network is not noise-free and the trial-to-trial variability of the response to identical stimuli can be used to quantify the randomness in the response that is *not* meaningful for encoding the stimulus. The measure of this randomness is called the conditional or 'noise' entropy $H[r|s]$ (Strong *et al.*, 1998). Conversely, by applying unique stimuli, the full repertoire of neuronal response patterns can be sampled in order to form an estimate of the total response entropy, $H[r]$. The total response entropy quantifies the randomness of the neural response due both to noise and stimulus-evoked activity patterns. The mutual information between the stimulus process, s, and the network response process, r, is the amount of the total response entropy that is not due to noise

$$I[r, s] = H[r] - H[r|s]. \tag{48}$$

In order for this definition to be meaningful, we must explicitly define the network response, r. For the following analysis, the response on trial k for unit j is given by Eq. 34. The response to the first 5 trials of both unique and repeated stimuli were discarded to allow the network's firing rate to adapt (Fig. 25; Section 4.4.1). Following previous work (Yu *et al.*, 2010; Crumiller *et al.*, 2011), $r_{j,k}(t)$ was transformed into a set of Fourier coefficients, $u_{j,k}^{(f_n)}$, each of which belongs to a complex sinusoidal basis

function, $\phi^{f_n}(t)$, of frequency f_n

$$u_{j,k}^{(f_n)} = \int_0^T r_{j,k}(t)\phi_{f_n}(t)dt. \tag{49}$$

If our assumptions concerning the stationarity and finite correlation time of the neural response are correct, then $u_{j,k}^{(f_n)}$ form a set of independent Gaussian random variables, each of which is sampled $K-5$ times for each stimulus subtype. Fig. 21 shows the quantile-quantile plots for the real components of 100 randomly chosen coefficients from 5 cells. Each line compares the quantiles of a coefficient obtained from a particular component frequency against the corresponding quantile of the standard normal distribution. The fact that these points generally fall on a straight line indicates that the Fourier coefficients are drawn from a re-scaled standard-normal distribution. Because these plots cover each drug condition for both unique and repeated stimuli, the Gaussianity of the coefficients appears to be robust across the connectivity states. Additionally, we tested the null hypothesis that the sample Fourier coefficients originated from a Gaussian distribution using the Lilliefors test, across experimental conditions. The results are summarized in Table 5. For the great majority of coefficients, the null hypothesis could not be rejected at the $\alpha = 0.05$ significance level.

Next, we calculated the Pearson product-moment correlation coefficient matrix for the real part of the first 250 Fourier coefficients for 5 cells, across drug conditions, for both unique and repeated stimuli (Fig. 22(a)). Fig. 22(b) shows the off-diagonal elements of these correlation matrices across units. For a multivariate Gaussian distribution, the pairwise independence of variables is equivalent to a zero correlation. Therefore, the histograms of off-diagonal correlation entries should be tightly centered around a zero correlation value. A t-test can be used to determine whether the statistical fluctuations in the observed correlations between different Fourier coefficients are significantly different than the null hypothesis $\rho_o = 0$ (Feller, 1968). The

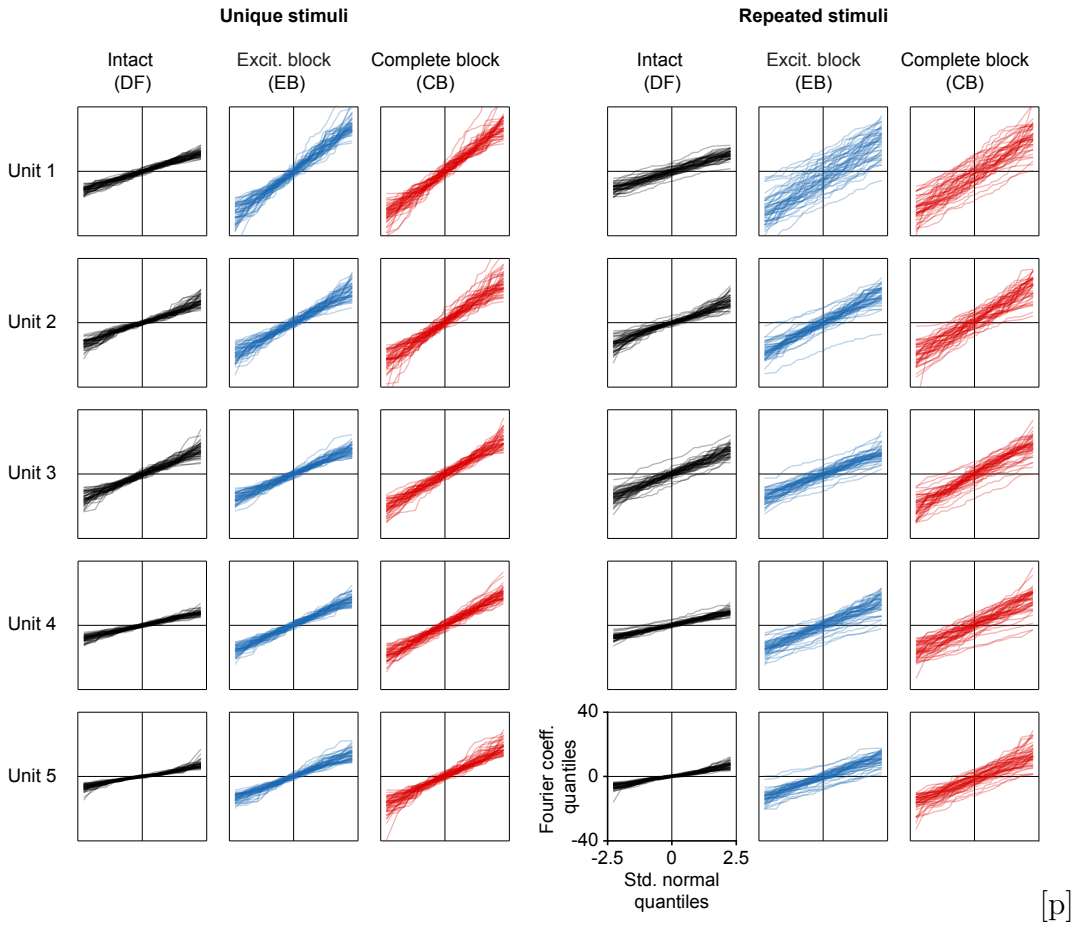

[p]

Figure 21: Quantile-quantile plots of Fourier-information coefficients against the standard normal. For each drug condition (Section 4.2.3) and for each stimulation process (repeated or unique stimuli), the quantiles of 45 samples (one per stimulus trial) of 100 randomly chosen Fourier coefficients are plotted against the quantiles of the standard normal distribution for 5 units. The majority of these data points fall on a straight lines that pass close to the origin. This indicates the generating distribution of each Fourier coefficient is similar in shape to a re-scaled standard normal distribution.

Table 5: Percent (%) of sample coefficients for which H_o: *the coefficient was drawn from a distribution belonging to the Normal family,* could not be rejected at the $\alpha = 0.05$ significance level. Values were obtained using a Lilliefors test on all Fourier coefficients where $f_n < 100$ Hz.

	Unique Stimuli			Repeated Stimuli			
	Intact (DF)	Inhib. (EB)	Decoup. (CB)	Intact (DF)	Inhib. (EB)	Decoup. (CB)	Mean
Unit 01	95.27	94.46	95.30	94.83	94.43	94.36	94.77
Unit 02	88.93	95.27	95.07	86.50	95.30	95.17	92.71
Unit 03	94.26	94.76	95.10	94.36	95.27	95.43	94.86
Unit 04	94.26	94.40	94.50	94.96	95.27	94.66	94.67
Unit 05	80.99	95.10	94.70	83.76	94.46	94.46	90.58
Unit 06	94.96	94.36	94.66	94.93	95.17	95.20	94.88
Unit 07	89.66	94.36	94.76	86.26	93.90	94.76	92.28
Unit 08	94.26	94.76	95.23	94.26	94.76	95.17	94.74
Unit 09	92.80	94.60	94.73	93.63	94.80	94.23	94.13
Unit 10	93.33	94.96	94.83	94.33	95.37	94.10	94.49
Mean	91.87	94.70	94.89	91.78	94.87	94.75	

two-sided t-statistic is

$$t = \frac{\rho(u^{(f_{n1})}, u^{(f_{n2})})\ \sqrt{K-2}}{\sqrt{1-\rho(u^{(f_{n1})}, u^{(f_{n2})})^2}}, \tag{50}$$

where $\rho(u^{(f_{n1})}, u^{(f_{n2})})$ is the sample correlation coefficient between two different Fourier coefficients, $n1 \neq n2$, from a single unit. This test statistic is from a t-distribution with $K - 2 = 43$ degrees of freedom. We computed t for $\sim$4.5 million randomly chosen off-diagonal correlations across 10 cells for both unique and repeated stimuli, and for all drug conditions. The results of these tests are summarized in Table 6. For the great majority of coefficient pairs, across experimental conditions, the null hypothesis could not be rejected at the $\alpha = 0.05$ significance level.

After confirming the Gaussianity and independence of Fourier coefficients, we could proceed to calculate entropy spectra, $H_j^{(f_n)}$. For a single spike train

$$H_j^{(f_n)} = \frac{1}{2}\log_2(2\pi e \mathrm{Var}\{u_j^{(f_n)}\}). \tag{51}$$

When $u_j^{(f_n)}$ are derived from unit j's responses to repeated stimuli, Eq. 51 results in the noise entropy spectrum, $H_j^{(f_n)}[r|s]$. When $u_j^{(f_n)}$ are derived from unit j's responses to unique stimuli, Eq. 51 results in the total entropy spectrum, $H_j^{(f_n)}[r]$. Using the noise and total entropy spectra, the definition of mutual information in Eq. 48 can

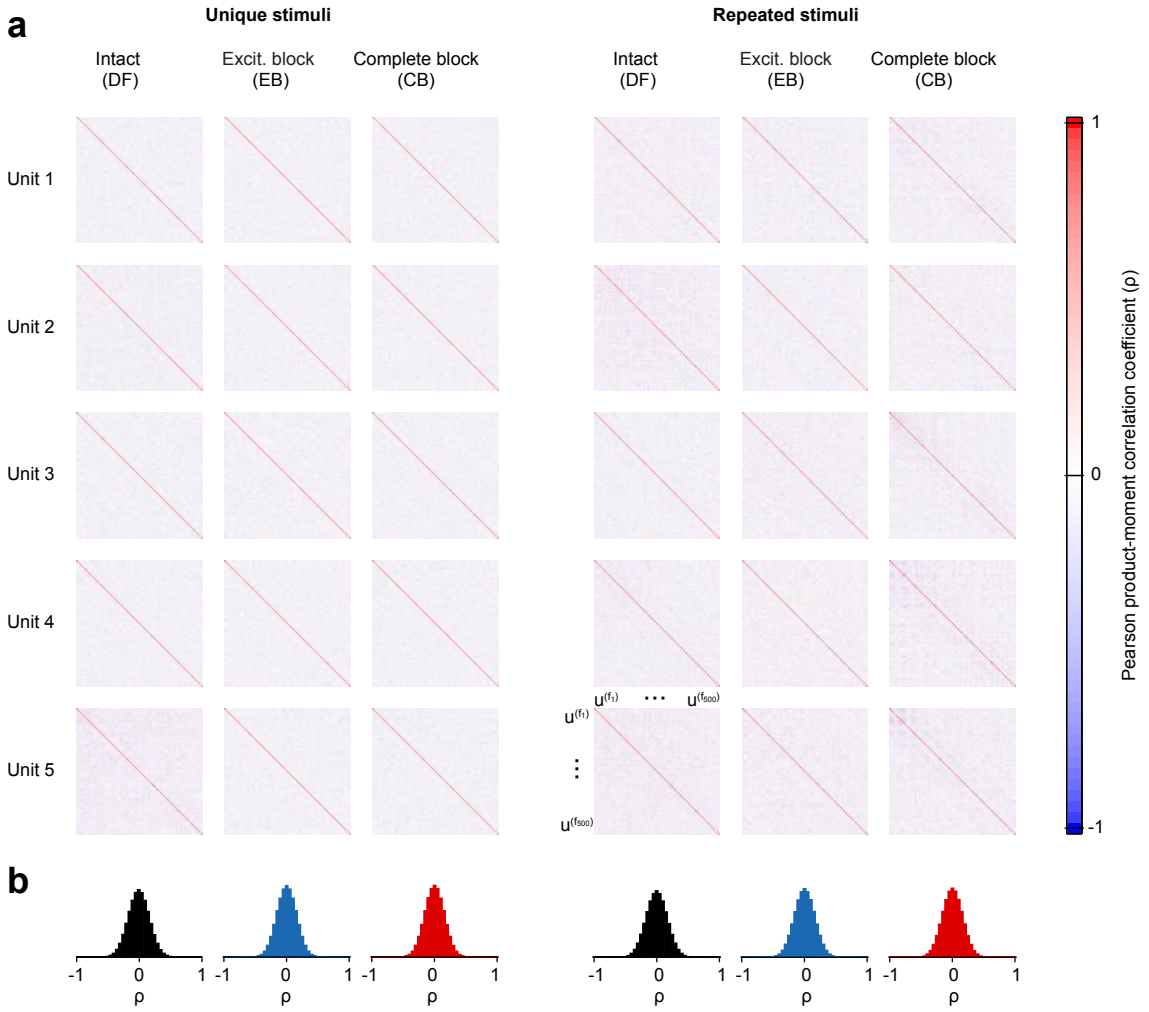

Figure 22: Lack of correlations between Fourier-information coefficients. (a) The sample correlation coefficient matrices for the first 250 Fourier coefficients are shown for each drug condition and for each stimulation protocol. Each coefficient is estimated from 45 samples. Although there are some deviations, the values of the off-diagonal elements are generally low, indicating a lack of correlation between Fourier coefficients derived from different frequencies. (b) Histogram of all off-diagonal coefficients for every cell from a particular culture. The dominant value of the off-diagonal correlation coefficient is zero and there are no off-diagonal entries with absolute values above 0.5. The mean of each distribution (found by first linearizing entries via a Fisher transform, taking the mean, and then performing an inverse Fisher transform) is zero to 4 significant digits for each distribution. Combined with the evidence that the Fourier coefficients are Gaussian random variables (Fig. 21), their lack of correlation implies the statistical independence, as well.

Table 6: Percent (%) of sample coefficients for which H_o: *the correlation coefficient between* $u^{(f_{n1})}$ *and* $u^{(f_{n2})}$ *where* $n1 \neq n2$ *is 0*, could not be rejected at the $\alpha = 0.05$ significance level. Values were obtained using a t-test for all pairs of Fourier coefficients where $f_n < 100$ Hz. See text for details.

	Unique Stimuli			Repeated Stimuli			
	Intact (DF)	Inhib. (EB)	Decoup. (CB)	Intact (DF)	Inhib. (EB)	Decoup. (CB)	Mean
Unit 01	97.31	97.44	97.46	96.79	97.10	97.07	97.20
Unit 02	95.80	97.46	97.47	95.58	97.30	97.05	96.78
Unit 03	97.39	97.41	97.40	97.21	97.02	97.15	97.26
Unit 04	97.29	97.40	97.44	97.01	97.01	96.90	97.17
Unit 05	94.25	97.42	97.23	94.68	96.89	96.86	96.22
Unit 06	97.36	96.80	97.29	97.31	96.59	96.79	97.02
Unit 07	95.85	97.23	97.43	95.21	95.57	96.64	96.32
Unit 08	96.87	97.31	97.45	97.00	96.55	97.15	97.06
Unit 09	96.10	97.31	97.32	95.94	96.94	96.62	96.70
Unit 10	96.74	97.43	97.28	96.19	96.57	96.44	96.78
Mean	96.50	97.32	97.38	96.29	96.75	96.87	

be made a function of individual frequency components according to

$$I_j^{(f_n)}[r,s] = H_j^{(f_n)}[r] - H_j^{(f_n)}[r|s]. \tag{52}$$

Because the Fourier coefficients form a set of independent variables, the total and noise entropies of the spiking process are sums over individual frequency contributions

$$H_j[r] = H_{j,total} = \sum_{n=1}^{\infty} H_j^{(f_n)}[r], \qquad H_j[r|s] = H_{j,noise} = \sum_{n=1}^{\infty} H_j^{(f_n)}[r|s], \tag{53}$$

and the total information in the spiking response of unit j, I_j, is calculated using Eq. 48. To generalize these calculations to populations of J units, Eq. 51 is rewritten as

$$H_J^{(f_n)} = \frac{1}{2} \sum_{j \in J} \log_2(2\pi e \lambda_j^{(f_n)}), \tag{54}$$

where $\lambda_j^{(f_n)}$ are the principle components of the covariance matrix of Fourier coefficients $u_j^{(f_n)}$ across units at a particular frequency value. After using Eq. 54, calculations proceed identically from Eq. 52, but with the 'j' subscript replaced by 'J'.

$$I_j^{(f_n)}[r,s] = H_J^{(f_n)}[r] - H_J^{(f_n)}[r|s]. \tag{55}$$

All entropy and information measures presented here are normalized by time (i.e. they are rates).

Finally, we define the fractional redundancy of the network response, R. R quantifies the degree to which the responses of units encode the same information concerning the stimulus input. The fractional redundancy spectrum is defined as

$$R_{i,j}^{(f_n)}[r,s] = \frac{I_i^{(f_n)}[r,s] + I_j^{(f_n)}[r,s] - I_{i,j}^{(f_n)}[r,s]}{I_{i,j}[r,s]}, \tag{56}$$

and the total fractional redundancy is equal to

$$R_{i,j} = \sum_{f_n} R_{i,j}^{(f_n)}[r,s]. \tag{57}$$

4.4 Results

4.4.1 The population spiking response to continuously-varying optogenetic stimulation

We previously showed that continuously-varying optogenetic stimulation can be used to deliver highly repeatable subthreshold current waveforms to individual neurons (Chapter 3) (Tchumatchenko *et al.*, 2013). Using the proper parameters, this type of stimulation can drive subthreshold voltage fluctuations in cultured neurons that mimic the temporal and amplitude characteristics of those obtained from *in-vivo* patch clamp recordings (Destexhe *et al.*, 2003). Using time-varying photostimulation, we delivered subthreshold stimuli to excitatory neurons embedded within dissociated cortical networks while systematically manipulating network connectivity using selective synaptic blockers (Fig. 23).

Approximately one week after the development of functional synapses, dissociated cortical networks begin to engage in highly synchronized bouts of population firing activity, called 'network bursts' (Wagenaar *et al.*, 2006c). The variability of firing displayed by individual units during spontaneous bursting activity can be summarized using the coefficient of variation of the interspike interval (ISI) distribution ($\mathrm{CV_{ISI}}$), which is defined as the standard deviation of the ISI histogram derived from a particular unit divided by its sample mean, $\mathrm{CV_{ISI}}=\sigma_{ISI}/\mu_{ISI}$ (Abbott and Dayan, 2001).

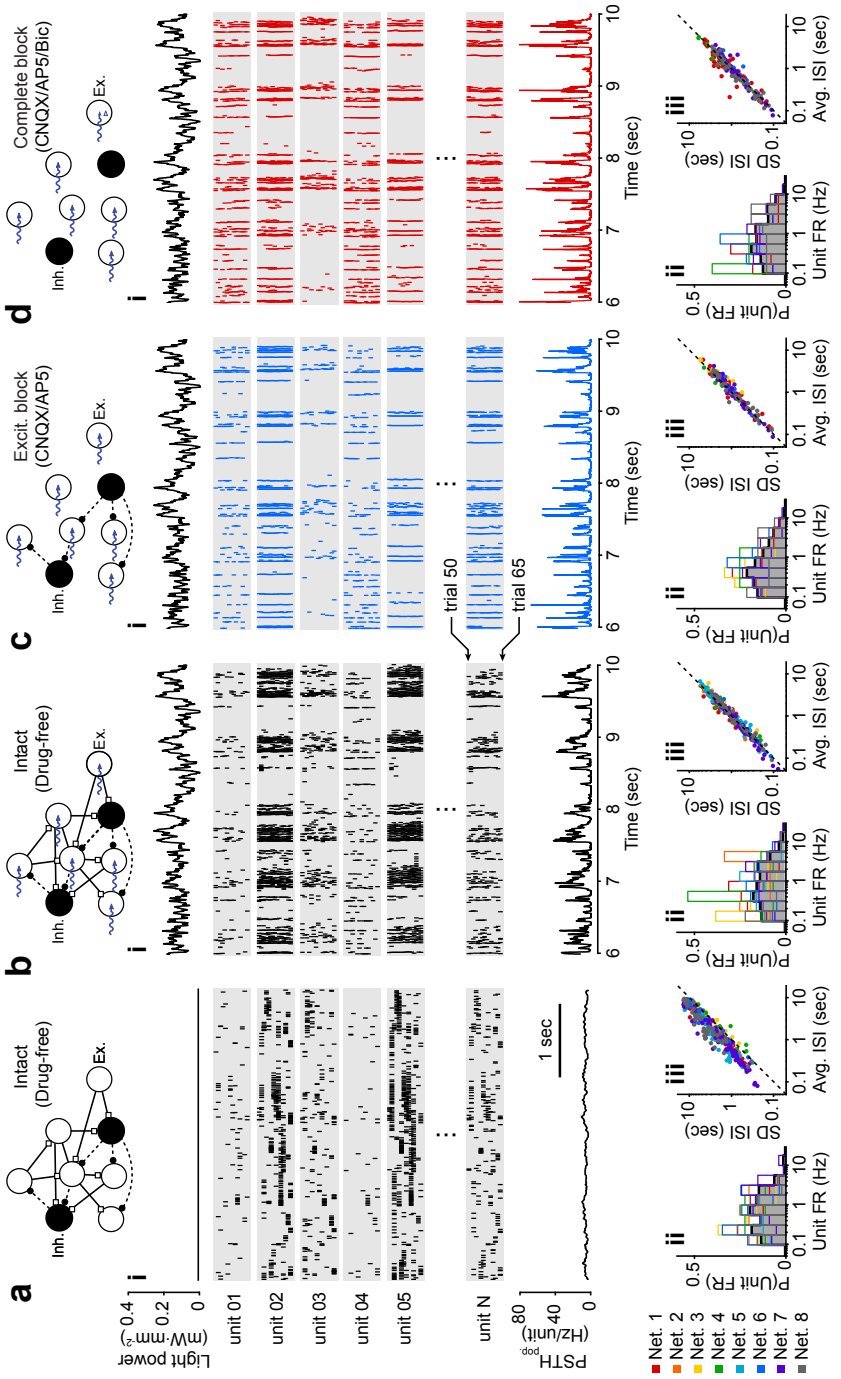

Figure 23: Network response to time-varying optical stimuli. Each panel of the figure summarizes **(a)** spontaneous activity in the intact network, **(b)** evoked activity in the intact network, **(c)** evoked activity with inhibitory transmission intact and excitatory transmission blocked, and **(d)** evoked activity in the synaptically decoupled network. Each main panel contains three subpanels, **i, ii, and iii**. **(i)** A schematic depicting the network configuration and 4-second set of various time-series data collected during repeated stimulus application. The stimulus waveform, 15 trials for firing rasters for 6 units, and the population PSTH are shown. **(ii)** The firing rate (FR) distribution, and **(iii)** μ_{ISI} versus σ_{ISI} for each unit. An offset from the identity line (dashed) indicates a deviation from $\mathrm{CV}_{\mathrm{ISI}} = 1$ (note log scale).

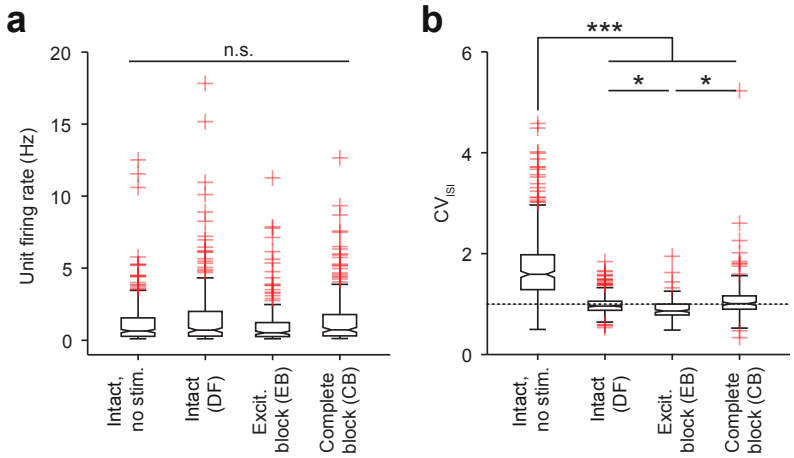

Figure 24: Continuously-varying photostimulation rearranges spike times but does not affect firing rates. **(a)** Box and whisker plot summaries of the distribution of evoked firing levels for individual units during spontaneous activity during the DF state, and evoked activity in the DF, EB, and CB states. Center-lines denote medians. Whiskers denote the 25th percentile - 1.5 $\times$ the interquartile range (IQR) and the 75th percentile + 1.5 $\times$IQR, respectively. Red crosses denote outliers. Indentations provide comparison intervals. Median firing rates were: during spontaneous activity in DF 0.64 Hz, during evoked activity in DF 0.70 Hz, EB 0.51 Hz, and CB 0.72 Hz. **(b)** Same as (a) for the CV_{ISI}. Dotted line indicates Poisson firing statistics. The median CV_{ISI}s were: during spontaneous activity in DF 1.59, during evoked activity in DF 0.97, EB 0.89, and CB 1.04. Sample sizes, $n_{NoStim.} = 308$ units (8 cultures), $n_{DF} = 273$ units (8 cultures), $n_{EB} = 159$ units (6 cultures), and $n_{CB} = 175$ units (5 cultures). Significance thresholds, $P > 0.05$ (n.s.), $P < 0.01$ (*), and $P < 0.0001$ (***).

The CV_{ISI} is a dimensionless measure of ISI irregularity that can be compared directly to *in-vivo* data. For instance, regular spiking cells in V1 and area MT with reasonably low firing rates (i.e. those in which firing is not regularized by the refractory period) have $CV_{ISI} \simeq 1$, indicating irregular, Poisson-like spiking statistics (Softky and Koch, 1992, 1993). Since bursting activity produces an extreme degree of variability in the ISI distribution - very small ISIs occur during a burst and very large ISIs occur between bursts - we observed a median CV_{ISI} during spontaneous activity that was considerably elevated (Figs. 23, 24(b)) compared to values obtained from sensory cortical cells in-vivo, where $CV_{ISI} \simeq 1$ (Softky and Koch, 1992, 1993).

To examine the most basic effects of connectivity on evoked network firing dynamics, we repeatedly delivered a single randomly-fluctuating optical waveform to dissociated cortical networks while monitoring the evoked spiking response using

MEAs (Sections 4.2.4, 4.2.2, 4.2.5). We refer to this protocol as 'repeated stimulation', s_k^{rep}, in which the same Gaussian waveform s was applied for K trials such that $s_1^{\text{rep}} = s_2^{\text{rep}} = \cdots = s_K^{\text{rep}}$. We then compared spontaneous and evoked firing rates and irregularity for individual units, across drug conditions.

When repeated optical stimuli were applied to the network, spiking patterns of individual units contained firing events that were tightly locked to the repeated stimulus waveform across trials (Fig. 23(b,i)). Although spiking was entrained by the optical stimulus, the unit firing rate distribution was not affected by optical stimuli (Figs. 23, 24(a)). However, the median CV_{ISI} during optical stimulation was significantly reduced compared to that obtained from spontaneous activity, and was similar to values typically obtained from cortical sensory cells responding to external stimuli (Softky and Koch, 1992, 1993) (Figs. 23, 24(b)). The lack of change in the firing rate combined with a significant change in CV_{ISI} indicates that although photostimulation strongly influenced the temporal characteristics of action potential generation, it did not impose extra spikes. Instead, it rearranged the timing of spikes that would have occurred in the absence of stimulation such that they were entrained to the stimulus signal. Because continuously-varying optical stimuli do not temporally override ongoing network dynamics in the way that pulsed electrical or optical stimuli do, their influence on spike generation coexists with other activity variables that influence the subthreshold voltage dynamics of cells within the network, such as ongoing synaptic signaling.

To examine the effect of synaptic connectivity on evoked spiking patterns, we replayed optical stimuli to the networks after we had altered network connectivity using bath application of two combinations of synaptic blockers. In the first condition, α-Amino-3-hydroxy-5-methyl-4-isoxazolepropionic acid (AMPA) and N-Methyl-D-aspartic (NMDA) receptors were blocked using bath applied CNQX and AP5, respectively. In this state, the main forms of excitatory synaptic drive are eliminated

from the network (verified by the absence of post-synaptic currents during whole-cell voltage clamp recordings of individual neurons, data not shown). In the second condition, both excitatory and γ-aminobutyric acid-A ($GABA_A$) receptors were blocked by the co-application of CNQX, AP5, and bicuculline (Section 4.2.3). In this state, virtually all synaptic activity is removed (verified through voltage clamp recordings of individual neurons, data not shown). We refer to the fully connected, drug free state as 'DF', the excitatory transmission blocked state as 'EB', and the fully disconnected, complete block state as 'CB'.

Although spontaneous firing levels fell to nearly zero in both EB and CB states (Fig. 25(b)), the evoked EB and CB firing rates were not significantly different compared to spontaneous or evoked levels in the DF state (Fig. 24(a)). In the EB state, the median CV_{ISI} dropped by a small, but significant, amount compared to that of evoked DF activity. During CB, the median CV_{ISI} returned to the same level as observed during the evoked DF state, approximately 1.0 (Fig. 24(b)). These results indicate that even during large changes in connectivity that greatly affect spontaneous activity levels, continuously-varying photostimulation imposes irregular spike trains that return each unit's firing to pre-drug levels. One feature of network activity that was significantly affected by connectivity was the amount of time it took the network firing rate to adapt to the stimulus onset. We found that networks in the DF state took a significantly longer time to adapt to time-varying stimuli than those in the CB state (Fig. 25(a,c)). This indicates that the presence of synaptic connectivity slows adaptation to time-varying stimuli. In the connected network (DF state), it took 10-30 seconds for firing rate adaptation to occur. Upon the removal of synaptic transmission (CB state), firing consistently fell to a steady-state within $\sim$10 seconds of stimulus onset (Fig. 25(a,c)).

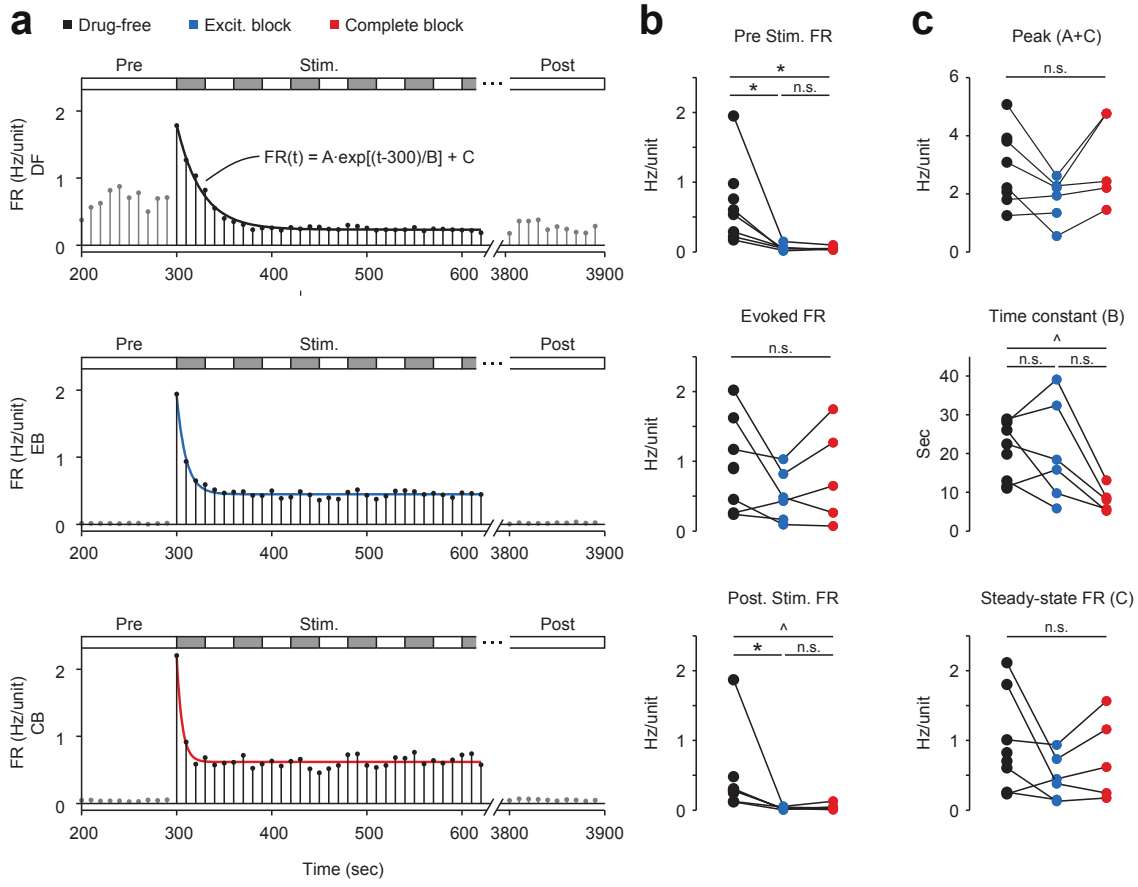

Figure 25: Population firing levels and rate adaptation to continuously-varying photostimulation. **(a)** Population firing rate profiles for a single culture during the onset of continuously-varying optical stimulation in DF (top), EB (middle), and CB (bottom) connectivity states. Stimulation begins at 300 sec. Interleaved grey/white bars indicate repeated and unique stimuli, each of which is a 30-second Gaussian waveform (Section 4.2.5). Firing rate adaptation was fit with an exponential function, which is shown in the top plot. Bin size, 10 sec. **(b)** Pre-stimulus spontaneous activity levels (top), evoked activity levels (middle), and post-stimulus spontaneous activity levels (bottom) for each culture in each drug condition. **(c)** Peak firing rate (top), time constant (middle), and steady-state firing rate (bottom) parameters for the exponential fit to the population firing rate during stimulus onset. See equation in (a, top). Significance thresholds, $P > 0.05$ (n.s.), $P < 0.05$ (^), $P < 0.01$ (*).

4.4.2 Linear and nonlinear contributions of connectivity on the spiking response

Measurements of firing rates, ISI variability, and firing adaptation allow us to make quantitative comparisons to *in-vivo* spiking activity, but they do not provide a complete description of how changes in synaptic connectivity affect the population spiking response. When compared to the DF state, the EB and CB states seem to incur qualitative changes in the temporal characteristics of evoked responses that are plainly visible in spike times of each unit's response (Fig. 23). These qualitative changes appear to affect spiking in isolated units as well as the coordination between unit responses.

To characterize the role of network connectivity in the temporal characteristics of the spiking response, we fit a linear-nonlinear cascade (LN) model to unit responses for each synaptic configuration. An LN model is a phenomenological description of the transformation from a time-varying stimulus to the PSTH . It consists of a linear receptive field (RF) followed by a static, rectifying nonlinearity (Fig. 26(a)). To estimate the RF of each unit, we used a technique modified from (Chichilnisky, 2001) that corrects for the temporal correlations present in our stimulus (Section 4.3.2). The stimulus was then convolved with the RF of each neuron to produce a 'filtered stimulus', which was compared to the measured PSTH in order to fit the static NL for each unit. Fig. 26(c) displays 800 ms sections of filtered stimuli along with the measured and LN-generated PSTHs for a typical unit. We performed an identical fitting procedure for the population PSTH (Section 4.3.1; Fig. 26(c)).

After fitting LN models to the unit and population responses, we measured three parameters of the RF and NL for each unit and population tested: the full width at half maximum of the RF, the 'threshold' (θ in Eq. 42) of the NL, and the 'gain' (α in Eq. 42) of the NL (Fig. 42(b)). We found that connectivity had significant effects on nonlinear components of the response for individual units, but that linear

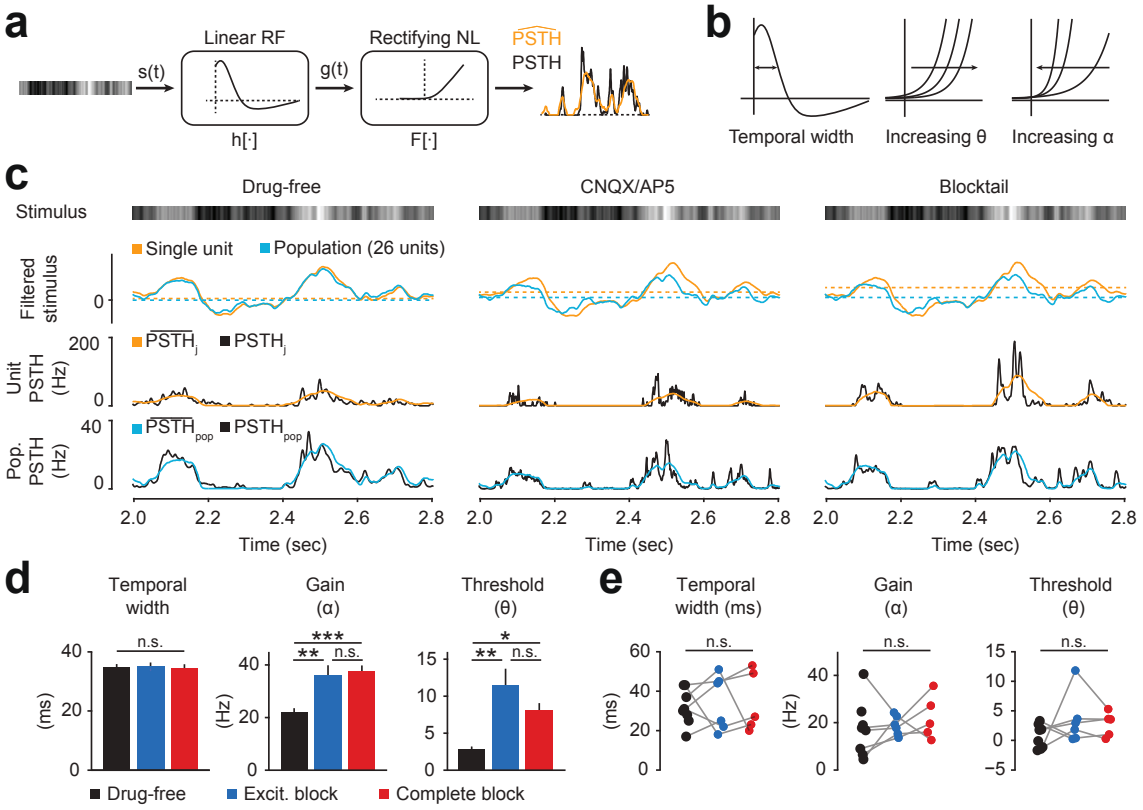

Figure 26: Synaptic connectivity linearizes the neuronal response to time-varying input. **(a)** A linear-nonlinear cascade is used to model the neuronal response. A temporal sequence of light intensities is passed through a linear filter (RF; normalized to unit variance) to produce the filtered stimulus, $g(t)$. $g(t)$ is passed through a rectifying nonlinearity to produce an estimate of the PSTH for each unit. **(b)** Changes in the LN model across units and drug conditions are quantified by measuring the temporal width of each units' receptive field, the 'threshold' parameter θ and the 'gain' parameter α. **(c)** Time-series traces of the stimulus input, the filtered stimulus (solid) and threshold (dashed), and the true (black) and estimated PSTH for both a single unit (yellow) and the average population response (blue) across drug conditions. **(d)** Measures of the linear and nonlinear response properties for individual units. The mean temporal width was: DF 34.6±1.2 s, EB 35.2±1.3 s, CB 34.5±1.5 s. The mean gain (α) was: DF 2.9±0.4, EB 11.6±2.3, CB 8.1±1.0. The mean threshold (θ) was: DF 21.9±1.7 Hz, EB 36.1±3.8 Hz, CB 37.4±2.4 Hz. Error bars denote s.e.m. **(e)** Same as (d) for population response fits. Sample sizes, $n_{DF} = 116$ units (8 cultures), $n_{EB} = 67$ units (6 cultures), and $n_{CB} = 60$ units (5 cultures). Significance thresholds, $P > 0.05$ (n.s.), $P < 0.01$ (*), $P < 0.001$ (**), and $P < 0.0001$ (***).

response properties were not affected. The RF width was the same in the DF, EB, and CB states (Fig. 26(d)). However, during the EB and CB states, the NL threshold increased 400% amd 280%, respectively, compared to the DF state. Additionally, the NL gain during EB and CB was increased by 65% and 72%, respectively, compared to the DF condition (Fig. 26(d)). The preservation of the linear response across connectivity conditions might be attributed to the spatially uniform stimulus input, which was applied to the entirety of the dendtric arbor. Because of this, the passive filtering properties of the dendrite may have dominated the linear response of each cell, irrespective of connectivity.

Increases in the firing threshold, θ, for units in the presence of excitatory synaptic blockade is perhaps unsurprising. For instance, this might occur if excitatory input provided a steady-state conductance that was roughly proportional to network activity levels but was not temporally correlated to the stimulus input. On the other hand, if synaptic activity was temporally related to the stimulation process, there should be effects on the linear response across connectivity conditions. However, we saw no evidence of this. Instead, the threshold parameter was highest in the EB condition, when excitatory transmission was removed but inhibitory transmission was left intact. This effect was lessened somewhat during the CB condition, but the threshold remained elevated due to the absence of any synaptic drive. However increased NL thresholds were accompanied by corresponding increases in the NL gain. This meant that although the threshold was harder to reach in the EB and CB conditions, more spikes were generated when it was crossed. This may account for the fact that average firing rates were unchanged across connectivity conditions. Perhaps most interesting, were the relatively low threshold and gain parameters encountered in the DF state. This meant that a greater portion of the filtered stimulus (the linear response) was transformed into a firing rate compared to the EB and CB states, and that the temporal features of the filtered stimulus were less distorted because the NL was shallow.

These results show that the presence of synaptic connectivity linearizes the network response to time-varying stimuli. This finding is consistent with several long-standing theories of recurrent cortical circuit dynamics (van Vreeswijk and Sompolinsky, 1996, 1998; Douglas *et al.*, 1995). However, those studies focused on the linearization of the population response. Here, we found that the response of individual units is linearized by connectivity.

To quantify the effects of altered connectivity on the dynamics of the population response, we fit the NL model to the population PSTH_{pop} (Eq. 37; Fig. 26(c)). Interestingly, there were no significant differences in the RF or NL parameters across connectivity states. This suggests that the processes of averaging the response across units nullifies changes to the NL response of individual units (Fig. 26(e)). However, averaging is only one possible operation for producing a population response (Abbott and Dayan, 1999). An infinite number of alternative functions might better take advantage of changes in higher order statistics of the response, such as the relative firing precision and correlations between units, could be used in order to faithfully transmit a sensory message. For this reason, we continue our analyses by focusing on the response properties of individual units and their interactions, without assuming that averaging is required to produce the population response.

4.4.3 Effects of connectivity on firing precision and temporal decorrelation

Next, we characterized how neuronal firing precision and inter-neuronal coordination were affected by changes in network connectivity. We started by quantifying the trial-to-trial temporal precision of individual units' responses to repeated optical stimuli. Under the assumption that spikes produced by individual units are relatively well separated, the width of each unit's PSTH autocorrelation provides a measure of the temporal jitter between repeated stimulus trials (Desbordes *et al.*, 2008). To determine the width of the PSTH autocorrelation, we fit the central peak with a Gaussian

function, and defined the PSTH precision to be the standard deviation of the fitted Gaussian function (τ_R, Fig. 27(a); Section 4.3.1).

There was a substantial increase in firing precision after the removal of synaptic connectivity. The mean value of τ_R dropped from 7.7 ms in the DF state to 5.6 and 6.3 ms in EB and CB conditions, respectively, indicating a reduction in trial-to-trial firing jitter (Fig. 27(c, left)). This suggests that synaptic input, especially excitatory input, acts in part as background noise that jitters spike timing. A prominent feature of the time series traces produced by the LN model is a striking difference between the correlation time-scale of the filtered stimulus and that of the measured PSTH (Fig. 26(c)). The RF of each unit can be thought of as feature selector that emphasizes stimulus characteristics that tend to drive firing. The filtered stimulus therefore provides a base time course that be compared to that of the full response. As in ref. (Butts *et al.*, 2007), we defined the 'relative precision' as the precision of the PSTH divided by the filtered stimulus precision,τ_{FS}, which was defined analogously to τ_R using $g_j(t)$ rather than the PSTH_j (Eq. 41; Section 4.3.3). Fig. 27(b, left) shows the PSTH and filtered stimulus autocorrelation functions in all drug conditions for a single unit. The PSTH was considerably more precise than the filtered stimulus across units and connectivity states (Fig. 27(b, right)). Conversely, there was no significant difference in the precision of the filtered stimuli across connectivity states (Fig. 27(c, middle)). This agrees with our previous results showing a lack of change in the linear response properties of units despite changes in connectivity (Fig. 26(d)).

The relative precision was high (greater than 4) across all synaptic configurations, indicating that the units' responses were precise and sparse relative to the stimuli they encoded. The mean relative precision was significantly enhanced by the removal of synapses (Fig. 27(c, right)). Together, these observations suggest that changes in the nonlinear component of a unit's response, acting independently of the linear

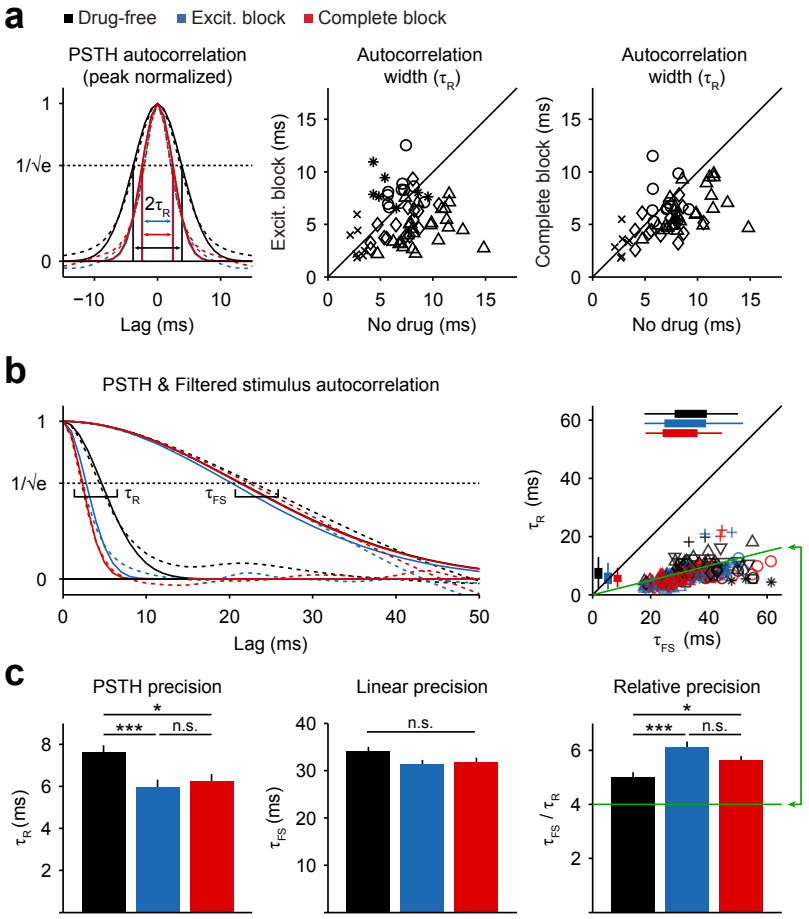

Figure 27: The full neuronal response precision is dependent on recurrent connectivity, but the linear response is not. **(a)** *Left,* example PSTH autocorrelation functions (dashed) and Gaussian fits (solid) for a single unit across drug conditions. The standard deviation of the Gaussian fits (τ_R, arrows) provides a measure of full temporal response precision. *Right,* scatter plots compare τ_R for units in the DF condition against the EB or CB conditions. Different symbols denote the culture that each unit was derived from. **(b)** *Left,* the full response precision (τ_R) is compared to the linear, filtered-stimulus precision (τ_{FS}) for a single unit across drug conditions. *Right,* τ_{FS} plotted against τ_R for each unit in each drug condition. The ratio of τ_{FS} to τ_R defines the relative precision. **(c)** The PSTH, linear, and relative precision distributions are compared across drug conditions. Mean τ_R for DF 7.7±0.3 ms, EB 5.6±0.3 ms, and CB 6.3±0.3 ms. The mean τ_{FS} was: for DF 34.2±1.7, EB 31.4±1.7, and CB 31.8±1.2. The mean relative precision was: for DF 5.0±0.4, EB 6.1±0.4, and CB 5.6±0.3. Error bars denote s.e.m. Sample sizes, $n_{DF} = 116$ units (8 cultures), $n_{EB} = 67$ units (6 cultures), and $n_{CB} = 60$ units (5 cultures). Significance thresholds, $P > 0.05$ (n.s.), $P < 0.01$ (*), and $P < 0.0001$ (***).

RF, are capable of affecting a unit's temporal firing precision via increases in the firing threshold and response gain. Further, the reduction in the temporal width of the PSTH autocorrelation compared to that of the filtered stimulus implies that nonlinear rectification temporally decorrelates the stimulus signal in all configurations, particularly in the EB and CB network states. This suggests that synaptically decoupled networks may be more efficient encoders of time-varying stimuli, since messages carried by individual units are less related to one another than in the DF state (however, see Table 7).

4.4.4 Connectivity and pairwise response correlations

The above results quantify the isolated response properties of individual units during different connectivity states. However, it is likely that changes in synaptic connectivity also lead to changes in interneuronal coordination which have not been captured by our analysis to this point. To quantify how synaptic connectivity affected neuronal coordination, we calculated the cross-correlation function between the PSTHs of units from the same network. We started by computing the correlation coefficient between each pair of units recorded from the same network, ρ_R (Eq. 46; Fig. 28(a)). To deduce whether changes in neuronal correlations were the result of alterations to the linear or nonlinear properties of each unit's response, we then calculated the cross-correlation function between units' filtered stimuli, ρ_{FS}, for comparison to the full response correlation ρ_R. Finally, we calculated the standard deviation of a peak-centered Gaussian fit to the cross-correlation function, $\tau_R^{i,j}$, which provides a measure of repeatable temporal coordination of two units over trials (Fig. 28(b); Section 4.4.3).

PSTH correlation coefficients, ρ_R, exhibited significant changes to due to alterations in network connectivity (Fig. 28(a)). The mean correlation coefficient between unit PSTHs was highest in the DF state and dropped significantly during excitatory synaptic blockade. Correlation levels recovered somewhat during full synaptic

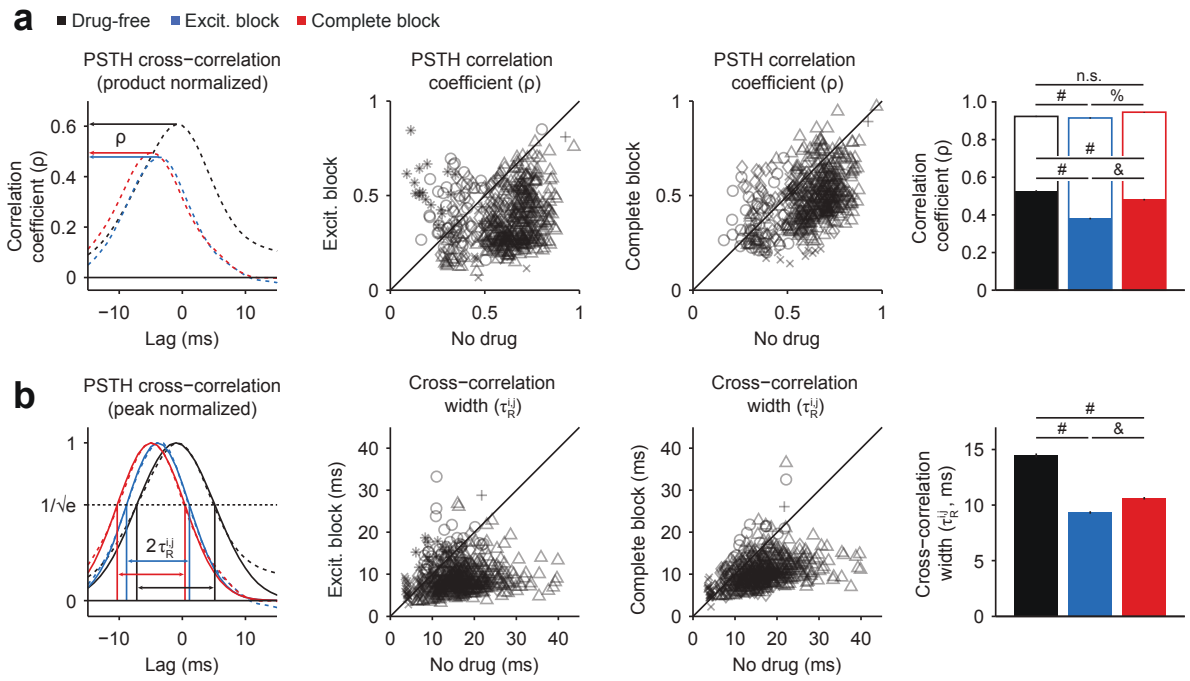

Figure 28: Connectivity increases response correlations but decreases the precision of pairwise neural coordination. **(a)** *Left,* example normalized PSTH cross-correlation functions from a single pair of units across drug conditions. *Middle,* scatter plots compare ρ_R for units in the DF condition against the EB or CB conditions. Scatter plot symbols identify the culture that each unit was derived from. *Right,* ρ_{FS} (empty bars) and ρ_R (filled bars) distributions are compared across drug conditions. The mean value of ρ_{FS} dropped by a small, but significant amount in the EB condition compared to the DF and CB conditions. The mean ρ_{FS} was for DF 0.92±0.0032, EB 0.91±0.0032, and CB 0.94±0.0019. Mean values of ρ_R were markedly decreased compared those of ρ_{FS}, and were significantly different across all connectivity states. The mean ρ_R was for DF 0.52±0.0044, EB 0.37±0.0041, and CB 0.48±0.0041. Error bars denote s.e.m. **(b)** *Left,* example PSTH cross-correlation functions (dashed) and Gaussian fits (solid) for a pair of units across drug conditions. The standard deviation of the Gaussian fits ($\tau_R^{i,j}$) provides a measure of the coordinated timing precision of two neurons across trials. *Middle,* scatter plots compare $\tau_R^{i,j}$ for units in the DF condition against the EB or CB conditions. Scatter plot symbols identify the culture that each unit was derived from. *Right,* $\tau_R^{i,j}$ distributions are compared across drug conditions. The mean $\tau_R^{i,j}$ was for DF 14.5±0.19 ms, EB 9.4±0.12 ms, and CB 10.7±0.12 ms. Error bars denote s.e.m. Sample sizes, $\mathrm{n_{DF}} = 1226$ combinations (8 cultures), $\mathrm{n_{EB}} = 518$ combinations (6 cultures), and $\mathrm{n_{CB}} = 497$ combinations (5 cultures). Significance thresholds, $P > 0.05$ (n.s.), $P < 10^{-5}$ (%), and $P < 10^{-7}$ (#).

blockade, although they remained significantly reduced compared to DF (Fig. 28(a, right)). Interestingly, although the correlation between the linear responses of units, $\rho_F S$, changed significantly across drug conditions, its value was consistently high and the changes in the mean value of $\rho_F S$ were small compared to the shifts seen in ρ_R due to changes in connectivity.

Our measurement of correlation includes contributions from the spatial and temporal characteristics of the stimulus input (signal correlations) and those arising from shared connectivity (noise correlations) (Averbeck *et al.*, 2006). Both types of correlation are important for neural encoding and decoding in several sensory and motor systems (Abbott and Dayan, 1999; Ecker *et al.*, 2011; Salinas and Sejnowski, 2001). Under the assumption that the CB condition provided complete blockade of synaptic connectivity (although, see Hales *et al.* 2012), we can make several observations about the correlation coefficients presented in Fig. 28(b). First, the mean correlation coefficient in the CB state, $\rho_R, \mathrm{CB} = 0.48$, represents the 'isolated signal correlation' for our system. This is because the correlated variability of each unit's trial-to-trial response, which relies on synaptic communication, should be completely removed. Second, the fact that $\rho_R, \mathrm{EB} = 0.38$ is less than ρ_R, CB suggests that inhibition actively decorrelates neuronal activity in our preparation. Third, there is a large drop in correlations when comparing those derived from the linear response to the full PSTH (Fig. 28(a, right)). Due to their spatial uniformity, stimuli are perfectly correlated across cells, and this is reflected by nearly perfect correlations in optically-evoked intracellular currents during continuously-varying stimulation (Tchumatchenko *et al.*, 2013). This extreme correlation is captured in the linear responses of cells, but drops considerably in the full response (Fig. 28(a, right)). This indicates that nonlinear processing decorrelates the stimulus input. The degree of decorrelation depends on network connectivity. Nonlinear processing removed 44% of correlations in the linear response in the DF state, 59% in the EB state, and 49% in the CB state.

In addition to the changes in strengths of the correlations, we also detected significant alterations in the temporal coordination of units across trials in different connectivity states. The mean temporal width of the PSTH, $\tau_R^{i,j}$, cross-correlation function showed a substantial decrease in EB and CB states compared to the DF state (Fig. 28(b)). Reductions in $\tau_R^{i,j}$ indicate that units within networks lacking excitatory synaptic connections were more likely to produce action potentials at the same time points relative to the stimulus waveform during each trial. Combined with the correlation coefficient results, this indicates that units in the fully connected DF state were more likely to produce spikes synchronously but those synchronous spiking events had more temporal variability relative to the stimulus input across trials compared to the EB and CB connectivities. In other words, units in the DF state were more likely to co-produce an imprecise response to the stimulus input, suggesting a detrimental effect on information transmission compared to the EB and CB states.

4.4.5 Effects of connectivity on information transmission

We next accessed how changes in synaptic connectivity influenced network encoding properties by calculating the mutual information between the spiking response and the stimulation process. To do this, we applied a secondary type of input, 'unique stimuli', which were interleaved with repeated stimulus trials (Fig. 25(a); Section 4.2.5). During unique stimuli, a new realization of the same Gaussian random process used to produce the repeated stimulus, s, was applied for each trial such that $s_1^{\text{uni}} \neq s_2^{\text{uni}} \neq \cdots \neq s_K^{\text{uni}}$.

Repeated and unique stimuli reveal different features of the population response that can be used to estimate their mutual information (Strong *et al.*, 1998). If neural encoding of the stimulus is noise-free and has a finite correlation time, then each repeated stimulus presentation will result in precisely the same network response. In reality, the encoding process is noisy and introduces trial-to-trial variability in the

response to repeated applications of the same stimulus. The effects of this noise are quite apparent in the jitter of spike timing across trials (Fig. 23). The extent of this jitter is quantified by the conditional (or 'noise') entropy, H_{noise} (Eq. 53) which measures the variability of the network response that is not useful for encoding the stimulus. On the other hand, by applying a different stimulus realization for each trial (unique stimuli), the full repertoire of neuronal response patterns can be sampled, and the total variability of neuronal response can be quantified by the total entropy H_{total} (Eq. 53). H_{total} measures the variability of the population response that results from noise as well as the repertoire of activity patterns that contain information about the stimulus. Therefore, the difference between H_{total} and H_{noise} is the mutual information between the stimulus and response

$$I = H_{total} - H_{noise}. \tag{58}$$

If the length of each stimulus trial is much longer than the correlation time of the spiking response, then H_{total} and H_{noise} can be conveniently estimated in the Fourier domain and represented as density spectra across frequencies (Yu *et al.*, 2010; Crumiller *et al.*, 2011) . This technique can be applied to the response of individual units or the ensemble response. For the latter case, the method takes into account reductions in total and noise entropy due to correlations between units' responses (Eq. 54; Section 4.3.4).

We first quantified how connectivity affected information transmission in the isolated unit response to time-varying optical stimuli (Fig. 29). Fig. 29(a, left) shows the total and noise entropy spectra for a single unit in each synaptic configuration. For this particular unit, the total entropy was greater than the noise entropy in the ∼0-90 Hz frequency band, indicating that stimulus information content within the unit's spiking response was limited to this range. For frequencies greater than ∼90 Hz, the total entropy converged to the noise entropy, indicating a lack of information content. The area between these two curves is the mutual information between the

stimulus and response (Fig. 29(b, left).

We found that each unit's response harbored stimulus information within the 0-90 Hz band across connectivity states (Fig. 29(a, middle)). However, we did not detect a systematic effect of connectivity on the entropy rates, $H_{j,total}$ or $H_{j,noise}$ (Fig. 29(a, right)). Unlike entropy rates, information rates of individual units were greatly affected by network connectivity (Fig. 29(b, middle)). We found that decreased synaptic connectivity significantly increased information rates in single units. The mean information rate of units doubled from $\sim$12 bits/sec in the DF state to $\sim$24 bits/sec (200% of DF) in the EB state, and then further increased to $\sim$27 bits/sec (225% of DF) in the CB state (Fig. 29(b, right).

Changes in information rates for single unit responses reflect increased temporal precision in disconnected compared to connected network states (Butts *et al.*, 2007) (Fig. 27). However, altered connectivity strongly affects the pairwise coordination of unit responses (Fig. 28), which suggests that the information rate of the joint response may not match the trends seen in isolated unit responses. Because activity between units is correlated, simply adding each unit's information content to arrive at a pairwise information rate is not a valid procedure. Interactions between units must be taken into consideration. For instance, if two neurons have a one-to-one mapping between their respective responses to a common stimulus signal, then no more information is gained from examining one spike train compared to both. On the other hand, correlations between unit responses can serve as a source of information that improves stimulus encoding (Schneidman *et al.*, 2003) (Table 7). The method we employ to calculate information rates is sensitive to all correlations between units' responses that can be directly sampled, and therefore is appropriate for evaluating the information content of the pairwise response (Yu *et al.*, 2010) (Section 4.3.4).

To explore the joint encoding properties of neurons during different states of connectivity, we calculated the information content between paired unit responses and

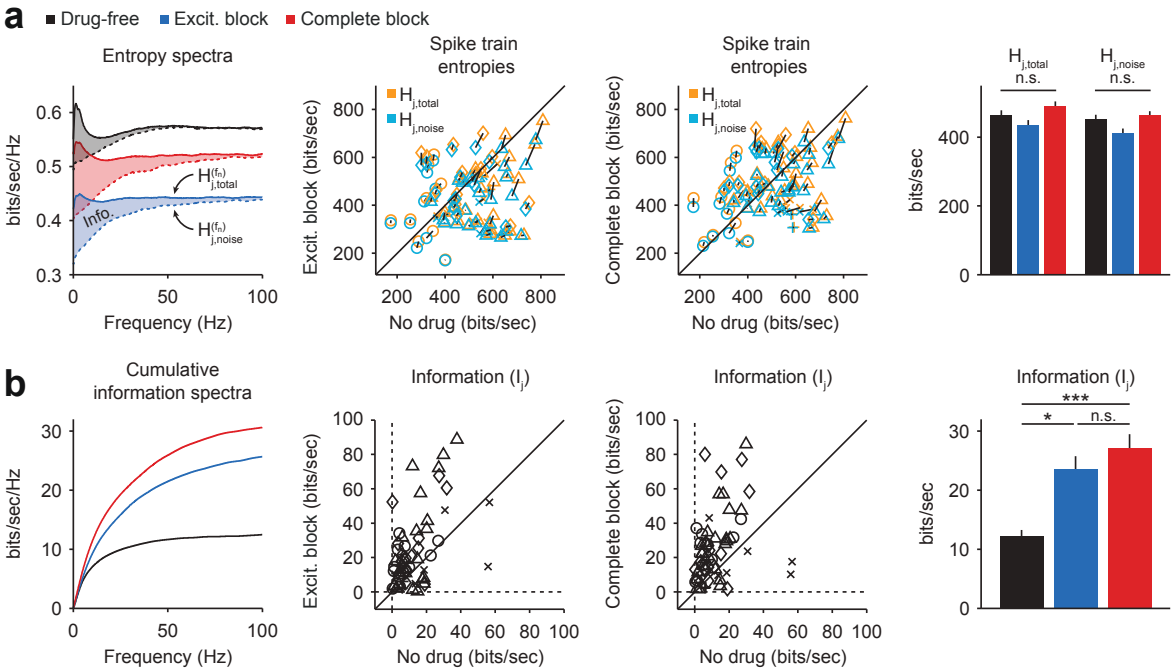

Figure 29: Connectivity decreases the mutual information between the stimulus and single unit responses. **(a)** *Left,* total entropy ($H_{j,total}$, solid lines) and noise entropy ($H_{j,noise}$, dashed lines) spectra for a single unit across drug conditions. The difference between the two lines is the information rate, in bits/second, at each frequency. *Middle,* scatter plots compare $H_{j,total}$ and $H_{j,noise}$ for units in the DF condition against the EB and CB connectivity states. Symbols identify the culture that each unit was derived from. Black lines indicate the stimulus/response information content for each unit and the slope of this line indicates the relative information in the compared drug conditions. *Right,* mean entropies ±s.e.m. for each drug condition. **(b)** *Left,* unit-averaged cumulative information spectra across drug conditions for a single culture (Eq. 52). *Middle,* scatter plots compare I_j for units in the DF condition against the EB or CB conditions. *Right,* spike train information distributions compared across drug conditions. The mean information rates were for DF 12.2±1.1 bits/sec, EB 23.5±2.2 bits/sec, and CB 27.1±2.4 bits/sec. Error bars denote s.e.m. Sample sizes, $n_{DF} = 96$ units (6 cultures), $n_{EB} = 60$ units (5 cultures), and $n_{CB} = 60$ units (5 cultures). Significance thresholds, $P > 0.05$ (n.s.), $P < 0.01$ (*), $P < 0.0001$ (***).

Table 7: Example of synergistic pairwise encoding. The table displays the joint and marginal probability distributions for outputs produced by a pair of toy neurons. Each neuron produces an output, r_1 and r_2, that can take values 0 or 1 in response to a single stimulus input, s. s takes values s_1 and s_2 with equal probability. The information contained in the isolated unit responses is $I_{r_1;s} = I_{r_2;s} = 0$ bits, but the information content of the joint response, $\vec{r} = [r_1, r_2]$, is $I_{\vec{r};s} = 0.3963$ bits. Values were calculated from the definition of mutual information, $I(r,s) = \sum_{r,s} p(r,s) \log_2 \left(\frac{p(r,s)}{p(r)p(s)} \right)$. The fractional redundancy is therefore $R = (0 - 0.3963)/0.3963 = -1.0$. This is due to the correlated pairwise response to s_1 resulting from $p(r_{1,2} = y | r_{2,1} = y, s = s_1) = 1$.

$\mathbf{p(\vec{r}, s)}$

	$\vec{r} = [r_1, r_2]$				
	[0,0]	[0,1]	[1,0]	[1,1]	$p(s)$
s_1	0.25	0	0	0.25	0.5
s_2	0.125	0.125	0.125	0.125	0.5
$p(\vec{r})$	0.375	0.125	0.125	0.375	

$\mathbf{p(r_1, s), p(r_2, s)}$

	r_1		r_2		
	0	1	0	1	$p(s)$
s_1	0.25	0.25	0.25	0.25	0.5
s_2	0.25	0.25	0.25	0.25	0.5
$p(r)$	0.5	0.5	0.5	0.5	

the stimulus input, $I_{i,j}$, in each drug condition (Eq. 55 with $J = \{i, j\}$). Fig. 30(a, left) shows the cumulative information spectra for a pair of units across each drug condition (dotted lines). We found that reductions in connectivity greatly improved pairwise stimulus encoding (Fig. 30(a, middle)). Mean information rates increased from 22 bits/sec in the DF case to 49 bits/sec (220% of DF) and 57 bits/sec (260% of DF) in the EB and CB cases, respectively. We found that pairwise information levels were almost always less than the sum of the information content of constituent units, indicating a redundant encoding process across all drug conditions. Additionally, increases in the pairwise information rate due to decreased connectivity were more extreme than occurred in the case of isolated unit responses (Fig. 29(b)). This suggests that the pairwise response of units in the DF state are more likely to provide redundant information than pairwise responses in the EB or CB states.

The redundancy of the pairwise response quantifies the degree to which each unit provides an independent message about the stimulation process. The redundancy is

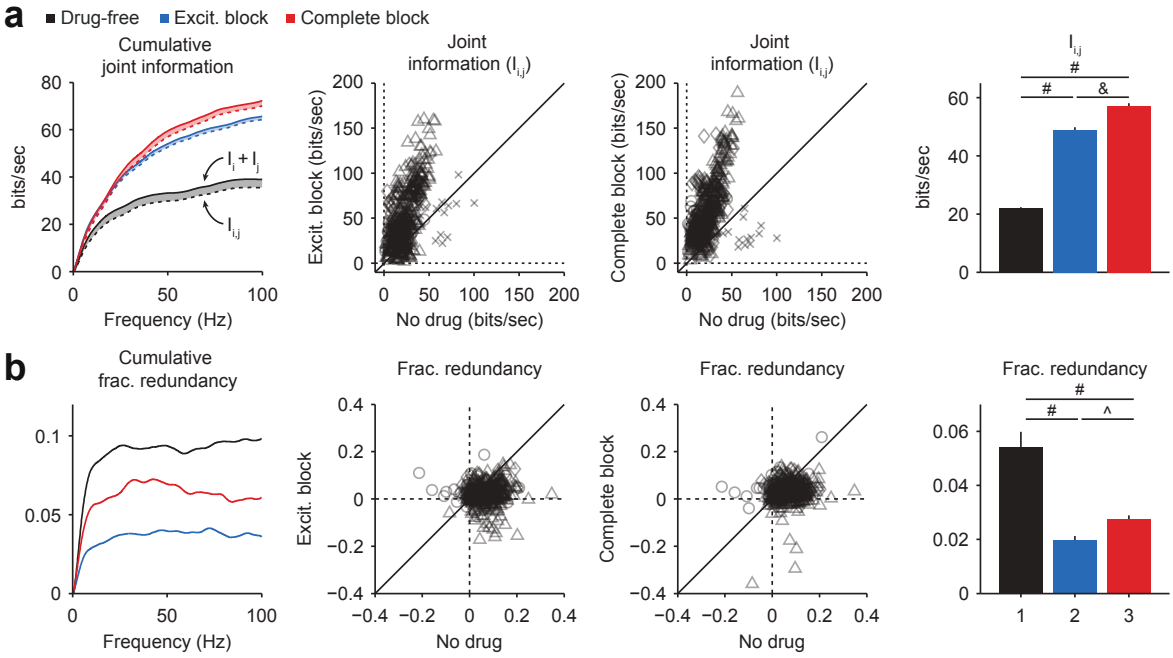

Figure 30: Connectivity causes over-representation of the stimulation process. **(a)** *Left,* cumulative summed (solid lines) and pairwise (dashed lines) information spectra across drug conditions for a single pair of units. The height of the shaded area between the two lines is the redundancy at a particular frequency. *Middle,* scatter plots compare $I_{i,j}$ for populations in the DF condition against EB or CB conditions. Symbols identify the culture that the population was derived from. *Right,* $I_{i,j}$ distribution for each population across connectivity states. The mean $I_{i,j}$ was for DF 22.0±0.4 bits/sec, EB 48.9±1.0 bits/sec, and CB 57.1±1.0 bits/sec. **(b)** *Left,* cumulative fractional redundancy spectra for the units in (a, left). *Middle,* scatter plots compare R for populations in the DF condition against EB or CB conditions. *Right,* R distribution across connectivity states. The mean R was for DF 0.054±0.0057, EB 0.020±0.0013, and CB 0.028±0.0013 bits/sec. Sample sizes: $\mathrm{n_{DF}} = 1127$ pairs (6 cultures), $\mathrm{n_{EB}} = 497$ pairs (5 cultures), and $\mathrm{n_{CB}} = 497$ pairs (5 cultures). Significance thresholds, $P > 0.05$ (n.s.), $P < 0.05$ (^), $P < 10^{-6}$ (&), $P < 10^{-7}$ (#).

defined as the the summed information rate of each unit minus their joint information. Because individual units had very different information rates, we calculated the fractional redundancy (R, Eq. 57), which is normalized by the joint information between two units (Schneidman *et al.*, 2003). $R = 1$ indicates that all of information contained in pairwise response is available within the response of a single member of the pair. $R = 0$ indicates that each unit conveys a statistically independent message about the stimulation process. $R < 0$ indicates that the correlated activity in the population response conveys information not present when the single units are considered in isolation (i.e. the encoding process is 'synergistic'; Table 7) (Schneidman *et al.*, 2003).

We found that unit pairs in the DF network tended to over-represent the stimulus input, providing significantly more redundant information in their pairwise response compared to units in the disconnected states (Fig. 30(b, left)). These results indicate that increased correlations between neurons in the DF state (Fig. 28) provided no synergistic effect on the encoding process (on average) as has been seen in other preparations (Brenner *et al.*, 2000). Interestingly, the redundancy values measured from our networks in the DF state are similar to those of retinal ganglion cells sharing a receptive field (Puchalla *et al.*, 2005). This suggests that the structure of connectivity may not matter in the context of response redundancy. Finally, we found that the CB state produced a more redundant response than the EB state (Fig. 30(b, left)). Inhibitory connectivity also actively decorrelates the pairwise response compared to the uncoupled network (Fig. 28(a, left)) in our preparation. Together, these results indicate that the response decorrelation incurred through intact inhibitory connectivity results in a more efficient encoding process compared to the decoupled network, even though raw information rates are highest in the CB case.

4.5 Discussion

The majority of studies investigating the encoding properties of neural circuits examine how the statistics of sensory stimuli (for instance, visual or auditory stimuli with a 'natural' correlation structure (Lesica *et al.*, 2007; Butts *et al.*, 2007; Kayser *et al.*, 2010; Rieke *et al.*, 1995)) affect how sensory messages are transformed by cells and pathways. Here, we took a different approach. We sought to relate gross aspects of network connectivity, rather than the statistics of stimulus input, to resultant neural encoding properties. We previously demonstrated that Gaussian continuously-varying optogenetic stimulation produces *in vivo*-like subthreshold voltage fluctuations in individual neurons (Tchumatchenko *et al.*, 2013) (Chapter 3). We used this technique to deliver stimuli to excitatory neurons embedded in randomly connected networks of cortical cells while systematically altering network connectivity using selective synaptic receptor blockade. We therefore could directly investigate how well-defined alterations in network connectivity affected the encoding of identical stimuli. Our approach revealed several interesting roles of connectivity in neural encoding, especially in regard to nonlinear aspects of time-varying signal transduction, that do not appear to rely on specific connectivity architecture.

Our analysis began with the most basic characteristic of the neural response: the firing rate. Surprisingly, we found no difference between the average firing rate of units during spontaneous activity in the DF condition and evoked activity across connectivity conditions (Fig. 24). This occurred in spite of the fact that individual units' responses were tightly locked to the driving stimulus. This indicates that instead of adding additional spikes to ongoing activity, time-varying optical stimulation rearranges the timing of spikes that would have occurred in the absence of stimulation. Changes in connectivity had no effect on the average rate of spikes produced during stimulation. This hints at the existence of short-term homeostatic processes

that can quickly adapt to large perturbations in connectivity such that evoked firing is maintained at a 'desired' level. Additionally, we found that the irregularity of evoked spike trains was similar to that of spike trains from sensory cortical cells *in vivo* (Softky and Koch, 1993, 1992).

Although evoked firing rates and spiking irregularity did not change across connectivity states, the temporal characteristics of the evoked response were greatly affected. The removal of excitatory connectivity increased the severity of the nonlinear response properties of individual units (i.e. the static nonlineary more closely resembled a Heaviside function when excitatory connectivity was removed). Stated differently, this shows that the presence of excitatory synaptic transmission makes each unit's spiking response more closely resemble a linear transformation of the stimulus process. Previous studies have predicted that strong recurrent connectivity may linearize the population-averaged response to time-varying stimuli (van Vreeswijk and Sompolinsky, 1998, 1996). However, we found no significant difference in the severity of the nonlinear features of the population-averaged response across connectivity states (Fig. 26(e)). Interestingly, we did find that the response of *individual* units was linearized by connectivity (Fig. 26(d)).

The precision of evoked spike trains across trials (the jitter referenced to the stimulation process) was also affected by changes in connectivity. We found that both the precision of individual unit spike timing and the precision of temporal coordination between units were increased by the removal of excitatory connectivity. These changes in spiking precision could be explained by modification of units' nonlinear response properties. Further, we found that nonlinear processing temporally decorrelated the neural response across drug conditions, and that this effect was especially pronounced when excitatory connectivity was removed. This corresponded to identified changes in the characteristics of nonlinear processing: an increase in both the threshold and gain of the nonlinearity, which was most pronounced in the EB connectivity condition

(Fig. 26). These results are in strong agreement with a recent study investigating the effects of nonlinear processing on stimulus-decorrelation in retinal ganglion cells (RGCs) (Pitkow and Meister, 2012). In that study, an LN model was used to show that the linear interaction, which represented lateral connectivity, could account for only a small fraction of the effects on temporal and spatial stimulus decorrelation, and that most of the decorrelation effect was derived from the nonlinearity of each RGC. However, our results differ from this study in terms of the physiological locus of nonlinear processing. We found that nonlinear processing was altered by changes in synaptic connectivity, which is assumed to be represented by the linear components of most LN models.

Models of sensory neurons, especially RGCs or visual thalamic cells, typically capture the effects of connectivity by adding linear terms to represent synaptic interaction and refractoriness. However, our results demonstrate that changes in connectivity primarily affect nonlinear features of the spiking response, and leave linear processing unaltered. These changes in nonlinear characteristics cannot be captured by additional stages of linear stimulus filtering or by the addition of linear filtering terms for synaptic or refractory effects (Truccolo *et al.*, 2005; Pillow *et al.*, 2008). Recently, McFarland et al. produced a model, dubbed the nonlinear input model (NIM), which implements the stimulus processing as an arbitrary number of separate, potentially nonlinear, transformations on the stimulus input (McFarland *et al.*, 2013). These input pathways are capable of representing nonlinear processing resulting from connectivity. An intuitive example is ON-OFF retinal ganglion cells, which respond to both increases and decreases in stimulus contrast, and thus need two forms of nonlinear rectification (one sensitive to ON stimulus dimensions and the other to OFF) for accurate response prediction (McFarland *et al.*, 2013). Because connectivity affects the nonlinear response characteristics of cells in our preparation, the emphasis that the NIM places on nonlinear processing prior to spike generation seems to be justified.

Incidentally, for data presented here, we have good knowledge of both the stimuli delivered to our networks and their true connectivity state. Therefore, the data set produced by this study may serve as a validation set for generalized point-process models and the NIM, which seek to infer connectivity (or more generally, 'upstream' transformations) based upon the spiking response of cells to a common stimulation process.

The effects of connectivity on unit response properties translate to effects on information transmission. Stimulus information contained in unit responses more than doubled when synaptic interaction was removed from the network. Increased information rates due to the reductions in synaptic connectivity might be loosely related to the data-processing theorem, which states that transformations on a signal can, at best, preserve information in the signal (Shannon, 1948). Therefore, one might guess that the removal of synapses amounts to the removal of a significant noise source, and the fidelity of the response of the disconnected network was improved since this noise was no longer present. Indeed, the highest information rates in single units and the paired response were produced by the disconnected network, even though the pairwise response precision of the disconnected network was slightly lower than that of the EB network state.

However, this interpretation is complicated when the pairwise response is considered. Under these circumstances there is increased redundancy in the response of the disconnected network compared to when only excitatory transmission is blocked. This means that although on average there is more information contained in the pairwise response of cells in the disconnected network, the pairwise response represents less of the total information available in the individual responses of constituent units compared to when inhibition is left intact. The minimal redundancy of the EB state appears to result from the decorrelating effects of inhibition on the pairwise response

(Fig. 28), especially since pairwise correlations capture the dominant form of interaction even between large numbers of units in cultured cortical networks (Schneidman *et al.*, 2006).

Based upon these results, one might conclude that since synapses reduce information transmission, they impede network function. This would be true if the only function of neural circuits was to faithfully transmit sensory messages. However, this is not the case. Information measures do not consider the meaning or 'importance' of stimulus messages. To do this, one must examine the neural response from the perspective of neural *decoding*: the production of some behavioral output based upon the neural response. Our analysis of neural *encoding* was free of assumptions concerning the relative importance of various stimuli or spiking patterns, but simply analyzed the potential utility of the neural response. On the other hand, a valid decoding procedure can result from an infinite number of possible transformations on neural activity. Optimal decoding is also difficult to define since the performance of a decoder is dependent on an error measure between a 'correct' transformation of sensory stimuli and the achieved motor output (Schneidman *et al.*, 2003). Note that this definition is distinct from other interpretations of decoding, which define decoding as the estimation of the conditional probability distribution $p(s|r)$, to make the problem of optimal decoding more tractable.

It is especially hard for us to guess the functional role of changes in network encoding properties because cultured networks are not integrated into a behaving system, so decoding is not a concept that holds any meaning. Other studies have integrated cultured cortical networks into robotic animal bodies, capable of executing simple behaviors by decoding ongoing neural activity (DeMarse *et al.*, 2001; Chao *et al.*, 2008). In this case, it could be that the linearizion of the neural response and increased redundancy in the intact network act to highlight salient features of stimulus input, resulting in improved behavioral performance. Indeed, this seems

to be the case for populations of retinal ganglion cells, which are highly redundant encoders of natural visual scenes (Puchalla *et al.*, 2005) but whose correlations can be used to improve stimulus reconstruction (Pillow *et al.*, 2008).

Finally, in our analysis we treat the encoding process as a stationary transformation on stimulus inputs to produce a response. However, the widely accepted function of synapses is to allow changes in the input/output relationship of a network such that its response properties can be updated through learning. Synapses provide networks with a large set of free parameters, and therefore a wide set of potential dynamics that can be accessed to make the neural response useful for behavior. Without synapses the repertoire of potential behavioral outputs would decrease drastically. To summarize all of the above points, the existence of synapses may reduce information transmission, but they are required to make information transmission useful to an organism.

In this study, we used continuously-varying optogenetic stimulation to create a wide-bandwidth, genetically specified communication channel with a genetically defined input layer of excitatory cells embedded within randomly connected networks of cortical neurons. This configuration mimics the structure of large scale computer models of cortical networks (Brunel, 2000; Vogels *et al.*, 2005; Vogels and Abbott, 2009; van Vreeswijk and Sompolinsky, 1996, 1998; Douglas *et al.*, 1995; Izhikevich *et al.*, 2004; Izhikevich, 2006), offering similar levels of access to spiking patterns of constituent cells, but using living neurons. This approach is applicable to a much more general set of experimental circumstances than we have described in this study, and can be improved with the incorporation of new technologies for neural recording. For instance, continuously-varying photostimulation can be combined with high-density microelectrode arrays, which allow spiking activity to be recorded from virtually every neuron in a dissociated cortical network or retinal preparation (Fiscella *et al.*, 2012; Bakkum *et al.*, 2013). This would provide a complete measurement of the population

spiking response in order to verify the results obtained from incomplete populations, like those presented here.

Our technique allows for direct interrogation of neural circuits with extremely repeatable stimuli that mimic natural synaptic input. This provides a means for more straightforward investigations of the isolated response properties of sensory circuits. Additionally, time-varying optical stimuli allows for precise manipulation of spiking patterns in brain structures several synapses removed from a sensory organ. This highlights its potential use in the development of improved sensory prosthetic devices. We envision that future instantiations of this technique will extend its ability to control firing patterns of particular neural populations by incorporating spatial light-modulation and real-time feedback (Chapter 5).

CHAPTER V

OPTOGENETIC FEEDBACK CONTROL OF NEURONAL FIRING

Optogenetic tools allow genetically-specified neural activation and silencing, and facilitate artifact-free electrical readout of evoked neural activity. The ability to electrically measure, and optically modulate, spiking activity forms the basis of a feedback loop that can be used to control neural activation. Here we present a feedback control technology that automatically adjusts optical stimulation in real-time to precisely control spiking activity. We characterize the system's ability to control neural activity in dissociated cortical networks, over timescales ranging from seconds to days, and in vibrissal somatosensory thalamus of rats during whisker stimulation. We demonstrate how the system can be used to decouple neuronal firing levels from ongoing changes to network excitability due either to 24-hour periods of glutamatergic neurotransmission blockade or impinging vibrissal sensory drive. This technology greatly enhances the precision with which optical stimulation can control neural activity, and allows causally related variables of circuit activation to be studied independently.

5.1 Introduction

The population firing rate is the most robust correlate of sensory and motor information in the brain. It can be used to decode the direction of arm movements (Georgopoulos *et al.*, 1988), the perception of visual motion (Steinmetz *et al.*, 1987), and an animal's physical location within an environment (Brown *et al.*, 1998). Because of this, precise control of neuronal firing levels in targeted brain regions would provide a powerful approach for dissecting neural circuit function and would advance the development of sensory prostheses.

Optogenetic approaches are used to provide genetically specified, millisecond timescale, spike timing control in single neurons (Mattis *et al.*, 2011), and gross modulation of population firing levels (Yizhar *et al.*, 2011a), during simultaneous, artifact-free electrical recording. The ability to simultaneously perturb and measure neural activity encapsulates the basic elements of a feedback loop, which can be exploited to control neural activation. Precisely controlling the firing level of a specified neuronal population in the face of ongoing modulatory input, changes in cognitive state, changes in sensory drive, and/or neuronal adaptation would improve our ability to infer its causal relationship with information transmission and behavior. Further, the ability to control population firing in spite of behaviorally-, pharmacologically-, or genetically-induced changes in network excitability would allow the direct effects of these perturbations on circuit plasticity to be disentangled from those due to changes in activity levels.

Feedback is used in many situations to linearize input/output relationships, decouple causally-related system variables, and provide control over system variables. This has been exemplified in single-cell electrophysiology by the voltage clamp, which uses a feedback circuit to control the cellular membrane potential. More recently, a diverse set of specialized techniques that employ feedback control have emerged for studying adaptation in neuronal micro-circuits (Ahrens *et al.*, 2012), using electrical stimulation to control spike latency (Wallach *et al.*, 2011) and firing levels (Wagenaar *et al.*, 2005; Newman *et al.*, 2013), improving brain-computer interfaces (Velliste *et al.*, 2008), inducing motor plasticity (Jackson *et al.*, 2006a), and improving motor rehabilitation (Moritz *et al.*, 2008). Real-time optogenetic stimulation has recently been used to control motor behavior in *Caenorhabditis elegans* (Stirman *et al.*, 2011; Leifer *et al.*, 2011) and introduce fictive sensory information into somatosensory cortex during active whisking in mice (O'Connor *et al.*, 2013). Additionally, closed-loop activation of halorhodopsin expressed in excitatory principal cells (Paz *et al.*, 2012),

or channelrhodopsin expressed in inhibitory interneurons (Krook-Magnuson *et al.*, 2013), has proven capable of real-time seizure intervention *in vivo*. However, these studies did not update stimuli based on ongoing neural activation, which is necessary for true real-time control of neural activity. We sought a technology that could precisely specify neural activity levels over a wide dynamic range, and that was general enough to be applied across experimental preparations and time scales.

Here we describe a general framework for using multi-modal, closed-loop optogenetic stimulation to control population firing activity *in vitro* and *in vivo*. Using this method, microelectrodes are used to sample extracellular, single-unit spiking activity. Electrode voltages are then streamed to a real-time electophysiology platform, which detects and sorts action potentials at low latency and computes the instantaneous firing rate (Chapter 2). The firing rate is compared to a target, and stimulation parameters are updated such that the error between the target and the measured firing level is minimized. Using dissociated cortical networks grown on microelectrode arrays, we show that optogenetic feedback provides precise, rapidly-settling control of network firing levels. We then extend this method to control mean network activity levels over many hours. We demonstrate the utility of long term activity control *in vitro* by locking network firing to pre-drug levels during 24-hour blockade of excitatory synaptic transmission. In doing so, we decoupled the effects of reduced glutamatergic neurotransmission on changes in network excitability from secondary effects due to changes in network firing levels to show their unique roles in homeostatic increases in network excitability. Finally, we show how optogenetic feedback control can be used to control firing activity in vibrissal somatosensory thalamus of rats over a wide dynamic range. We demonstrate how the system can be used to decouple background firing levels from fluctuating levels of vibrissal sensory drive without corrupting the fine-scale temporal structure of whisker-evoked spike trains.

5.2 Methods

5.2.1 *In-vitro* methods

5.2.1.1 Viral transfections

Cell culture was performed as described in Chapter 2, Section 2.2.1. Concentrated aliquots of AAV2-CaMKIIKα-hChR2(H134R)-mCherry and AAV2-CaMKIIKα-eNpHR3.0-eYFP were produced by the University of Carolina Chapel Hill Vector Core. When cultures reached 1 to 5 days *in vitro* (DIV), viral aliquots were diluted to $1{\cdot}10^{12}$ c.f.u.$\cdot$ml^{-1} and 1 μL was added to 1 mL culturing medium. Infected cultures were incubated for 3 days with the viral solution before a the culturing medium was exchanged. The fluorescent signal of the mCherry reporter protein was monitored in 3 sister cultures over the days post infection using an LSM510 confocal microscope (Carl Zeiss AG, Oberkochen, Germany). Identical laser power and imaging settings were used for each imaging session. The fluorescent signal increased monotonically before plateauing at $\sim$3 weeks *in vitro* (Fig. 31(a,b)). Additionally, the functional reactivity of the cultures to 465 nm centered and 590 nm centered optical stimuli was probed in the weeks following infection (Fig. 31(c)). The ability of ChR2$_{\mathrm{R}}$ and eNpHR3.0 to affect network firing levels mirrored the expression time course of the marker proteins. All experiments were carried out on cultures that were 3 to 4 weeks old.

5.2.1.2 Multichannel electrophysiology

Microelectrode voltages were amplified and bandpass filtered between 1 Hz and 5 kHz using a 60 channel MEA60 analog amplifier (Multichannel Systems, Reutlingen, Germany). When stored in a 35 °C incubator, the temperature of the amplifier exceeded 37 °C. Therefore, the the culture was regulated to 35 °C using a servo-controlled (Modular One Technology, Parker, TX) solid state Peltier heater/cooler mounted below the recording amplifier (Fig. 33(a); Appendix C). Analog signals were digitized

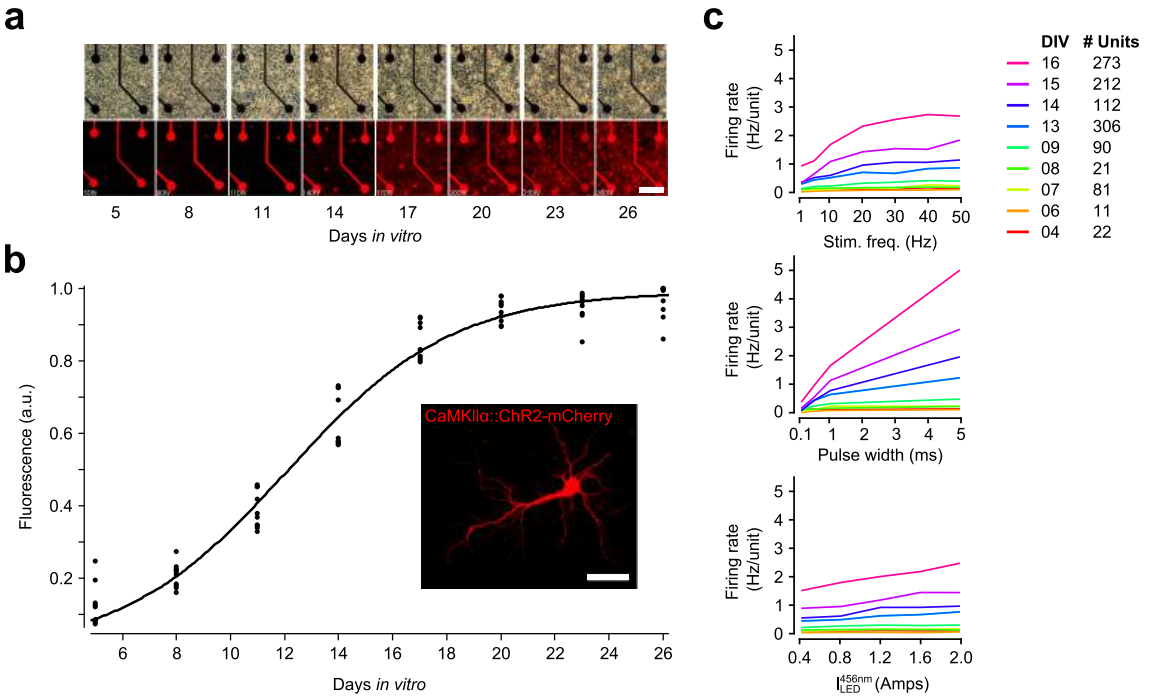

Figure 31: Expression time course of AAV2-CaMKIIα-ChR2(H134R)-mCherry. **(a)** Phase-contrast and confocal imaging of a single region of interest (ROI), containing 4 microelectrodes, performed over the first 26 days *in vitro* (DIV). Cultures were transduced at 1 DIV. **(b)** To quantify the expression time course, three or four ROIs were imaged in three cultures over the first 26 DIV. For each ROI and DIV, the integrated intensity of 600-690 nm light through the emission filter was calculated and then normalized by the maximal integrated intensity over the 26 day imaging period (black dots). A sigmoid of the form $\frac{a}{1+exp(bx+c)}$ was fit to the resulting data using nonlinear regression (r^2=0.98; MATLAB curve-fit toolbox). The half maximal expression point occurred at ~12 DIV. **(c)** The time-course of $ChR2_R$ function was measured by recording the evoked network spiking response in three networks over the first 16 DIV. Each experiment applied 140 trains of 30 second stimulation periods, each consisting of a random combination of pulse frequency (1, 5, 10, 20, 30, 40, and 50 Hz), pulse width (0.1, 0.5, 1.0, and 5.0 ms), and 465 nm LED intensity (0.2, 0.4, 0.6, 0.8, and 1.0 Amps). Stimulus bouts were separated by 30 seconds and were applied in random order. Colored lines show the average neuronal firing rate, across all three networks, at a set value for particular stimulation parameters. For example, the average network firing rate, $\langle f[t] \rangle$, for a stimulus frequency of 20 Hz is

$$\langle f[t] \rangle = \langle [\text{Firing Rate}(\text{Stim. Freq}, \text{Pulse Width}, \text{I}_{\text{LED}}) | \text{Stim. Freq} = 20\text{Hz}] \rangle$$

where $\langle \cdot \rangle$ indicates the average over time and units. The legend indicates the number of units used to produce each line for each DIV. The monotonicity of these functions across development (except for large values of pulse frequency) indicate the achievable evoked firing levels at different developmental points and the usefulness of each of the three stimulus parameters for constructing an effective control input.

and processed by the NeuroRighter multichannel electrophysiology platform (Rolston *et al.*, 2009a; Newman *et al.*, 2013). Amplified electrode voltages were digitally filtered using a 3rd order Butterworth filter with a passband of 300 to 5000 Hz. Extracellular action potentials were detected using a voltage threshold of 5 times the RMS noise on each electrode. A spike classifier was trained for each channel by collecting a set of spike waveforms, projecting them into their first two principal components, and fitting a mixture of K Gaussians to the resulting 2D sample distribution using expectation maximization. K was deduced automatically using a minimum description length cost function. Following training, spikes were then classified online with a maximal latency of $\sim$5 ms. The details of NeuroRighter's spike detection/sorting algorithms are presented in Appendix A.

5.2.1.3 Optical stimulator

To deliver optical stimuli, we used a custom N-channel enhancement mode MOSFET current source to drive a single blue LED (LZ4-00B200, LEDEngin, San Jose, CA) and 3 amber LEDs wired in series (LZ4-00A100, LEDEngin). LEDs were butt-coupled to a 4-to-1 randomized fiber bundle (Schott AG, Mainz, Germany), which then fed light into the Köhler illumination train mounted beneath the MEA amplifier (Fig. 32 and Fig. 33(a)). We confirmed the spatial homogeneity of of light at the culturing surface using a BC106-VIS CCD-based beam profiler (Thorlabs, Newton, NJ; Fig. 32(b)). The static current/irradiance relationship for each LED set used in our configuration is shown in Fig. 32(a). The rise time of pulses was $\sim$10 μs to source 500 mA to an LED. A full design specification is available online (https://potterlab.gatech.edu/main/newman/wiki).

5.2.1.4 Functional expression

To characterize the ability of ChR2_R to increase population activity, we scanned three parameters of ChR2_R excitation in open-loop: 0.1-5 ms pulse width, 1-40

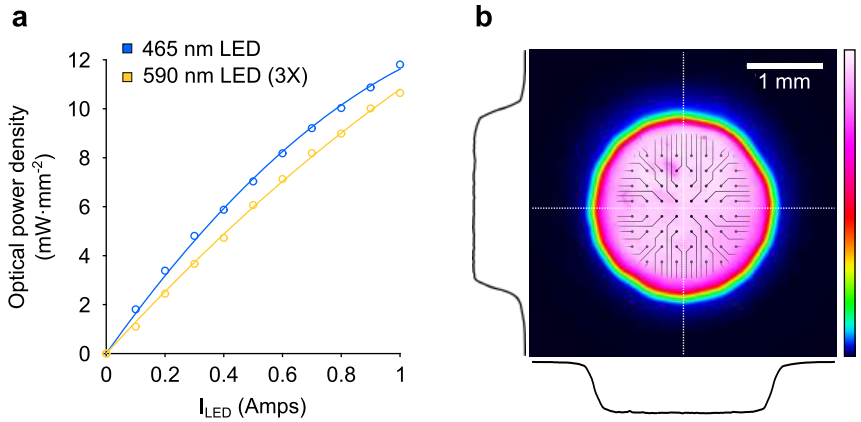

Figure 32: Optical characteristics of in-vitro stimulator. **(a)** Optical power density at the culture as a function of forward diode current for a single 465 nm LED and three 590 nm LEDs wired in series. **(b)** Colormap indicating the uniform spatial light intensity profile projected onto the MEA surface using a Köhler illuminator (Fig. 33), along with cross sectional intensity profiles through the horizontal and vertical center of the illuminated region (dotted white lines). The MEA image is superimposed on the profile to provide an indication of scale.

Hz stimulation frequency, and 0.1-1.5 Amps through a 465±11 nm FWHM LED, which corresponds to 1.6-13.4 mW·mm^{-2} at the culturing surface in our configuration (Fig. 32(a)). We found that all three parameters provided smooth, positive, monotonic relationship with the average population firing rate at any point approximately 1 week after viral transduction, and that the functional ability of ChR2$_{\mathrm{R}}$ co-varied with its expression time-course (Fig. 31(a)). Therefore, we used a single control variable, called U_{C}, to simultaneously modulate the pulse-width, stimulation frequency, and optical power of 465 nm stimulation (see stimulus definitions below).

To characterize the ability of eNpHR3.0 to decrease population firing, we delivered 30 second long stimulus pulses ranging from 0 to 1 Amp to three 590±10 nm FWHM LEDs wired in series, throughout development. These LED currents corresponded to ∼1.3-10.8 mW·mm−2 in our configuration (Fig. 32(a)). We observed a negative, monotonic relationship between the optical power of the LED and population firing throughout development. Therefore, we defined a control input U_{eNpHR} as the forward diode current of the 590 nm LED (Fig. 31(b); see stimulus definitions below).

5.2.1.5 Feedback controllers

Feedback controllers were implemented using the NeuroRighter plug-in interface, which grants on-the-fly access to NeuroRighter's data streams to user written plug-in code (Newman *et al.*, 2013) (Chapter 2). Every $dt = 10$ ms, the average network firing rate, $f[t]$ was calculated using action potentials produced by sorted units and passed through a first-order averaging filter

$$f[t] = \alpha r[t] + (1 - \alpha) f[t - dt] \tag{59}$$

where

$$\alpha = \frac{2}{\tau/(2 \cdot dt) + 1} \tag{60}$$

defines a $\tau = 2.5$ second time constant and $r[t] = \text{no. spikes/no. units}/dt$ is the instantaneous firing rate during the 10 ms bin, averaged across all detected units. The firing rate was then compared to a desired firing rate, f^*, and the error between the two

$$e_f[t] = f^* - f[t] \tag{61}$$

was used to generate stimulus signals using either a proportional integral (PI) or on-off control scheme. The PI controller was defined in a recursive form as

$$u[t] = u[t-1] + K\left(e_f[t] - e_f[t-1] + \frac{T_s}{T_i} e_f[t]\right) \tag{62}$$

where $K = 0.1$ is the proportional gain, $T_i = 1$ s is the integral time constant, and $T_s = 0.01$ s is the period of the control loop. $u[t]$ was then transformed into stimulus input signals according to

$$U_{\mathrm{C}} = u[t] + \Delta_1 \tag{63}$$

$$U_{\mathrm{H}} = -u[t] + \Delta_2. \tag{64}$$

$\Delta_{1,2} = 0.25$ determine the degree of overlap in ChR2_R (channelrhodopsin) and eNpHR3.0 (halorhodopsin) activation, respectively. U_C was transformed into pulses of blue light according to

$$\text{Pulse freq.}_{\,465\,\text{nm}} = 10U_\text{C} + 10\,(\text{Hz}) \tag{65}$$

$$\text{Pulse width}_{\,465\,\text{nm}} = 5U_\text{C}\,(\text{ms}) \tag{66}$$

$$\text{LED current}_{\,465\,\text{nm}} = 1.5U_\text{C}\,(\text{Amps}). \tag{67}$$

U_H was transformed into continuously modulated yellow light according to

$$\text{LED current}_{\,590\,\text{nm}} = U_\text{H}\,(\text{Amps}). \tag{68}$$

U_C and U_H were bounded between 0 and 1 to prevent integral windup and unreasonably high stimulation intensities. Twenty seconds prior to the start of each 60-second control epoch a 10-second train of $U_\text{C} = 1.0$ stimuli were applied, which we found increased control stability by preventing oscillations at the start of the control epoch (Fig. 37). This conditioning stimulus train is referred to as a 'pre-pulse' in Figs. 38 and 37.

The on-off controller was defined for the blue LED as

$$I_f[t] = \sum_{k=0}^{t} e_f[k] \tag{69}$$

$$\text{Stim}[t] = \begin{cases} \text{Apply 5 ms pulse} & \text{if } I_f[t] > 0 \\ \text{Off} & \text{Otherwise} \end{cases} \tag{70}$$

1.5 A was delivered to the LED during each pulse and a maximal stimulation frequency of 10 Hz was enforced.

5.2.2 *In-vivo* methods

5.2.2.1 Experimental preparation

All procedures were approved by the Georgia Institute of Technology Institutional Animal Care and Use Committee and followed guidelines established by the National Institutes of Health. Female sprague-dawley rats (250-300g) underwent an initial survival surgery, during which the viral vector (AAV2-CaMKIIa-hChR2(H134R)-mCherry, UNC Viral Vector Core, Chapel Hill, NC) was delivered to the left thalamus using stereotactic coordinates: 2-4 mm posterior to bregma, 2.5-3.5 mm lateral to midline, 4.5-5.5 mm below cortical surface. The injection was delivered at 0.2uL/min for 5min for a total of 1uL. The animals were allowed to recover for 3-4 weeks, providing time for the $ChR2_R$ expression to reach functional levels.

In a second acute surgery, the rodents were initially anesthetized with 4% isoflurane before intraperitoneal injection of sodium pentobarbital (50mg/kg weight) for long term anesthesia. Following the initial bolus, sodium pentobarbital was administered intravenously through the tail vein. Throughout the experiment, measurements of the heart rate, respiratory rate, and response to toe pinch stimuli were used to monitor and titrate the depth of anesthesia, and the body temperature was maintained at 37C by a servo-controlled heating blanket (FHC, Bowdoinham, ME). Animals were mounted in a stereotactic frame and a craniotomy was performed over the left parietal cortex to allow access to the ventral postero-medial (VPm) region of the thalamus (coordinates: 2-4 mm posterior to bregma, 2.5-3.5 mm lateral to midline, 4.5-5.5 mm below cortical surface).

5.2.2.2 Electrophysiology

The 'optrode' consisted of a multimode optical fiber (105um core diameter, 125um coating diameter, 0.22 NA, Thorlabs, Newton, NJ) and two quartz coated platinum-tungsten microelectrodes (80um diameter, Thomas Recording, Giessen, Germany).

The microelectrodes were pulled and ground to an impedance of 1-2 MΩ at 1kHz. The optical fiber was also ground to a fine point, producing a spherical, rather than conical, pattern of light delivery. The optrode was advanced to the ventral posteriomedial (VPm) region of the thalamus using a precision microdrive (Knopf Instruments, Tujunga, CA). Single and multi-unit activity were band-pass filtered between 300 and 5000 Hz and digitzed at 24.414 kHz using an RZ2 multi-channel bioacquisition system (Tucker Davis Technologies, Alachua, FL). The principal vibrissa was determined by manually deflecting individual whiskers and observing the multi-unit activity.

5.2.2.3 Whisker stimulation

Whiskers were trimmed at approximately 12 mm from the face, and were inserted into a glass pipette fixed to the end of a calibrated multi-layered piezoelectric bimorph bending actuator (range of motion, 1 mm; bandwidth, 200 Hz; Physik Instrumente (PI), Auburn, MA) positioned 10 mm from the vibrissa pad. Vibrissae were always deflected in the rostral-caudal plane. Punctate deflections consisted of exponential rising and falling phases (99% rise time, 5 ms; 99% fall time, 5 ms), with angular deflection velocities of 133, 262, or 522 deg·s^{-1}.

5.2.2.4 Closed-loop optical stimulation

A model LRS-0473-PFM diode-pumped solid-state laser (Laserglow Technologies, Toronto, Canada) was used to deliver blue (473 nm) light to the VPm thalamus and stimulate the ChR2$_{\mathrm{R}}$-expressing cells. The laser allows analog modulation up to 10 kHz for the delivery of a continuously varying light intensity as determined by the closed-loop the controller. The controller was implemented on the Tucker-Davis RZ2's digital signal processors using the RPvdsEx graphical programming language. The PI control loop was equivalent to Eqs. (59)-(62) with the exception that $\tau = 5$

s. The PI control output, $u[t]$, was converted into a 0-10 volt laser control signal

$$U_{\text{Laser}} = 10u[t] \tag{71}$$

which was monotonically, but nonlinearly, related to the continuous-wave laser power (Fig. 43). The maximum light power density delivered during the experiments was $\sim$150 mW$\cdot$mm^{-2}, but typically only 1-10 mW$\cdot$mm^{-2} was needed to drive neural activity in ChR2$_{\text{R}}$ expressing neurons (Fig. 43).

5.3 Results

5.3.1 Development of a closed-loop, *in-vitro* optical stimulation system

Effective feedback control of spiking activity requires the ability to both sense and modulate neuronal firing levels. The first of these requirements is fulfilled using extracellular electrophysiological methods both *in vitro* and *in vivo*. To address the second requirement, optogenetic methods offer a powerful means to activate and suppress neuronal firing (Boyden *et al.*, 2005; Han and Boyden, 2007). Previous studies have described stimulation patterns, expression systems, and opsin types for evoking or silencing activity in neurons (Mattis *et al.*, 2011; Zhang *et al.*, 2011; Yizhar *et al.*, 2011a; Chow *et al.*, 2010). However, these studies have focused on the ability of microbial opsins to precisely elicit or cancel spikes rather than their ability to smoothly modulate firing levels.

To characterize the range of evoked firing levels that could be reliably achieved using multimodal optical stimulation, we developed a system to sense and optically modulate network activity in dissociated cortical networks, in real-time (Fig. 33(a)). The open-access NeuroRighter electrophysiology platform was used to record and process electrical activity from a 59-channel, substrate-embedded microelectrode array (MEA) (Newman *et al.*, 2013). To stimulate the networks, NeuroRighter drove a multicolor LED bank that was concentrated onto the cell layer using a custom Köhler illuminator (Fig. 32). Channelrhodopsin-2(H134R) (ChR2$_{\text{R}}$) (Nagel *et al.*, 2005) and

halorhdopsin-3.0 (eNpHR3.0) (Gradinaru *et al.*, 2008) were expressed in excitatory cells using a CaMKIIα promoter (Section 5.2). We used confocal microscopy to monitor expression of marker protein levels throughout development (Fig. 31(a-b)).

To characterize the functional expression of ChR2_R, we performed stimulus parameter sweeps throughout development using a blue LED (465±11 nm FWHM; Fig. 31(c)). We found that increases in stimulus frequency, pulse-width, and LED current could be used to increase evoked activity levels(Fig. 31(b)). Therefore we defined a ChR2_R stimulation variable, U_C, that simultaneously modulated all three parameters of pulsed blue light (Section 5.2). A second control variable used to activate eNpHR3.0, U_H, was defined as the current supplied to the amber LED (590±10 nm FWHM) during continuous operation. To characterize these control signals, 50 random values of U_C and U_H were applied to two networks for randomly interleaved, 60-second stimulus epochs. Evoked population firing rates were positively correlated with U_C and negatively correlated U_H (Fig. 33(b)). The efficacies of U_H and U_C for increasing or decreasing firing levels saturated near their half-maximal values ($U_\text{H} = 0.60$ to $U_\text{C} = 0.54$ corresponding to 0.03 to 13.51 Hz/unit, respectively). The monotonic relationship between U_C and U_H compared to network firing levels indicated their applicability to closed-loop control.

To test the robustness of U_C and U_H during altered network excitability, we repeated the 60-second stimulation protocols in the presence of 20 μM 6-cyano-7-nitroquinoxaline-2,3-dione (CNQX), 50 μM (2R)-amino-5-phosphonovaleric acid (AP5), or 20 μM bicuculline. These drugs blocked AMPAergic, NMDAergic, and GABAergic neurotransmission, respectively. CNQX and AP5 both caused marked reductions in spontaneous firing levels (-74.2% and -66.6%, respectively). Bicuculine increased network activity compared to the pre-drug condition by 357%. Each drug affected signal propagation within the networks as evidenced by systematic changes in the peri-stimulus time histogram (probe stimulus: 10 Hz, 1 ms pulse width, 5

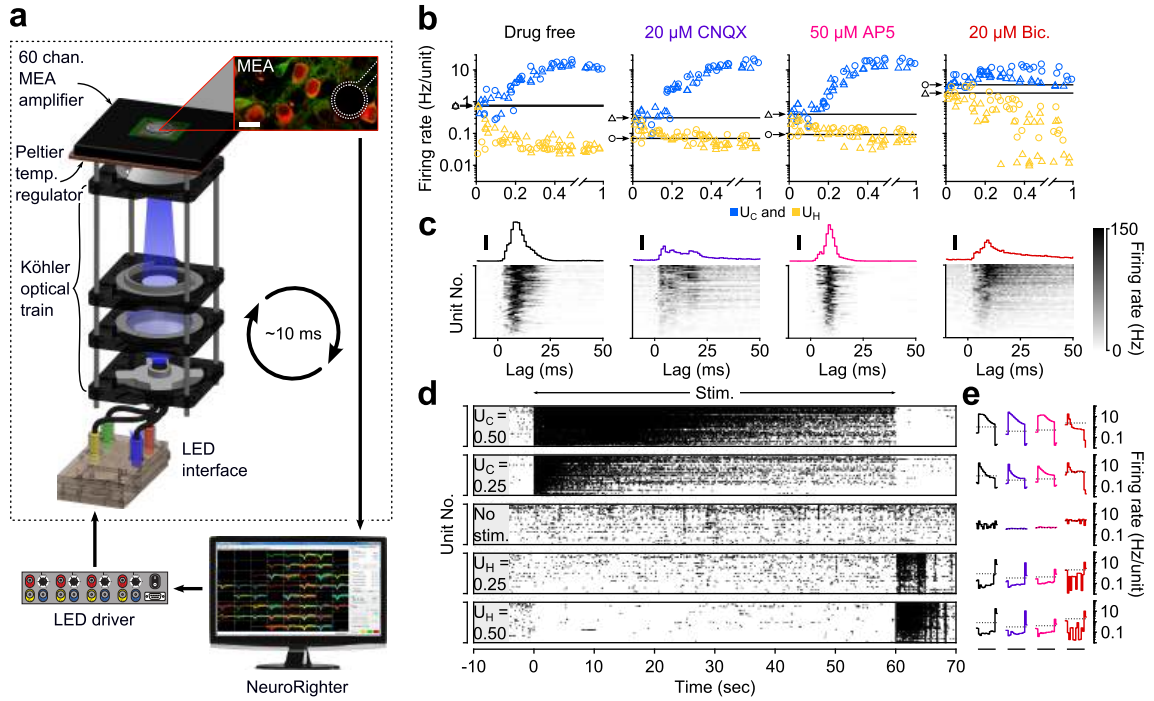

Figure 33: Optogenetic modulation of network activity *in vitro*. **(a)** Multichannel recording, processing, and stimulation system. A 60-channel amplifier detects extracellular electrical activity produced by cells close to electrodes (white outline). Neurons express $ChR2_R$-mCherry (red) and eNpHR3.0 under the CaMKIIα promoter (green: immunoreactivity for CaMKIIα; scalebar: 20 μm). Electrode voltages are processed in real-time and can be used to update an LED stimulator feeding a Köhler illuminator below the MEA. The dotted box indicates the boundary of the culturing incubator. **(b)** Time-averaged firing rates of two cultures ($\triangle$ and $\bigcirc$) in response to 60 second applications of randomly valued U_C and U_H during different forms of synaptic blockade. Black horizontal bars indicate the spontaneous firing level of each culture and blue and yellow symbols indicate the mean firing level at the corresponding value of U_C and U_H, respectively. **(c)** PSTH of individual units (grey scale) and the unit-averaged PTSH in response to 1 millisecond 5 mW·mm^{-2} blue light pulses for each drug condition. Scale bars, 50 Hz/unit. **(d)** Raster plots for 87 detected units during 60 second applications of U_C and U_H. The firing rate evoked by stimulation using a particular value of U_C and U_H decays over the course of the protocol. **(e)** The trial-averaged firing rate profiles for the stimulus levels presented in (d) across drug conditions. Black horizontal lines indicate the 60 second stimulation period. Colors correspond to the drug conditions above each panel in (b). Dotted lines indicate spontaneous firing levels. Note the log scale.

$mW{\cdot}mm^{-2}$; 200 stimuli per histogram; Fig. 33(c)). In spite of changes in network excitability, for CNQX- and AP5-treated networks the dynamic range of the control signal was similar to the pre-drug condition (0.04 to 13.97 Hz/unit for CNQX, and 0.07 to 13.37 Hz/unit for AP5; Fig. 33(b)). Bicuculline greatly reduced the dynamic range of evoked network activity indicating a loss of reliable open-loop activity modulation (0.01 to 6.66 Hz/unit; Fig. 33(b)).

Although time-averaged firing levels were positively correlated with U_{C} and negatively correlated with U_{H} (Fig. 33(b)), stimuli lost effectiveness throughout each 60-second trial (Fig. 33(d,e)). This effect was consistent across drug conditions and matches previous characterizations of multiunit activity during extended periods of optical stimulation *in vivo* (Anikeeva *et al.*, 2012). The decreasing efficacy of network activation using $\mathrm{ChR2_R}$ is likely due to network adaptation, rather than changes in $\mathrm{ChR2_R}$-mediated photocurrents (Mattis *et al.*, 2011) (Chapter 3). The deceasing efficacy of firing suppression using eNpHR3.0 is likely due to increases in network excitability from intracellular $\mathrm{Cl^-}$ accumulation (Raimondo *et al.*, 2012) and decreases in outward photocurrents due to pump desensitization during prolonged light application (Mattis *et al.*, 2011). In both cases, activity adaptation to optical stimuli is difficult to predict and compensate for *a-priori*. We therefore hypothesized that feedback control could be used to adjust stimuli in real-time to compensate for fluctuations in neuronal excitability, network activity, and opsin dynamics.

5.3.2 Proportional-integral control of network firing

To demonstrate the basic functionality of optogenetic feedback control, we devised a simple proportional-integral (PI) controller to hold network activity in dissociated cortical networks at various target levels. The PI algorithm updated U_{C} and U_{H} in real-time in order to minimize the difference between the measured network firing rate and a target level (Section 5.2). For each network tested, we presented the controller

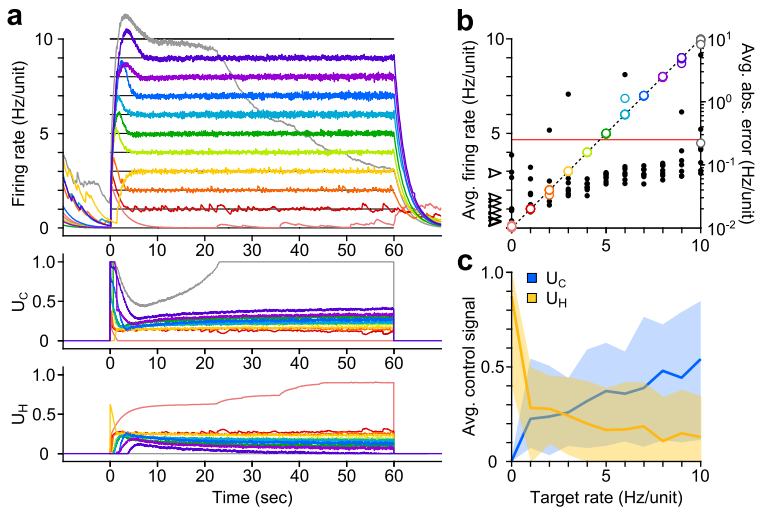

Figure 34: PI optical feedback allows precise control of network firing levels over one-minute epochs. **(a)** (top) Network firing rate during different trials (colors). Target firing levels (black lines) ranged from 0 to 10 Hz and were applied in random order. (bottom) Control signals, U_{C} and U_{H}, required during closed-loop control. For this network, the controller saturated while attempting to clamp network firing at 10 Hz/unit, resulting in a control failure (grey trace). **(b)** (Left axis, colors): Time-averaged firing rates for seven different networks during PI control . The dotted line is identity. The spontaneous firing rates of each network are indicated by black arrows. (Right axis, black markers): Mean absolute error between the measured and target firing for each network as a function of the target rate. Control failure occurred for each point that lay above the red line (average absolute error $>$ 0.25 Hz/unit). **(c)** Time- and culture-averaged control signals versus target firing rates. The shaded areas indicate the minimum and maximum value across networks. All temporal averages in this figure were taken over the final 30 seconds of the control epoch.

with one-minute long, randomly ordered target rates from 0-10 Hz/unit (Fig. 34(a)). Twenty seconds prior to the start of each control epoch, a 10 second train of 1 Hz, 5 ms pulse width, full optical power ($\sim$13 mW$\cdot$mm^{-2}; Fig. 32) conditioning stimuli were applied using the blue LED (Referred to as 'pre-pulse in Figs. 37 and 38; Section 5.2).

We quantified the accuracy of firing rate control by calculating the mean absolute error between the target and measured firing level for each target rate (Fig. 34(b)). A trial was considered successful if the average absolute tracking error over the final 30 seconds of the control epoch was less than 0.25 Hz/unit (red bar in Fig. 34(b)). Successful tracking was achieved in the majority of trials (7 cultures, 71/77 trials). The tracking error tended to increase with target rate, and occasionally the stimulator saturated at its maximal intensity before the trial was complete (e.g., the 10 Hz/unit target in Fig. 34(a)). The settling time of the measured firing rate at the target

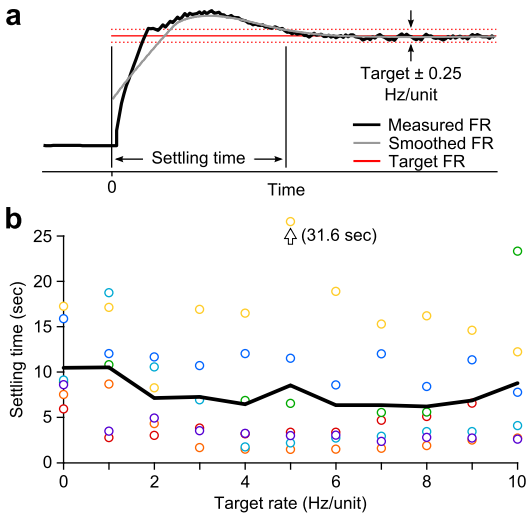

Figure 35: PI settling time. **(a)** The settling time was defined as the time-point at which the smoothed firing rate (grey line; LOWESS with a 2.5 second smoothing window and a tri-cube weight function) entered and stayed within the the boundaries defined by the target rate $\pm$ 0.25 Hz/unit (dotted red lines). **(b)** The settling time did not show a strong relationship with the target firing rate and was highly variable across cultures (7 cultures, colors).

value varied across preparations and was not correlated with the target rate (mean 7.83$\pm$1.74 sec; Fig. 35).

The amplitudes of the control signals required during successful control trials were highly variable across networks, even for the same target rate (Fig. 34(c); Fig. 45). This variability reflects heterogeneous network characteristics such as varying levels of intrinsic excitability, opsin expression efficiency, synaptic connectivity, glial subnetwork activity levels, and developmental processes (Wagenaar *et al.*, 2006c). The large variability of control signals required to achieve similar target rates underscores the importance of feedback to achieve precise control of network activity across preparations. Additionally, it indicates that open-loop stimulation with fixed parameters would not be capable of eliciting repeatable firing levels across networks.

Because a wide dynamic range in evoked network activity levels could be maintained during glutamatergic synaptic blockade (Fig. 33(a)), we hypothesized that closed-loop control in a pharmacologically altered network would be possible as well. To test this, we used the PI controller to clamp network firing levels to targets between

0 and 10 Hz/unit in the presence of 20 μM CNQX or 50 μM AP5 (Fig. 36(a)). For both drugs, controller performance was equivalent to the drug-free case and control failure was isolated to high target rates (9-10 Hz/unit) when the stimulator saturated (Fig. 36(b-e)). We also tested closed-loop control in the presence of 20 μM bicuculline but found that reliable PI control was not possible (Fig. 36). This is likely due to the strongly destabilizing effects of bicuculline on intrinsic network dynamics which overpower optical input and cause the controller to oscillate (Fig. 37).

To demonstrate control robustness over extended trial periods, the PI controller was used to track a set of randomly selected, 5-minute long target firing levels which switched without downtime (Fig. 38). Only a single pre-pulse train was applied (Fig. 38(c)). During each 5-minute segment at a particular target value, rapid changes in the control signal made second-to-second adjustments, while slower changes occurred over minutes. These longer time scale changes in the control signal were especially prevalent for target rates far above spontaneous firing levels (Fig. 38(c)). This likely reflects short-term synaptic depression and changes in cellular excitability that accrue over each 5-minute control epoch.

Using open-loop stimulation, non-stationary opsin and network dynamics would limit the precision of optical stimulation for controlling neuronal firing levels across trials and preparations. By using real-time feedback to automatically compensate for second-to-second changes in stimulus efficacy, we were able to control population spiking activity over a wide dynamic range.

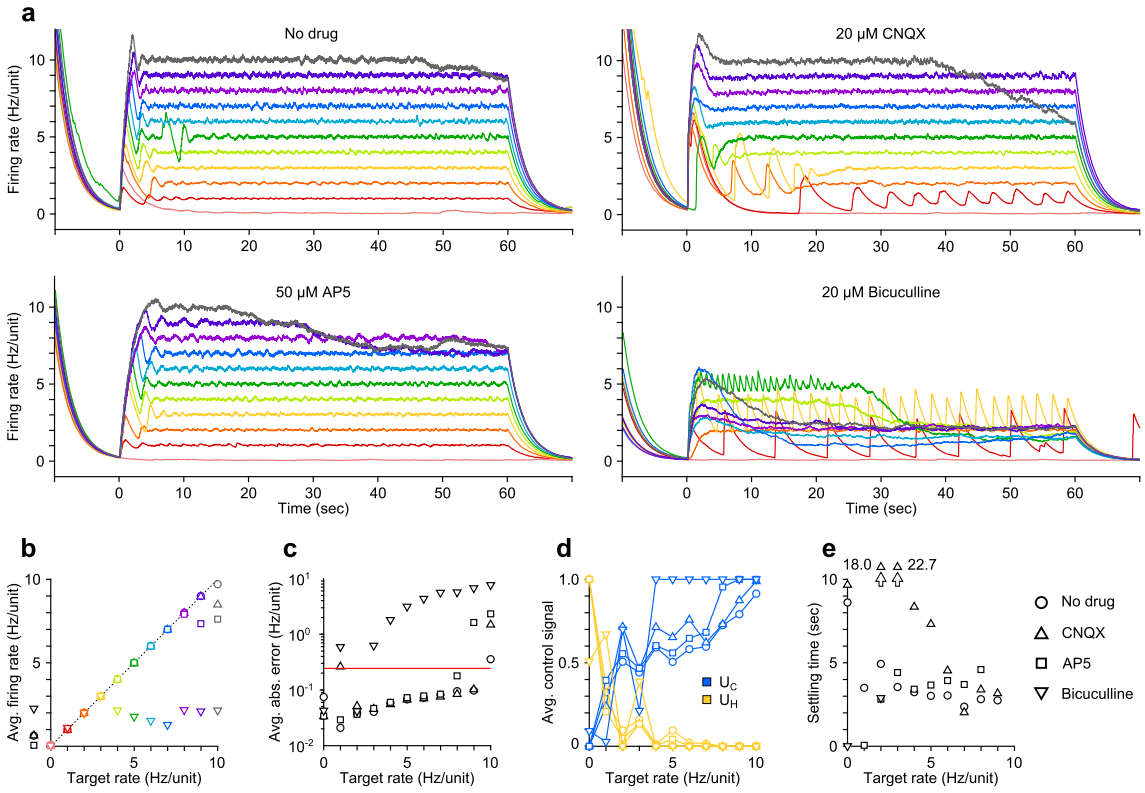

Figure 36: PI control of firing levels during synaptic blockade. **(a)** Network firing rate for different trials (colors) in the presence of various competitive neurotransmitter receptor antagonists (○ no drug, △ 20 μM CNQX, □ 50 μM AP5, ▽ 20 μM bicuculline). Trials were presented in a random sequence that was repeated across drug conditions. **(b)** Time-averaged network firing rates during PI control, for each drug tested. Spontaneous firing rates of the network during each pharmacological condition are represented by black symbols to the left of the ordinate axis. **(c)** Mean absolute error between the measured and target firing for each pharmacological condition as a function of the target rate. Control failure occurred for each point above the red line (average absolute error $>$ 0.25 Hz/unit). CNQX destabilized the network somewhat, likely though the removal of recurrent inhibition, and resulted in a control failure for the 2 Hz/unit target. AP5 reduced the dynamic range of evoked activity and slowed the rise time of the population response, which is apparent during control onset in (a). Bicuculline strongly destabilized network activity and resulted in control failure for all but two target rates: 0 and 2 Hz/unit. In the presence of bicuculline, average network firing levels could not be pushed higher than $\sim$2 Hz/unit. Interestingly, the only successful non-zero target rate was the one closest to the spontaneous network firing rate in the presence of bicuculline. **(d)** Time-averaged control signals and **(e)** settling times (Fig. 35) versus target rate for each pharmacological condition. All temporal averages in this figure were taken over the final 30 seconds of the control epoch.

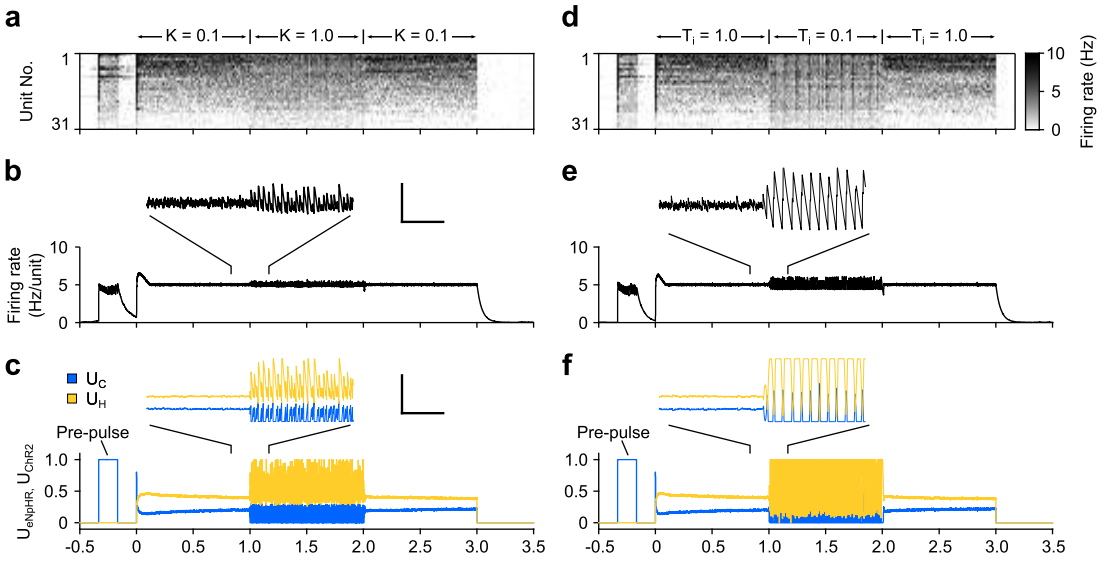

Figure 37: Parameter choice during closed-loop stimulation affects closed-loop stability. **(a)** Firing rate histogram for individual units, encoded by the grey scale the right. The PI controller was engaged at time zero using $K = 0.1$ and $T_i = 1.0$ s. After 1 minute, the proportional gain was increased to 1.0. At 2 minutes, it was reset to 0.1. **(b)** Average firing rate of the network during the clamp. The floating trace shows a zoomed portion of the firing rate during the transition in proportional gain. An increase in oscillations around the set-point occurs as a result. Vertical and horizontal scale bars represent 1 Hz/unit and 2 s, respectively. **(c)** Control signals designated by the PI controller. The pre-pulse can be seen before the closed loop system is engaged (Section 5.2). Following the increase in proportional gain, oscillations around the target rate are amplified indicating a decrease in closed-loop stability. The floating trace shows a zoomed portion of the control signals during transition in proportional gain. Vertical and horizontal scale bars represent $U_{\mathrm{C,H}} = 0.5$ and 2 s, respectively. **(d-f)** Same as (a-c) except that the integral time constant, T_i, was changed instead of the proportional gain.

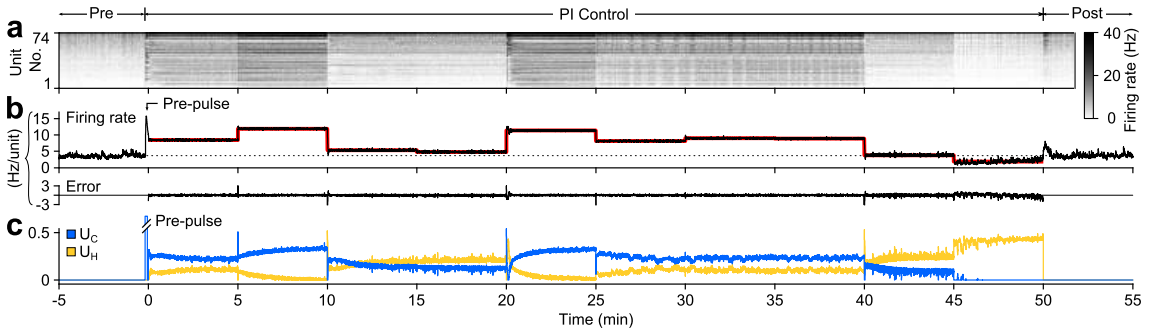

Figure 38: PI feedback control to track a changing target rate **(a)** Firing rate of detected units. Each row displays the firing rate of a particular unit, encoded by the grey-scale to the right (1 second bins). **(b)** The average firing rate of the network (black) and the target firing rate (red) and the error signal during different control periods. The pre-control firing rate is indicated by a dotted line. **(c)** Optical control signals delivered by the PI controller during the control epoch.

5.3.3 Long-term on-off control of average firing rates

In-vitro preparations offer stable electrophysiological access over long time periods. To exploit this experimental stability, we developed a second controller to clamp average network firing at elevated levels for many hours. This controller consisted of a simple on-off algorithm: when the integral error between the target firing rate and the measured firing rate crossed zero, the controller applied a 5 millisecond blue light pulse (Section 5.2).

We tested the functionality of on-off control over 12-hour epochs for target rates of 0.75, 1, 2, 3, 4, 5, and, 6 Hz/unit in a single culture (Fig. 39). Each 12-hour control period was flanked by recordings of spontaneous firing activity to identify potential persistent effects of long-term firing rate elevation. The on-off controller was capable of clamping target rates up to 5 Hz/unit for the duration of the 12 hour protocol but failed at the 6 Hz/unit target at $\sim$7 hours (Fig. 39(a-b)).

Due to their long duration, these experiments took place over the course of approximately 3 weeks, during which spontaneous network activity levels displayed considerable variations ($\sim$0.7-2.5 Hz/unit; Fig. 40(a)). Because of this, the difference between spontaneous firing levels and the target firing rate was not solely dependent on the target firing level. We found that the mean stimulation level required during each control epoch was better correlated to the difference between the target rate and spontaneous firing levels prior to closed loop control than to the target level alone (Fig. 40(b)). This indicates that the long-term changes in network excitability are reflected in the control signals (Fig. 39(c,d); Fig. 40(a)) and demonstrates that closed-loop optical stimulation can be used to study developmental changes in excitability that occur over the course of weeks. Interestingly, prolonged increases in network firing did not induce a homeostatic decrease in network firing during the post-control period (Fig. 40(c)).

The on-off and PI control schemes have unique advantages and disadvantages that

make them applicable to different experimental contexts. While the on-off controller provides long-term stability, the periodic stimuli used by the PI controller provide a relatively long minimal update time for the control loop (Section 5.3.2). Therefore, the PI controller is better suited to provide rapid response times. However, the periodic stimuli delivered by the PI controller are imposed on spiking correlations between units, resulting in a highly periodic firing structure (Fig. 39(e)). This contrasts the aperiodic, synchronized bouts of firing that are a common feature of developing neural circuits including those in the retina, hippocampus, spinal-cord, and dissociated cortical cultures (Wagenaar *et al.*, 2006c; O'Donovan *et al.*, 1998; Feller, 1999). The on-off controller was better able to preserve spontaneous activity correlations for low stimulation frequencies (Fig. 39(e)). For target rates that required higher stimulation rates, a periodic correlation structure reemerged.

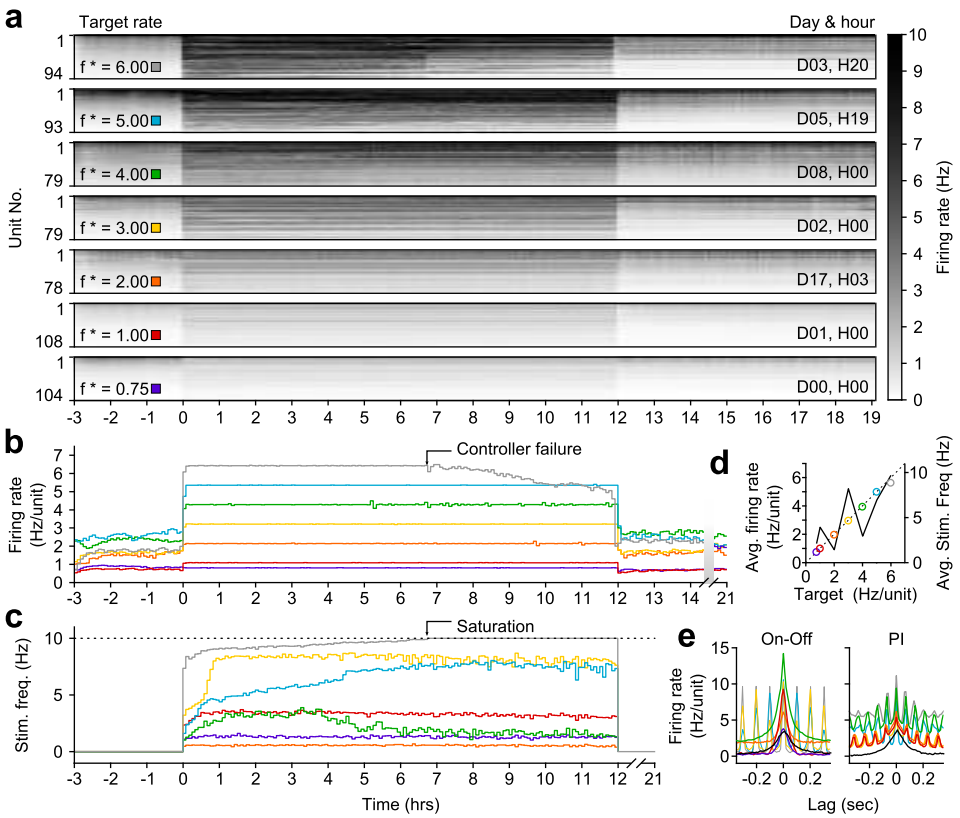

Figure 39: On-off feedback control of population firing rate over 12-hour epochs. (a) Firing rates of detected units during 12-hour control periods are represented using the grey-scale to the right. At time 0, the on-off controller was engaged and the average network rate was clamped firing to the target rate indicated to the left of each chart. The day and hour of each protocol, relative to the first experiment, is shown to the right. Units are sorted by their mean firing rate during the 3-hour period prior to closed-loop control. (b) The network firing rate during each control epoch (5 minute bins). The color map corresponds to the target rates shown in (a). (c) Closed-loop stimulation frequency over the course of the 12-hour clamp. For a target rate of 6 Hz/unit, the controller saturated at the maximal frequency of 10 Hz at around 7 hours into the control epoch, and target tracking failed as a result. (d) Time- and unit-averaged firing rates (colors, left axis) and control signal (black, right axis) across each 12-hour clamping period. The dotted line is identity. (e) The average cross-correlation function between 30 randomly selected units during on-off or PI control are plotted for each target rate. The correlation function for spontaneous activity is shown in black. When low stimulation frequencies were required, the unimodal correlation structure of spontaneous activity was preserved using on-off control. All data presented in this figure were obtained from a single culture over the course of 2 weeks.

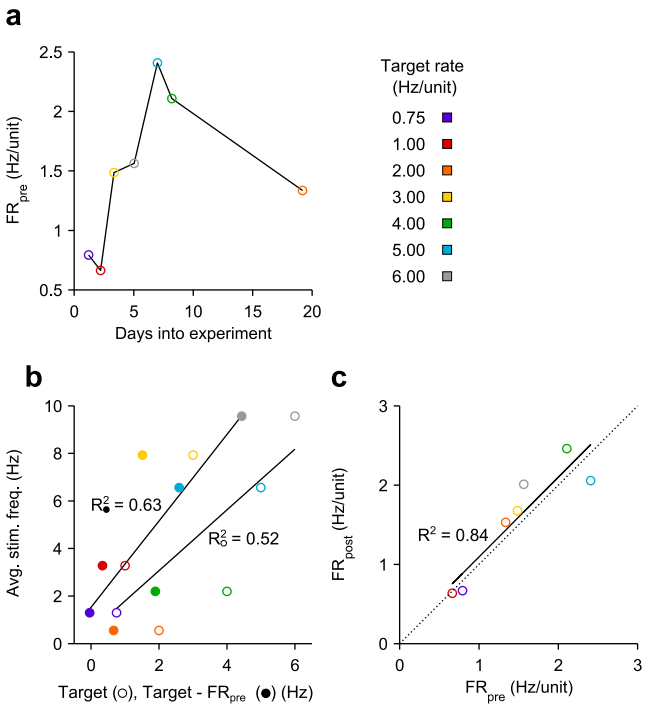

Figure 40: Characteristics of on-off control over weeks *in vitro*. **(a)** Spontaneous, pre-stimulation firing rates over the course of experiments. Spontaneous excitability changes smoothly across the ∼20 days during which 12-hour firing rate control experiments were conducted. **(b)** The average stimulation frequency required to achieve firing rate control is plotted against the target rate (○) and the the difference between the target rate the pre-stimulation spontaneous firing level (●). The linear fit is improved when the spontaneous excitability is taken into account, indicating that network excitability reliably influences the intensity of stimulation required to achieve firing rate control. **(c)** The spontaneous firing rate before each 12-hour protocol versus the spontaneous firing rate following each protocol exhibits a strong linear relationship (black line) that is insignificantly different from identity (dashed line). This indicates the absence of a homeostatic decrease in network activity as a result of chronically elevated firing levels in the absence of pharmacological agents.

5.3.4 Decoupling network spiking activity and glutamatergic neurotransmission, *in vitro*

To demonstrate the scientific utility of optogenetic feedback control, we first used it to decouple neuronal activity states from pharamacological activity perturbations *in vitro*, and then to lock firing during sensory input perturbations *in vivo*. These experiments were carried out in collaboration with Ming-fai Fong. Many *in-vitro* studies have used chronic application of glutamatergic neurotransmission blockers or sodium channel blockers to reduce network activity levels, and induce homeostatic increases in network excitability (Turrigiano *et al.*, 1998). Because both types of pharamcological perturbation suppress firing, it has been difficult to parse the individual roles of neurotransmission and spiking for triggering homeostatic up-regulation of synaptic strength.

To address this, we treated networks with glutamatergic receptor antagonists (CNQX or AP5) while using the on-off controller to clamp network activity at pre-drug levels over 24-hour periods (Section 5.2). Bath application of 20 μM CNQX caused a marked reduction in network spiking activity compared to the pre-drug period (two cultures, -89.5 and -66.1%). Using on-off control, spiking activity was returned to the pre-drug levels for the duration of the 24-hour stimulation period in both cultures (mean stimulation frequency 0.72 and 0.19 Hz ;Fig 41(a-d)). Following closed-loop stimulation, but while CNQX was still in the bath, network firing levels again dropped compared to the pre-drug condition (-59.7 and -79.6 %), indicating that the drug had not been metabolized over the 24 hour stimulation period. Following washes with culturing medium, the firing rate was elevated compared to pre-drug firing levels (+186.4 and +121.1%, evaluated over 6 hours following drug removal). Fig. 41(e) summarizes the relative spiking activity levels during each of the five epochs of the experiment for the two cultures tested.

Like CNQX, bath application of 50 μM AP5 caused strong suppression of network

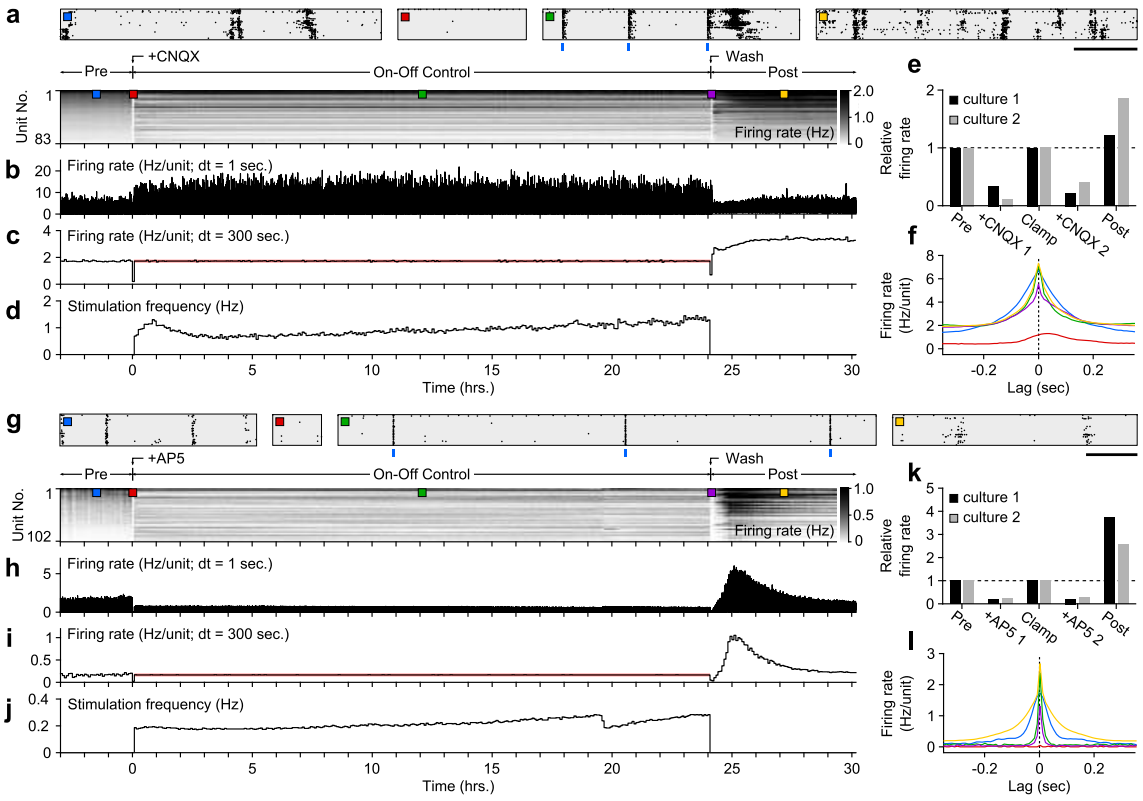

Figure 41: Decoupling spiking and neurotransmission using on-off feedback control. (a) Summary of unit spiking activity over the course of the protocol. Rastergrams (top) show zoomed portions of spiking activity taken from discrete epochs during the experiment. Blue bars indicate stimulus times. Horizontal scale bar, 1 s. (bottom) Firing rate histogram for the duration of the 33-hour recording for each unit, using 5-minute bins. Firing levels are indicated by the grey-scale to the right. CNQX was added at time 0 and removed 24 hours and 10 minutes later. Closed loop stimulation began 5 minutes after CNQX addition and lasted 24 hours. Colored boxes indicate the location of the zoomed rastergrams. (b) The average unit firing rate using 1-second bins and (c) 5-minute bins. The red line indicates the target rate. (d) Closed-loop stimulation frequency. (e) Time- and unit-averaged firing rates for each epoch, normalized to the pre-drug firing level. (f) The average unit-unit cross-correlation function for each epoch (50 units). (g-k) Same as (a-f) but using AP5 to perturb network activity instead of CNQX.

activity compared to pre-drug firing levels (two cultures, -87.4 and -85.7 %). On-off control was able to clamp firing to pre-drug levels for the duration of the 24-period (mean stimulation frequency 0.21 and 0.71 Hz). Following closed-loop stimulation, but while AP5 was still in the bath, the firing rates dropped suggesting the maintained efficacy of AP5 (-73.5 and -80.4 %). Following medium exchanges to remove AP5 from the bath, the firing levels in each network were dramatically elevated compared to pre-drug levels (+257 and +373 %).

On-off control reliably compensated for the effects of CNQX or AP5 on network activity. The average closed-loop stimulation effort required to compensate for both forms of glutamatergic blockade were low compared to those required to maintain chronic elevations in network activity (Fig. 39(d)). For on-off control in the presence of CNQX, pre-drug network activity correlations were largely maintained during the control period (Fig. 41(f)). For AP5 treated networks, network activity correlations maintained a unimodal shape during the control epoch, but dropped off more quickly for longer temporal lags. This is likely due to NMDA's role in signal propagation in dissociated cortical networks (Nakanishi and Kukita, 1998). Perhaps most interestingly, both drugs caused marked increases in network activity levels after they were removed even though average firing levels were clamped to pre-drug levels during drug treatment. This suggests that chronic reductions in glutamatergic transmission directly increase network excitability (Chapter 6).

5.3.5 Control of single unit activity during fluctuating sensory drive, *in vivo*

In collaboration with Daniel Millard and Garrett Stanley, we next evaluated the functionality of optogenetic feedback control in the intact rodent brain. The rat vibrissal pathway is a widely studied model of sensory information transduction due to its well defined feed-forward anatomy. Classically, sensory perturbations are applied to the vibrissae of anesthetized rats or mice while spiking patterns are recorded downstream,

in thalamus or cortex. Drugs commonly used for anesthesia have profound effects on evoked and background firing (Simons *et al.*, 1992), receptive field properties (Friedberg *et al.*, 1999), and subthreshold voltage statistics (Constantinople and Bruno, 2011) in the vibrissal pathway, which likely influences its encoding properties.

We used optogenetic feedback to control background firing in single units of the thalamic ventral posteromedial nucleus (VPm) in anesthetized rats during vibrissa stimuli. An optrode consisting of a 125 μm diameter fiber-optic bonded to a tungsten microelectrode was used to perform single-unit, extracellular recordings of thalamocortical unit (TCUs). Spiking sequences were used to estimate a firing rate, which was fed into a PI controller in order to update the continuous-wave power of a 473 nm diode-pumped solid-state (DPSS) laser coupled to the fiber-optic (Fig. 42(a); Section 5.2).

We used the controller to clamp firing rates in TCUs at increasing target levels for 30-second epochs until control failure (Fig. 42(b)). In all cases, we were able to clamp TCU firing at target rates higher than the cell's spontaneous firing levels (3 TCUs). The range of achievable target firing rates was variable across cells (e.g 1-8 Hz vs. 1-30 Hz; Fig. 42(c)). The nonlinear input/output relationship of our DPSS laser meant that the effective range of optical intensities resided in a narrow band of the full scale control input accepted by the laser (Fig. 43). Additionally, the nonlinear relationship between the target firing level and the average optical power indicates that small changes in light intensity map to a wide range of evoked firing levels (Fig. 42(d)). Both of these observations suggest that open-loop calibration of laser power to achieve a specific target level would be very difficult.

In the awake animal, spontaneous and evoked sensory thalamic spike trains tend to be highly irregular (Poggio and Viernstein, 1964). We examined spike train irregularity across target rates by calculating the coefficient of variation of the ISI distribution (CV_{ISI}) for each TCU. Across target rates, we found a CV_{ISI} close to 1,

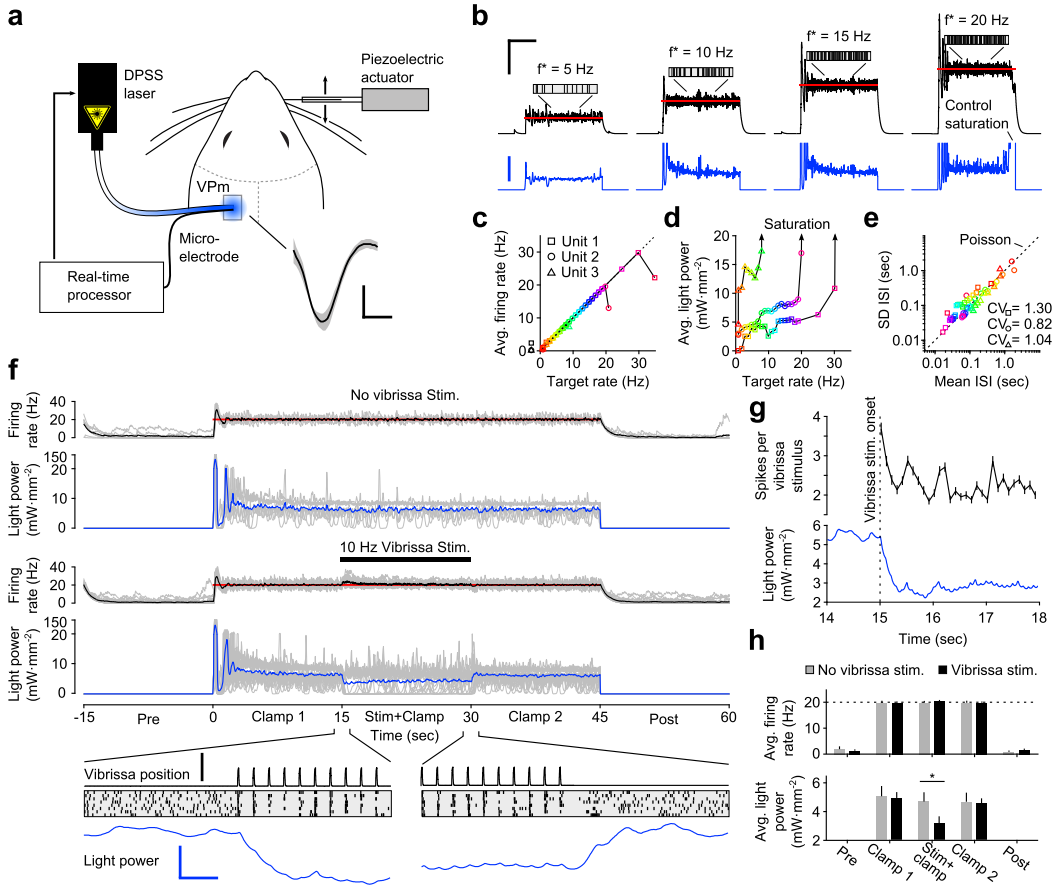

Figure 42: Firing rate control of isolated units, *in vivo*. **(a)** Single unit extracellular recordings were performed in thalamic VPm and used to update the optical power of a stimulating DPSS laser. The primary vibrissa was deflected along the rostral-caudal plane using a computer-controlled piezoelectric bending actuator to provide sensory perturbations during closed-loop control. A representative TCU waveform is shown. Shaded region is ± standard deviation. Vertical and horizontal scale bars represent 100 μV and 1 ms, respectively. **(b)** Single-trial closed-loop firing rate control in the absence of sensory input. Traces show the target firing rate (red), measured firing rate (black), and light power (blue). Inset spike trains are shown for each target rate. Vertical scale bars, 10 Hz (black) and 10 mW·mm^{-2} (blue). Horizontal scale bar, 10 s. **(c)** Measured versus target firing rates for 3 TCUs. Data points are color coded by the target rate. Black symbols at left represent the spontaneous firing rate of each TCU. **(d)** Average laser power required for each target rate. **(e)** Mean versus standard deviation of the inter-spike interval distribution for each target rate and cell. The coefficient of variation of the interspike interval, CV_{ISI}, is calculated for each cell. The identity line (dotted) line indicates Poisson spiking statistics. **(f)** Real-time control during external sensory drive. The firing rate of a single TCU cell (grey lines: single trials; black lines, average) was clamped at 20 Hz (red line) for 45-seconds (32 trials). During 24 of the trials (bottom plots), a 15-second train of 10 Hz deflections was applied to the primary vibrissa, requiring the controller to compensate for afferent drive. The bottom traces display whisker stimulus waveform, raster plots, and the average control signal for 2-second windows during the start and stop of vibrissa stimulation. Vertical scale bars, 0.25 degrees (vibrissa position) and 2 mW·mm^{-2} (optical power). Horizontal scale bar, 250 ms. **(g)** The average number of spikes evoked by each whisker deflection compared to the average control signal over the 3 seconds following stimulus onset (errorbars: ± 1 SEM). **(h)** The average firing rate and average control signal during each phase of a control epoch (errorbars: ± 1 SEM; significant differences, based on paired t-tests, are marked by asterisks, p< 0.05)

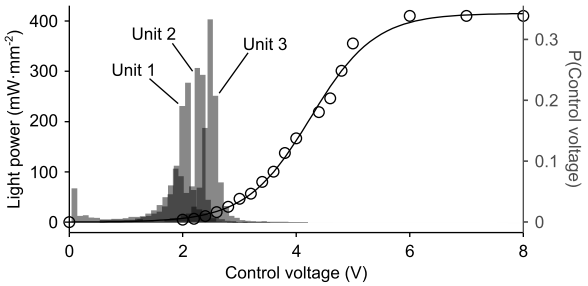

Figure 43: Laser power is a steep nonlinear function of control voltage. The light power density at the fiber tip is plotted as a function of the input voltage generated by the PI controller (Eq. 71) along with a best-fit sigmoid function of the form $\frac{a}{1+exp(bx+c)}$ (left axis; black). Control voltage histograms are shown for each of the three thalamocortical units from Fig. 42(b-e) (right axis; grey). The full range of laser intensities was not used during closed loop control. Control signals were instead concentrated at the bottom of the laser activation curve.

indicating an irregular, Poisson-like spiking process (Fig. 42(d); Fig. 44(a)). This suggests that optogenetic feedback control can be used to mimic awake spiking statistics in anesthetized animals.

We hypothesized that the controller could maintain a set firing level even during fluctuating sensory drive. To test this, we used the controller to lock the firing rate of a TCU at 20 Hz while periodic sensory stimuli of varying intensity were delivered to the primary vibrissa (defined as the whisker that best drove activity in the recorded TCU; Section 5.2) using a piezoelectric bending actuator (10 Hz, 133-522 deg·s^{-1}, Fig. 42(a)). During stimulation epochs, vibrissa deflections reliably evoked stimulus-locked trains of action potentials and caused the controller to automatically reduce laser power to accommodate this increased sensory drive (Fig. 42(f-h)). Although the temporal pattern of spiking was locked to vibrissa deflections (Fig. 44), the mean firing level was maintained at the 20 Hz target rate during stimulus episodes (24 trials, Fig. 42(h)). We found that the fine-scale temporal correlation between the control input and evoked firing during stimulation was negligible in comparison to the effect of vibrissa position (Fig. 44(b)). This is important because precise temporal spiking patterns carry information in the vibrissal sensory pathway (Wang *et al.*, 2010; Bruno, 2011). Therefore, closed-loop control of continuous optical power is a

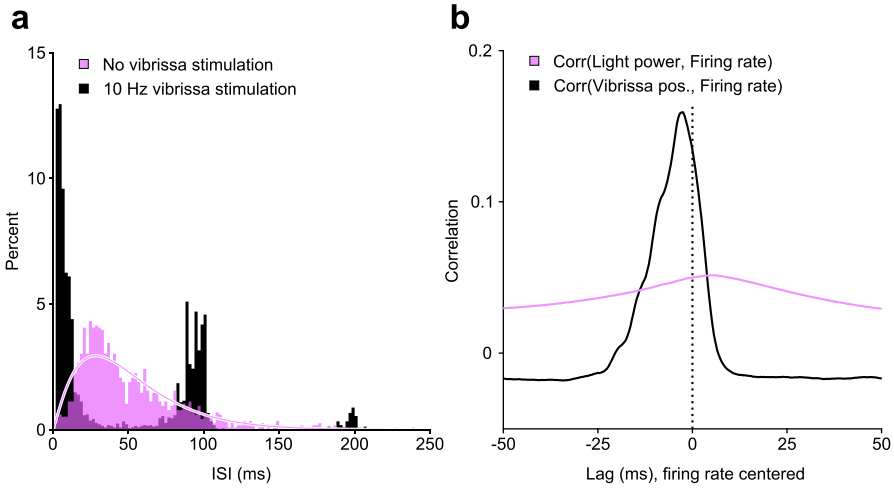

Figure 44: Whisker stimuli and closed-loop optical stimulation act at distinct time scales. **(a)** As shown in Fig. 42(c), the spiking patterns of isolated units in the absence of vibrissa but during closed-loop firing rate control were irregular, with Poisson-like firing statistics. This results in an inter-spike interval distribution (pink) that is well approximated by a Gamma distribution, which encapsulates an exponential decay for longer intervals and an initial refractory period (pink line: best fit Gamma distribution). In contrast, the periodic ISI distribution during closed-loop control and vibrissa stimuli is phase-locked to the 100 ms period of vibrissa deflections. **(b)** Normalized cross correlation between the optical input and firing rate compared to that between the vibrissa position and firing rate (bin size 0.4096 ms). The peak correlation between vibrissa position and neural firing rate occurs at a negative lag, suggesting a causal relationship. The peak correlation between optical power and neural firing rate occurs at a positive lag, suggesting that the laser power reacts to changes in neural firing. The different widths of the correlation functions indicate that closed loop control and vibrissa stimuli act over relatively long and short time scales, respectively. All data presented in this figure were derived from the same unit, whose spiking was locked at an average firing rate of 20 Hz. This indicates that although the controller determined the baseline firing level of the cell, it was not imposing specific spike times. Instead, temporal firing patterns were imposed on top of closed-loop rate control using sensory stimulation.

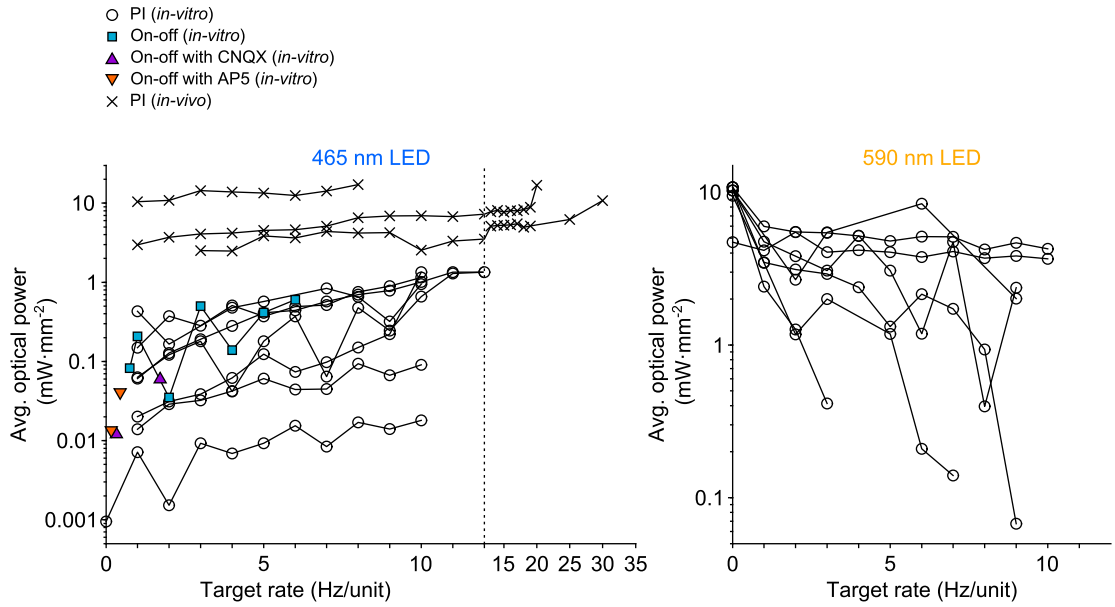

Figure 45: A wide range of optical power was required during closed loop stimulation. Optical power density at 465±11 nm FWHM (left plot) and 590±10 nm FWHM (right plot) temporally averaged over 1-minute (*in-vitro* PI controller, Fig. 34), 12-hour (*in-vitro* on-off controller, Fig. 39), 24-hour (*in-vitro* on-off controller with CNQX and AP5, Fig. 41 of main text), or 30 second (*in-vivo* PI controller; Fig. 42(b-e)) control epochs versus the corresponding target firing rate. Lines connect data points derived from the same culture (*in-vitro* data) or units (*in-vivo* data). Only successful trials are shown. The required light intensity during closed loop control varied widely and depended on the target rate, the control algorithm, the type of neural preparation being controlled, and variability in cell-to-cell and culture-to-culture excitability within preparation types. This highlights the ability of closed-loop control to compensate for the imposed variability across experimental preparations and the intrinsic variability of neural circuits, in order to achieve a target activity level.

means to modulate baseline excitability without distorting the fine-scale temporal structure of sensory-evoked spike trains. This stands in contrast to most optogenetic stimulation methods, which use pulses of light to impose spike times on cells and neural populations, overriding the temporal statistics of sensory evoked spike trains.

5.4 Discussion

Optogenetic feedback can be used to precisely control neuronal firing levels during perturbations that strongly affect network excitability, across time scales ranging from seconds to days, both *in vitro* and *in vivo*. Using this new approach, insights can be made into neural control of motor action, sensory encoding and adaptation, activity homeostasis, and even memory formation. This is especially relevant given

the recent focus on the dynamic nature of neural coding, and the need for stimulation technologies capable of controlling highly non-stationary neural circuitry (Stanley, 2013).

The control algorithms and apparatuses used in this study are simple and straightforward. We expect that they will be tailored to allow robust control in specific experimental contexts. For instance, the incorporation of spatial light modulation would allow optical inputs to be steered towards the spike initiation zones of individual cells in order to minimize light exposure (Fig. 45) and abnormal conductances. Additionally, with more sophisticated control algorithms, for instance those incorporating models of feed-forward neural dynamics, optogenetic feedback could be used to compensate for destabilizing pharmacological perturbations such as those that disrupt inhibitory synaptic transmission. Further, optogenetic feedback might be used to control experimental measurements more complex than firing levels. For example, closed-loop optical stimulation has been proposed to control measurements of coherence and phase in oscillatory network activity (Witt *et al.*, 2013). Additionally, optical stimulation could be made contingent on specific behavioral outputs or complex spatiotemproal activity patterns associated with specific behaviors, *in vivo*. With improved real-time control hardware and algorithms, we expect that optogenetic feedback control will be incorporated into a multitude of experimental contexts requiring precise control of neuronal activity. Eventually, it may also be incorporated into clinical devices for sensory and motor prostheses, and closed-loop neuromodulation therapies.

CHAPTER VI

DIRECT INDUCTION OF SYNAPTIC SCALING BY REDUCED AMPA-RECEPTOR ACTIVATION*

Activity deprivation in developing neural circuits triggers compensatory mechanisms in order to maintain appropriate activity levels, which are collectively referred to as homeostatic plasticity. The most widely studied form of homeostatic plasticity is synaptic scaling, which adjusts the weight of synapses connecting to a cell by a global, multiplicative factor in inverse relation to activity within the cell. Synaptic scaling is thought to provide a means to stabilize neural firing without disrupting the relative strengths of synapses, thus maintaining network stability without disturbing memory engram-bearing synapses. Here we use optogenetic feedback control to show that synaptic scaling is induced by decreased AMPA-receptor activation even when firing rates remain normal. This indicates that the role of synaptic scaling is not to control neuronal spiking levels, but to regulate the amount of afferent excitatory input to the cell. Our findings have significant implications for the role of synaptic scaling in the simultaneous maintenance of circuit stability and memory engrams.

6.1 Introduction

During learning and development, rapid changes in network structure can cause neural circuits to become unstable. Mathematical models predict that, in isolation, competitive Hebbian modification of synapses causes their weights to increase until saturating at some maximal value (Miller and MacKay, 1994; von der Malsburg, 1973). The unstable tendencies of neural circuitry appear to be the cost of its malleability, and necessitate negative feedback mechanisms so that normal activity levels can be

**Contributions:* M.F., J.P.N., and P.W. designed all experiments. M.F. performed all experiments. J.P.N. created software and hardware for, and helped perform, experiments involving closed-loop optical stimulation. M.F. performed all data analysis and made the figures.

maintained during structural modification (Abbott and Nelson, 2000). Homeostatic plasticity encompasses a set of mechanisms that tune circuit excitability in inverse proportion to deviations from an activity setpoint, such that activity is maintained within functional bounds (Turrigiano and Nelson, 2004; Marder and Goaillard, 2006). These compensatory processes are thought to be especially important for tuning sensory cortical circuits during development (Desai *et al.*, 2002; Wilhelm and Wenner, 2008) and following injury (Fröhlich *et al.*, 2008; Topolnik *et al.*, 2003; Nita *et al.*, 2006). Homeostatic plasticity mechanisms exert a stabilizing effect either by regulating ion-channel expression to affect neuronal excitability (Marder and Goaillard, 2006; Turrigiano *et al.*, 1994) or by modulating the strength of excitatory synapses (Turrigiano *et al.*, 1998; Song *et al.*, 2000). The best studied form of homeostatic plasticity is synaptic scaling, a phenomenon in which the distribution of single-vesicle (miniature) post-synaptic currents received by a neuron is collectively shifted to higher (upscaling) or lower (downscaling) values by a multiplicative factor (Turrigiano *et al.*, 1998). This shift occurs in inverse relation to the degree of neural activity over an extended time period, and therefore exerts negative feedback to tame runaway excitability.

Although synaptic scaling has proven to be a ubiquitous feature of developing neuronal networks, *in vitro* (Turrigiano *et al.*, 1998; Stellwagen and Malenka, 2006; Burrone *et al.*, 2002) and *in vivo* (Desai *et al.*, 2002; Wilhelm and Wenner, 2008; Deeg and Aizenman, 2011), the precise mechanism by which neurons or neural circuits sense and adjust their own activity levels is hotly debated (Turrigiano, 2011b; Goold and Nicoll, 2010; Burrone *et al.*, 2002; Deeg and Aizenman, 2011; Wilhelm and Wenner, 2008; Stellwagen and Malenka, 2006; Ibata *et al.*, 2008; Leslie *et al.*, 2001; Sutton *et al.*, 2006; Béïque *et al.*, 2011; Hou *et al.*, 2008). Amid this debate, there are some agreements. For example, it has been demonstrated conclusively that upscaling can be induced either via the application of (1) drugs that completely abolish spiking activity (e.g. tetrodotoxin, a voltage-gated sodium channel blocker) or (2) drugs

that diminish excitatory neurotransmission (e.g. CNQX, a competitive antagonist of AMPA receptors) (Turrigiano *et al.*, 1998). However, the tight coupling between the effects of these two drugs on spiking and neurotransmission has made it difficult to determine which feature of network activity is measured to produce synaptic scaling.

To be concrete, consider the archetypal experimental protocol for inducing synaptic scaling in a primary neural culture: long-term ($\sim$24 hour) application of either CNQX or TTX (Turrigiano *et al.*, 1998). Using CNQX, AMPAergic excitatory drive is removed from the network, lowering firing activity, and provoking upscaling of synaptic strength. However, the precise form of activity reduction that leads to a scaling response is ambiguous. Are cells sensing a reduction in firing due to a loss of excitatory synaptic drive or directly sensing a reduction in excitatory transmission due to blockade of AMPAergic synapses? It is difficult to tell because AMPAergic blockade dramatically affects spiking levels. Conversely, the removal of spiking activity using TTX results in the same problem since spike-evoked neurotransmission is halted.

To study the individual contributions of spiking activity and AMPAergic neurotransmission levels to the upscaling process, these two forms of network activity must be independently manipulated. In Chapter 5, we demonstrated how optogenetic feedback control could be used to decouple average network spiking activity from the effects of selective excitatory synaptic blockade over 24-hour epochs. We found that spontaneous network firing levels, recorded after the drug had been removed, were elevated even though network spiking activity was maintained at pre-drug levels for the duration of the CNQX treatment. Therefore, the increases in network excitability that caused this elevated firing could not have been triggered by homeostatic compensation in response to decreased firing levels because firing was held at pre-drug levels throughout the treatment period. This result is at odds with the most widely

used models of homeostatic plasticity, which state that the regulation of intrinsic excitability and synaptic strength are based upon post-synaptic firing levels (Turrigiano, 2011a; Marder and Goaillard, 2006; Ibata *et al.*, 2008).

I worked in collaboration with Ming-fai Fong and Pete Wenner of Emory University to parse the independent roles of spiking and AMPAergic neurotransmission in the induction of synaptic upscaing. We show that reduced AMPAergic transmission can directly induce upscaling of synaptic strength, and that the upscaling process is independent of post-synaptic activity. To do this, we use optogenetic feedback control to restore population firing during 24-hour bath applications of CNQX. We then perform intracellular recordings of miniature excitatory post-synaptic current (mEPSC) amplitude to evaluate resultant changes in synaptic strength. We find that upscaling occurs in cultures treated with CNQX even when spiking activity is restored to pre-CNQX levels for the duration of the drug treatment. Further, the degree of scaling induced in these networks is identical to that of CNQX-treated, sister-matched cultures where spiking is left uncontrolled. These data provide strong evidence that upscaling results directly from decreases in AMPAergic neurotransmission rather than changes in spiking activity. This suggests that the function of upscaling is to maintain synaptic strength, rather than to homeostatically regulate neuronal spiking, as has been widely promoted in the literature (Turrigiano, 2011b; Ibata *et al.*, 2008; Leslie *et al.*, 2001). I discuss the consequences of this finding on several established theories of learning.

6.2 Methods

6.2.1 Viral transduction

Cell culture was performed as described in Chapter 2, Section 2.2.1. AAV9-hSynapsin-ChR2(H134R)-eYFP was produced by the University of Pennsylvania Vector Core. The genomic titer was 1×10^{13} c.f.u.$\cdot$mL^{-1}. 0.5 μL of the virus solution was added

to 1 mL growth medium at 1 DIV during the first medium exchange. Expression of the eYFP reporter protein was verified using a confocal microscope (Zeiss LSM 700; Fig. 46(b)).

6.2.2 MEA recordings

MEA recordings were performed in standard growth medium in the cell culture incubator using the Neurorighter acquisition system (Newman *et al.*, 2013) (Chapter 2). Voltages recorded through microelectrodes were amplified and bandpass filtered from 1 Hz to 5 kHz using a 60-channel analog amplifier (Multichannel Systems, MEA60-Up) and digitized at 25 kHz using the Neurorighter acquisition system. Voltage recordings were then digitally filtered with a 3rd order Butterworth bandpass filter at 200-3000Hz, and action potentials were detected at a threshold of ± 5 times the root mean square noise of each channel (see Appendix A).

6.2.3 Closed-loop optical stimulation

To deliver optical stimuli, a custom N-channel enhancement mode MOSFET current source was used to drive an LED (465$\pm$11 nm FWHM; LEDEngin). The LED was butt-coupled to a randomized fiber bundle (Schott, Mainz, Germany) which fed light to a Köhler illumination train mounted beneath the MEA amplifier. To control firing activity, we used an 'on-off' control algorithm (Chapter 5, Section 5.3.3). The target firing level was set to the average MEA-wide spike detection rate over the 3 hour period prior to drug application. The network firing rate was evaluated every 10 ms, and a stimulus was delivered if the integrated error signal between the target and measured firing rate became positive (Fig. 46). Each stimulus pulse resulted in uniformly distributed, 10.1 mW$\cdot$mm^2 light in the plane of the culture and lasted for 10 ms. The rise and fall times of each LED pulse were $\sim$10 μs (see Appendix B). Detailed methods concerning closed-loop optical control of neuronal firing can be found in Chapter 5.

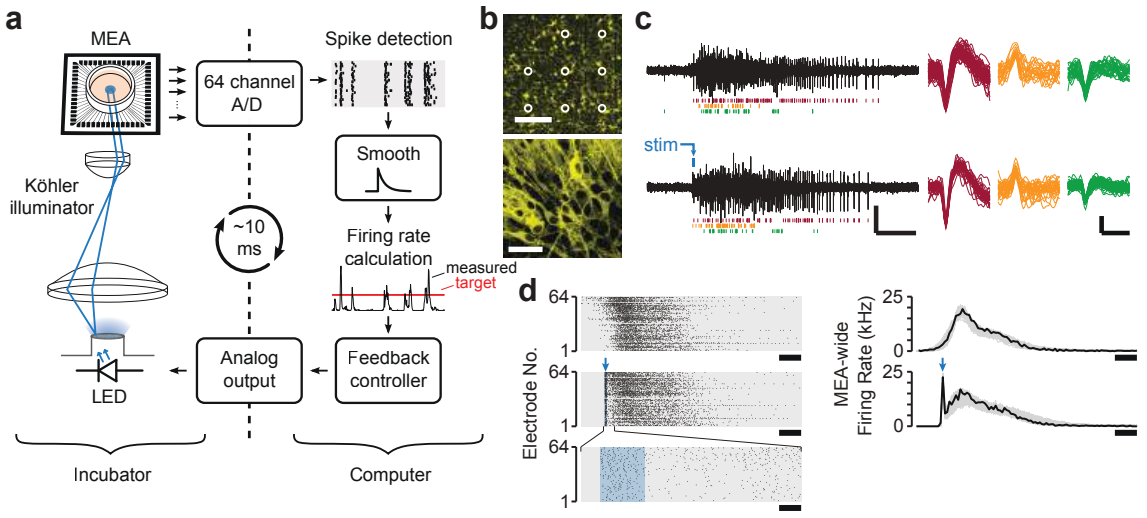

Figure 46: On-off control of network firing restores normal spiking in the presence of CNQX. **(a)** Schematic of the firing-rate control system. Network-wide activity levels are sampled by a 59-electrode MEA, digitized, and sent to a real-time processor. The processor calculates the instantaneous firing rate, compares it to a target rate, and applies optical stimuli to the network when necessary. **(b)** Confocal image of a dissociated cortical network expressing hSyn::ChR2-eYFP. Microelectrodes are circled in white. Scale bars, 200 μm (top) and 50 μm (bottom). **(c)** Comparison of spontaneous and optically-evoked bursts. *Left,* Voltage traces during a spontaneous burst in the absence of CNQX (top) and evoked activity on the same electrode in the presence of CNQX (bottom). The colored bars below each trace denote the action potential sequence of three units detected on the electrode. *Right,* Overlaid action-potential waveforms of the three detected units. Scale bars, 50 μV, 200 ms (left); 25 μV, 1 ms (right). **(d)** *Left,* Rastergram showing a spiking activity detected on all electrodes during a spontaneous bursts (top) or optically evoked burst (middle). The zoomed rastergram shows spiking directly evoked by the 10 ms optical pulse (blue area). Scale bars, 100 ms (top and middle), 5 ms (bottom). *Right,* Network firing rate profiles during spontaneous bursts in the absence of CNQX (top) and evoked bursts in the presence of CNQX (bottom). The black line is the average burst waveform. Gray traces are individual burst waveforms recorded during the 3-hour pre-drug recording (top) of and during the 24-hour CNQX with photostimulation protocol (bottom). The blue arrow denotes timing of the light pulse. Bin size, 10 ms. Scale bar, 100 ms.

6.2.4 Whole-cell voltage clamp recordings

Miniature excitatory postsynaptic currents (mEPSCs) were recorded from pyramidal-shaped cells during continuous perfusion of artificial cerebrospinal fluid (aCSF) containing (in mM): 126 NaCl, 3 KCl, 2 $CaCl_2$, 1.5 $MgSO_4$, 1 NaH_2PO_4, 25 $NaHCO_3$, and 25 D-glucose, and saturated with 95% O_2 and 5% CO_2 (pH 7.4, 315 mOsm). To isolate our recordings to AMPAergic mEPSCs (and not spike-evoked or inhibitory synaptic currents), the aCSF solution contained 1 μM TTX and 20 μM bicuculline. aCSF temperature was regulated at 35°C using an inline heater (Warner 64-0102). The pipette solution contained (in mM): 100 K-gluconate, 30 KCl, 10 HEPES, 2 $MgSO_4$, 0.5 EGTA, 3 ATP (pH 7.4, 290 mOsm). mEPSCs were recorded using an EPC8 amplifier (HEKA, Lambrecht/Pfalz, Germany). Pipette resistances were 2-8 MΩ.

6.2.5 Data analysis

mEPSCs were analyzed, blind to the treatment condition, using MiniAnalysis (Synaptosoft, Decatur, GA), and mEPSCs with amplitudes less than 5 pA were excluded from analysis. Both MEA recordings and extracted mEPSC data were analyzed using MATLAB (The Mathworks, Natick, MA). Statistical significance for firing and burst rate data was determined using a Kruskal-Wallis test and post-hoc Wilcoxon rank-sum tests with a Bonferroni adjustment. Statistical significance for mEPSC data was determined using one-way ANOVA and post-hoc t-tests with a Bonferroni adjustment. mEPSC amplitude distributions were compared using the Kolmogorov-Smirnov test.

6.3 Results

The majority of spiking activity in cultured cortical networks occurs in tightly synchronized bouts of network spiking activity called 'bursts' (Wagenaar *et al.*, 2006c).

Reduced spiking in networks treated with CNQX is due primarily to a reduction in the frequency of network bursting. Therefore, to restore spiking activity during CNQX treatment we used 'on-off' optical control, which we have shown is capable of reinstating network bursting activity in the presence of CNQX (Chapter 5, Section 5.3.4). Indeed, we found that although optical stimuli did produce some short-latency spiking activity, the vast majority of action potentials produced during closed loop optical stimulation in the presence of CNQX occurred during longer ($\sim$1 second long) bursts that occurred after the light had turned off (Figs. 46(d), 47). Additionally, we found that the patterns of spiking activity produced by single units (Fig. 46(c)), the time-course of network-wide bursting episodes (Figs. 46(d), 47), and the activity correlations between electrodes (Fig 48) were nearly identical during optically evoked bursting activity compared to spontaneous bursting before the addition of CNQX. These observations indicate that optical on-off control is capable of emulating spontaneous bursting activity during CNQX treatment.

To deduce the mechanistic trigger for synaptic upscaling, experiments were conducted on sets of sister cultures. With each set, cultures were assigned to one of the following experimental groups:

- **Group 1:** 24-hour application of DMSO as vehicle. These cultures experience normal AMPAergic and spiking activity levels (n=12 cultures).
- **Group 2:** 24-hour application 40 μM CNQX dissolved in DMSO. These cultures experience no AMPAergic transmission and reduced spiking levels (n=13 cultures).
- **Group 3:** 24-hour application 40 μM CNQX dissolved in DMSO and chronic, closed-loop optical stimulation. These cultures experience no AMPAergic transmission and normal spiking activity (n=5 cultures).

Experiments conducted on culture sets containing groups 1 or 2, but not 3, were used

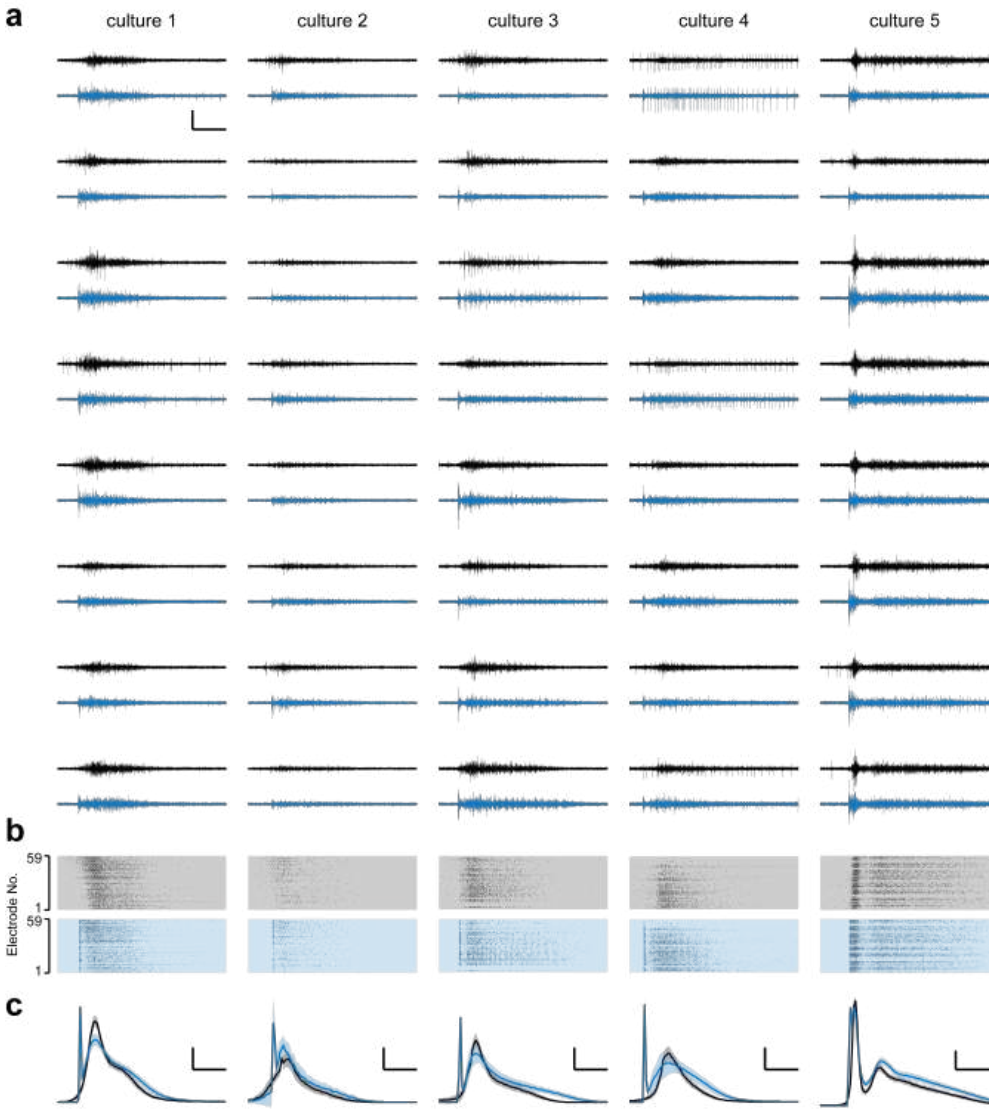

Figure 47: Optically evoked network bursts in the presence of CNQX mimic spontaneous bursts that occur in the absence of CNQX. **(a)** Voltage traces of bursts recorded from individual electrodes before adding CNQX (black) or optically-evoked bursts following CNQX application (blue). Recordings from the 8 electrodes for which activity was highest during the pre-drug period are shown for each culture. Scale bars, 100 μV, 200 ms. **(b)** Rastergrams showing spiking activity on all channels during the bursts shown in (a). Background colors have the same meaning as in (a). Scale bar, 200 ms. **(c)** The average array-wide spike detection rate during spontaneously occurring bursts in the absence of CNQX (black, averaged from 3 hours of activity) or during 24-hour closed-loop stimulation periods in the presence of CNQX (blue, averaged over the full 24 hour treatment period). Shaded regions denote standard deviation. Bin size, 10 ms. Scale bars, vertical: 5 kHz (cultures 1,3, 4, 5), 2 kHz (culture 2); horizontal: 200 ms (all cultures).

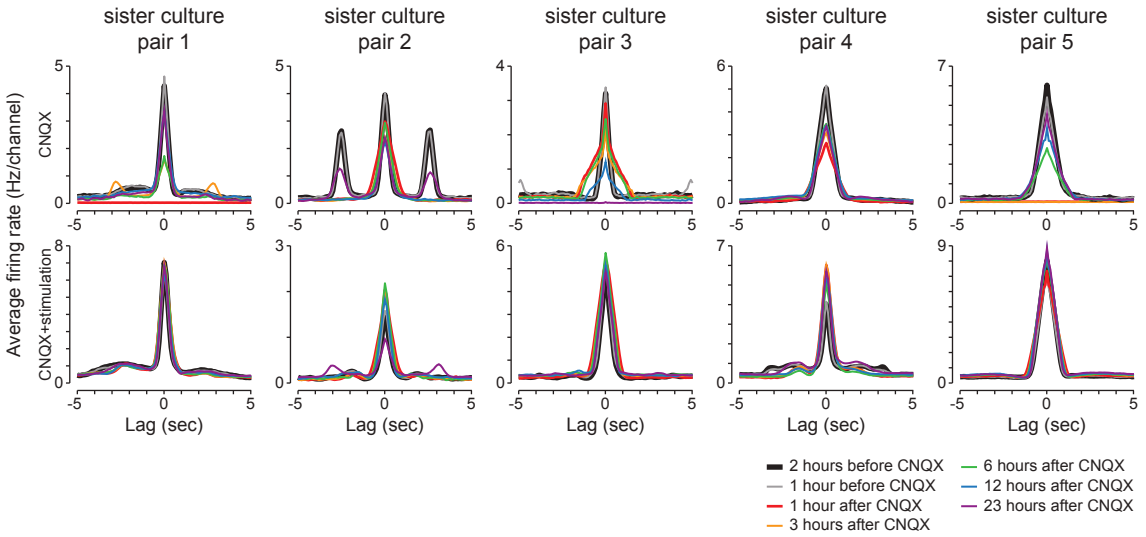

Figure 48: On-off control maintains pre-drug activity correlations in the presence of CNQX. A spike detection rate cross-correlation function was computed for each channel pair and then averaged over channel pairs to produce an average channel-to-channel correlation. These correlation functions were calculated at various time points before and after the addition of CNQX to the bath for 5 sister pairs of CNQX-treated cultures without closed-loop optical stimulation (top) and with closed-loop optical stimulation (bottom). On-off control maintains pre-CNQX activity correlations throughout the CNQX treatment period.

to calculate firing statistics (Figs. 48, 49) but not to compare mEPSC distributions (Fig. 50, 51). For comparison of mEPSC measurements, 5 triplicate culture sets, each spanning all three treatment conditions, were used. Because voltage clamp recordings could not be performed on all three cultures simultaneously, CNQX or DMSO application was staggered at 3 hour intervals. This way, we could perform whole-cell voltage clamp recordings on each culture during a 3 hour time window after the 24-hour drug treatment period for each culture had elapsed. Drugs were applied in random order for each culture set.

Although the degree to which CNQX affected network activity was variable, there was always a reduction in firing levels relative the pre-drug firing rate for the duration of the 24-hour treatment period in the presence of CNQX (Fig. 49(b,c)). In addition to average firing levels, the burst rate in CNQX-treated cultures was also decreased compared to vehicle-treated controls (Fig. 49(c)). In contrast, all CNQX-treated cultures that received closed-loop firing rate restoration showed no significant difference

from vehicle-treated controls in terms of average firing levels, burst rate, or interburst firing rate (Fig. 49(c)). These observations, combined with the above results concerning the similarity between light-evoked and spontaneous bursts (Figs. 47 and 48), indicate that closed-loop control reinstated normal network firing behavior in the absence of AMPAergic neurotransmission. Therefore, any changes in synaptic strength that we detected in these networks could not be due to changes in firing activity. Incidentally, we also note that the similarity between the bursts evoked by optical stimulation in the presence of CNQX and spontaneously occurring bursts indicates that network-wide bursts are largely NMDA receptor driven.

To quantify the degree to which synaptic strength changed in each experimental group, we recorded mEPSCs from individual cells using whole-cell voltage clamp following the 24-hour drug application period (Fig. 50(a)). We then extracted mEPSC waveforms and amplitude distributions for each experimental group. Our analyses of mESPC amplitudes were based strictly on data collected from triplicate sister networks (n = 5 triplicates).

We found that both CNQX-treated cultures without restored firing levels and CNQX-treated cultures with restored firing levels had mEPSC amplitude distributions that were significantly shifted compared to those of vehicle-treated control cultures. Further, we found that the mean and variance of these scaled distributions were virtually identical (Fig. 50(b)). Finally, we found that the upward shift in mEPSC amplitude distributions could be explained by a linear relationship, indicating that increases in synaptic strength were consistent with previous descriptions of upscaling (Turrigiano *et al.*, 1998), and not due to another type of shift in amplitude (Fig. 50(c,d)). Additionally, we detected significant increases in the detection frequency and charge per event of mEPSCs following CNQX-treated cultures (Fig. 51), indicating a potential pre-synaptic effect of chronic AMPAergic blockade during closed-loop stimulation. Interestingly, changes in mEPSC detection frequency

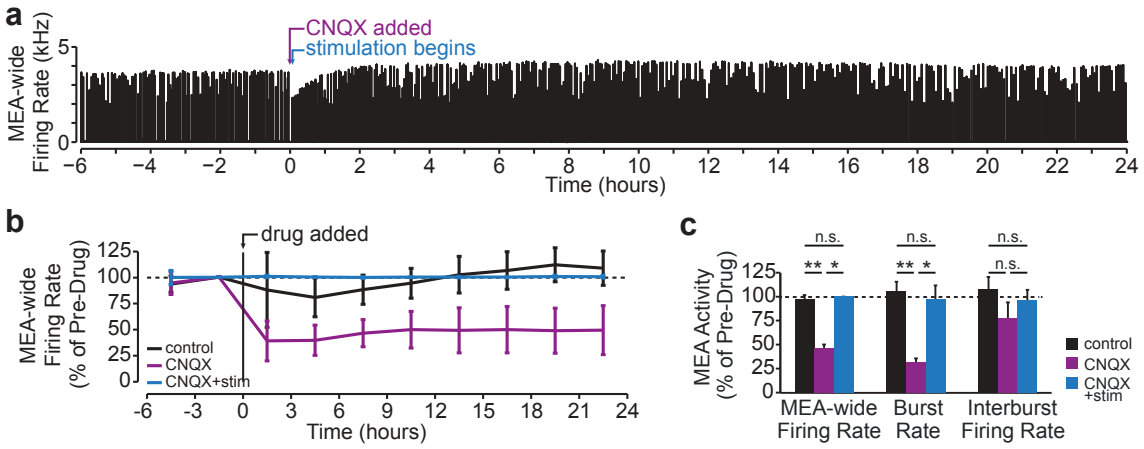

Figure 49: Optical on-off control provides reliable, long-term decoupling of AMPA receptor activation and network firing levels. **(a)** Firing restoration in the presence of CNQX. The controller was turned on 5 minutes after the addition of CNQX to the bath at 0 hours. For the initial 2 hours of control, the average firing rate is restored, but bursts have a lower amplitude compared to the pre-drug phase (bin size, 1 s). **(b)** Mean MEA-wide firing rates for cultures with restored spiking (bin size, 3 hrs; errorbars, ±s.d.; vehicle-treated controls, n=12 cultures; CNQX, n=13 cultures; CNQX and stimulation, n=5 cultures). **(c)** Time-averaged values of the MEA-wide firing rate, burst rate, and interburst firing rate over the 24-hour treatment period as a percent of pre-drug levels. We detected no difference between CNQX-treated cultures with optically restored activity and vehicle-treated controls in terms of any of these metrics (CNQX with stimulation: MEA-wide firing rate, 100.2±0.4%, p <0.6; burst rate, 97.7±32.0%, p <0.9; interburst firing rate, 96.2±24.9%, p <0.9). The MEA-wide firing rate and burst rate were significantly reduced in CNQX-treated networks that did not receive activity restoration compared to both vehicle-treated cultures and CNQX-treated networks with restored activity (CNQX without stimulation: MEA-wide firing rate, 31.2%±4.8%, $p < 1 \times 10^{-4}$; burst rate, 46.2±4.1%, p <1×10^{-4}).

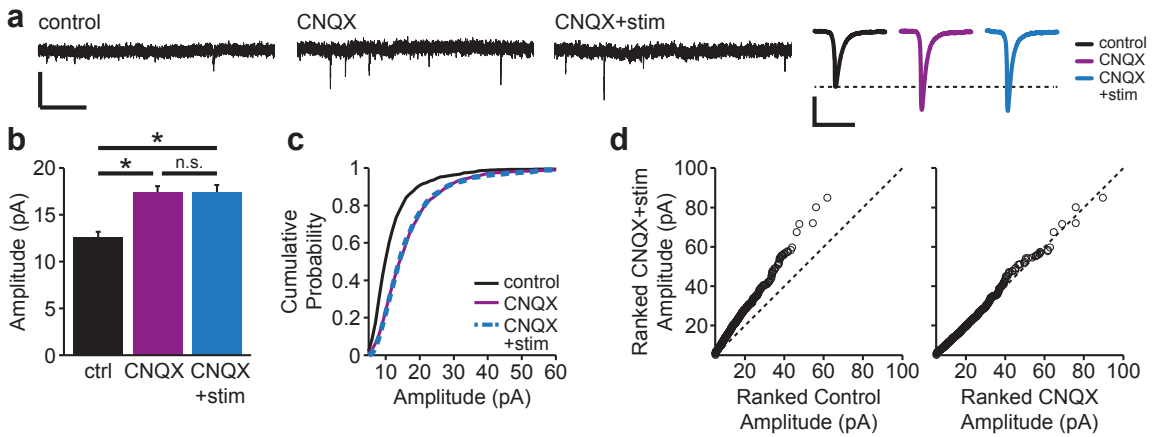

Figure 50: Reduced glutamatergic transmission directly triggers upward scaling. **(a)** *Left,* Sample current traces obtained from whole-cell patch clamp recordings of cells from each treatment condition. Scale bars, 25 pA, 200 ms. *Right,* Average mEPSC waveforms for each condition. Scale bars, 5 pA, 20 ms. **(b)** Mean mESPC amplitudes from cells derived from 5 sister culture triplicates. (control: 12.6±0.6 pA, n=44 cells; CNQX: 17.4±0.7 pA, n=51 cells, $p < 10^{-5}$; CNQX+photostimulation: 17.4±0.8 pA, n=46 cells, $p < 10^{-5}$). **(c)** Cumulative mEPSC amplitude distributions for each treatment condition. The multiplicatively scaled CNQX and CNQX+photostimulation distributions matched the control distribution (p>0.9 for both), and there was no detectable difference between the unscaled CNQX and CNQX+photostimulation distributions (p>0.9). **(d)** Sorted CNQX+photostimulation mEPSC amplitudes plotted against sorted control or CNQX-treatment amplitudes (R^2=0.998 and R^2=0.995, respectively). The dotted line indicates identity.

were insignificant in cultures treated with CNQX whose firing rate was not controlled. However, this result must be considered in the context of the 5 pA threshold imposed for mEPSC detection. It is possible that because the amplitudes of mEPSC following CNQX treatment were larger than those produced by vehicle-treated cultures, that more events were 'drawn out of the noise', producing an spurious increase in mEPSC *detection frequency* not related to the true frequency of mESPC generation by pre-synaptic cells. Regardless of potential pre-synaptic effects, our results indicate that the degree of scaling induced by bath applied CNQX is independent of CNQX's effects on firing activity in the network. Therefore, reduced AMPAergic transmission can directly and independently induce synaptic upscaling.

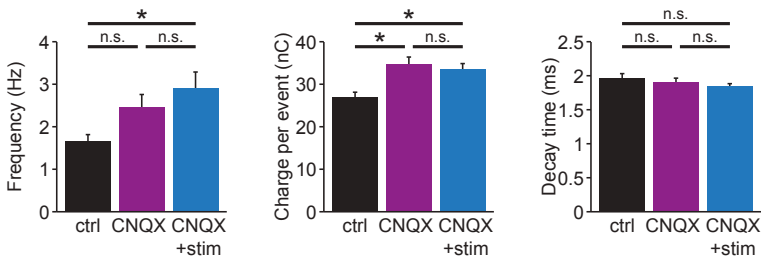

Figure 51: Various mESPC features following chronic drug treatment. Mean mEPSC detection frequency (control, 1.6±0.2 pA, n=44 cells; CNQX, 2.3±0.3 pA, n=51 cells; CNQX+photostimulation, 2.6±0.3 pA, n=46 cells; p <0.02), charge per event (control, 27.0±1.2 fC; CNQX, 34.8±1.6 fC; CNQX+photostimulation, 33.5±1.4 fC; $p < 10^{-3}$), and decay time (control, 2.0±0.06 ms; CNQX, 1.9±0.06 ms; CNQX+photostimulation, 1.8±0.04; p>0.2) for CNQX+photostimulation experiments. There are significant differences in frequency of control versus CNQX+photostimulation conditions ($p < 10^{-2}$), and in charge per event of control versus both CNQX cases (control vs. CNQX, $p < 10^{-3}$; control vs. CNQX+photostimulation, $p < 10^{-3}$).

6.4 Discussion

Hebbian learning rules dictate that synapses more likely to evoke post-synaptic neural activity are strengthened, and thus become more capable of evoking activity. When represented mathematically, this type of learning rule introduces a positive feedback into the update equations for synaptic weights that causes them to saturate at large values (Miller and MacKay, 1994; von der Malsburg, 1973; Abbott and Dayan, 2001). The stability problems associated with purely Hebbian learning rules and the existence of stabilizing constraints on the runaway of synaptic strength have been predicted for some time (von der Malsburg, 1973). In a seminal paper (Oja, 1982), Erkki Oja constructed a learning rule for the synapses contacting a simple, linear neuron model with the following features:

1. The weight of a synapse grows when it and the neuron are active simultaneously.

2. There is stable equilibirum point for the sum of the squared synaptic strengths that is equal to 1.

3. The return rate of the sum of the squared synaptic strengths back to its equilibrium point is proportional to the activity level of the neuron.

Rule 1 implemented a standard Hebbian update term. Rules 2 and 3 encapsulated the main features of synaptic scaling, which were to be verified experimentally in the following decades. Interestingly, Oja found that the effects of these simple constraints on the computational properties of the model cell were quite remarkable; after the synaptic weights had stabilized, the model neuron acted much like a principal component analyzer, producing a response equal to the linear combination of synaptic inputs that produced maximal variance (the principal component of the inputs). Since the initial hints of its existence (Ramakers *et al.*, 1990) and subsequent confirmation (Turrigiano *et al.*, 1998), synaptic scaling has fulfilled Oja's and many others' (von der Malsburg, 1973; Miller and MacKay, 1994) predicted role as a stabilizing counterbalance to Hebbian plasticity. Synaptic scaling seemed to be the key to a number of interesting computational and learning properties in neurons and neural circuits.

In accordance with Oja's model, the current understanding of the scaling process is that it adjusts synaptic weights in inverse proportion to post-synaptic firing levels. Indeed, two recent experimental studies provide evidence that synaptic scaling is a cell-autonomous process in which the post-synaptic spiking activity over long time periods (or even the membrane voltage in the absence of spiking (Leslie *et al.*, 2001)) dictate the up or down regulation of post-synaptic strength (Goold and Nicoll, 2010; Ibata *et al.*, 2008). In the stronger of these studies (Goold and Nicoll, 2010), downscaling was induced by chronically elevating spiking activity in a very sparse populations of neurons expressing ChR2 in organotypic hippocampal cultures. The authors employed intentionally inefficient ballistic transfection methods to deliver a ChR2 construct to a small number of cells ($\sim$1-10 per culture). Because only a few cells per network expressed by ChR2, spatially uniform illumination of the whole culture induced spiking in these cells, but likely did not perturb global network firing rates or neurotransmission levels. Using this assumption, the only activity change

that could have triggered a downscaling response was increased spiking activity due to optical stimulation. However, neither network spiking levels, intracellular spiking levels in ChR2, or neurotransmission levels were monitored or controlled during long-term photostimulation. The second study (Ibata *et al.*, 2008) found that so-called 'rapid' synaptic upscaling could be induced in isolated cells by using local, somatic micro-perfusions of TTX while leaving network AMPAergic transmission intact, but not by local blockade of AMPAergic input to the cell. Aside from the rather drastic decrease in the timescale required to induce a scaling compared to other studies, the authors used the accumulation of recombinant AMPA-type glutamate receptors fused with eYFP at individual synapses as a surrogate measure of synaptic strength. Without validation of how these fluorescent signals are related to functional measures of synaptic strength, such as mEPSC amplitude measurements, it is unclear if these results apply to synaptic scaling as originally defined, or to another form of plasticity.

In contrast to these studies, we continuously monitored the effects of photostimulation on network spiking activity and used a standard 24-hour treatment period. Further, we used closed-loop stimulation to actively control network firing such that there was minimal difference between activity levels prior to and following CNQX treatment. Finally, we used standard voltage clamp recordings of mEPSC amplitudes as a direct readout of synaptic strength. We found that the removal of AMPAergic transmission from the network was capable of inducing scaling even when network-wide spiking levels were normal for the duration of the drug treatment period. These results are inconsistent with the two studies described above, and Oja's original hypothesis concerning the induction of homeostatic synaptic regulation. However, our findings are supported by a number of experiments, carried out both *in vitro* and *in vivo*, that indicate synaptic receptor activation is at least involved in producing homeostatic increases in synaptic strength, if not fully required (Gonzalez-Islas and Wenner, 2006; Sutton *et al.*, 2006; Wilhelm and Wenner, 2008; Deeg and Aizenman,

2011; Béïque *et al.*, 2011; Hou *et al.*, 2008). Together, these results suggest that the cell-wide scaling effect induced by chronic activity blockade is a result of the spatially uniform nature of drug application used to induce scaling, and that compensatory increases in synaptic strength could occur in functional groups of synapses originating from different pathways (Deeg and Aizenman, 2011) or even in isolated synapses (Hou *et al.*, 2008; Béïque *et al.*, 2011).

In a particularly elegant study, Béïque *et al.* (2011) used inefficient transfection methods to overexpress an inwardly rectifying potassium channel (Kir2.1) in a small subset of neurons within dissociated cortical networks. They then identified individual spines of post-synaptic cells that received input from the Kir2.1-expressing neurons, and performed local, two-photon glutamate uncaging while using whole cell recordings to monitor syanptic currents to the post-synaptic neuron. They found that spines receiving input from Kir2.1-expressing cells, which had been deprived of normal levels of AMPA receptor activation during development, supported stronger currents in response the local glutamate compared to spines on the same dendritic arbor that had received normal input during development. This result indicates that the strength of *individual synapses* can be homeostatic regulated in inverse relation to the amount of AMPA receptor activation they receive during development. We must emphasize, however, that all results to date indicating a synapse-specific role for homeostatic synaptic regulation (including our results) apply to upscaling only, and it is entirely possible that a different set of mechanisms based upon post-synaptic depolarization are required to induce downscaling (Goold and Nicoll, 2010; Leslie *et al.*, 2001). Additionally, the existence of mechanisms for local homeostatic regulation of synaptic strength do not preclude the coexistence of global mechanisms.

However, if it is the case that the homeostatic regulation of synaptic strength truly is a 'synapse-autonomous', as opposed to a 'cell-autonomous', process, its role

as a stabilizer of neural activity fundamentally changes. Instead of regulating synaptic strength to maintain appropriate efferent (output) activity levels, synaptic scaling would regulate synaptic strength to maintain appropriate afferent (input) activity. The most troubling aspect of this change in function is that the regulatory processes occurring at different synapses might not be coordinated. Many theories of memory describe memory engrams as existing across synapses, requiring synaptic coordination. Mechanistic descriptions of cell-autonomous upscaling suggest that reductions in somatic action potentials lead to reduced voltage-gated calcium channel activation and subsequent reductions in cell-wide calcium signaling. This provides each synapse with a common measure of activity and therefore a common multiplicative adjustment factor (Turrigiano, 2011a). This form of synaptic scaling would provide an elegant mechanism for simultaneously preserving the relative weights of synapses and maintaining firing stability. However, our results suggest that the story may be more complicated. If each synapse is capable of adjusting its own value in accordance with the amount of afferent input it receives, then there is no guarantee that the relative weights of synapses will be preserved during homeostatic regulation. In order to fully understand the implications of the shift from cell-autonomous to synapse-autonomous homeostatic regulation, future studies must investigate if synapse-autonomous homeostatic synaptic regulation generalizes to downscaling, how it can function to stabilize network activity, and how it functions without destroying memory engrams. Perhaps the computational and stabilizing properties of networks governed by synapse-autonomous homeostatic regulation of synaptic strength will be even more impressive and robust than could be achieved via cell-autonomous mechanisms.

CHAPTER VII

CONCLUSION

In this dissertation, I have described new technologies that advance optogenetic control of neural activity. I showed how ChR2 can be used to deliver time-varying current fluctuations into cells in order to induce precise, irregular firing patterns. I then showed that updating optogenetic stimulation based upon ongoing neural activity permits effective control of firing levels over a wide range of time scales. After describing these methods, I demonstrated their utility in a variety of experimental contexts, including investigations concerning the effects of connectivity on population encoding, somatosensory signal transduction *in vivo*, and the mechanistic underpinnings of homeostatic synaptic regulation.

Aside from their performance, a major reason that single protein (Boyden *et al.*, 2005) optogenetic tools have been so widely adopted in neuroscience research is their ease of use. Neuroscience experiments are subject to considerable practical constraints that limit the value of fragile or expensive techniques. Modern optogenetic tools are easy to use, low cost, high-performance, and can be applied to many experimental preparations. In this thesis, I sought to extend the capabilities of existing optogenetic technologies without introducing additional barriers that would hamper their adoption. For instance, in Chapter 2 and Appendices A- C, I provided extensive designs for low-cost alternatives to commercial hardware and software for multichannel electrophysiology and optical stimulation. To implement feedback control capabilities using these devices, I focused on widely used and well characterized algorithms that require minimal levels of real-time processing. Finally, in Chapters 5 and 6, I demonstrated how optogenetic feedback control can be used to address a range of

important experimental questions both *in vitro* and *in vivo*, using simple equipment and procedures. As a result, the technologies presented in this thesis offer greatly improved control of neural activity without incurring significant increases in cost or complexity for labs already engaged in electrophysiology research.

Even so, as with any design process, there are many avenues for the improvement of these technologies. The brain is a complex system and there is no guarantee that the simple technologies presented here will be sufficient to control more complex aspects of neural function. This task may require more complex hardware and software arrangements to achieve adequate performance. Additionally, control over variables more complex than firing rates will likely be required for closed-loop optical control to meet its full potential. Moreover, although significant emphasis was placed on balancing performance and cost constraints during the design of the technologies presented here, labs or individuals that do not have thousands of dollars to spend on equipment are still excluded from the use of optogenetics and multichannel electrophysiology techniques. Below I discuss how the technologies presented in this thesis might be extended by recent advances in electronics and bioengineering to contend with more complex control problems and to overcome bottlenecks in real-time hardware cost.

7.1 Extending optogenetic feedback control of firing activity

The population firing rate is the strongest (known) neural correlate of sensory information and motor action. Because firing levels are a key feature of every neural system, techniques for properly controlling them support a wide range of potential applications. Further specialization may be required to account for more detailed measures of firing activity than were covered in this thesis.

To understand why, consider a population of J cells, each of which contributes a set of spikes, which occur at times $t_{i,j}$, where i is the index of a single spike produced

by cell j. The time-dependent neuronal firing rate is given by

$$R(t) = \frac{1}{J\Delta T} \int_{t}^{t+\Delta T} \left[\sum_{i,j} \delta(\tau - t_{i,j}) \right] d\tau, \tag{72}$$

where ΔT is a small time interval and δ is the Dirac delta function. Two features of this equation indicate that population firing levels are not quite as simple as they initially seem. First, this equation involves two averages, one over the time interval ΔT and the other over the set of neurons, J, both of which are non-invertible operations. The temporal arrangement of action potentials that occur within ΔT are ignored by the averaging procedure, and spatial firing relationships are discounted over all time scales. For example, synchronous versus asynchronous population spiking could be mapped to the same firing level. Additionally, large asymmetries between the firing rates of units within the population can result in the same average rate as homogeneous firing. Even so, we found that different control algorithms and optical input signals could reliably evoke distinct patterns of firing activity during closed-loop firing rate control (Chapter 5). For instance, PI control using pulsed stimuli produced highly synchronous firing (Section 5.3.2), on-off control reproduced network bursting seen during spontaneous activity (Section 5.3.3), and PI control using continuously-varying optical power produced highly irregular firing patterns *in vivo* (Section 5.3.5). However, these aspects of firing were not actively regulated by the controller; they were uncontrolled activity features that emerged via the implementation of particular algorithms and optical inputs. Therefore, we were not able to enforce strict performance bounds on these features of neural activity during closed-loop control.

More sophisticated control algorithms and optical stimulation hardware might be capable of controlling finer scale spatial or temporal features of neural activity in constituent neurons. An important feature of optogenetic tools is their ability to use genetic specificity to circumvent the need for spatially-modulated stimuli in order to manipulate activity levels in particular cellular subpopulations. However, this does

not preclude the usefulness of spatial light modulation for improving optogenetic feedback control (Reutsky-Gefen *et al.*, 2013; Leifer *et al.*, 2011; Stirman *et al.*, 2011). On the contrary, studies have effectively used closed-loop multisite electrical stimulation to control network firing levels while desynchronizing spiking activity (Wagenaar *et al.*, 2005). If spatial light modulation was incorporated into our feedback controller in a similar fashion, then closed-loop optical stimulation could potentially be used to control firing in unstable tissue, which does not seem to be possible with spatially uniform stimulation (Figs. 37, 36). Additionally, by directing light towards the somata or axon initial segments of individual neurons during closed-loop control, light exposure, abnormal ionic conductances, and passive dendritic filtering might be minimized (Grossman *et al.*, 2010).

If optical firing rate control is to be relevant for use in sensory prosthetic devices, then it is important that it operates at timescales appropriate for effective communication with neural tissue. This highlights an additional issue with Eq. 72: the choice of ΔT. This simple parameter has been the cause of a great ongoing debate in the field of computational neuroscience (Rieke *et al.*, 1997). What value of ΔT is small enough such that most of the information content present in the time-varying firing rate is captured, but not so small that unnecessary real-time computation is performed? If ΔT is too large, critical information-bearing features of the time-varying firing rate could be missed. In some sensory systems, information is conveyed at the millisecond timescale (Rieke *et al.*, 1997; Kayser *et al.*, 2010). If this temporal resolution is required for effective transmission of synthetic sensory information, the technologies presented here may require increased real-time performance to be useful.

Finally, although this thesis presents several case studies that demonstrate the utility of optogenetic feedback control, these studies have only scratched the surface in terms of the potential applications for this technology. In Chapter 6 I showed how optogenetic feedback control could be used to restore network firing levels during

the blockade of AMPAergic synapses. This was just one of many possible combinations. For instance, an alternative experiment might be to increase AMPAergic synaptic transmission using an allosteric modulator of the AMPA receptor, such as cyclothozide, while using closed-loop optogenetic inhibition to clamp network activity. Another option would be to indirectly control firing in excitatory cells by optogenetically actuating inhibitory cells within the network. Additionally, although we successfully controlled activity in somatosensory thalamus of rats during ongoing whisker stimulation, we did not investigate how this might affect sensory processing. For instance, how are the spatial characteristics of the cortical response affected by clamping activity within ventral posteromedial nucleus (Section 5.3.5) or reticular thalamus to various basal levels during whisker stimulation (Wang *et al.*, 2012)? Can real-time control of thalamic activity be used to control cortical sensory discrimination (Wang *et al.*, 2010)? The general importance of population firing levels for dictating neural function suggests that there will be an abundance of questions for which high-performance firing control is useful. I expect that in the years to come, the technical demands of these studies will guide the improvement of the methods presented in this thesis.

7.2 Beyond firing rate control

In the broadest sense, neural control entails the regulation of any measurable aspect of neural activity to within specified performance bounds. An obvious limitation of the technologies presented here is that they focus on controlling firing levels, which is just one of many important features of neural activity. Recent advances in biosensors and specialized optogenetic tools may allow for closed-loop optical control of neural signaling processes other than firing levels, extending the usefulness of the concepts presented in this thesis to a more complex set of control problems.

Neurotransmission is a ubiquitously important form of neural activity. Recently,

technologies have been introduced that may enable all optical, closed-loop control of neurotransmission. Ionotropic glutamate-binding receptors (iGluRs) coupled with fluorescent reporters provide millisecond time-scale readout of glutamatergic neurotransmission at individual synapses (Marvin *et al.*, 2013). Additionally, there are now several technologies available for direct optogenetic control of neurotransmssion. One approach showed that iGluRs conjugated with an allosteric photoswitch enabled optical glutamate receptor activation (Volgraf *et al.*, 2006). Another study used chromophore-assisted light inactivation of the SNARE complex, and the resultant disruption of neurotransmitter vesicle exocytosis, to optically inhibit arbitrary types of neurotransmission (Lin *et al.*, 2013). Together, these tools provide sensors and actuators that could conceivably be used for direct, closed-loop control of neurotransmission.

Aside from firing levels of constituent neurons, there are other electrical signatures of brain activity that may be readily controlled using real-time optogenetic feedback. Many studies postulate the oscillatory coherence between neural circuits plays an important role in attention, and may provide a flexible communication channel between neuronal populations (Fries, 2005). A recent computational study explored the potential of optogenetic feedback to control the relative phase of local field potentials recorded from two neuronal subpopulations, with the goal of controlling their phase coherence (Witt *et al.*, 2013). This approach may allow more straightforward, 'bottom-up' investigations of attention by examining the behavioral effects of forced coherence between different brain regions.

Aside from electrochemical signaling measurements, more abstract neural activity features may be used to drive closed-loop optogenetic stimulation. Many studies concerning neural sensory processing investigate how statistical features of the stimuli affect the encoding process. A long-term goal of this research is to inform the design of sensory prosthetic devices that use synthetic actuation of sensory circuits to

bypass non-functional sensory modalities. However, neural dynamics are highly non-stationary, and the optimal transformation of sensory measurements to stimulation is likely to change depending on brain state and with learning. Real-time measurements of response discriminability may be necessary for optimizing stimuli in order to achieve a robust synthetic communication channel with sensory circuits during ongoing alterations in brain state (Wang *et al.*, 2010; Stanley, 2013).

Finally, newly developed optogenetic tools have recently been used for synthetic manipulations of context-dependent memories in mice (Ramirez *et al.*, 2013). The use of optogenetic methods for influencing memory formation, for instance to improve context-dependent memory recall, is an exciting possibility. For example, perhaps navigational performance can be improved using optogenetic activation of reward circuits triggered by real-time decoding during hippocampal place-field replay events (Bendor and Wilson, 2012). Although synthetic memory control may be out of reach using current methods and technologies, the successful optogenetic manipulation of existing memories offers an enticing preview of what may become possible using closed-loop optogenetic control.

7.3 Democratizing real-time hardware

The technologies presented in this thesis were designed to minimize monetary and technical barriers that prevent widespread adoption. For instance, NeuroRighter (Chapter 2) costs about an order of magnitude less than a comparable commercial alternative. However, NeuroRighter, and systems like it (Lin *et al.*, 2010; Wagenaar *et al.*, 2006a), rely on commercial data acquisition cards that are expensive, difficult to scale, and are not explicitly designed for real-time operation. Additionally, low-level, on-board processing is often accessible only through proprietary software drivers, which offer limited options for full customization. These facts indicate that although the technologies presented here to do not impose additional financial burdens beyond

those of existing electrophysiology equipment, they do not greatly alleviate these burdens either. This is unfortunate because there is a general need for increased throughput in neurophysiology experiments, which are notorious for their lack of statistical power (Button *et al.*, 2013). In order for an average lab to operate many electrophysiology experiments simultaneously, a drastic reduction in cost is required.

Open-hardware projects, such as the Arduino[1] microcontroller platform, have demonstrated how competition and growth within the semiconductor industry can be leveraged for applications beyond those originally intended. If open-access neurophysiology hardware could circumvent the use of ready-made scientific instruments altogether, it would be more capable of reducing cost constraints and increasing real-time performance standards. Recent advances in bioacquisition hardware, mobile computing technologies, and real-time computing have opened new possibilities for substantially lowering the cost of high-performance, real-time control hardware.

There are currently more than 1 billion smartphones in use around the world. The explosive growth of the mobile computing industry has driven the development of powerful, low-cost chipsets for embedded processing. The ARM® architecture encompasses a family of reduced instruction set processor designs that are low-cost, high-performance, and often include powerful co-processors for digital signal processing (e.g. DSPs) or peripheral interfacing (e.g. FPGAs). Further, recent advances in single-chip biosignal amplification, filtering, and digitization have vastly reduced the cost and complexity of multichannel data acquisition (Du *et al.*, 2011)[2]. Finally, there have been several recent improvements in the stability and usability of real-time development tools for the Linux operating system[3] and software for utilizing hard real-time processing capabilities for electrophysiology research[4] (Lin *et al.*,

[1] `http://www.arduino.cc/`

[2] `http://www.intantech.com/`

[3] `https://www.kernel.org/pub/linux/kernel/projects/rt/`, `http://www.xenomai.org/`

[4] `http://www.rtxi.org/`

2010). Together, these technologies form the basic ingredients for a new generation of electrophysiology tools. They provide the performance required for the most technically demanding neurophysiology experiments, combined with the price-point and mass appeal of 'hacker'-friendly open hardware projects. I expect that this will soon enable a democratization of cutting-edge electrophysiology research, making the required materials for ultra-precise manipulation of neural circuity available to small labs, classrooms, and motivated individuals.

APPENDIX A

NEURORIGHTER USAGE AND EXAMPLES.*

Here I provided extended usage information for the NeuroRighter electrophysiology system. Aside from this text, NeuroRighter's code repositories, user's forum, and reference manuals will be available in electronic form for the foreseeable future on several websites:

- `https://code.google.com/p/neurorighter/`: **The NeuroRighter code repository.**
- `https://sites.google.com/site/neurorighter/`: **The NeuroRighter System Reference Manual/Wiki**
- `https://groups.google.com/forum/#!forum/neurorighter-users`: **The NeuroRighter User's Forum**
- `https://potterlab.gatech.edu/main/neurorighter-api-ref/`: **The NeuroRighter API Reference**

A.1 Scripted output

Real-time plugins have on-the-fly access to NeuroRighter's output servers. However, NeuroRighter's output servers can also be controlled in open-loop mode using predefined stimulation scripts, referred to here as 'scripted output'. Scripted output allows the generation of continuous, non-periodic, uninterrupted output streams on all of NeuroRighter's available output channels (Fig. 5, Table 1, and see Chapter 4 which

*Newman, J.P., Zeller-Townson, R, Fong, M.-f., Desai, S.A., Gross, R.E., Potter, S.M. Closed-loop, multichannel experimentation using the open-source NeuroRighter electrophysiology platform. *Front. Neural Circuits* **6:98**, 2013.

uses this feature extensively). Using scripted output, manipulation of electrical stimulation lines, analog outputs, and digital outputs occurs with 10 μs precision relative to the start of a clock-synchronized recording session. Scripts can be generated within MATLAB(R) (Mathworks, Natick, MA) or Octave[1] using three functions provided with a standard NeuroRighter installation: `makestimfile.m`, `makeauxfile.m`, and `makedigfile.m`. Each of these functions contains documentation in their file header, which can be accessed using the '`help`' command.

In the following example, we generate two output files that control NeuroRighter's analog and digital output streams, respectively. The first file produces 10 changes in the voltage of analog output channel 0 (AO.0). The second file encodes the voltage changes on AO.0 using the first 8 bits of the digital output port 0 (P0.0-7). Changes in the voltage of AO.0 and port state of P0.0-7 will occur once a second relative to the start of the recording, on the same 100 kHz clock edge.

```
t = (1:10)';                % 1,2,3,...,10 seconds
a = rand(10,1);             % 10 random voltages
c = zeros(size(a));         % use channel AO.0
d = ceil(a*255);            % encode 'a' with 8-bit resolution on P0.0-7

makeauxfile('myAuxTest',t,c,a);
makedigfile('myDigTest',t,d);
```

This MATLAB script produces two files, `myAuxTest.olaux` and `myDigTest.olaux`, which can be loaded into NeuroRighter's GUI for execution. The user must enable analog and digital output lines in NeuroRighter's hardware settings in order for these scripts to function (Chapter 2; Fig. 52(c)). This example illustrates an advantage of having direct access to the analog and digital output lines: because all physical inputs and outputs to and from NeuroRighter are synchronized to the same hardware clock, the digital output that encodes changes in analog voltage AO.0 can be recorded instead of AO.0's raw voltage. Since only changes in the state of the digital port are

[1] `http://www.gnu.org/software/octave/`

recorded, this vastly reduces the amount of disk space required to encode the delivered output stream.

Aside from the manipulation of the NI cards' analog and digital output lines, scripted protocols can be created to drive NeuroRighter's all-channel electrical microstimulation board. Below, we provide a MATLAB script that produces the scripted stimulation protocol used to generate Fig. 5.

```
% Stimulation protocol with 1 second epochs of a new or repeated
% realization of spatially uniform random, temporally Poisson,
% voltage-controlled square wave stimuli. New and repeated stimulation
% trials are interleaved in time with no down time between trials.

lambda = 15;                        % Poisson rate parameter (1/seconds)
num_trials = 100;                   % Number of random realizations
start_time = 60;                    % Protocol start time (seconds)

tot = start_time;                   % Total time;
T = [];                             % Stimulation times
C = [];                             % Stimulation channels

% Uniform random points over defined time epoch is equivalent
% to Possionian point process (exp dist. of times between stimuli).
rept = rand(lambda,1);
repc = 59*rand(size(rept));

for i = 1:num_trials

    % New random realization
    T = [T;tot(end) + rand(lambda,1)];
    C = [C;59*rand(size(rept))];
    tot = tot + 1; % 1 sec. increment

    % Repeated realization
    T = [T;tot(end) + rept];
    C = [C;repc];

end

% Waveform is +-0.75 volt, 400 us/phase, postive-first, square-wave.
% This can also be used as a current waveform by adjusting NR's
% hardware settings to enable current-controlled stimulation.
fs = 1e5;
w = [zeros(1,5) 0.75*ones(1,40) -0.75*ones(1,40) zeros(1,5)];
W = w(ones(size(T)),:);

% Write the file
makestimfile('pois-stim-protocol',T,C,W)
```

A.2 Using the real-time API

A real-time plugin is an externally compiled class library, written in C♯ or some other .NET supported language, that can be used for a wide variety of tasks. For instance, plugins allow on-the-fly manipulation NeuroRighter's electrical stimulation board as well as analog and digital output lines, with 10 μs precision. Plugins can also be used to change NeuroRighter's outputs as a function of incoming data, such as neural recordings, auxiliary analog inputs, or digital input channels in order to close the loop around neural tissue. Since plugins are externally compiled programs, they can be created without editing NeuroRighter's source code, and can reference third party libraries, such as those available for sending information over the Internet or for executing MATLAB code. In the following section we demonstrate the creation and use of real-time plugins with NeuroRighter.

A.2.1 Using a pre-compiled real-time plugin

A compiled plugin is a class library, or, in Microsoft parlance, a 'Dynamic-linked Library' (DLL) file. A DLL is a type of Windows file which contains compiled code that cannot be executed by itself (like an executable or '*.exe' file), but can be referenced or used by executable code. To start, we will detail the usage of a plugin that has already been complied and exists as a DLL file. The compiled DLLs that were used in the case-studies in Section 2.4 of Chapter 2 are available online[2], an can be used as described in the following paragraphs.

After downloading a pre-compiled plugin, we need to configure NeuroRighter's hardware settings to match the details of our recording system (Section 2.3.2.1; Table 1). Figure 52 outlines this process for a 64-channel MEA1060-Up amplifier (Multichannel Systems, Reutlingen, Germany) with a 1200X passband gain. First we enter

[2] `http://code.google.com/p/neurorighter/downloads/list`

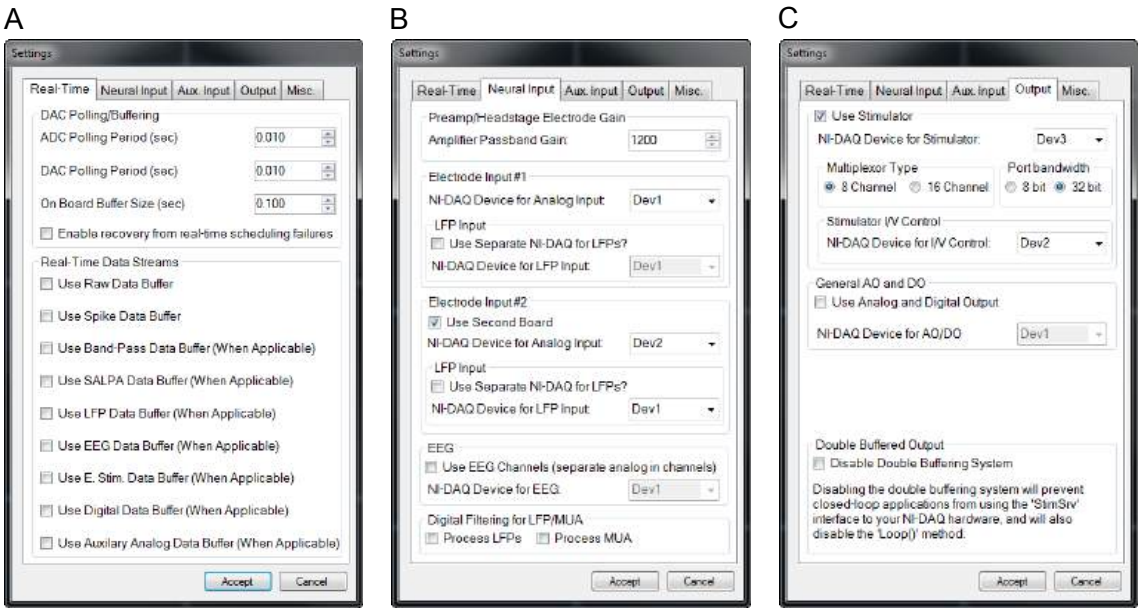

Figure 52: Configuring hardware settings for a real-time plugin. (A) The 'Real-Time' tab is used to adjust the hardware polling period and configure NeuroRighter's data servers. **(B)** The 'Neural Input' tab is used to configure multichannel amplifier settings and specifies which NI boards are used to acquire raw, LFP, and EEG voltages. **(C)** The 'Output' tab is used to configure electrical stimulation as well as generic analog and digital output lines.

the 'Real-time' tab (Fig. 52(a)) where we can specify the A/D and D/A polling periods (which determine the loop speed of the plugin), and where we select which data servers we want to expose to the plugin. For example, to run the closed-loop reaction time case-study (Section 2.4.1), we only needed to select the 'Spike Data' buffer. Data servers are inactive by default, in order to decrease computational overhead and memory requirements. Next, in the 'Neural Input' tab (Fig. 52(b)), we supply our amplifier gain and select the NI boards being used to route neural signals. Finally, in the 'Output' tab, we can define how to deliver electrical stimuli and whether we want to use generic digital or analog output lines.

After configuring hardware and streaming settings, we can load the plugin library. To do this, we open NeuroRighter's 'Stim/Output' tab (Fig. 53(a)) and then navigate to the 'Real-time Plugin' box (Fig. 53(b)). A plugin library is a collection of plugin classes that are all stored in the same file. To load a library, we click the '...' button in the Real-Time Plugin box and select the DLL file that we have downloaded or

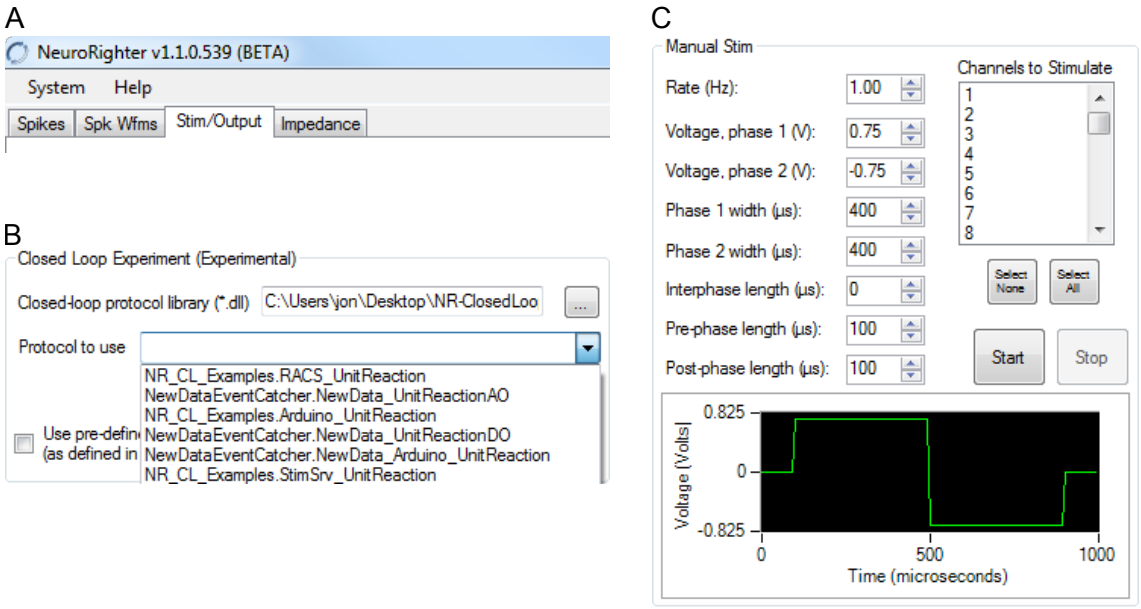

Figure 53: Loading a plugin library. **(A)** Plugin libraries are loaded through the 'Stim/Output' tab on the main NeuroRighter interface. **(B)** Once a plugin library is loaded, all the classes it encapsulates are exposed for execution. **(C)** Simple stimulus waveforms can be designed in NeuroRighter's GUI and accessed from a closed-loop plugin.

compiled. After we select a library, the drop down list underneath the load button is populated with the names of the individual real-time plugin classes that are stored inside the selected library.

After selecting the plugin we want to execute, we click the 'Start' button in the 'Real-Time Plugin' box to activate the plugin and begin data acquisition. The plugin can be interrupted at any time by clicking the 'Stop' button in the 'Real-Time Plugin' box. A final detail worth mentioning is that plugins can use stimulus waveforms that are designed within the NeuroRighter GUI (Fig. 53(c)) if the plugin references this `PredefinedWaveform` in its code. Referencing this GUI-defined waveform is a way to quickly configure stimulation parameters without writing any code or recompiling the plugin library.

A.2.2 Writing a real-time plugin

The source-code for all plugins used as case-studies in Chapter 2 text are available online[3]. Additionally, the code used to produce the first case-study from Chapter 2 (Section 2.4.1) is provided at the end of this appendix, in Section A.4. In this section, we walk through the steps required to write a custom real-time plugin for NeuroRighter.

Creating a real-time **plugin library** consists of creating a class library, writing a **plugin class** within that library, and adding special methods to the plugin class that will be activated by NeuroRighter. All plugin classes follow a similar code template, regardless of their complexity and have automatic access to NeuroRighter's data servers as well as NeuroRighter's stimulation servers. Different integrated development environments (IDEs) can be used to write a plugin library. Two good development options are Microsoft Visual Studio (Microsoft, Redmond, WA) or the open-source and free MonoDevelop[4]. The steps required for creating a plugin do not change significantly for different IDE options.

Our first step to write a new plugin is to create a new project that will contain our plugin library. This can be done by creating a new project of the type 'Class Library' in your IDE of choice (this should be something similar to: file→ new→ project→ class library). In general, the difference between an executable and a class library is that a class library lacks a generic entry point (nominally a '`main()`' method) from which to start code execution. Instead, it requires a parent executable to determine how the library code should be entered and executed at runtime. In our case, the parent executable is NeuroRighter, so we must make our newly created class library aware of NeuroRighter's existence. To do this, we reference the NeuroRighter

[3] `http://code.google.com/p/neurorighter/source/browse/NR-ClosedLoop-Examples/`
[4] `http://monodevelop.com/`

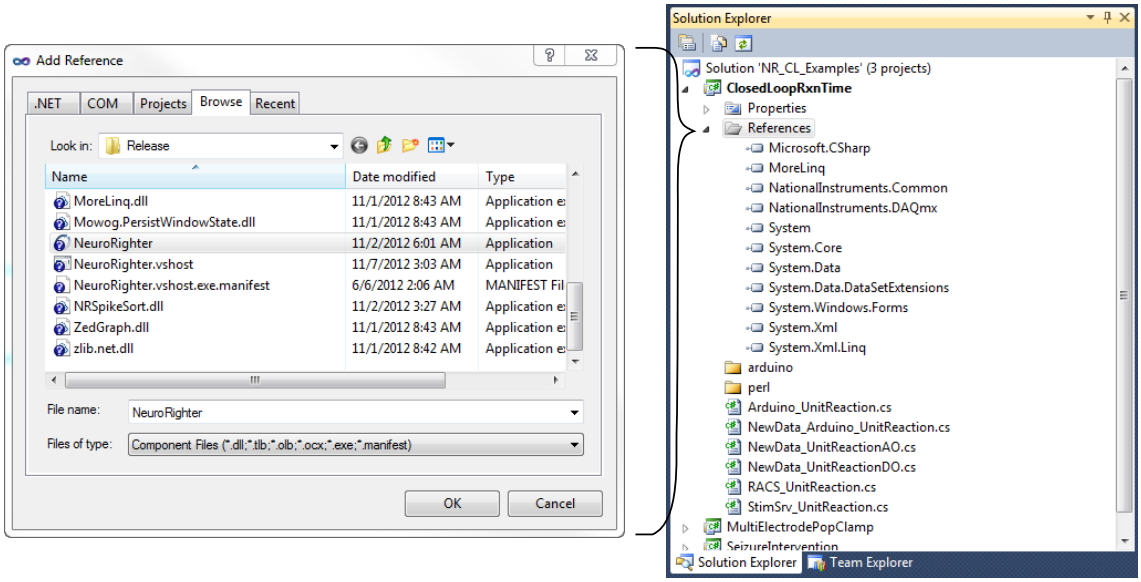

Figure 54: Referencing the NeuroRighter executable to create a real-time plugin.

executable from our library by adding NeuroRighter.exe to the 'References' list associated with our project (Fig. 54). This exposes NeuroRighter's public namespaces to our library, which then can be used by individual classes with the '`using`' keyword. These namespaces are described in Table 2, and referred to their as 'packages' to avoid programming jargon, and are reiterated here.

- **NeuroRighter.NeuroRighterTask** This namespace must be referenced in every real-time plugin class, as it contains the `NRtask` abstract class that all plugin classes must implement to integrate with NeuroRighter while it is running.
- **NeuroRighter.Server** This namespace provides access to NeuroRighter's `NRDataSrv` data server object and `NRStimSrv` output server object.
- **NeuroRighter.DataTypes** This namespace provides several data types that are used by `NRDataSrv` and `NRStimSrv` (e.g. `SpikeEvent`, `AuxOutEvent`, etc.).
- **NeuroRighter.dbg** This namespace provides access to a debugging tool that allows user messages to be logged to a text file along with timing information that is generated by NeuroRighter during plugin execution.

Next, we create a new class that will define our plugin. A plugin class inherits functionality from the base-class `NRTask` which provides automatic access to the following features.

- Overrideable methods for setting up (the `Setup()` method), executing (the `Loop()` method), and cleaning up (the `Cleanup()` method) a real-time loop within NeuroRighter.

- Access to NeuroRighter's server objects `NRDataSrv` and `NRStimSrv`, which are used to read from and write to hardware. Manipulation of the objects requires including the `Server` namespace, as mentioned above.

- Information concerning the state of the NeuroRighter executable, such as whether or not it is currently recording data and the file-paths being used to save data.

The basic structure of a plugin class mimics high-level programming languages for micro-controllers, such as Arduino[5]. Below, we provide an example of a very simple plugin.

```
using NeuroRighter.Output
namespace NRpluginExample
{
  public class HelloWorld: NRtask
  {
    override void Setup()
    {
      Console.WriteLine("Hello, World!");
    }

    override void Loop()
    {
      Console.WriteLine("I'm still here, World!");
    }

    override void Cleanup()
    {
      Console.WriteLine("Goodbye, World!");
    }
  }
}
```

In this example, `NRpluginExample` is the name of the library that is being created, and `HelloWorld` is the name of a single plugin class within that library. When we are finished writing our class, we can compile the class library. In our example, this

[5] `http://arduino.cc/en/`

would result in NRpluginExample.dll, which can be loaded into the NeuroRighter GUI as described above.

Once loaded into NeuroRighter, the 'Start' button is clicked which starts the plugin's execution along with data acquisition in NeuroRighter. When start is clicked, the `Setup()` method is called a single time. In our example, this would result in "Hello, World" being printed to the console (System→ Show Console, from within NeuroRighter). After the `Setup()` method finishes, NeuroRighter's input and output servers are activated, and the `Loop()` method is called periodically (Fig. 5), at a frequency specified by the DAC polling period (Fig. 52). This would result in "I'm still here, World!" being printed to the console many times, in rapid succession. Execution would continue until the user clicks the 'Stop' button, which calls the `Cleanup()` method. At this point our example plugin would display the message "Goodbye, World!" to the console and NeuroRighter's input and output servers would shut down.

A.2.3 Event-based methods

Note that, in contrast to the example above, a plugin is not required to override any of the three base methods supplied by the `NRTask` class. For example, instead of using the `Loop` function, which is executed periodically by NeuroRighter's output servers, we can execute code upon the capture of new data into NeuroRighter's input servers using `NewData` events (Sections 2.3.2.2 and A.4.2). For example, the following code snippet will write the line "New spikes captured" to the console immediately after new spikes are pushed to the `SpikeSrv` data stream. As shown in Fig. 7, this method provides the lowest feedback latency.

```
override void Setup()
{
  // Subscribe to the NewData event on the SpikeSrv data server
  NRDataSrv.SpikeSrv.NewData +=
    new EventDataSrv<NeuroRighter.DataTypes.SpikeEvent>.
      NewDataHandler(SpikeSrv_NewData);
}

// This method is called every time the SpikeSrv.NewData event fires
private void SpikeSrv_NewData()
{
  Console.Writeline("New spikes captured!");
}
```

A.2.4 Reading data within a plugin

Reading data streams within a plugin is performed using the `NRDataSrv` object. `NRDataSrv` contains a set of servers that buffer the most recent data collected by NeuroRighter. `NRDataSrv` encapsulates two general types of data, continuous data and packet data. **Continuous data** is defined by an NxM dimensional array, where N is the channel count, and M is the sampling frequency multiplied by the buffer's duration. Continuous data servers buffer raw voltage values from electrodes, auxiliary analog streams, or filtered outputs from the spike, SALPA, LFP and EEG streams. NeuroRighter's continuous data servers are listed in the top section of Table 8. **Packet data** is defined by asynchronous physical events, that are not necessarily temporally periodic (e.g. detected spikes). Like continuous data buffers, packet buffers contain data over the time period specified in hardware settings but, since they are not sampled continuously, the amount of data in these buffers can fluctuate. For example, if the spike detection rate increases, the number of spikes in `NRDataSrv.SpikeSrv` will increase. NeuroRighter's packet data servers are listed in the bottom section of Table 8.

All data servers are null by default in order to decrease computational overhead and memory requirements. They can be activated using the hardware settings GUI (Fig. 52(a)). The amount of data that is buffered by each server object can also be

Table 8: NeuroRighter's data servers. All servers are null unless activated using the hardware settings GUI.

	Server Name	Description
Continuous Data Servers	`NRDataSrv.AuxAnalogSrv`	Provides access to data from auxiliary analog channels
	`NRDataSrv.EEGSrv`	Provides access to data from EEG channels
	`NRDataSrv.LFPSrv`	Provides access to data from LFP channels
	`NRDataSrv.RawElectrodeSrv`	Provides access to raw electrode voltages.
	`NRDataSrv.FilteredElectrodeSrv`	Provides access to data produced by the 'spike filter' which is used to pass signals from ∼100 to 5000 Hz.
	`NRDataSrv.SalpaElectrodeSrv`	Provides access to data processed by the SALPA filter, which is used for rapid electrical artifact subtraction (Wagenaar and Potter, 2002)
Packet Data Servers	`NRDataSrv.SpikeSrv`	Provides access to recently detected spikes (containing time, channel, waveform, unit number, etc.)
	`NRDataSrv.AuxDigitalSrv`	Provides access to the state changes recently detected on the auxiliary digital input lines (time and port state)
	`NRDataSrv.StimSrv`	Provides access to recently recorded electrical stimuli (time, channel, voltage, etc.)

set in the hardware settings GUI. The default buffer history is 1 second. This means that at any point in time, the plugin has access to data that is up to 1 second old. If a plugin needs access to older data, hardware settings must be configured to allow for a longer buffer or the plugin must implement its own buffer to save past data values.

To read from continuous- or packet-based data servers, the `ReadFromBuffer` method is used. The `ReadFromBuffer` method is an attribute of each server object that takes start and stop sample indices as input arguments. For example, to read all the spikes that occurred between times 10 seconds and 12 seconds relative to the start of the recording, we could use the following code snippet:

```
// Convert required read start and stop times to samples
ulong start = (ulong) (10*NRDataSrv.SpikeSrv.SampleFrequencyHz);
ulong stop = (ulong) (12*NRDataSrv.SpikeSrv.SampleFrequencyHz);

// Read samples from the buffer
EventBuffer<SpikeEvent> recordedSpikes;
recordedSpikes = NRDataSrv.SpikeSrv.ReadFromBuffer(start, stop);
```

At this point, all the spikes recorded between seconds 10 and 12 are assigned to the `recordedSpikes` object (assuming they were available in the buffer when the read call was made). To find what samples are currently available, the `EstimateAvailableTimeRange()` method can be used. Alternatively, as described above, the data server can inform listening processes, like our plugin, whenever new data is available using a `NewData` event.

A.2.5 Generating output from a plugin

The easiest way to change NeuroRighter's outputs from within a plugin is to use the `NRStimSrv` object, which is automatically provided to classes that are derived from `NRTask`. This is not the only option to produce output with NeuroRighter. Standard communication protocols (TCP/IP, USB, RS232, etc.) as well as direct communication with the NI boards can also be used (see, for instance, Sections A.4.2 and A.4.3). Analogous to `NRDataSrv`, `NRStimSrv` encapsulates server objects that can be used to generate physical outputs from within a plugin. These servers are:

- **NRStimSrv.AuxOut** This server is used to write values to the analog auxiliary channels.
- **NRStimSrv.DigitalOut** This server is used to write digital values out to the auxiliary digital port.
- **NRStimSrv.StimOut** This server is used to write electrical stimuli.

Writing to these servers is accomplished using the `WriteToBuffer` method. For example, if we wanted a plugin to generate electrical stimuli at times 1.2, 1.5, 1.7 seconds, on channels 3, 7, and 9, using the waveform specified in the 'Manual Stim' GUI (Fig. 53(c)), we could use the following code segment within our plugin class:

```
// Define stimulus times and channels
double[] times = {1.2,1.5,1.7};
int[] channels = {3,7,9};

override void Setup()
{
  // Here, we access the waveform created within NR's 'Manual Stim' GUI
  double[] waveform = PredefinedWaveform;

  // Grab the output sampling frequency
  double fs = NRStimSrv.SamplingFrequencyHz;

  List<StimulusOutEvent> stimuli = new List<StimulusOutEvent>();
  for (int i = 0; i < times.Length; i++)
  {
    stimuli.Add(new StimulusOutEvent(channels[i],(ulong)(times[i]*fs), waveform));
  }

  // Add the stimuli to the buffer - one time write since we are in Setup()
  NRStimSrv.StimOut.WriteToBuffer(stimuli)
}
```

Like when reading data from input servers, the timing of these outputs are measured in samples since the experiment began. All output servers operate with a hard-coded 10 μs precision. To find the next sample available for writing on a particular output buffer during a real-time protocol, the `GetTime()` or `GetCurrentSample()` methods can be used.

For more information regarding the usage and creation of real-time plugins with NeuroRighter, visit NeuroRighter's website and examine the example code provided in Section A.4.

A.3 Spike detection and sorting with NeuroRighter

A.3.1 Spike detection and validation

Putative spikes are detected as voltage samples, $v_k[t]$ for which

$$|v_k[t]| > \gamma V_k^{\mathrm{RMS}}, \tag{73}$$

where γ is a user-defined coefficient (Table 9). When the detection criterion is met, $v_k[t]$ is searched for a voltage peak or trough following the threshold crossing. V_k^{RMS} is defined as the average of lowest 10% of RMS values calculated from a group of 100 millisecond data windows of voltage values taken from channel k. This method prevents overestimates of V_k^{RMS} by excluding windows with large amounts of spiking activity from the RMS calculation (Wagenaar *et al.*, 2006a). V_k^{RMS} can be a fixed value, based upon the first 10 seconds (100 windows) of a recording or the 10 seconds after the user clicks the 'Retrain' button. Alternatively, V_k^{RMS} can be calculated adaptively using a sliding 10 second window to adapt to changes in channel noise levels. Following detection, a short voltage 'snippet', aligned at the absolute voltage peak, is then extracted from the raw trace. The number of voltage samples included in each snippet is user-defined (Table 9).

Following detection, spike snippets are validated as true action potentials using

Table 9: User defined parameters for spike detection, validation, and sorting.

	Parameter	Description	Typical Value
Detection	Threshold (γ)	RMS multiplier defining detection threshold	4-7
	Pre-spike time	Time before spike to store in snippet	0.5 msec
	Post-spike time	Time following spike to store in snippet	1.5 msec
	Noise estimation algorithm	Method used to estimate RMS noise	adaptive/fixed
	Spike alignment algorithm	Method used to align spikes	align by peak
Validation	Min. spike width	Minimum allowable spike width	80 μsec
	Max. spike width	Maximum allowable spike width	1500 μsec
	Max spike amplitude	Maximum allowable peak-to-peak amplitude	500 μV
	Min. spike slope	Minimum average absolute spike slope	2-5 μV/samp.
	Dead time	Detection pause following validation	0.5-1 msec
Sorting	Projection type	Method to project spike snippets into feature space	PCA
	Projection dimension	Dimensionality of feature space projection	2
	Max. K	Maximal number of units per recording channel	4
	P-value	P-value to consider a classified spike an outlier	0.01

a series of tests based on waveform slope, width and peak-to-peak amplitude (Figure 55, Table 9). If a spike is successfully validated, a detection pause is enforced on the channel of origin to prevent multiple detections of a single spike that contains multiple peaks. Following spike validation, the spike snippet and associated information (time of occurrence, channel, etc.) is pushed to the `SpikeSrv.Buffer` data stream (Table 1).

A.3.2 Spike sorting

NeuroRighter uses an automated Gaussian mixture modeling algorithm to classify spikes based on low-dimensional features of their waveform shape (Xu and Wunsch, 2009). The algorithm is implemented using the Aforge.NET and Accord.NET libraries for machine learning[6]. The following explanation of the spike sorting algorithm applies to a single recording channel. During an actual recording, spike sorting is performed for all recording electrodes that have been enabled in the hardware settings GUI.

First, a training data set is collected. This consists of a set of spike snippets, $\{X_n\} \in \mathbb{R}^D$ where D is the number of voltage samples in each waveform. After a user-defined number of spikes have been collected, the classifier can be trained. To do this, waveforms are first projected into a low dimensional feature space, $\{Y_n\}_{n=1}^{N} \in \mathbb{R}^M$,

[6] `http://accord-net.origo.ethz.ch/` and `http://code.google.com/p/aforge/`

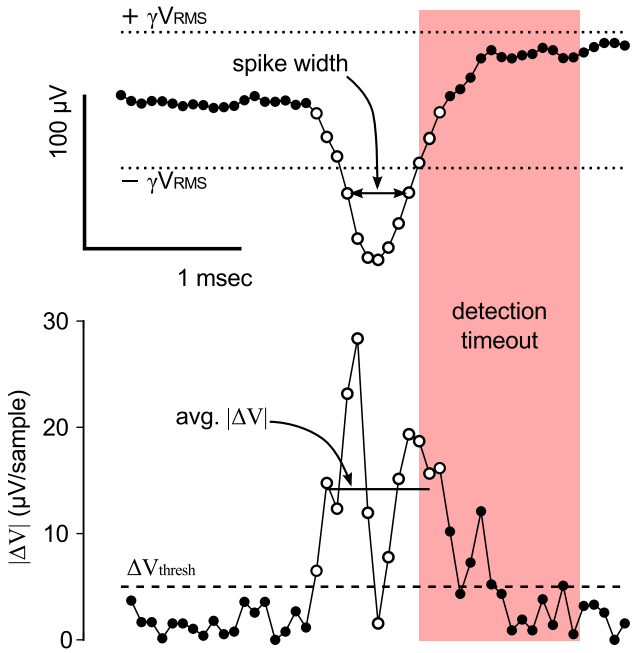

Figure 55: Spike detection and validation in NeuroRighter is a multi-step process. Spikes are detected as voltage events that exceed the estimated RMS noise level for a given channel (Top). Putative spikes are then validated using *ad hoc* tests based on the spike width and rectified slope (Bottom).

$M < D$ using one of several available methods (principle component analysis, take the peak voltage value, or take the peak voltage and and after-polarization amplitude). Next, a mixture of K Gaussians is fit to $\{Y_n\}_{n=1}^{N}$ using the expectation maximization algorithm (EM) (Dempster and Laird, 1977), initialized using K-means clustering. Following EM convergence, the minimum description length (MDL) is calculated as

$$\mathrm{MDL}(K) = \frac{1}{2} N_p \log(N * M) - \log p_y(y|K, \theta), \tag{74}$$

where N_p is the number of free parameters in θ and $\log p_y(y|K, \theta)$ is the maximized log-likelihood of the training set $\{Y_n\}_{n=1}^{N}$ according to the Gaussian mixture parametrized by θ. MDL therefore weighs model complexity against the goodness-of-fit of a given mixture (Xu and Wunsch, 2009). The value of K is iteratively decremented, and the model fitting and calculation of the MDL proceeds for each decreased model order. The value of K, and corresponding mixture, that minimizes the MDL is selected for online classification. The starting value of K is user-settable.

Following training, spikes are classified online. The unit number of each projected

datum is defined as,

$$\kappa_n = \arg\max_K p_y(y_n|K,\theta). \tag{75}$$

The Mahalanobis distance between the classified datum, y_n and its putative component distribution, $f_\kappa(y)$, is then calculated as

$$d_n = [(y_n - \mu_\kappa)^\intercal C_\kappa (y_n - \mu_\kappa)]^{1/2}. \tag{76}$$

Here, (μ_κ, C_κ) are the (mean, covariance) pair for $f_\kappa(y)$. A Pearson's χ^2-test is performed to detect outliers in comparison with a χ^2 distribution fit to the Mahalanobis distances derived from the training data (Filzmoser, 2004). Outliers remain unsorted (they are assigned to $\kappa_n = 0$).

A.4 Latency measurement plugin code

Below we provide the code to produce the three NeuroRighter plugins used to measure NeuroRighter's closed-loop response latency in Section 2.4.1. Each example is a C♯ class file that is derived from the `NRTask` base class. After making the proper API references and inheriting methods from `NRTask`, calls can be made to NeuroRighter's input and output servers. Each of these classes follows one of the basic structures outlined in code listing 1 and was created using the steps detailed in Section A.2. Aside from these examples, the code used to produce all case-studies presented in Chapter 2 (with the exception of the Silent Barrage robotic embodiment) are available on NeuroRighter's code repository[7].

A.4.1 StimSrv-based real-time loop

```
/// <summary>
/// This class uses StimSrv to produce a series of 32-bit digital pulses in
/// response to spikes produced by two, pre-specified units. Each pulse encodes
/// the unit number that produced the spike and the time (32-bit sample integer)
/// that the spike occurred. This method uses double buffering and therefore
/// results in a large reaction latency.
/// </summary>

// References
using System;
using System.Collections.Generic;
using System.Linq;
using System.Text;
using NeuroRighter.NeuroRighterTask;
using NeuroRighter.DataTypes;
using NeuroRighter.Server;
using NeuroRighter.Network;

namespace NR_CL_Examples
{
    class StimSrv_UnitReaction : NRTask
    {
        // Unit that we will react to with a digital pulse
        private int[] units = { 1, 2 };

        // Internal variables
        private ulong lastSampleRead = 0;
        protected EventBuffer<SpikeEvent> newSpikes;
```

[7] http://code.google.com/p/neurorighter/source/browse/NR-ClosedLoop-Examples/

```
ulong nextAvailableSample;

// When using StimSrv, most setup tasks are taken care of automatically.
protected override void Setup()
{
    nextAvailableSample = 0;
}

// Loop is called periodically by the double buffering system when the
// read-head has exhausted all the samples in one of the buffers and
// that buffer is made available for writing.
protected override void Loop(object sender, EventArgs e)
{
    // First, figure out what history of spikes we have
    ulong[] spikeTimeRange =
            NRDataSrv.SpikeSrv.EstimateAvailableTimeRange();

    // Is there any new data yet?
    if (spikeTimeRange[1] > lastSampleRead)
    {
        // Try to get the number of spikes within the available time range
        newSpikes =
                NRDataSrv.SpikeSrv.ReadFromBuffer(lastSampleRead, spikeTimeRange[1]);

        // Update the last sample read
        lastSampleRead = spikeTimeRange[1];
    }
    else
    {
        return;
    }

    // Is one of my units in here?
    List<SpikeEvent> unitGSpikes =
            newSpikes.Buffer.Where(x => x.Unit == units[0]).ToList();
    List<SpikeEvent> unitTSpikes =
            newSpikes.Buffer.Where(x => x.Unit == units[1]).ToList();

    // Get the current buffer sample and make sure that we are going
    // to produce stimuli that are in the future
    ulong currentLoad =
            NRStimSrv.StimOut.GetNumberBuffLoadsCompleted() + 1;
    nextAvailableSample =
            currentLoad * (ulong)NRStimSrv.GetBuffSize();

    // Create the output buffer
    List<DigitalOutEvent> DigitalOutBuffer =
            new List<DigitalOutEvent>();

    for (int i = 0; i < unitGSpikes.Count; i++)
    {
        // Use the native digital output server to send digital change
        DigitalOutBuffer.Add(
                new DigitalOutEvent(nextAvailableSample, 71));
```

```
                SpikeEvent sG = unitGSpikes[0];
                DigitalOutBuffer.Add(
                        new DigitalOutEvent(nextAvailableSample + 10,
                                        (uint)sG.SampleIndex));
            }
            for (int i = 0; i < unitTSpikes.Count; i++)
            {
                // Use the native digital output server to send digital change
                DigitalOutBuffer.Add
                        (new DigitalOutEvent(nextAvailableSample, 84));
                SpikeEvent sT = unitTSpikes[0];
                DigitalOutBuffer.Add
                        (new DigitalOutEvent(nextAvailableSample+10,
                                                        (uint)sT.SampleIndex));
            }

            if (DigitalOutBuffer.Count > 0)
                NRStimSrv.DigitalOut.WriteToBuffer(DigitalOutBuffer);
        }

        // Shutdown StimSrv etc.
        protected override void Cleanup()
        {
            Console.WriteLine("Terminating protocol...");
        }
    }
}
```

A.4.2 NewData-based real-time loop

```
/// <summary>
/// This class produces a series of 32-bit digital pulses in response to
/// spikes produced by two, pre-specified units. Each pulse encodes the unit
/// number that produced the spike and the time (32-bit sample integer)
/// that the spike occurred.
/// </summary>

// References
using System;
using System.Collections.Generic;
using System.Linq;
using System.Text;
using NeuroRighter.NeuroRighterTask;
using NeuroRighter.DataTypes;
using NeuroRighter.Server;
using NeuroRighter.Log;
using NationalInstruments.DAQmx;
using NationalInstruments;
using System.Windows.Forms;
using System.ComponentModel;
using MoreLinq;

namespace NewDataEventCatcher
{
    class NewData_UnitReactionDO : NRTask
    {
        // Unit that we will react to with a digital pulse
        int[] units = { 1, 2 };

        // Internal variables
        int numberOfSpikesReactedTo = 0;
        uint spkSamp; // The sample of the latest spike detection

        // NI Stuff
        Task DOTask;
        DigitalSingleChannelWriter DOWriter;

        // Take the first 32-bit port
        string DOChannel1 = "/Dev1/Port0/line0:31";

        // The sample frequency of the output channel
        double DOSampleFreqHz = 10000.0;

        protected override void Setup()
        {
            // Subscribe to the NewData event on the spikes input server
            NRDataSrv.SpikeSrv.NewData +=
                    new EventDataSrv<NeuroRighter.DataTypes.SpikeEvent>.
                    NewDataHandler(SpikeSrv_NewData);

            // Setup an digital on demand output line. Make sure that you don't
            // reserve this line through the Hardware Settings GUI in
```

```
    // NeuroRighter for digital input or output. Also, make sure that
    // double-buffering is disabled.
    try
    {
        // Create and configure tasks. This is unbuffered, on-demand
        // output to reduce response latency.
        DOTask = new Task("DOTask");
        DOTask.DOChannels.CreateChannel(
                DOChannel1,
                "DOChannel1",
                ChannelLineGrouping.OneChannelForAllLines);
        DOTask.Timing.SampleTimingType = SampleTimingType.OnDemand;

        // Verify tasks and reserve the port and clock lines
        DOTask.Control(TaskAction.Verify);
        DOTask.Control(TaskAction.Reserve);

        // Create and configure writers
        DOWriter = new DigitalSingleChannelWriter(DOTask.Stream);

        // Clear the port
        DOWriter.WriteSingleSamplePort(true, 0);
    }
    catch (Exception ex)
    {
        MessageBox.Show(ex.Message);
    }
}

// There is no loop function needed when doing closed loops based on
// NewData events. In this case, the NewData Event will trigger the
// NewData Event Handler to react with whatever code you want.
// Here is the NewData event handler:
private void SpikeSrv_NewData
        (object sender, NewEventDataEventArgs<SpikeEvent> eArgs)
{
    // Is my unit in here? (eArgs automatically contains the new data on
    // the spike server. No read is required.)
    List<SpikeEvent> unit1Spikes =
            eArgs.NewDataBuffer.Buffer.Where(x => x.Unit == units[0]).ToList();
    List<SpikeEvent> unit2Spikes =
            eArgs.NewDataBuffer.Buffer.Where(x => x.Unit == units[1]).ToList();

    // In the case that the first unit spiked
    if (unit1Spikes.Count > 0 && unit2Spikes.Count == 0)
    {
        // Write a digital pulse representing the detected unit and
        // the time it occurred
        spkSamp =
                (uint)unit1Spikes.MaxBy(x => x.SampleIndex).SampleIndex;
        WriteDO(units[0]);
        numberOfSpikesReactedTo++;
    }
    // In the case that the second unit spiked
```

```
            if (unit1Spikes.Count == 0 && unit2Spikes.Count > 0)
            {
                // Write a digital pulse representing the detected unit and
                // the time it occurred
                spkSamp =
                        (uint)unit2Spikes.MaxBy(x => x.SampleIndex).SampleIndex;
                WriteDO(units[1]);
                numberOfSpikesReactedTo++;
            }

            // In the case that both spiked in the new data buffer
            if (unit1Spikes.Count > 0 && unit2Spikes.Count > 0)
            {
                // Write a digital pulse representing the detected unit and
                // the time it occurred
                uint spkSamp1 =
                        (uint)unit1Spikes.MaxBy(x => x.SampleIndex).SampleIndex;
                uint spkSamp2 =
                        (uint)unit2Spikes.MaxBy(x => x.SampleIndex).SampleIndex;
                uint[] spkSamps = {spkSamp1,spkSamp2};
                spkSamp = spkSamps.Max();
                WriteDO(units[0] + units[1]);
                numberOfSpikesReactedTo++;
            }
        }

        // This method interacts with the NI Card to produce digital pulses
        public void WriteDO(int whichUnit)
        {
            // Write a sample that says which unit fired
            DOWriter.WriteSingleSamplePort(true, whichUnit);

            // Write a sample that says when the unit fired
            DOWriter.WriteSingleSamplePort(true, spkSamp);

            // Clear the port
            DOWriter.WriteSingleSamplePort(true, 0);
        }

        // Dispose the National Instruments virtual channel objects
        protected override void Cleanup()
        {
            DOTask.Stop();
            DOTask.Dispose();
        }
    }
}
```

A.4.3 Arduino-based real-time loop

```
/// <summary>
/// This class uses an RS232 serial communication protocol to generate digital
/// pulses using an Arduino micro-controller board in response to spikes produced
/// by particular units. The ascii_response.ino or digital_reaction.ino script
/// must be running on the Arduino prior to executing this protocol.
/// </summary>

// References
using System;
using System.Collections.Generic;
using System.Linq;
using System.Text;
using NeuroRighter.NeuroRighterTask;
using NeuroRighter.DataTypes;
using NeuroRighter.Server;
using System.IO.Ports;

namespace NR_CL_Examples
{
    class Arduino_UnitReaction : NRTask
    {
        // Unit that we will react to with a digital pulse
        private int[] units = { 1, 2 };

        // I/O variables
        private ulong lastSampleRead = 0;
        protected EventBuffer<SpikeEvent> newSpikes;

        // Serial Port
        private SerialPort serialPort1;

        // Initialize the plugin
        protected override void Setup()
        {
            try
            {
                // Serial port object and properties (RS232)
                System.ComponentModel.IContainer components
                    = new System.ComponentModel.Container();
                serialPort1 = new SerialPort(components);
                serialPort1.PortName = "COM3";
                serialPort1.BaudRate = 9600;
                serialPort1.Open();

                if (!serialPort1.IsOpen)
                {
                    Console.WriteLine("Failed to connect to device.");
                    return;
                }
            }
            catch (Exception ex)
            {
```

```
            Console.WriteLine(ex.Message);
        }

        // Turns on the serial port
        serialPort1.DtrEnable = true;

        // Callback for text coming back from the Arduino
        serialPort1.DataReceived += OnReceived;

        // Give it 2 secs to start up the sketch
        System.Threading.Thread.Sleep(2000);

        Console.WriteLine("Serial-communication established.");
    }

    protected override void Loop(object sender, EventArgs e)
    {
        // First, figure out what history of spikes we have
        ulong[] spikeTimeRange =
        NRDataSrv.SpikeSrv.EstimateAvailableTimeRange();

        // Is there any new data yet?
        if (spikeTimeRange[1] > lastSampleRead)
        {
            // Get the number of spikes within the available time range
            newSpikes =
                NRDataSrv.
                SpikeSrv.
                ReadFromBuffer(lastSampleRead,spikeTimeRange[1]);

            // Update the last sample read
            lastSampleRead = spikeTimeRange[1];
        }
        else
        {
            return;
        }

        // Is my unit in here?
        List<SpikeEvent> unitGSpikes =
                newSpikes.Buffer.Where(x => x.Unit == units[0]).ToList();
        List<SpikeEvent> unitTSpikes =
                newSpikes.Buffer.Where(x => x.Unit == units[1]).ToList();

        for (int i = 0; i < unitGSpikes.Count; i++)
        {
            // Use the serial port to send a command to the Arduino
            serialPort1.Write(new byte[] { 1 }, 0, 1);
        }
        for (int i = 0; i < unitTSpikes.Count; i++)
        {
            // Use the serial port to send a command to the Arduino
            serialPort1.Write(new byte[] { 2 }, 0, 1);
        }
```

```
        }

        // Callback from Arduino
        private void OnReceived(object sender, SerialDataReceivedEventArgs c)
        {
            try
            {
                // write out text coming back from the Arduino
                Console.Write(serialPort1.ReadExisting());
            }
            catch (Exception exc)
            {
                Console.Write(exc.Message);
            }
        }

        // Shut down the serial port on protocol termination
        protected override void Cleanup()
        {
            serialPort1.Close();
        }
    }
}
```

APPENDIX B

CYCLOPS: AN ULTRA-PRECISE, FAST LED DRIVER

Here I provide performance and usage information for the 'Cyclops' high-power LED driver. Additional design information, PCB design files, Gerber files for PCB fabrication, etc. can be found on the following websites:

- `https://potterlab.gatech.edu/main/newman/wiki`: **Hardware and software wiki on the Potter lab server.**
- `https://github.com/jonnew/Cyclops-LED-Driver`: **The public Cyclops Driver design repository.**

B.1 Circuit Specification

The Cyclops Driver (revision 2, -R2) is a circuit that can drive high power light-emitting diodes (LEDs). In the context of this thesis work, it has been used primary for optogenetic stimulation of neurons. However it can be used to drive LEDs for any application where a fast switching, ultra-stable, high power light source is required (e.g. fluorescent imaging). The device is designed to source up to 4 amps @ 40 volts, so a single PCB can drive several high power LEDs in series. The printed circuit board (PCB) is modular. Multiple PCBs, each driving a particular set of LEDs, can be stacked on top of one another while sharing a single power supply.

B.1.1 Feedback modes

The main functional component of the device is a feedback assisted, power, enhancement-mode N-MOSFET. Current is drawn from the source pin of the FET in accordance with one of two feedback modes: current feedback or auxiliary feedback. In both cases, the FET acts as a variable resistor which is controlled in inverse relation to

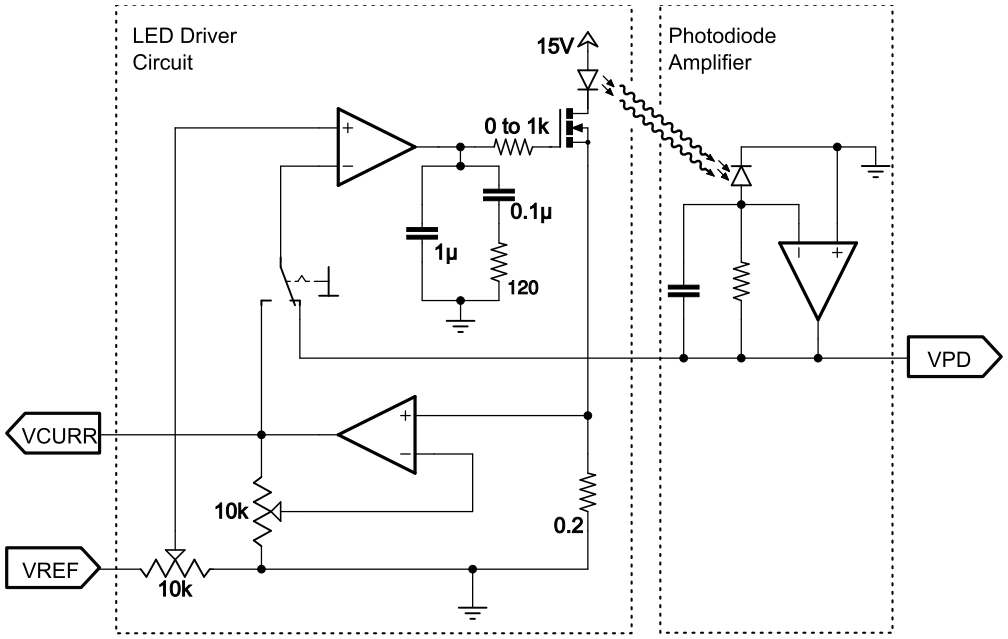

Figure 56: Schematic of the Cyclops driver circuit. A single input voltage, V_REF, is driven by an external D/A converter. The circuit can be switched between two modes: current feedback and optical feedback. In current feedback mode, the current supplied to the LED (V_CURR) is forced to follow the V_REF signal. In optical feedback mode, the light power emitted from the LED (V_PD), which is measured using a photodiode and converted to a voltage using a transimpedance amplifier, is forced to follow the reference voltage. Optical feedback ensures that the fluctuating light waveforms follow V_REF even in the face of changing LED temperature.

the gate voltage. The difference between the two feedback modes is in how the gate voltage is regulated.

- In **current feedback mode**, the gate voltage is adjusted such that the voltage drop across the sense resistor (0.2 Ω resistor in Fig. 56) is equal to a user-supplied reference voltage.

- In **auxiliary feedback mode**, some external voltage that has a positive and monotonic relationship with optical power is provided as a feedback signal.

B.1.1.1 Current feedback

Using the circuit in current feedback mode ensures that the forward diode current across the LED is precisely modulated according the the voltage at the V_REF pin. This configuration is a standard method for driving LEDs because the relationship

between current and LED irradiance is smooth and monontonic. This means that more current through the LED will generate more light power (while staying within the LED's absolute maximum ratings, of course). However, the relationship between current and irradiance is not linear. For most LEDs, it looks like a logarithmic function. Additionally, the efficiency of the LED is inversely related to its temperature. So, as the LED operates and heats up, the amount of light it produces drops even when the current is held constant. The severity of an LED's temperature dependence and current/irradiance nonlinearity depend on the type of LED (the semiconductor used and who made it) and the effectiveness of thermal management. These properties should be clearly documented in the LED's data sheet. With a quality LED and proper thermal management, the effects of temperature and static current/irrandiance nonlinearity are fairly minimal and can be ignored in most circumstances.

B.1.1.2 Optical feedback

When extremely stable, linear control of light power is required, the auxiliary feedback port can be used to compensate for the temperature dependence and static nonlinearity of the current/irradiance relationship of the LED. For example, when the auxiliary voltage is supplied by a amplified photodiode that is somewhere indecent to radiation from the LED (Fig. 56), the gate voltage at the FET is adjusted such that the measured light power matches a DAC-supplied reference voltage. This configuration is referred to as **optical feedback mode**. For the experiments in Chapters 3 and 4, I operated the circuit in optical feedback mode. To measure light power, I used the PDA36 adjustable transimpedance amplified photodiode from ThorLabs. However, a custom amplified photodiode can be assembled for a fraction of the price (Wagenaar, 2012).

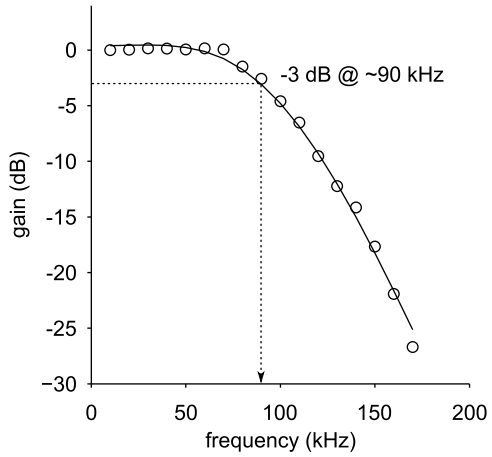

Figure 57: Small signal bandwidth of the Cyclops LED driver. The -3 dB point occurs at ∼90 kHz.

B.1.2 Performance

The following summary of device performance pertains to optical feedback mode. All characterizations were carried out using the Thorlabs PDA36 adjustable transimpedance amplified photodiode at a gain of 20 dB (100x) tied to the auxiliary input of the Cyclops in parallel with a 50 Ohm load while driving a blue XPE LED (Cree Inc., Durham, NC). The PDA36 has a bandwidth of 1 MHz at this gain/load setting, which is much faster than the Cyclops. For this reason, the bandwidth measurements presented here are likely comparable to those for current-feedback mode.

The small-signal bandwidth of the circuit (i.e. the performance not limited by the current slew rate) is shown in Fig. 57. Fig. 57 indicates that the device is capable of modulating LED brightness to around 90 kHz before its half-power point. Fig. 58(a) provides a demonstration of the device for tracking large signal steps. The rise time for a 5 mW·mm^{-2} increase in light intensity (at the photodiode) is approximately 10 μs. Note that this is an on-to-on step; a step from off-to-on incurs an additional delay of ∼50 μs, but a comparable rise time. To achieve this step in light power, approximately 500 mA needed to be sourced to the LED, indicating an approximate current slew rate of 50 mA/μs. Fig. 58(b) shows the device driving an LED to follow

a filtered Guassian waveform, generated by an external DAC, such as those used in Chapters 3 and 4.

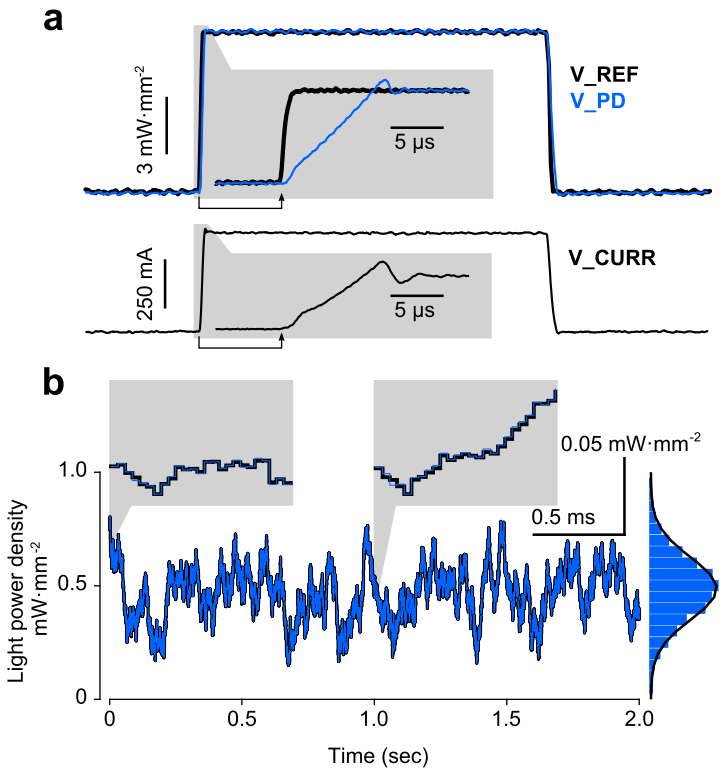

Figure 58: Step performance and bandwidth of the Cyclops LED driver in optical feedback mode. **(a)** Transient response to a large, 1 millisecond step in light power. V_REF was stepped such that ∼V_CURR = 500 mA was required for the measured light power, V_PD, to track V_REF. Arrows indicate the step time. Inset figures show the zoomed transient response of three voltage states, V_REF, V_PD, and V_CURR (see Fig. 56). The rise time of the measured light power is approximately 10 μs. This rise time is determined by the current slew rate of the circuit, which is 50 mA/μs, shown in the zoomed inset of V_CURR. This slew rate is affected by the snubber network preceding the gate of the N-MOSFET and the reactance of the LED. **(b)** Performance of the circuit following a filtered Gaussian random process with mean and standard deviation light intensity of 0.5 and 0.2 mW·mm^{-2}, respectively, and a time constant of $\tau = 50$ ms. V_REF is shown in grey and the measured light power, V_PD, is shown in blue. An amplitude histogram and the corresponding best-fit Gaussian for the processes is shown to the right. One millisecond snippets of the time series are displayed within the insets so that the finer temporal aspects of the signals can be viewed. The scale bar refers to these snippets.

B.2 Building the circuit

The Cyclops-R2 PCB was designed to be low-cost and easy to manufacture. Exclusively, 0.1-inch pitch or greater, through-hole components were used in order make board construction easy. Below I provide information on constructing and using the circuit.

B.2.1 Bill of materials

A full bill of materials, excluding the PCB itself, is provided in Table 10. Most of the components required to construct the circuit can be obtained from Digi-Key. For the two parts that cannot be ordered from Digi-Key, the number provided in the 'Digi-Key No.' column of Table 10 is preceded by a '*', and an alternate supplier is given parenthetically.

B.2.2 PCB fabrication

I suggest one of two options for PCB fabrication:

1. OSH Park. PCBs can now be ordered directly from OSH Park. They are available at my shared projects page located here.

2. Advanced Circuits. Advanced Circuits offers a no-minimum-quantity, $33.00 PCB deal for students.

B.3 Tuning the circuit

Before using the driver, several trimpots must be tuned to ensure proper operation. The following checklist describes a basic setup procedure. These steps can be modified so long as signals and power supply rails stay within the manufacturer provided specifications for the ICs on the board and the LED being driven. Fig. 59 provides a visual reference for the pins, jumpers, and trimmers referred to in these steps.

Table 10: Bill of materials for the Cyclops driver.

Name	Description	Part No.	Digi-Key No.	Quantity
Integrated Circuits				
LM324N	quad opamp	LM324N	296-1391-5-ND	1
317	positive voltage reg	LM317AHVT	LM317AHVT-ND	1
N-MOSTFET	n-channel power FET	FQP30N06L	FQP30N06L-ND	1
REF02Z	prec. voltage ref	REF02CPZ	REF02CPZ-ND	1
Passive Components				
REG_ADJ	5K Trimmer	PV36P103C01B00	490-2869-ND	1
REF_ADJ, I_MEAS_K, CTL_K	10K Trimmer	PV36P103C01B00	490-2856-ND	3
R_CURR	resistor, 0.2 ohm, 1%	PAC500002007FAC000	PPC5D.20CT-ND	1
R8	resistor, 120 ohm	PR01000101200JR500	PPC120W-1CT-ND	1
R10	resistor, 240 ohm	PR01000102400JR500	PPC240W-1CT-ND	1
R12	resistor, 470 ohm	PR01000104700JR500	PPC470W-1CT-ND	1
R9	resistor, 1 kohm	PR01000101001JR500	PPC1.0KW-1CT-ND	1
R2	resistor, 1.5 kohm	PR01000101501JR500	PPC1.5KW-1CT-ND	1
R3,4	resistor, 10 kohm	PR01000101002JR500	PPC10KW-1CT-ND	2
C2,4,6,7	capacitor, 0.1 uF	RDEF51H104Z0K1C03B	490-5401-ND	4
C3,5	capacitor, 1 uF	ECA-1HM010	P5174-ND	2
C8	capacitor, 10 uF	ECA-1CM100	P5134-ND	1
ON	On/Off LED, 20 mA	LTL1CHTBK4	160-1602-ND	1
N.A.	5A fuse, blade	0891005.NXS	F5927-ND	1
N.A.	2A fuse, blade	0891002.NXT	F3675-ND	1
Electro-mechanical				
FUSE	fuse holder	3557-2	3557-2K-ND	1
N.A.	TO-220 heat sink	507002B00000G	HS112-ND	2
TEST	ST3P through hole	A27AV	A27AW-ND	1
CURR/AUX	SPDT right angle	A12AH	A12AH-ND	1
J3-6	2 pos. jumper header	87224-2	A26543-ND	4
J1,2	2X3 pos. jumper header	87227-3	A26569-ND	2
V_IN1	red banana tip jack	05-0752-001	J109-ND	1
N.A.	red banana tip plug	105-0302-001	J103-ND	1
LED+	yellow banana tip jack	105-0757-001	J113-ND	1
N.A.	yellow banana tip plug	105-0307-001	∗530-105-0307-1(mouser)	1
+12V	white banana tip jack	105-0751-001	J108-ND	1
N.A.	white banana tip plug	105-0301-001	J300-ND	1
GND1,2 LED-	black banana tip jack	105-0753-001	J110-ND	3
N.A.	black banana tip plug	105-0303-001	J104-ND	3
POW2	2 pos. screw term (pow)	282834-2	A98333-ND	1
EXT_CTL_K	3 pos. screw term (pot)	282834-3	A98334-ND	1
LED_OUT	4 pos. screw term (out)	282834-4	A98335-ND	1
I/O_BLOCK	5 pos. screw term (in)	282834-5	A98336-ND	1
V_CTL, V_CURR, V_REF, V_AUX	BNC connector 50 Ohm	1-1634613-0	A97554-ND	4
N.A.	20 mm standoff, 4-40	8799	8799K-ND	4
N.A	2X4 DIP socket	1-390261-2	A100204-ND	1
N.A.	2X7 DIP socket	1-390261-3	A100205-ND	1
POW1, MECH1,2,3	4 pos. power header	ESQ-102-24-G-D	∗ESQ-102-24-G-D (samtec)	4
Power Supply				
N.A.	HD48-3-AG	48 volt, 3 amp, linear	179-2335-ND	1

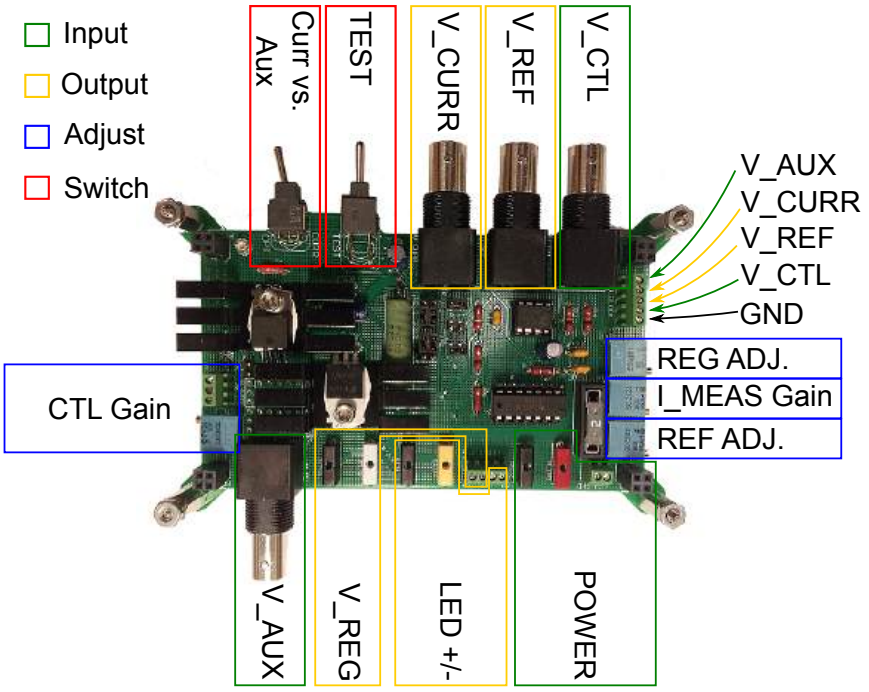

Figure 59: Cyclops LED driver pinout.

1. Obtain a power supply which can source at least 1 amp at 15 volts. You can use a switching supply, since the current sourced to the LED is regulated.

2. Obtain a multimeter capable of measuring resistance and DC voltage.

3. Tune the LM317 voltage regulator output to around 12 VDC.

    - Put your multimeter in DC voltage measurement mode.
    - Tie the negative probe to ground and the positive probe to the positive lead (either the tip-jack or screw terminal) of V_REG.
    - Provide power (>=15V) to the POWER terminals using either the tip-jack connectors or the screw terminals
    - Examine the voltage at V_REG. Turn the REG_ADJ trimpot until the measured voltage is ∼12 VDC.
    - Note that V_REG is made available as an output on the PCB, and therefore can be used to drive external boards, fans, etc so long as <1 amp is drawn

and sufficient current headroom is provided for LED operation.

4. Adjust the voltage reference level, V_REF. V_REF is an on-board reference voltage for the TEST switch. It serves the purpose of the V_CTL signal when the TEST switch is engaged without needing an external (e.g. DAC-supplied) source.

   - Put your multimeter in DC voltage measurement mode.
   - Tie the negative probe to ground and the positive probe to the TP_5V test point, which located between the V_CURR BNC connector and the TEST switch.
   - Examine the voltage at TP_5V. Turn the REF_ADJ trimpot until the measured voltage is 5.00 VDC.

5. Next we must ensure that upon the first test of the LED driver, it will not source too much current to the LED and destroy it. The conversion from the V_CTL input to the current through the LED, assuming the circuit is functioning properly, is ILED (Amps)= V_CURR (Volts) = V_REF (Volts) = CTL Gain $*$ V_CTL (Volts). V_CURR is the measured current, and V_REF is the desired current level. The CTL Gain trimpot scales signals from the V_CTL pin, which are 0-5 volts, into a lower range so that the circuit does not fry the LED. For instance, if a 5 volt TTL pulse is applied to V_CTL, and CTL_GAIN is set to 1/5, then 1 amp will be sourced to the LED.

   - Put your multimeter in DC voltage measurement mode.
   - Use a BNC converter to tie the multimeter input to the V_REF output BNC connector.
   - The circuit operates under the assumption that a the maximal value of V_CTL is 5 volts. This makes it suitable for being driven by a TTL

line if pulsed stimuli are required. For this reason, we can examine the current that will be sourced to an LED by engaging the TEST switch and measuring the resulting scaled voltage, V_REF with our multimeter

- To start, adjust the CTL_GAIN trimpot until the measured voltage is ∼200 mV, which will correspond to 200 mA sourced to the LED.

6. Test the LED.

   - Obtain a high power LED. Ensure that it can handle the 200 mA current that we are about to supply to it. Tie its cathode to LED+ and anode to LED-, respectively, using either the tip-jack connector or the screw terminal. Make sure the LED has adequate thermal management. Consult the LED's data sheet for recommended thermal management options.
   - Ensure that the CURR/AUX switch is pointed toward CURR. This means that the circuit will used current feedback when regulating the current supplied to the LED. If the device is left in AUX mode, and there is a high impedance at the V_AUX input (e.g. nothing is plugged in), the circuit will appear not to function.
   - Flip the TEST switch and the LED will turn on, with 200 mA flowing across the diode. **Don't look directly at the LED.**

7. Now, time-varying input, from 0-5 volts, can be tied to the V_CTL pin to drive the LED.

APPENDIX C

A SERVO-CONTROLLED PELTIER HEATER/COOLER FOR REGULATING CULTURE TEMPERATURE

My thesis work often involved MEA recordings lasting many hours. It was important to precisely regulate the culture temperature over the course of these long experiments. In our lab, MEA recordings are obtained from a 60-channel MEA amplifier, which is located within a culturing incubator. The amplifier can dissipate substantial amounts of heat, especially during electrical stimulation. Therefore the culture must be actively cooled during long-term recordings to prevent medium evaporation and resultant increases in medium osmolarity. To solve this problem, our lab has previously used Peltier regulators to control the amplifier's temperature. I improved upon the lab's thermal regulator design by incorporating a servo-controller to precisely regulate the culture's temperature even during very long epochs of electrical stimulation. Here I describe this system.

C.1 Design

The Peltier temperature regulator used in my experiments is modified from a design introduced by Daniel Wagenaar in his PhD dissertation (Wagenaar, 2006). A mechanical drawing and photographs of the finished device are shown in Figs. 60 and 61, respectively. The device consists of two copper plates separated by a flat thermoelectric Peltier heater/cooler. Depending on the direction of current flow through the Peltier device, heat will be pumped from the UPPER PLATE to the LOWER PLATE or vice-versa, allowing bidirectional temperature control, which is not available using the heater integrated into the 60-channel MEA amplifier (MEA1060-Up, Multichannel Systems, Germany). The copper plates are held together using Teflon bolts in order to minimize passive thermal coupling. During use, the MEA amplifier sits atop the UPPER PLATE, which draws heat to the LOWER PLATE where it is dissipated

from a passive heat sink. The whole assembly is stored in a culturing incubator. I have also created a secondary version of this device that provides a trans-illumination port and mounting points for a Köhler illuminator following straightforward modifications of the design presented here (Fig. 33(a)).

Thus far, the design is essentially identical to Daniel's original version of the device. However, in Daniel's device, the Peltier module was driven by an external power supply set to deliver a constant current during operation. I found that during long experiments, especially those involving a lot of electrical stimulation (e.g. Fig. 10), a constant drive current did not provided adequate temperature regulation over the duration of the experiment, and condensation would often form on the culturing lid (Potter and DeMarse, 2001). For this reason, I modified Daniel's design by adding a servo-controller that regulated current to the Peltier device in order to precisely control the temperature of the MEA amplifier.

This system used an MOT7000 precision temperature controller (Modular One Technology, Parker, TX; Fig. 61), which was integrated into a MOT700-EVM evaluation board. Essentially, this device is a bipolar constant current source with an integrated PID controller. The PID controller compares an internally supplied reference voltage to an external temperature measurement obtained from a thermistor, which is implanted in the UPPER PLATE. Current is sourced to the Peltier module such that the difference between the measured and reference voltages is minimized. This device provides several outputs, such as the instantaneous current supplied to the Peltier module, a temperature over/under alarm, and the temperature measurement, which can be monitored or recorded during a long-term experiment.

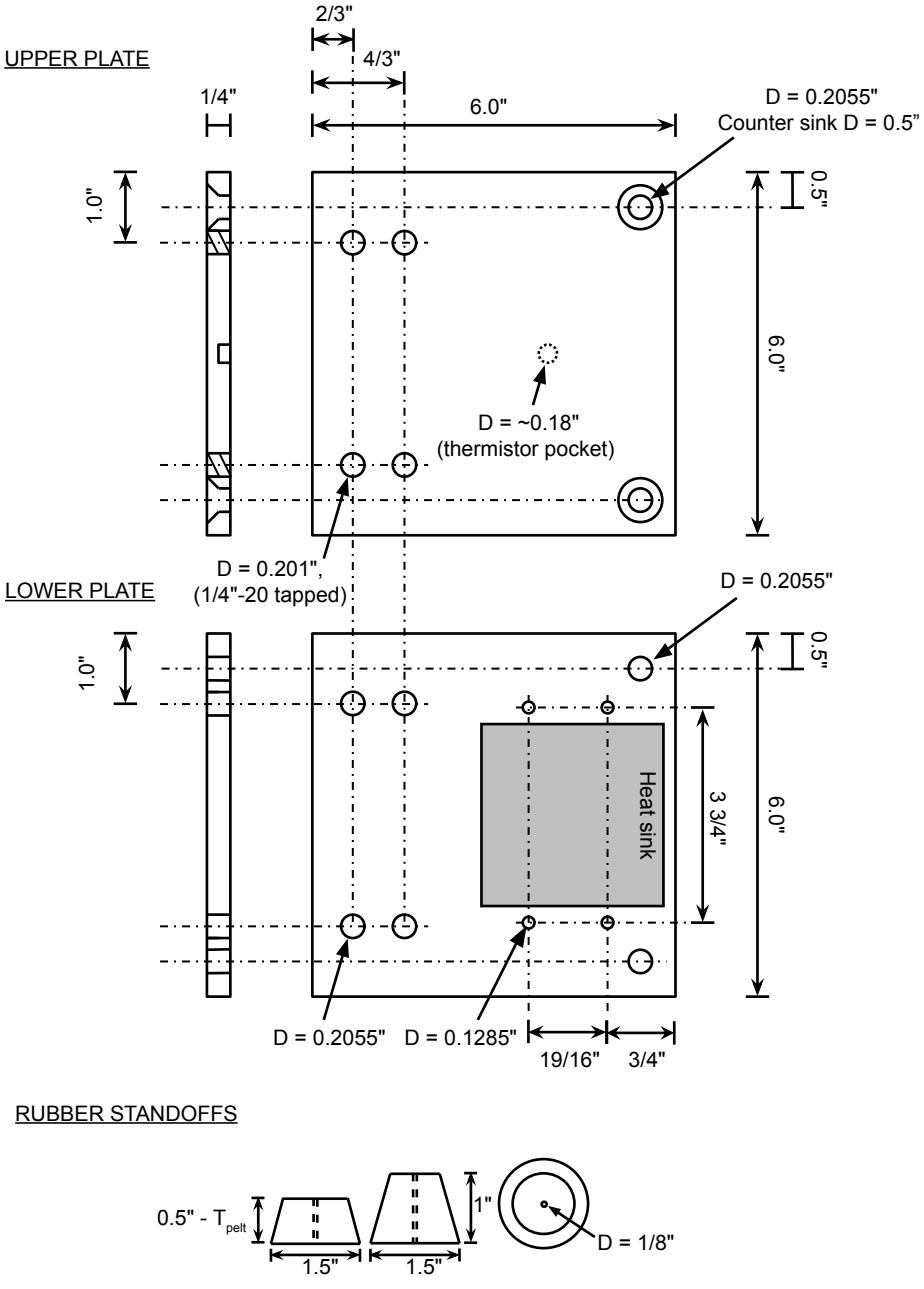

Figure 60: **Mechanical drawing of the Peltier temperature regulator's basic components.**

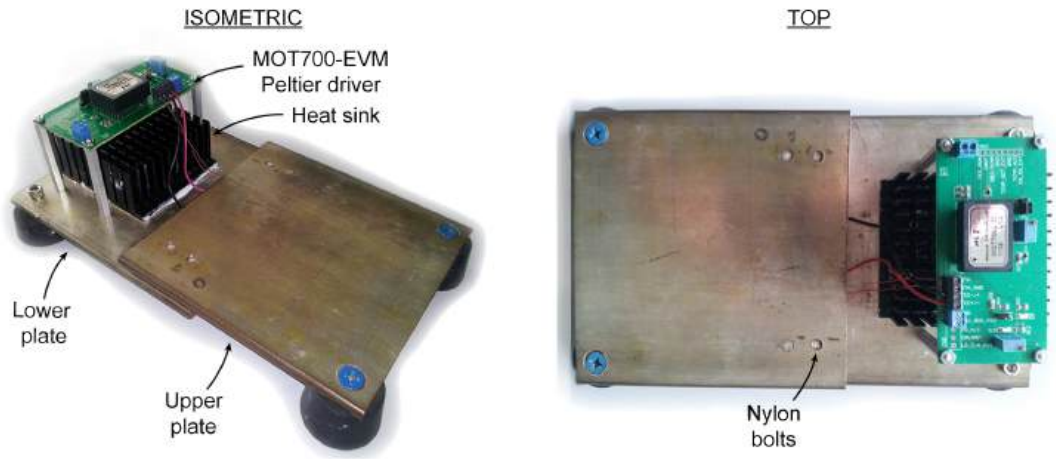

Figure 61: The assembled Peltier temperature regulator.

C.2 Assembly

The device can be assembled in an hour or so. The required tools are as follows:

- Bandsaw
- Drill Press
- Bit set (ANSI)
- Tap Set (ANSI)
- Deburring tool
- Metal file
- Dremel tool with rough sandpaper attachment
- Spirit level

To assemble the device, follow the steps below while referring to Figs. 60 and 61 along with Table 11.

1. Cut the copper plate into two 6 in. square pieces using a bandsaw. Make sure to use a fence on bandsaw table. File the sharp copper edges until rounded. File only against the file grain; going in both directions dulls the file.

2. Mark hole placement on the UPPER PLATE as per Fig. 60. Drill the holes using a drill press making sure to use a vice which is secured to the drill press stage. The drill speed should be 100-200 surface feet per minute (SFM) for copper. Note that this speed is dependent on the diameter of your drill bit according to

$$\text{Spindle speed (RPM)} = \frac{\text{SFM}}{\frac{1}{12} \times \pi \times \text{tool diameter (in.)}}. \tag{77}$$

Plunge the bit slowly, making sure to clear debris using compressed air. Deburr the holes with a deburring tool. Countersink the holes on the UPPER PLATE to accommodate the flat head machine screws such that the amplifier will make flush contact with the UPPER PLATE.

3. Drill a small pocket into the bottom of the UPPER PLATE that can accommodate the thermistor. The precise location of this pocket is not important. However, moving it closer to the Peltier module will result in more stable PID control loop.

4. Lay the LOWER PLATE flush over the UPPER PLATE and clamp both together in a square vise. Mark hole placement on the UPPER PLATE using the pre-drilled holes in LOWER PLATE as a guide. Drill these holes with the drill press, deburr, and tap if necessary.

5. If RUBBER FEET need to be cut, do so with a bandsaw or hack saw whist being careful not to lose your fingers. For my device, I used standard styrene-butadiene rubber stoppers with pre-drilled center holes.

6. Apply thermal grease to both sides of the Peltier module and press onto the LOWER PLATE between the four holes at the front. When the plate is viewed from the rear, the positive lead of the Peltier module should be on the right of LOWER PLATE. Sandwich the module between the LOWER PLATE and the

UPPER PLATE using the nylon bolts. If the nylon bolts project above the top surface of the UPPER PLATE, remove this excess material with a Dremel tool such that the screws are flush with the top of the UPPER PLATE.

7. Mount the larger RUBBER FEET onto the UPPER PLATE using the machine screws. Make sure the top surface of the screws is flush with the UPPER PLATE via proper countersinking. Attach the smaller RUBBER FEET to the LOWER PLATE using 1/4"-20 X 1" bolts. Use a spirit level to make sure the UPPER PLATE is approximate horizontal. If the device is not level, use washers between the RUBBER FEET and the PLATES to make adjustments where needed.

8. Apply thermal adhesive to the back of the the passive heat sink and press onto the LOWER PLATE as shown in Fig. 60. Make sure that there is flush surface contact between the heat sink and the copper plate.

9. Mount the MOT700-EVM onto the LOWER PLATE using 4 aluminum stand-offs. The MOT700-EVM should be positioned over the passive heat sink (Fig. 61). Finally, using thermal adhesive, glue a 10 kΩ negative temperature coefficient (NTC) thermistor into the small pocket previously drilled into the bottom of the UPPER PLATE. After the glue has dried, tie the thermistor's anode and cathode to the appropriate screw terminals on the MOT700-EVM board. The MOT700-EVM board should be powered from a 3.3-5V benchtop supply. For instructions on adjusting the temperature set-point and tuning the circuit, refer to the MOT700-EVM user manual.

Table 11: Bill of materials for the Peltier temperature regulator.

Name	Description	Supplier	Part No.	Quantity
Mechanical				
Copper plate	Copper alloy 110, 1/4" T., 6" W., 1' L.	McMaster-Carr	8964K422	1
Nylon bolts	Nylon cap screw 1/4"-20, 3/4" L.	McMaster-Carr	91244A140	4
4-40 bolts	Socket head cap screw 4-40, 3/4" L.	McMaster-Carr	91251A113	4
4-40 nuts	Hex nut 4-40 thread size, 1/4" W., 3/32" H.	McMaster-Carr	90257A005	2
Steel bolts	Socket head cap screw 1/4"-20 Thread, 1" L.	McMaster-Carr	91251A542	2
Machine screw	Flat head machine screw 1/4"-20 Thread, 3/4" L.	McMaster-Carr	91500A540	4
PCB standoff	Hex standoff, male/female, 4-40	Digi-Key	8412K-ND	4
Thermal grease	Silicon thermal dielectric compound	Digi-Key	473-1097-ND	1
Thermal adhesive	Arctic Silver arctic alumina	Newegg	AATA-5G	1
Heat sink	Rectangular alu. heat sink	Digi-Key	102-1489-ND	1
Electrical				
Peltier module	40 mm L., 40 mm W., 4 mm H., 6.0 A	Digi-Key	102-1678-ND	1
Peltier driver	MOT7000 evaluation board	Modular One	MOT700-EVM	1
Thermistor	10 kΩ NTC Thermistor	Digi-Key	495-2142-ND	1

C.3 Performance

To measure the device's performance, I filled the culturing well of an old MEA with phosphate buffered saline (PBS) and mounted the MEA in a 60-channel amplifier. I then placed the amplifier on the Peltier regulator, which was contained within a culturing incubator regulated to 35°C. I used the Peltier device to regulate the powered amplifier's temperature over a 1-hour time period. I recorded the Peltier module drive current and the UPPER PLATE temperature, which were provided by the MOT700-EVM, using NeuroRighter's auxiliary analog input lines. Additionally, I used a secondary 10 kΩ NTC thermistor, which was submerged in the saline bath in the culturing chamber, to measure the PBS temperature. To convert the thermistor's temperature to a voltage, I used a Warner Instruments TM-3 thermistor converter to obtain a 0.1 V/°C temperature measurement. Fig. 62 shows these measurements over a 1-hour regulation period.

There was an oscillation in the control loop, which is apparent in the measurements of the Peltier drive current and the UPPER PLATE temperature (Fig. 62(Middle, Bottom)). This indicates that the PID control loop is likely unstable due to the phase shift between thermal actuation by the Peltier module and the measurement at the

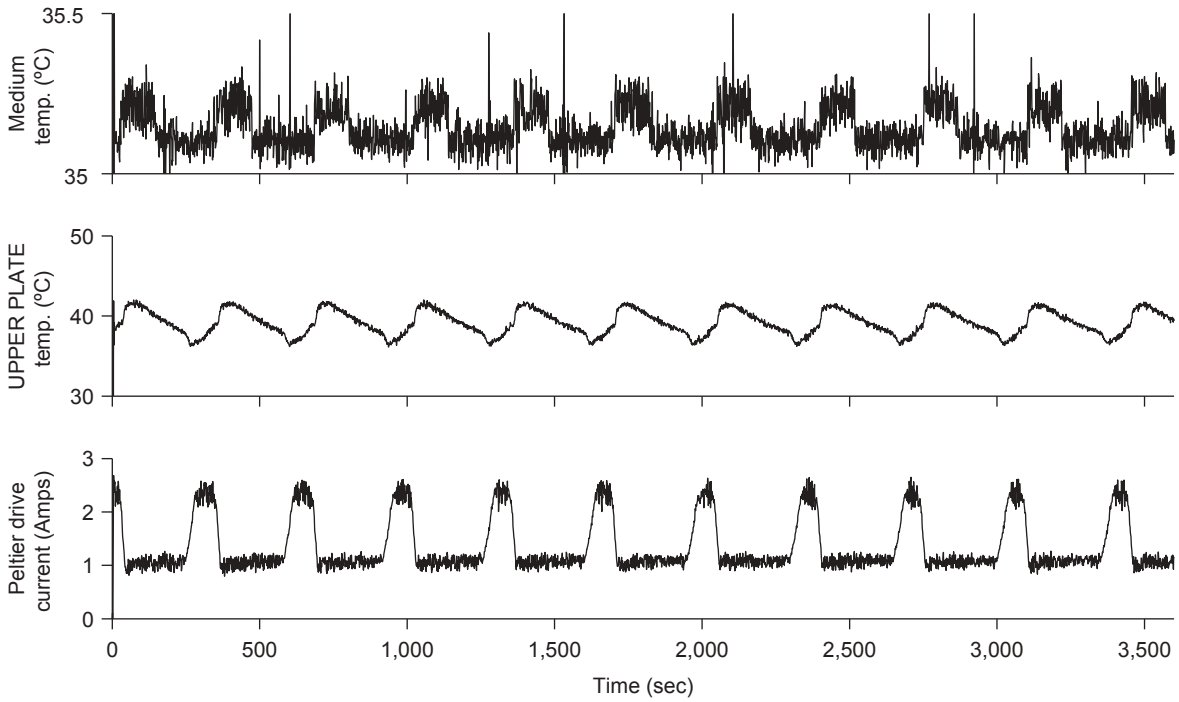

Figure 62: Culture temperature regulation over a 1-hour time period. *Top,* Temperature of the culturing medium and, *Middle,* the UPPER PLATE over a 1-hour time period. *Bottom,* Drive current supplied to the Peltier module.

thermistor, which is introduced by the copper plate. However, I found that the large thermal inertia of the copper plate smoothed this oscillation and provided worst-case temperature jitter of $\sim 0.2\,^{\circ}\mathrm{C}$ within the PBS (Fig. 62 (Top)). To stabilize the control loop, the thermistor could be moved closer to the Peltier module. However, I found the performance of the device adequate for my experiments because no condensation formed on the culturing lid.

Bibliography

Abbott, L. and Dayan, P. (2001). *Theoretical Neuroscience: Computational and Mathematical Modeling of Neural Systems*. The MIT Press, Cambridge, MA.

Abbott, L.F. and Dayan, P. (1999). The effect of correlated variability on the accuracy of a population code. *Neural Comput.*, 11:91–101.

Abbott, L.F. and Nelson, S.B. (2000). Synaptic plasticity: taming the beast. *Nat. Neurosci.*, 3:1178–1183.

Ahrens, M.B., Li, J.M., Orger, M.B., Robson, D.N., Schier, A.F., Engert, F., *et al.* (2012). Brain-wide neuronal dynamics during motor adaptation in zebrafish. *Nature*, 485:471–477.

Airan, R.D., Thompson, K.R., Fenno, L.E., Bernstein, H., and Deisseroth, K. (2009). Temporally precise in vivo control of intracellular signalling. *Nature*, 458:1025–1029.

Akerboom, J., Carreras Calderón, N., Tian, L., Wabnig, S., Prigge, M., Tolö, J., *et al.* (2013). Genetically encoded calcium indicators for multi-color neural activity imaging and combination with optogenetics. *Front. Mol. Neurosci.*, 6:2.

Anikeeva, P., Andalman, A.S., Witten, I., Warden, M., Goshen, I., Grosenick, L., *et al.* (2012). Optetrode: a multichannel readout for optogenetic control in freely moving mice. *Nat. Neurosci.*, 15:163–170.

Arabzadeh, E., Petersen, R.S., and Diamond, M.E. (2003). Encoding of whisker vibration by rat barrel cortex neurons: implications for texture discrimination. *J. Neurosci.*, 23:9146–9154.

Armstrong, C., Krook-Magnuson, E., Oijala, M., and Soltesz, I. (2013). Closed-loop optogenetic intervention in mice. *Nat. Protoc.*, 8:1475–1493.

Arsiero, M., Lüscher, H.R., and Giugliano, M. (2007). Real-time closed-loop electrophysiology: towards new frontiers in in vitro investigations in the neurosciences. *Arch. Ital. Biol.*, 145:193–209.

Averbeck, B.B., Latham, P.E., and Pouget, A. (2006). Neural correlations, population coding and computation. *Nat. Rev. Neurosci.*, 7:358–366.

Azin, M. and Guggenmos, D.J. (2011). A battery-powered activity-dependent intracortical microstimulation IC for brain-machine-brain interface. *IEEE J. Solid-State Circuits*, 46:731–745.

Azouz, R. and Gray, C.M. (2000). Dynamic spike threshold reveals a mechanism for synaptic coincidence detection in cortical neurons in vivo. *PNAS*, 97:8110–8115.

Bakkum, D., Chao, Z., and Potter, S. (2008a). Spatio-temporal electrical stimuli shape behavior of an embodied cortical network in a goal-directed learning task. *J. Neural. Eng.*, 5:310–323.

Bakkum, D.J., Chao, Z.C., and Potter, S.M. (2008b). Long-term activity-dependent plasticity of action potential propagation delay and amplitude in cortical networks. *PloS One*, 3:e2088.

Bakkum, D.J., Frey, U., Radivojevic, M., Russell, T.L., Müller, J., Fiscella, M., *et al.* (2013). Tracking axonal action potential propagation on a high-density microelectrode array across hundreds of sites. *Nat. Commun.*, 4:2181.

Bakkum, D.J., Gamblen, P.M., Ben-Ary, G., Chao, Z.C., and Potter, S.M. (2007). MEART: The Semi-Living Artist. *Front. Neurorob.*, 1:5.

Banghart, M., Borges, K., Isacoff, E., Trauner, D., and Kramer, R.H. (2004). Light-activated ion channels for remote control of neuronal firing. *Nat. Neurosci.*, 7:1381–1386.

Barlow, H. (1961). Possible principles underlying the transformation of sensory messages. In W.A. Rosenblith, editor, *Sensory Communication*, pages 217–234. MIT Press, Cambridge, MA.

Béïque, J., Na, Y., Kuhl, D., Worley, P.F., and Huganir, R.L. (2011). Arc-dependent synapse-specific homeostatic plasticity. *PNAS*, 108:816–821.

Bendor, D. and Wilson, M.A. (2012). Biasing the content of hippocampal replay during sleep. *Nat. Neurosci.*, 15:1439–1444.

Berndt, A., Schoenenberger, P., Mattis, J., Tye, K.M., Deisseroth, K., Hegemann, P., *et al.* (2011). High-efficiency channelrhodopsins for fast neuronal stimulation at low light levels. *PNAS*, 108:7595–7600.

Bi, G.q. and Poo, M.m. (1998). Synaptic modifications in cultured hippocampal neurons: dependence on spike timing, synaptic strength, and postsynaptic cell type. *J. Neurosci.*, 18:10464–10472.

Blau, A., Neumann, T., Ziegler, C., and Benfenati, F. (2009). Replica-moulded polydimethylsiloxane culture vessel lids attenuate osmotic drift in long-term cell cultures. *J. Biosci.*, 34:59–69.

Borst, A. and Theunissen, F.E. (1999). Information theory and neural coding. *Nat. Neurosci.*, 2:947–957.

Boyden, E.S., Zhang, F., Bamberg, E., Nagel, G., and Deisseroth, K. (2005). Millisecond-timescale, genetically targeted optical control of neural activity. *Nat. Neurosci.*, 8:1263–1268.

Brenner, N., Strong, S.P., Koberle, R., Bialek, W., and de Ruyter van Steveninck, R.R. (2000). Synergy in a neural code. *Neural Comput.*, 12:1531–1552.

Brillinger, D. (1981). *Time Series: Data Analysis and Theory*. SIAM, Philadelphia, PA.

Brown, E., Frank, L., Tang, D., Quirk, M.C., and Wilson, M. (1998). A statistical paradigm for neural spike train decoding applied to position prediction from ensemble firing patterns of rat hippocampal place cells. *J. Neurosci.*, 18:7411–7425.

Brunel, N. (2000). Dynamics of sparsely connected networks of excitatory and inhibitory spiking neurons. *J. Comput. Neurosci.*, 8:183–208.

Bruno, R. and Sakmann, B. (2006). Cortex is driven by weak but synchronously active thalamocortical synapses. *Science*, 312:1622–1627.

Bruno, R.M. (2011). Synchrony in sensation. *Curr. Opin. Neurobiol.*, 21:701–708.

Burrone, J., O'Byrne, M., and Murthy, V. (2002). Multiple forms of synaptic plasticity triggered by selective suppression of activity in individual neurons. *Nature*, 420:414–418.

Button, K.S., Ioannidis, J.P.A., Mokrysz, C., Nosek, B.A., Flint, J., Robinson, E.S.J., *et al.* (2013). Power failure: why small sample size undermines the reliability of neuroscience. *Nat. Rev. Neurosci.*, 14:365–376.

Butts, D., Weng, C., Jin, J., Yeh, C., Lesica, N., Alonso, J., *et al.* (2007). Temporal precision in the neural code and the timescales of natural vision. *Nature*, 449:92–95.

Cardin, J., Carlen, M., Meletis, K., Knoblich, U., Zhang, F., Deisseroth, K., *et al.* (2009). Driving fast-spiking cells induces gamma rhythm and controls sensory responses. *Nature*, 459:663–667.

Chao, Z.C., Bakkum, D.J., and Potter, S.M. (2008). Shaping embodied neural networks for adaptive goal-directed behavior. *PLoS Comput. Biol.*, 4:e1000042.

Chichilnisky, E.J. (2001). A simple white noise analysis of neuronal light responses. *Network-Comp. Neural*, 12:199–213.

Chow, B.Y., Han, X., Dobry, A.S., Qian, X., Chuong, A.S., Li, M., *et al.* (2010). High-performance genetically targetable optical neural silencing by light-driven proton pumps. *Nature*, 463:98–102.

Cole, K.S. (1949). Dynamic electrical characteristics of the squid axon membrane. *Annu. Rev. Physiol.*, 3:253–258.

Constantinople, C.M. and Bruno, R.M. (2011). Effects and mechanisms of wakefulness on local cortical networks. *Neuron*, 69:1061–1068.

Crumiller, M., Knight, B., Yu, Y., and Kaplan, E. (2011). Estimating the amount of information conveyed by a population of neurons. *Front. Neurosci.*, 5:90.

da Costa, N.M. and Martin, K.A.C. (2011). How thalamus connects to spiny stellate cells in the cat's visual cortex. *J. Neurosci.*, 31:2925–2937.

Darbon, P., Scicluna, L., Tscherter, A., and Streit, J. (2002). Mechanisms controlling bursting activity induced by disinhibition in spinal cord networks. *Eur. J. Neurosci.*, 15:671–683.

Deeg, K.E. and Aizenman, C.D. (2011). Sensory modality-specific homeostatic plasticity in the developing optic tectum. *Nat. Neurosci.*, 14:548–550.

DeMarse, T.B., Wagenaar, D.A., Blau, A.W., and Potter, S.M. (2001). The neurally controlled animat: biological brains acting with simulated bodies. *Auton. Robot*, 11:305–310.

Dempster, A.P. and Laird, N.M. (1977). Maximum likelihood from incomplete data via the EM algorithm. *J. R. Stat. Soc.*, 39:1–38.

Desai, N.S., Cudmore, R.H., Nelson, S.B., and Turrigiano, G.G. (2002). Critical periods for experience-dependent synaptic scaling in visual cortex. *Nat. Neurosci.*, 5:783–789.

Desai, S.A., Rolston, J.D., Guo, L., and Potter, S.M. (2010). Improving impedance of implantable microwire multi-electrode arrays by ultrasonic electroplating of durable platinum black. *Front. Neuroeng.*, 3:5.

Desbordes, G., Jin, J., Weng, C., Lesica, N.A., Stanley, G.B., and Alonso, J.M. (2008). Timing precision in population coding of natural scenes in the early visual system. *PLoS Biol.*, 6:e324.

Destexhe, A., Rudolph, M., and Pare, D. (2003). The high-conductance state of neocortical neurons *in vivo*. *Nat. Rev. Neurosci.*, 4:739–751.

Douglas, R.J., Koch, C., Mahowald, M., Martin, K.A., and Suarez, H.H. (1995). Recurrent excitation in neocortical circuits. *Science*, 269:981–985.

Du, J., Blanche, T.J., Harrison, R.R., Lester, H., and Masmanidis, S.C. (2011). Multiplexed, high density electrophysiology with nanofabricated neural probes. *PloS One*, 6:e26204.

Ecker, A., Berens, P., Tolias, A.S., and Bethge, M. (2011). The effect of noise correlations in populations of diversely tuned neurons. *J. Neurosci.*, 31:14272–14283.

Esteller, R., Echauz, J., and Tcheng, T. (2001). Line length: an efficient feature for seizure onset detection. In *Proc. 23rd Int. Conf. IEEE EMBS*, volume 2, pages 1707–1710.

Feller, M. (1999). Spontaneous correlated activity in developing neural circuits. *Neuron*, 22:653–656.

Feller, W. (1968). *An Introduction to Probability Theory and Its Applications*. John Wiley and Sons, New York, NY.

Field, G.D., Gauthier, J.L., Sher, A., Greschner, M., Machado, T.a., Jepson, L.H., *et al.* (2010). Functional connectivity in the retina at the resolution of photoreceptors. *Nature*, 467:673–677.

Filzmoser, P. (2004). A multivariate outlier detection method. In *Proc. 7th Int. Conf. on Computer Data Analysis and Modeling*, volume 1, pages 18–22.

Fiscella, M., Farrow, K., Jones, I.L., Jäckel, D., Müller, J., Frey, U., *et al.* (2012). Recording from Defined Populations of Retinal Ganglion Cells Using a High-Density CMOS-Integrated Microelectrode Array with Real-Time Switchable Electrode Selection. *J. Neurosci. Meth.*, 211:103–113.

Friedberg, M., Lee, S., and Ebner, F. (1999). Modulation of receptive field properties of thalamic somatosensory neurons by the depth of anesthesia. *J. Neurophysiol.*, 81:2243–2252.

Fries, P. (2005). A mechanism for cognitive dynamics: neuronal communication through neuronal coherence. *Trends Cogn. Sci.*, 9:474–480.

Fröhlich, F., Bazhenov, M., and Sejnowski, T. (2008). Pathological effect of homeostatic synaptic scaling on network dynamics in diseases of the cortex. *J. Neurosci.*, 28:1709–1720.

Gal, A., Eytan, D., Wallach, A., Sandler, M., Schiller, J., and Marom, S. (2010). Dynamics of excitability over extended timescales in cultured cortical neurons. *J. Neurosci.*, 30:16332–16342.

Geffen, M.N., Broome, B.M., Laurent, G., and Meister, M. (2009). Neural encoding of rapidly fluctuating odors. *Neuron*, 61:570–586.

Georgopoulos, A., Kettner, R.E., and Schwartz, A. (1988). Primate motor cortex and free arm movements to visual targets in three-dimensional space. II. Coding of the direction of movement by a neuronal population. *J. Neurosci.*, 8:2928–2937.

Gonzalez-Islas, C. and Wenner, P. (2006). Spontaneous network activity in the embryonic spinal cord regulates AMPAergic and GABAergic synaptic strength. *Neuron*, 49:563–575.

Goold, C.P. and Nicoll, R.A. (2010). Single-cell optogenetic excitation drives homeostatic synaptic depression. *Neuron*, 68:512–528.

Gradinaru, V., Thompson, K., and Deisseroth, K. (2008). eNpHR: a Natronomonas halorhodopsin enhanced for optogenetic applications. *Brain Cell Biol.*, 36:129–139.

Gradinaru, V., Zhang, F., Ramakrishnan, C., Mattis, J., Prakash, R., Diester, I., *et al.* (2010). Molecular and cellular approaches for diversifying and extending optogenetics. *Cell*, 141:154–65.

Grenander, U. and Rosenblatt, M. (1957). *Statistical analysis of stationary time series*. John Wiley and Sons, New York, NY.

Grossman, N., Poher, V., Grubb, M.S., Kennedy, G.T., Nikolic, K., McGovern, B., *et al.* (2010). Multi-site optical excitation using ChR2 and micro-LED array. *J. Neural Eng.*, 7:16004.

Gunaydin, L.A., Yizhar, O., Berndt, A., Sohal, V.S., Deisseroth, K., and Hegemann, P. (2010). Ultrafast optogenetic control. *Nat. Neurosci.*, 13:387–392.

Hales, C.M., Rolston, J.D., and Potter, S.M. (2010). How to culture, record and stimulate neuronal networks on micro-electrode arrays. *J. Visualized Exp.*, 39:e2056.

Hales, C.M., Zeller-Townson, R., Newman, J.P., Shoemaker, J.T., Killian, N.J., and Potter, S.M. (2012). Stimulus induced high frequency oscillations are present in neuronal networks on microelectrode arrays. *Front. Neural Circuits*, 6:29.

Hamill, O.P., Marty, A., Neher, E., and Sakmann, B. (1981). Improved patch-clamp techniques for high-resolution current recording from cells and cell-free membrane patches. *Pflügers Archiv*, 391:85–100.

Han, X. and Boyden, E. (2007). Multiple-color optical activation, silencing, and desynchronization of neural activity, with single-spike temporal resolution. *PloS One*, 2:e299.

Harvey, C.D., Collman, F., Dombeck, D.A., and Tank, D.W. (2009). Intracellular dynamics of hippocampal place cells during virtual navigation. *Nature*, 461:941–946.

Hawkins, C.A. and Mellanby, J.H. (1987). Limbic epilepsy induced by tetanus toxin: A longitudinal electroencephalographic study. *Epilepsia*, 28:431–444.

Higgs, M.H. and Spain, W.J. (2009). Conditional bursting enhances resonant firing in neocortical layer 2-3 pyramidal neurons. *J. Neurosci.*, 29:1285–1299.

Horn, B.K.P. and Schunck, B.G. (1981). Determining optical flow. *Artif. Intell.*, 17:185–203.

Hou, Q., Zhang, D., Jarzylo, L., Huganir, R.L., and Man, H.Y. (2008). Homeostatic regulation of AMPA receptor expression at single hippocampal synapses. *PNAS*, 105:775–780.

Ibata, K., Sun, Q., and Turrigiano, G.G. (2008). Rapid synaptic scaling induced by changes in postsynaptic firing. *Neuron*, 57:819–826.

Izhikevich, E., Gally, J., and Edelman, G. (2004). Spike-timing dynamics of neuronal groups. *Cereb. Cortex*, 14:933–944.

Izhikevich, E.M. (2006). Polychronization: computation with spikes. *Neural Comput.*, 18:245–282.

Jackson, A., Mavoori, J., and Fetz, E.E. (2006a). Long-term motor cortex plasticity induced by an electronic neural implant. *Nature*, 444:56–60.

Jackson, A., Moritz, C.T., Mavoori, J., Lucas, T.H., and Fetz, E.E. (2006b). The Neurochip BCI: towards a neural prosthesis for upper limb function. *IEEE Trans. Neural Syst. Rehabil. Eng.*, 14:187–190.

Jacobson, G., Diba, K., Yaron-Jakoubovitch, A., Oz, Y., Koch, C., Segev, I., *et al.* (2005). Subthreshold voltage noise of rat neocortical pyramidal neurones. *J. Physiol.*, 564:145–160.

Jimbo, Y., Tateno, T., and Robinson, H.P. (1999). Simultaneous induction of pathway-specific potentiation and depression in networks of cortical neurons. *Biophys. J.*, 76:670–678.

Josef, K., Saranak, J., and Foster, K.W. (2006). Linear systems analysis of the ciliary steering behavior associated with negative-phototaxis in chlamydomonas reinhardtii. *Cell Motil. Cytoskeleton*, 63:758–777.

Kayser, C., Logothetis, N.K., and Panzeri, S. (2010). Millisecond encoding precision of auditory cortex neurons. *PNAS*, 107:16976–16981.

Kispersky, T.J., Economo, M.N., Randeria, P., and White, J.A. (2011). GenNet: a platform for hybrid network experiments. *Front. Neuroinform.*, 5:11.

Krook-Magnuson, E., Armstrong, C., Oijala, M., and Soltesz, I. (2013). On-demand optogenetic control of spontaneous seizures in temporal lobe epilepsy. *Nat. Commun.*, 4.

Lampl, I., Reichova, I., and Ferster, D. (1999). Synchronous membrane potential fluctuations in neurons of the cat visual cortex. *Neuron*, 22:361–374.

Ledoux, E. and Brunel, N. (2011). Dynamics of networks of excitatory and inhibitory neurons in response to time-dependent inputs. *Front. Comput. Neurosci.*, 5:25.

Leifer, A.M., Fang-Yen, C., Gershow, M., Alkema, M.J., and Samuel, A.D.T. (2011). Optogenetic manipulation of neural activity in freely moving Caenorhabditis elegans. *Nat. Methods*, 8:147–152.

Lesica, N.A., Jin, J., Weng, C., Yeh, C.I., Butts, D., Stanley, G.B., *et al.* (2007). Adaptation to stimulus contrast and correlations during natural visual stimulation. *Neuron*, 55:479–491.

Leslie, K.R., Nelson, S.B., and Turrigiano, G.G. (2001). Postsynaptic depolarization scales quantal amplitude in cortical pyramidal neurons. *J. Neurosci.*, 21:RC170.

Lin, J.Y., Lin, M.Z., Steinbach, P., and Tsien, R.Y. (2009). Characterization of engineered channelrhodopsin variants with improved properties and kinetics. *Biophys. J.*, 96:1803–1814.

Lin, J.Y., Sann, S., Zhou, K., Nabavi, S., Proulx, C., Malinow, R., *et al.* (2013). Optogenetic Inhibition of Synaptic Release with Chromophore-Assisted Light Inactivation (CALI). *Neuron*, 79:241–253.

Lin, R.J., Bettencourt, J., White, J.A., Christini, D.J., and Butera, R.J. (2010). Real-time experiment interface for biological control applications. In *Proc. IEEE EMBS*, volume 2010, pages 4160–4163.

Litt, B. and Echauz, J. (2002). Prediction of epileptic seizures. *Lancet Neurol.*, 1:22–30.

Madhavan, R., Chao, Z.C., and Potter, S.M. (2007). Plasticity of recurring spatiotemporal activity patterns in cortical networks. *Phys. Biol.*, 4:181–193.

Magri, C., Whittingstall, K., Singh, V., Logothetis, N.K., and Panzeri, S. (2009). A toolbox for the fast information analysis of multiple-site LFP, EEG and spike train recordings. *BMC Neurosci.*, 10:81.

Mainen, Z.F. and Sejnowski, T.J. (1995). Reliability of spike timing in neocortical neurons. *Science*, 268:1503–1506.

Marder, E. and Goaillard, J.M. (2006). Variability, compensation and homeostasis in neuron and network function. *Nat. Rev. Neurosci.*, 7:563–574.

Marmont, G. (1949). Studies on the axon membrane. *J. Cell. Comp. Physiol.*, 34:351–381.

Martin, K.A.C. (2002). Microcircuits in visual cortex. *Curr. Opin. Neurobiol.*, 12:418–425.

Marvin, J.S., Borghuis, B.G., Tian, L., Cichon, J., Harnett, M.T., Akerboom, J., *et al.* (2013). An optimized fluorescent probe for visualizing glutamate neurotransmission. *Nat. Methods*, 10:162–170.

Mattis, J., Tye, K., Ferenczi, E., Ramakrishnan, C., O'Shea, D., Prakash, R., *et al.* (2011). Principles for applying optogenetic tools derived from direct comparative analysis of microbial opsins. *Nat. Methods*, 99:159–172.

McFarland, J.M., Cui, Y., and Butts, D.A. (2013). Inferring nonlinear neuronal computation based on physiologically plausible inputs. *PLoS Comput. Biol.*, 9:e1003143.

Miller, K. and MacKay, D. (1994). The role of constraints in Hebbian learning. *Neural Comput.*, 6:100–126.

Minerbi, A., Kahana, R., Goldfeld, L., Kaufman, M., Marom, S., and Ziv, N.E. (2009). Long-term relationships between synaptic tenacity, synaptic remodeling, and network activity. *PLoS Biol.*, 7:e1000136.

Miyashita, T., Shao, Y.R., Chung, J., Pourzia, O., and Feldman, D.E. (2013). Long-term channelrhodopsin-2 (ChR2) expression can induce abnormal axonal morphology and targeting in cerebral cortex. *Front. Neural Circuits*, 7:45.

Moritz, C.T., Perlmutter, S.I., and Fetz, E.E. (2008). Direct control of paralysed muscles by cortical neurons. *Nature*, 456:639–642.

Mormann, F., Andrzejak, R.G., Elger, C.E., and Lehnertz, K. (2007). Seizure prediction: the long and winding road. *Brain*, 130:314–33.

Morrell, M.J. (2011). Responsive cortical stimulation for the treatment of medically intractable partial epilepsy. *Neurology*, 77:1295–304.

Müller, J., Bakkum, D.J., and Hierlemann, A. (2013). Sub-millisecond closed-loop feedback stimulation between arbitrary sets of individual neurons. *Front. Neural Circuits*, 6:121.

Nagel, G., Brauner, M., Liewald, J.F., Adeishvili, N., Bamberg, E., and Gottschalk, A. (2005). Light activation of channelrhodopsin-2 in excitable cells of Caenorhabditis elegans triggers rapid behavioral responses. *Curr. Biol.*, 15:2279–2284.

Nagel, G., Szellas, T., Huhn, W., Kateriya, S., Adeishvili, N., Berthold, P., *et al.* (2003). Channelrhodopsin-2, a directly light-gated cation-selective membrane channel. *PNAS*, 100:13940–13945.

Nakanishi, K. and Kukita, F. (1998). Functional synapses in synchronized bursting of neocortical neurons in culture. *Brain Res.*, 795:137–146.

Neef, A., El Hady, A., Nagpal, J., Broeking, K., Afshar, G., Geisel, T., *et al.* (2011). Continuous dynamic photostimulation - delivering defined, in-vivo-like fluctuating stimuli with channelrhodopsins. In *Neurosci. Meet. Plan.*, volume 225.05. Washington, DC.

Nelson, T.S., Suhr, C.L., Freestone, D.R., Lai, A., Halliday, A.J., Mclean, K.J., *et al.* (2011). Closed-loop seizure control with very high frequency electrical stimulation at seizure onset in the Gaers model of absence epilepsy. *Int. J. Neural Syst.*, 21:163–173.

Nerbonne, J., Richard, S., Nargeot, J., and Lester, H. (1984). New photoactivatable cyclic nucleotides produce intracellular jumps in cyclic AMP and cyclic GMP concentrations. *Nature*, 310:74–76.

Newman, J.P., Zeller-Townson, R., Fong, M.f., Desai, S.A., and Potter, S.M. (2013). Closed-loop, multichannel experimentation using the open-source NeuroRighter electrophysiology platform. *Front. Neural Circuits*, 6:98.

Nita, D.a., Cissé, Y., Timofeev, I., and Steriade, M. (2006). Increased propensity to seizures after chronic cortical deafferentation in vivo. *J. Neurophysiol.*, 95:902–913.

O'Connor, D.H., Hires, S.A., Guo, Z.V., Li, N., Yu, J., Sun, Q.Q., *et al.* (2013). Neural coding during active somatosensation revealed using illusory touch. *Nat. Neurosci.*, 16:958–965.

O'Donovan, M.J., Chub, N., and Wenner, P. (1998). Mechanisms of spontaneous activity in developing spinal networks. *J. Neurobiol.*, 37:131–145.

Oja, E. (1982). A simplified neuron model as a principal component analyzer. *J. Math. Biology*, 15:267–273.

Okun, M. and Lampl, I. (2008). Instantaneous correlation of excitation and inhibition during ongoing and sensory-evoked activities. *Nat. Neurosci.*, 11:535–537.

Ostojic, S. and Brunel, N. (2011). From spiking neuron models to linear-nonlinear models. *PLoS Comput. Biol.*, 7:e1001056.

Paninski, L. (2003). Convergence properties of three spike-triggered analysis techniques. *Network-Comp. Neural*, 14:437–464.

Paz, J.T., Davidson, T.J., Frechette, E.S., Delord, B., Parada, I., Peng, K., *et al.* (2012). Closed-loop optogenetic control of thalamus as a tool for interrupting seizures after cortical injury. *Nat. Neurosci.*, 16:64–70.

Pillow, J.W., Shlens, J., Paninski, L., Sher, A., Litke, A.M., Chichilnisky, E.J., *et al.* (2008). Spatio-temporal correlations and visual signalling in a complete neuronal population. *Nature*, 454:995–999.

Pitkow, X. and Meister, M. (2012). Decorrelation and efficient coding by retinal ganglion cells. *Nat. Neurosci.*, 15:628–635.

Poggio, G. and Viernstein, L. (1964). Time series analysis of impulse sequences of thalamic somatic sensory neurons. *J. Neurophysiol.*, 27:517–545.

Potter, S. (2001). Distributed processing in cultured neuronal networks. *Prog. Brain Research*, 130:49–62.

Potter, S.M. and DeMarse, T.B. (2001). A new approach to neural cell culture for long-term studies. *J. Neurosci. Methods*, 110:17–24.

Prinz, A.A., Abbott, L.F., and Marder, E. (2004). The dynamic clamp comes of age. *Trends Neurosci.*, 27:218–24.

Puchalla, J.L., Schneidman, E., Harris, R.a., and Berry, M.J. (2005). Redundancy in the population code of the retina. *Neuron*, 46:493–504.

Raimondo, J., Kay, L., Ellender, T., and Akerman, C. (2012). Optogenetic silencing strategies differ in their effects on inhibitory synaptic transmission. *Nat. Neurosci.*, 15:1102–1104.

Ramakers, G., Corner, M., and Habets, A. (1990). Development in the absence of spontaneous bioelectric activity results in increased stereotyped burst firing in cultures of dissociated cerebral cortex. *Exp. Brain. Res.*, 79:157–166.

Ramirez, S., Liu, X., Lin, P.A., Suh, J., Pignatelli, M., Redondo, R.L., *et al.* (2013). Creating a false memory in the hippocampus. *Science*, 341:387–391.

Reger, B.D., Fleming, K.M., Sanguineti, V., and Alford, S. (2000). Connecting brains to robots: an artificial body for studying the computational properties of neural tissues. *Artif. Life*, 324:307–324.

Reutsky-Gefen, I., Golan, L., Farah, N., Schejter, A., Tsur, Land Brosh, I., and Shoham, S. (2013). Holographic optogenetic stimulation of patterned neuronal activity for vision restoration. *Nat. Commun.*, 4:1509.

Rich, M.M. and Wenner, P. (2007). Sensing and expressing homeostatic synaptic plasticity. *Trends Neurosci.*, 30:119–125.

Rieke, F., Bodnar, D.A., and Bialek, W. (1995). Naturalistic stimuli increase the rate and efficiency of information transmission by primary auditory afferents. *Proc. R. Soc. B*, 262:259–265.

Rieke, F., Warland, D., de Ruyter van Steveninck, R., and Bialek, W. (1997). *Spikes: Exploring the Neural Code*. MIT Press.

Robinson, J.T., Jorgolli, M., Shalek, A.K., Yoon, M.H., Gertner, R.S., and Park, H. (2012). Vertical nanowire electrode arrays as a scalable platform for intracellular interfacing to neuronal circuits. *Nat. Nanotechnol.*, 7:180–184.

Rolston, J.D., Gross, R.E., and Potter, S.M. (2009a). A low-cost multielectrode system for data acquisition enabling real-time closed-loop processing with rapid recovery from stimulation artifacts. *Front. Neuroeng.*, 2:12.

Rolston, J.D., Gross, R.E., and Potter, S.M. (2009b). Common median referencing for improved action potential detection with multielectrode arrays. In *Conf. Proc. IEEE Eng. Med .Biol. Soc.*, pages 1604–1607.

Rolston, J.D., Gross, R.E., and Potter, S.M. (2010). Closed-loop, open-source electrophysiology. *Front. Neurosci.*, 4:31.

Rolston, J.D., Wagenaar, D.A., and Potter, S.M. (2007). Precisely timed spatiotemporal patterns of neural activity in dissociated cortical cultures. *Neuroscience*, 148:294–303.

Rosin, B., Slovik, M., Mitelman, R., Rivlin-Etzion, M., Haber, S.N., Israel, Z., *et al.* (2011). Closed-loop deep brain stimulation is superior in ameliorating parkinsonism. *Neuron*, 72:370–84.

Roy, S.A. and Alloway, K.D. (2001). Coincidence detection or temporal integration? What the neurons in somatosensory cortex are doing. *J. Neurosci.*, 21:2462–73.

Sáez, I. and Friedlander, M.J. (2009). Synaptic output of individual layer 4 neurons in guinea pig visual cortex. *J. Neurosci.*, 29:4930–4944.

Salinas, E. and Sejnowski, T. (2001). Correlated neuronal activity and the flow of neural information. *Nat. Rev. Neurosci.*, 2:539–550.

Schneidman, E., Berry, M.J., Segev, R., and Bialek, W. (2006). Weak pairwise correlations imply strongly correlated network states in a neural population. *Nature*, 440:1007–1012.

Schneidman, E., Bialek, W., and Berry, M.J. (2003). Synergy, redundancy, and independence in population codes. *J. Neurosci.*, 23:11539–11553.

Shannon, C. (1948). A mathematical theory of communication. *AT&T Tech. J.*, 27:379–423.

Shannon, C. and Weaver, W. (1949). *The Mathematical Theory of Communication*. University of Illinois Press, Champaign, IL.

Sharon, D. and Grinvald, A. (2002). Dynamics and constancy in cortical spatiotemporal patterns of orientation processing. *Science*, 295:512–515.

Sharpee, T., Rust, N., and Bialek, W. (2004). Analyzing neural responses to natural signals: maximally informative dimensions. *Neural Comput.*, 250:223–250.

Shimazaki, H. and Shinomoto, S. (2010). Kernel bandwidth optimization in spike rate estimation. *J. Comput. Neurosci.*, 29:171–182.

Simons, D., Carvell, G., Hershey, A., and Bryant, D. (1992). Responses of barrel cortex neurons in awake rats and effects of urethane anesthesia. *Exp. Brain Res.*, 91:259–272.

Softky, W.R. and Koch, C. (1992). Cortical Cells Should Fire Regularly, But Do Not. *Neural Comput.*, 4:643–646.

Softky, W.R. and Koch, C. (1993). The highly irregular firing of cortical cells is inconsistent with temporal integration of random EPSPs. *J. Neurosci.*, 13:334–350.

Sohal, V.S., Zhang, F., Yizhar, O., and Deisseroth, K. (2009). Parvalbumin neurons and gamma rhythms enhance cortical circuit performance. *Nature*, 459:698–702.

Song, S., Miller, K.D., and Abbott, L.F. (2000). Competitive Hebbian learning through spike-timing-dependent synaptic plasticity. *Nat. Neurosci.*, 3:919–926.

Stanley, G.B. (2013). Reading and writing the neural code. *Nat. Neurosci.*, 16:259–263.

Steinmetz, M., Motter, B., Duffy, C., and Mountcastle, V. (1987). Functional properties of parietal visual neurons: radial organization of directionalities within the visual field. *J. Neurosci.*, 7:177–191.

Stellwagen, D. and Malenka, R.C. (2006). Synaptic scaling mediated by glial TNF-alpha. *Nature*, 440:1054–1059.

Stirman, J.N., Crane, M.M., Husson, S.J., Wabnig, S., Schultheis, C., Gottschalk, A., *et al.* (2011). Real-time multimodal optical control of neurons and muscles in freely behaving Caenorhabditis elegans. *Nat. Methods*, 8:153–158.

Strong, S.P., Koberle, R., de Ruyter Van Stevenvick, R.R., and Bialek, W. (1998). Entropy and Information in Neural Spike Trains. *Phys. Rev. Lett.*, 80:197–200.

Sun, F.T., Morrell, M.J., and Wharen, R.E. (2008). Responsive cortical stimulation for the treatment of epilepsy. *Neurotherapeutics*, 5:68–74.

Supèr, H. and Roelfsema, P.R. (2005). Chronic multiunit recordings in behaving animals: advantages and limitations. *Prog. Brain Res.*, 147:263–282.

Sutton, M.A., Ito, H.T., Cressy, P., Kempf, C., Woo, J.C., and Schuman, E.M. (2006). Miniature neurotransmission stabilizes synaptic function via tonic suppression of local dendritic protein synthesis. *Cell*, 125:785–799.

Tchumatchenko, T., Geisel, T., Volgushev, M., and Wolf, F. (2010). Signatures of synchrony in pairwise count correlations. *Front. Comput. Neurosci.*, 4:1.

Tchumatchenko, T., Malyshev, A., Wolf, F., and Volgushev, M. (2011). Ultrafast Population Encoding by Cortical Neurons. *J. Neurosci.*, 31:12171–12179.

Tchumatchenko, T., Newman, J.P., Fong, M.f., and Potter, S.M. (2013). Delivery of continuously-varying stimuli using ChR2. *Front. Neural Circuits*, In Press.

Topolnik, L., Steriade, M., and Timofeev, I. (2003). Partial cortical deafferentation promotes development of paroxysmal activity. *Cereb. Cortex.*, 13:883–893.

Truccolo, W., Eden, U., Fellows, M.R., Donoghue, J.P., and Brown, E. (2005). A point process framework for relating neural spiking activity to spiking history, neural ensemble, and extrinsic covariate effects. *J. Neurophysiol.*, 93:1074–1089.

Turrigiano, G. (2011a). Homeostatic Synaptic Plasticity: Local and Global Mechanisms for Stabilizing Neuronal Function. *Cold Spring Harb. Perspect. Biol.*, 4:1–17.

Turrigiano, G. (2011b). Too many cooks? Intrinsic and synaptic homeostatic mechanisms in cortical circuit refinement. *Annu. Rev. Neurosci.*, 34:89–103.

Turrigiano, G., Abbott, L.F., and Marder, E. (1994). Activity-dependent changes in the intrinsic properties of cultured neurons. *Science*, 264:974–977.

Turrigiano, G. and Nelson, S. (2004). Homeostatic plasticity in the developing nervous system. *Nat. Rev. Neurosci.*, 5:97–107.

Turrigiano, G.G., Leslie, K.R., Desai, N.S., Rutherford, L.C., and Nelson, S.B. (1998). Activity-dependent scaling of quantal amplitude in neocortical neurons. *Nature*, 391:892–896.

van Vreeswijk, C. and Sompolinsky, H. (1996). Chaos in neuronal networks with balanced excitatory and inhibitory activity. *Science*, 274:1724–1726.

van Vreeswijk, C. and Sompolinsky, H. (1998). Chaotic balanced state in a model of cortical circuits. *Neural Comput.*, 10:1321–1371.

Velliste, M., Perel, S., Spalding, M.C., Whitford, A.S., and Schwartz, A.B. (2008). Cortical control of a prosthetic arm for self-feeding. *Nature*, 453:1098–1101.

Vogels, T., Rajan, K., and Abbott, L. (2005). Neural network dynamics. *Ann. Rev. Neurosci.*, 28:357–376.

Vogels, T.P. and Abbott, L.F. (2009). Gating multiple signals through detailed balance of excitation and inhibition in spiking networks. *Nat. Neurosci*, 12:483–491.

Volgraf, M., Gorostiza, P., Numano, R., Kramer, R.H., Isacoff, E.Y., and Trauner, D. (2006). Allosteric control of an ionotropic glutamate receptor with an optical switch. *Nat. Chem. Biol.*, 2:47–52.

von der Malsburg, C. (1973). Self-organization of orientation sensitive cells in the striate cortex. *Kybernetik*, 14:85–100.

Wagenaar, D., DeMarse, T.B., and Potter, S.M. (2006a). MEABench: A toolset for multi-electrode data acquisition and on-line analysis. In *Proc. 2nd Int. IEEE EMBS Conf. on Neural Eng.*, pages 518–521.

Wagenaar, D.A. (2006). *Development and Control of Epileptiform Bursting in Dissociated Cortical Cultures*. Ph.D. thesis, California Institute of Technology.

Wagenaar, D.A. (2012). An optically stabilized fast-switching light emitting diode as a light source for functional neuroimaging. *PloS One*, 7:e29822.

Wagenaar, D.A., Madhavan, R., Pine, J., and Potter, S.M. (2005). Controlling bursting in cortical cultures with closed-loop multi-electrode stimulation. *J. Neurosci.*, 25:680–688.

Wagenaar, D.A., Nadasdy, Z., and Potter, S.M. (2006b). Persistent dynamic attractors in activity patterns of cultured neuronal networks. *Phys. Rev. E: Stat., Nonlinear, Soft Matter Phys.*, 73:51907.

Wagenaar, D.A., Pine, J., and Potter, S.M. (2004). Effective parameters for stimulation of dissociated cultures using multi-electrode arrays. *J. Neurosci. Methods*, 138:27–37.

Wagenaar, D.A., Pine, J., and Potter, S.M. (2006c). An extremely rich repertoire of bursting patterns during the development of cortical cultures. *BMC Neurosci.*, 7:11.

Wagenaar, D.A. and Potter, S.M. (2002). Real-time multi-channel stimulus artifact suppression by local curve fitting. *J. Neurosci. Methods*, 120:113–120.

Wagenaar, D.A. and Potter, S.M. (2004). A versatile all-channel stimulator for electrode arrays, with real-time control. *J. Neural. Eng.*, 1:39–45.

Wallach, A., Eytan, D., Gal, A., Zrenner, C., and Marom, S. (2011). Neuronal response clamp. *Front. Neuroeng.*, 4:3.

Wang, Q., Millard, D.C., Zheng, H.J.V., and Stanley, G.B. (2012). Voltage-sensitive dye imaging reveals improved topographic activation of cortex in response to manipulation of thalamic microstimulation parameters. *J. Neural Eng.*, 9:026008.

Wang, Q., Webber, R.M., and Stanley, G.B. (2010). Thalamic synchrony and the adaptive gating of information flow to cortex. *Nat. Neurosci.*, 13:1534–1541.

Warland, D., Landolfa, M., Miller, J.P., and Bialek, W. (1992). Reading between the spikes in the cereal filiform hair receptors of the cricket. In *Analysis and modeling of neural systems*, pages 327–333. Springer.

Warland, D.K., Reinagel, P., and Meister, M. (1997). Decoding visual information from a population of retinal ganglion cells. *J. Neurophysiol.*, 78:2336–5230.

Wilhelm, J.C. and Wenner, P. (2008). GABAA transmission is a critical step in the process of triggering homeostatic increases in quantal amplitude. *PNAS*, 105:11412–11417.

Witt, A., Palmigiano, A., Neef, A., El Hady, A., Wolf, F., and Battaglia, D. (2013). Controlling the oscillation phase through precisely timed closed-loop optogenetic stimulation: a computational study. *Front. Neural Circuits*, 7:49.

Xu, R. and Wunsch, D.C. (2009). *Clustering*. John Wiley & Sons, Oxford, UK.

Yizhar, O., Fenno, L.E., Davidson, T.J., Mogri, M., and Deisseroth, K. (2011a). Optogenetics in neural systems. *Neuron*, 71:9–34.

Yizhar, O., Fenno, L.E., Prigge, M., Schneider, F., Davidson, T.J., OShea, D.J., *et al.* (2011b). Neocortical excitation/inhibition balance in information processing and social dysfunction. *Nature*, 477:171–178.

Yu, Y., Crumiller, M., Knight, B., and Kaplan, E. (2010). Estimating the amount of information carried by a neuronal population. *Front. Comput. Neurosci.*, 4.

Zanos, S., Richardson, A.G., Shupe, L., Miles, F.P., and Fetz, E.E. (2011). The Neurochip-2: an autonomous head-fixed computer for recording and stimulating in freely behaving monkeys. *IEEE Trans. Neural Syst. Rehabil. Eng.*, 19:427–435.

Zeller-Townson, R., Ben-Ary, G., and Gamblen, P. (2011). Silent barrage: interactive neurobiological art. *Proc. 8th ACM Conf. on Creativity and Congnition*, pages 407–408.

Zemelman, B., Lee, G., Ng, M., and Miesenböck, G. (2002). Selective photostimulation of genetically chARGed neurons. *Neuron*, 33:15–22.

Zhang, F., Vierock, J., Yizhar, O., Fenno, L., and Tsunoda, S. (2011). The Microbial Opsin Family of Optogenetic Tools. *Cell*, 147:1446–1457.

Zhang, F., Wang, L., Boyden, E., and Deisseroth, K. (2006). Channelrhodopsin-2 and optical control of excitable cells. *Nat. Methods*, 3:785–792.

Zhao, S., Cunha, C., Zhang, F., and Liu, Q. (2008). Improved expression of halorhodopsin for light-induced silencing of neuronal activity. *Brain Cell Biol.*, 36:141–154.